Transiting Super-Earth Exoplanets: Search and Characterisation

by

Diana Dragomir

B.Sc., McGill University, 2005
M.Sc., McGill University, 2008

A THESIS SUBMITTED IN PARTIAL FULFILLMENT OF
THE REQUIREMENTS FOR THE DEGREE OF

DOCTOR OF PHILOSOPHY

in

The Faculty of Graduate Studies

(Astronomy)

THE UNIVERSITY OF BRITISH COLUMBIA

(Vancouver)

November 2012

Abstract

The only way to measure the diameter of a planet outside the Solar System is if it transits its host star. Transit data combined with radial velocity (RV) data give an exoplanet's mass. Mass and volume yield density, so transits give unique insights into the interior structure of an exoplanet. Super-Earths are a class of exoplanet with masses a few times that of Earth, for which no examples exist in our Solar System.

The goals of this thesis: to detect and characterise transits of exoplanets (particularly super-Earths) discovered via RV surveys orbiting bright stars. The observational tool: MOST (Microvariability & Oscillations of STars) - a microsatellite housing an optical telescope which can monitor stars with high precision. We searched 12 super-Earth candidate systems, applying special data reduction and analysis techniques. The search gives upper limits on the transit depths of 11 of the planets. For GJ 581 e (innermost planet of an M dwarf system), the 1σ upper limit excludes most transiting configurations for a planet with water ice or H/He compositions. MOST data of HD 97658 rejected a claim of a transit detection in this system. The timely MOST rejection cancelled observatory programmes dedicated to follow up on the transit claim, preventing the waste of valuable time on major facilities.

In parallel with the MOST survey, we analysed a decade of ground-based photometry to exclude most transiting configurations for the massive exoplanet HD 192263 b. We showed that the star's rotation period does not coincide with the planet's orbital period, as was previously reported. We also find evidence for an 8-year activity cycle in the host star.

The twelfth star in the MOST survey is 55 Cancri, whose innermost planet (55 Cnc e) has an orbital period of less than a day and transits the star. We present 42 days of new MOST photometry of this system,

and derive one of the most precise radius values (1.99 ± 0.08 Earth radii) known for any super-Earth. We explore the possibility of star-exoplanet interaction, and set a limit on the albedo (reflectivity) of the planet, which has implications for its atmospheric composition.

Preface

This thesis is partly based on three published papers and a fourth that is in preparation.

The code used for the reduction of MOST photometry was written by Jason Rowe (NASA Ames Research Center). I have used this code for the reduction of all the MOST photometry presented in this thesis.

I have reduced, analysed and interpreted the photometry presented in Chapter 4 myself.

The work presented in Chapter 6 has been published in the *Astrophysical Journal*: Dragomir, Diana; Kane, Stephen R.; Henry, Gregory W.; Ciardi, David R.; Fischer, Debra A.; Howard, Andrew W.; Jensen, Eric L. N.; Laughlin, Gregory; Mahadevan, Suvrath; Matthews, Jaymie M.; Pilyavsky, Genady; von Braun, Kaspar; Wang, Sharon X.; Wright, Jason T., 2012, ApJ, 754, 37. I have carried out the analysis of the photometry and radial velocity data and interpretation of the results myself, with a few suggestions from Jaymie Matthews (University of British Columbia) and Stephen Kane (Caltech). I wrote most of the paper with the exception of Section 6.3, which was written by Stephen Kane. The APT photometry was acquired and reduced by Gregory Henry (Tennessee State University). The code used for the Fourier analysis (*Period04*) was developed by Patrick Lenz and Michel Breger (both at University of Vienna). The radial velocity measurements were obtained by Andrew Howard (University of Hawaii), while the code used to analyse them was developed by Sharon Wang and Jason Wright (both at Pennsylvania State University). The SME analysis was done by Debra Fischer (Yale University).

The research presented in Chapter 7 has been published in the *Astrophysical Journal*: Dragomir, Diana; Matthews, Jaymie M.; Kuschnig, Rainer;

Rowe, Jason F.; Gladman, Brett J.; Guenther, David B.; Moffat, Anthony F. J.; Rucinski, Slavek M.; Sasselov, Dimitar; Weiss, Werner W., 2012, ApJ, 759, 2. For these observations on GJ 581, I have done the data reduction, analysis, interpretation and paper writeup myself. I have also written the code used for the artificial transit injection and recovery procedure. For the Fourier analysis, I again used *Period04* which was developed by Patrick Lenz and Michel Breger.

The research presented in Chapter 8 has been published in the *Astrophysical Journal Letters*: Dragomir, Diana; Matthews, Jaymie M.; Howard, Andrew W.; Antoci, Victoria; Henry, Gregory W.; Guenther, David B.; Johnson, John A.; Kuschnig, Rainer; Marcy, Geoffrey W.; Moffat, Anthony F. J.; Rowe, Jason F.; Rucinski, Slavek M.; Sasselov, Dimitar; Weiss, Werner W., 2012, ApJL, 759, L41. For this work on HD 97658b, I have done the data reduction, analysis and interpretation of the photometric data myself. I have also written most of the paper myself, with the exception of Section 8.3, which was written by Andrew Howard. The acquisition, reduction and analysis of the radial velocity measurements, as well as the figures pertaining to Section 8.3 were also done by Andrew Howard.

I wrote the draft of a manuscript on the new MOST photometry of the 55 Cnc system (acquired in 2012), so a paper is currently in preparation. This includes the work described in Chapter 9. I led the study pertaining to these data. I reduced the photometry, developed a Markov Chain Monte Carlo code and used it to analyse the photometry. I am also responsible for the interpretation of the results.

Table of Contents

Appendix

List of Tables

List of Figures

List of Abbreviations

APT	Automated Photoelectric Telescope
AU	Astronomical Unit
CCD	Charged Coupled Device
CVZ	Continuous Viewing Zone
MOST	Microvariability and Oscillations of STars
RM	Rossiter-McLaughlin
RV	Radial Velocity
SSA	South Atlantic Anomaly
SSZ	Sun Sensor Zone
TERMS	Transit Ephemeris Refinement and Monitoring Survey

Acknowledgements

I would like to thank my high school science teachers, Lise Provost who encouraged me through science fairs despite my teenage shyness, and Mary Zarif who helped inspire both a love of science and a love of teaching. I am grateful to Robert Rutledge for his encouragement and supervision of my first real research project in astronomy during my undergraduate studies at McGill University. Andrew Cumming has sparked my interest in exoplanet research, and has maintained it through two years of patient and supportive advising during my Master's degree.

Thanks to fellow McGill officemate and Master's student Hugo Olivares for triggering constructively distractive conversations on a variety of topics (sometimes I triggered them too). During the four years I spent at UBC, I have met many other grad students who have made my academic and social life that much more pleasant. I would like to thank Thomas Pfrommer, Kelsey Hoffman, Ronald Gagne, Sanaz Vafaei, Laura Kasian, Stephanie Flynn and Melissa Anholm for listening, supporting or commiserating with me as befit the situation. Yet many more were the good times sharing laughs or life philosophies over drinks. Victoria Antoci and Thomas Kallinger have always been ready to offer guidance for my work and contributed to many insightful conversations. I will always count them among my friends.

I am grateful to Kaspar von Braun, Christian Schwab, David Ciardi, Greg Henry, Suvrath Mahadevan, Peter McCullough, Heather Knutson, Jason Wright, Zach Gazak, Brett Gladman, Bekki Dawson and Josh Winn for fruitful discussions and useful recommendations during the write-up of manuscripts of which we shared authorship. I wish to thank the MOST Science Team - Jason Rowe, Dimitar Sasselov, Anthony Moffat, Werner Weiss, David Guenther and Slavek Rucinski - as well as collaborators Michaël Gillon and Andrew Howard for their valuable contributions to several aspects of the research presented in this thesis. A big thank you goes to Jamie Wells for his part in scheduling the MOST observations on which most of this thesis is based. I also thank my Ph.D. supervisory committee for constructive advice and comments on my work. I am especially grateful to my visiting fellowship advisor at IPAC, Stephen Kane, who has welcomed me into the

TERMS collaboration and given me the opportunity to expand my professional horizon in countless ways. I wish to thank him for his unfailing encouragement, boundless enthusiasm and geniality.

I would not have completed this thesis without the patient guidance and expertise of my Ph.D. supervisor Jaymie Matthews. He has encouraged my research even as it sometimes went in unplanned directions, which has led to interesting projects and new collaborations. I thank him for sharing his vast knowledge and providing me with advice and resources as needed, yet allowing me to follow my own work style. His passion for astronomy is inspiring and reminds me of why I chose to become an astronomer.

I wish to thank Camille Bélanger-Champagne, Agnieszka Barszcz and Cédric Migliorini for their continuing friendship since our undergraduate days. I am glad to have had their support despite the distance and I cherish every get-together we've had. I have made many friends in Vancouver, all of whom have contributed to making the four years I have spent in this city unforgettably fantastic. Thank you Nam Musterer, Carmen and Jakob Emmel, Michael McCormick, Jaya Viswanathan, Thomas Pfrommer, Vichi Antoci and Christina Schallenberg for being by my side during the good times and the less good, for your helpful advice and for reminding me to make time to enjoy this beautiful city we live in.

I am infinitely grateful to Francis for being a constant source of love and strength in my life. You have helped me surmount the obstacles and reminded me to be proud of my achievements. Thank you for knowing when to hold my hand and when to let go. Thank you for always believing in me.

I thank my parents and my sister for pushing me to persevere, for encouraging my studies, for inspiring me to be brave and follow my dreams. Thank you for putting things in perspective when I did not remember how to do it myself. Your unconditional love and support have always seen me through my endeavors, and especially through this degree.

I acknowledge support from a Fonds Québécois de Recherche sur la Nature et les Technologies Doctoral Research Scholarship. Part of the research presented in this thesis was supported by a Infrared Processing and Analysis Center/California Institute of Technology Visiting Graduate Student Fellowship. I also acknowledge support from a UBC Four-Year Fellowship. This research has made use of the Exoplanet Orbit Database and the Exoplanet Data Explorer at exoplanets.org.

Dedication

To my parents and sister.

Chapter 1

Introduction

The first confirmed and widely accepted exoplanet was discovered in 1992 orbiting a pulsar [264]. In 1995, the first exoplanet around a main-sequence star was announced [1] [171]. Since then, the rate of exoplanet discoveries has been steadily increasing. Over 770 exoplanets (including nearly 100 multiple-planet systems) and more than 2300 exoplanet candidates are currently known.

These planets have turned out to be very different from those within our Solar System. Most of the confirmed exoplanets are gas giants that orbit very close to their host stars with periods of only a few days. Many of them have low densities compared to "local" giant planets like Jupiter and Neptune. There are also exoplanets with larger but very eccentric orbits. These unexpected properties of exoplanets (e.g. Jupiter-mass planets in small orbits, high orbital eccentricities, orbits highly inclined and even retrograde compared to the spin of the host star, etc.) have raised new challenges for planet formation and evolution as well as for understanding their dynamical history.

This chapter provides an overview of the techniques used for exoplanet detection and the properties of currently known exoplanets.

[1] It should be noted that the first exoplanet detection and the first detection of an exoplanet around a main-sequence star (γ Cephei b) was made in 1988 [41]. However, it was only confirmed in 2002 [105]. The planet HD 114762b was first detected in 1989 [144], but was also fully confirmed only several years later.

1.1 Detection and Characterisation Techniques

1.1.1 Pulsar Timing

The first planets outside the Solar System were discovered orbiting the pulsar PSR 1257+12 [264]. Pulsars, the dense rapidly spinning remnants of stars which have undergone a supernova explosion, have very regular rotation periods which can be measured with great precision by the arrival times of radio pulses as a pulsar's radio beams sweep over the Earth. Thus, changes in the regular arrival times and anomalies in the timing of the radio pulses are readily detected. In the case of PSR 1257+12, such irregularities indicated the presence of three sub-stellar companions that have masses comparable to that of the Earth [263].

It is not yet clear how these planets came to be. If they formed prior to the star's transformation into a pulsar, they would have been unlikely to survive the supernova explosion. The planets around PSR 1257+12 are believed to have formed from a protoplanetary disk left over by the supernova or by the dynamical disruption of a binary companion [62, 186].

Since 1992, astronomers have found evidence for planetary mass companions around two other pulsars. PSR 1719-14 hosts a Jupiter-mass, but very dense companion which is likely an ultra low-mass carbon white dwarf [7]. Its high density and pressure suggest it is likely crystallized, leading to the object's "diamond planet" label. PSR B1620-26 b is a planet candidate orbiting a pulsar-white dwarf binary located near the core of a globular cluster [6, 216].

1.1.2 The Radial Velocity (RV) Method

The most quantitatively productive detection method so far has been the radial velocity method, having led to the discovery of about 450 exoplanets since 1995 and the confirmation of nearly 250 more.

A star with a companion moves in an orbit around the center of mass of the system, and so does the companion. If the companion is a planet, it is generally too faint to be detected directly from the light it reflects and emits.

However, the motion it induces in the star leads to small periodic shifts in the wavelengths of the stellar spectral lines, called Doppler shifts. The lines are slightly shifted towards shorter wavelengths as the star approaches the observer, and towards longer wavelengths as the star moves away from the observer in its tiny orbit around the centre of mass of the system. As an example, Jupiter induces a velocity variation in the Sun's motion of 12 m/s with a period of 12 years. The closer a planet orbits its parent star, and the more massive it is, the larger the velocity variation induced in the star.

Evidently, RVs must first be corrected for the orbital motion of the Earth. Once this is accomplished, the RV measurements allow the orbital parameters (period, eccentricity, semi-major axis, time of periastron and argument of periastron[2]) of the planet to be determined. However, since this method delivers only the stellar velocity component along the line of sight, no information about the orbital inclination (i) relative to the plane of the sky is obtained. Still, this sets a lower limit on the true stellar velocity relative to the centre of mass and therefore, if the mass of the star can be estimated (generally from its spectral type and luminosity class, or increasingly often from asteroseismology), a lower limit on the mass of the exoplanet. The minimum mass ($M_p \sin i$) is the true mass (M_p) only if the orbital inclination is 90°.

The first attempts at detecting unseen companions around main-sequence stars using the radial velocity method began in 1979 [40]. In 1995 the technique was employed, via the ELODIE spectrograph, in the discovery of 51 Pegasi b, the first announced planet to orbit a main-sequence star other than our Sun [171]. This gas giant, which orbits very close to its star with a period of just 4.23 days, also became the first of a new class of planets called 'hot Jupiters'.

A RV precision of 13 m/s [171] was sufficient to measure the signal induced by 51 Pegasi b on its parent star (see Figure 1.1). Today, RV variations of exoplanet host stars can be detected with measurement errors down to about 1 m/s [116, 183] and sometimes even smaller using high-resolution,

[2]The argument of periastron describes the orientation of the planet's orbit relative to the line of sight. It is undefined for a circular orbit.

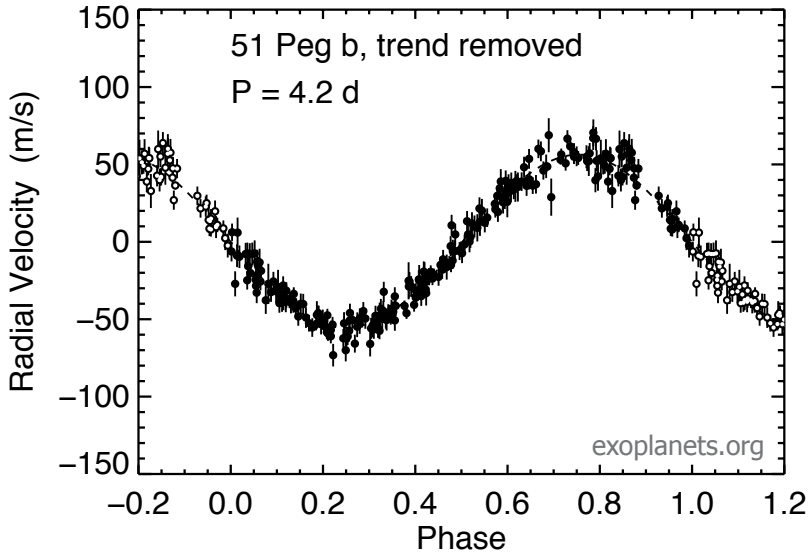

Figure 1.1: Radial velocity measurements of 51 Peg b plotted as a function of the planet's orbital phase. A long term trend present in the radial velocities was removed prior to folding the measurements at the planet's period. The data was obtained from the Exoplanet Orbit Database [268] and the figure was produced interactively using the Exoplanet Data Explorer at exoplanets.org.

high-precision spectrographs such as HARPS (High Accuracy Radial Velocity Planet Searcher) [184] at the La Silla Observatory in Chile and HIRES (High Resolution Echelle Spectrometer) [35] at the Keck Observatory in Hawaii. Such high-precision radial velocities enable the detection of exoplanets with masses as low as a few times that of the Earth (now known as super-Earths).

To calibrate spectroscopic RV measurements, either the simultaneous thorium-argon or the iodine cell techniques are used. The former technique, employed on the HARPS instrument, involves two side-by-side fibers: one receives the light from the star being observed while the other is illuminated with a thorium-argon lamp [11]. The spectra from the two fibers are recorded

simultaneously to minimise any instrumental shifts, and then compared in order to search for minute Doppler shifts in the lines of the stellar spectrum. Alternatively, a glass cell containing iodine gas can be placed in the path of the star light, superimposing the iodine lines on the stellar spectrum [163]. Any shifts in the spectral lines of the star can then be measured against the well known wavelengths of the iodine lines. This is the technique used by HIRES. Though both techniques have led to numerous exoplanet discoveries, they are limited to observations of relatively bright stars (generally $V < 10$, with some M dwarfs as faint as $V \approx 12$) because of the large dispersion of light required for high spectral resolution.

1.1.3 The Transit Method

A small fraction of exoplanetary systems have orbits whose planes are sufficiently closely aligned with our line of sight that we see the planet passing in front of the disk of the parent star, resulting in a tiny drop in the observed brightness of the star. Such a transit event can provide a wealth of information about the planet which cannot otherwise be obtained. Transits occur once every orbital period of the exoplanet. The relative decrease in flux caused by the planet blocking out part of the starlight during transit is

$$\frac{\Delta F}{F} = \left(\frac{R_p}{R_\star}\right)^2, \tag{1.1}$$

where R_P is the planetary radius and $R_\star$ is the stellar radius. This simple equation does not take into account limb darkening (the diminishing of the intensity of the stellar disk away from its centre due to the fact that light is escaping from shallower depths in the star - hence dominated by less dense gas of cooler temperatures - close to the observed limb, or edge, of the stellar disk) but provides a good first approximation of the transit depth. An example of a light curve with periodic planetary transits is shown in Figure 1.2. A single transit with a best-fitting transit model superimposed is seen in Figure 1.3.

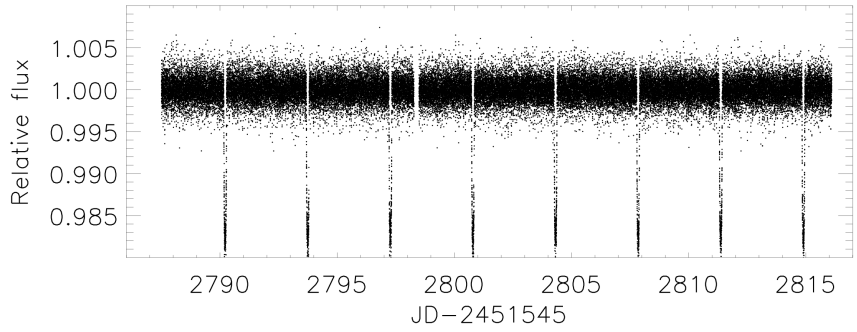

Figure 1.2: Light curve of HD 209458, showing several transits of HD 209458b with a period of 3.52 days. The photometry was acquired with the MOST space telescope (see Section 3.1.1).

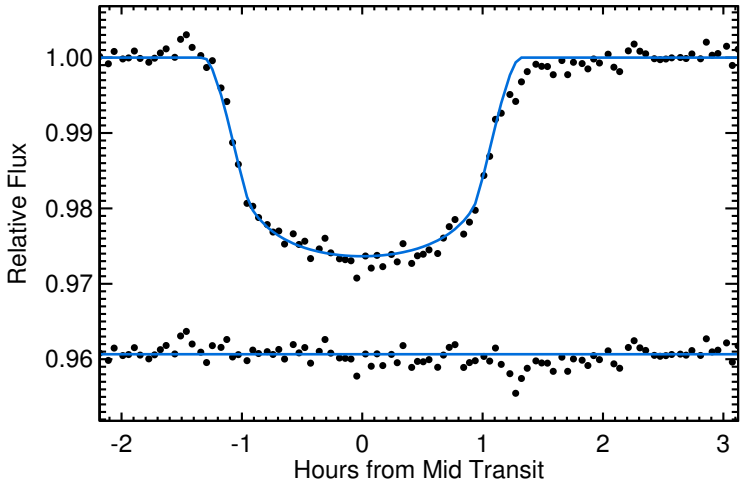

Figure 1.3: Transit light curve of WASP-6b, with best-fitting transit model superimposed. The residuals from the transit model are shown below the transit. The photometry was acquired using the Cerro Tololo Inter-American Observatory 1.0m telescope. A version of this figure was originally published in Dragomir et al. (2011) [72].

Transit observations make it possible to determine the orbital inclination and the planetary radius. With the inclination known (in conjunction with the minimum mass determined from RV measurements), the planetary mass can be obtained, and with the radius, the mean density of the planet. The density is a very valuable quantity as it allows constraints to be placed on the planet's composition.

The probability that a known radial-velocity-detected exoplanet on a circular orbit transits its star is [201]

$$p_t = \frac{R_\star + R_p}{a} \approx \frac{R_\star}{a}, \tag{1.2}$$

where a is the semi-major axis (which, for a circular orbit, is equivalent to the distance between the planet and the parent star). The closer the planet is to the star, and/or the larger the star, the higher the transit probability becomes. If the planet is in an eccentric orbit, using the approximation $R_\star + R_p \approx R_\star$, the probability becomes [14]

$$p_t = \frac{R_\star}{a(1-e^2)}, \tag{1.3}$$

where e is the orbital eccentricity. After integrating the transit probability over all values of the argument of periastron (ω) [14], it ensues that larger values of e lead to higher transit probabilities. However, it should be noted that this is simply a geometric result. Even so, though equation 1.3 breaks down as e approaches 1, such orbits would bring the planet *inside* the star at periastron passage, and therefore are not physically plausible in any case. Figure 1.4 shows the transit probability as a function of orbital period (related to the semi-major axis by Kepler's third law), for three different values of orbital eccentricity.

In 2000, HD 209458b became the first exoplanet system in which transits were detected. The planet was originally discovered with the RV technique and subsequent follow-up photometric observations acquired during

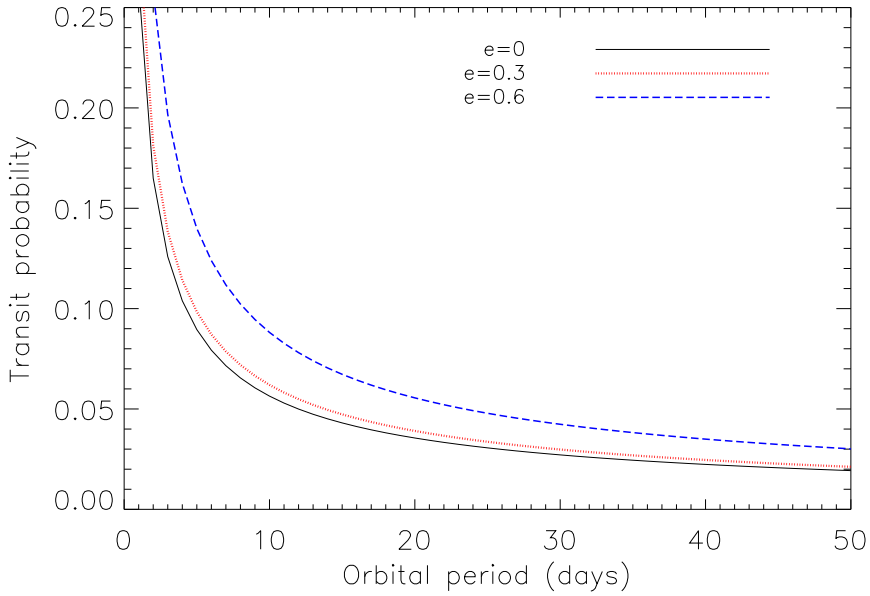

Figure 1.4: Transit probability as a function of orbital period, for three values of orbital eccentricity (e), assuming 1 $R_{\odot}$ for the stellar radius and 1 R_{Jup} for the planetary radius.

predicted transit times showed that this planet does indeed cross the disk of its star [50, 112]. Like 51 Pegasi b, HD 209458b has a short orbital period of 3.52 days. However, unlike the case of 51 Pegasi b, its radius is known from the transit measurements to be 1.4 R_{Jup}, while its mass is only 0.7 M_{Jup} [223] (where R_{Jup} and M_{Jup} correspond to the radius and mass of Jupiter, respectively). These values lead to a density of 0.37 g cm^{-3}, which is lower than that of any of the Solar System planets.

Despite the fact that the transit probability is generally small, the yield of the transit planet detection method has been increasing rapidly during the last few years thanks to the advent of several transit surveys, in particular the Kepler space mission. While RV measurements must usually be acquired for one star at a time, transit surveys can monitor many stars simultaneously. Further, fainter stars can be observed than is possible for the RV technique.

This means that in the field of view of a single telescope, there can be hundreds, thousands and in some cases hundreds of thousands of stars that can be searched for transits. Even if only one in a hundred stars hosts a planet, transit surveys can in principle be more productive than RV surveys. It turns out that number is actually much larger, as will be explained in more detail in Section 1.2.

Transit surveys can suffer from various kinds of so-called "false positives", and so require additional tests to verify the planetary origin of a transit. Common sources of false positives are a low-mass stellar object in an eclipsing binary and grazing eclipsing binaries, both of which can give rise to a small dip in the brightness of the other star in the system. These scenarios can be identified as false positives if alternating eclipses (caused by the other star passing in front of the "first", half the orbital period of the system later) are measured. If the two stars have different brightnesses, the alternating eclipses should have different depths, thus excluding a planetary nature for both companions. However, for grazing eclipsing binaries or binaries with a very faint stellar companion, this test often does not work. In these situations, one conclusive way to verify the nature of the transiting or eclipsing companion is by taking RV measurements of the system. In fact, the RV technique is used to follow up any transiting candidate orbiting a sufficiently bright star, in order to determine its mass.

The current major ground-based dedicated transit surveys are TrES (Trans-Atlantic Exoplanet Survey) [179], XO [172], WASP (Wide Angle Search for Planets) [188] and HATNet (Hungarian Automated Telescope Network) [8]. The common principle to all of these consists of using small telescopes (5-20 cm aperture) with a wide field of view to monitor a large section of sky. Transit candidates are then verified using RV measurements, and those that survive are observed with a larger telescope to determine the transit parameters with higher precision.

There are also two space-based transit surveys, Kepler [27] and CoRoT [5]. Since they are located above the Earth's atmosphere, these instruments are capable of producing very precise photometry which makes possible the discovery of increasingly smaller exoplanets. The Kepler mission in particu-

lar has so far brought about the discovery of over two thousand very diverse transiting exoplanet candidates, challenging and revolutionising many areas of this field of research.

The scientific return of transiting exoplanets can be significant beyond the determination of their densities. An exoplanet's atmosphere can be studied during transit by measuring the transit properties (such as depth) at different wavelengths. From such spectrophotometric observations it is possible to obtain a crude spectrum of the planet. This has been accomplished for a few hot Jupiters [51, 191, 218] and recently for a super-Earth [20, 56].

In some cases, the secondary eclipse of an exoplanet (occurring when the planet is eclipsed by the star) has also been measured. When performed at infrared wavelengths, this measurement leads to upper limits on or an estimate of the planet's thermal emission, and hence its temperature [48, 64, 65]. In the visible, the secondary eclipse measures the amount of starlight scattered by the planet and thus enables the albedo (reflectivity) of the planet to be constrained [138, 198].

1.1.3.1 Transit Timing Variations

If a transiting exoplanet is part of a multiple planet system, the gravitational influence of the other planets can affect the strict periodicity of its transit times [2, 114]. These variations in the transit times effectively betray the presence of other, often non-transiting planets in the system. Indeed, planetary companions that orbit farther from the parent star have a smaller geometric transit probability, and the orbits of planets in a multiple system are not usually perfectly co-planar, which means that outer planets are less likely to transit even if the innermost planet does. Kepler-19 is the first system for which this effect has been convincingly measured [10]. The mid-transit times of the innermost planet, which is a super-Earth with a period of 9.3 days, shift by up to 5 minutes, indicating the presence of an additional companion. The parameters of this indirectly detected companion are more difficult to constrain, but upper limits of 160 days and 6 M_{Jup} can be placed

on its orbital period and mass, respectively.

When transit timing variations can be measured in multiple planet systems where more than one planet transit, more information becomes available. The orbital periods can be determined for all the planets for which transits are detected, and their masses can also be more tightly constrained. An example of such a system is Kepler-9, in which 2 of the 3 known transiting planets induce timing variations of up to one hour on each other's transits, allowing both lower and upper limits to be placed on their masses [113].

1.1.3.2 Rossiter-McLaughlin Effect

A transiting planet can sometimes also be detected via RV measurements, offering further insight into the dynamics of that system. As the planet crosses the disk of the star, it sequentially blocks out some of the blue-shifted and then some of the red-shifted light from the star if it orbits in the same direction as the stellar rotation (see top part of Figure 1.5). If the planet is in a retrograde orbit (moving in the direction opposite to the rotation of the star), it will first block out red- and then blue-shifted light.

This phenomenon, called the Rossiter-McLaughlin (RM) effect [173, 196], manifests itself as an **apparent** change in the radial velocity of the star. When observed, it makes possible the determination of the angle between the orbital axis of the transiting planet and the star's rotation axis (see bottom part of Figure 1.5), as well as the direction of the planet's motion relative to the rotation of the star [91].

1.1.4 Other Methods

There are a few other exoplanet detection methods. These often probe different regions of planetary parameter space, which is important for progress towards a more complete understanding of exoplanetary systems.

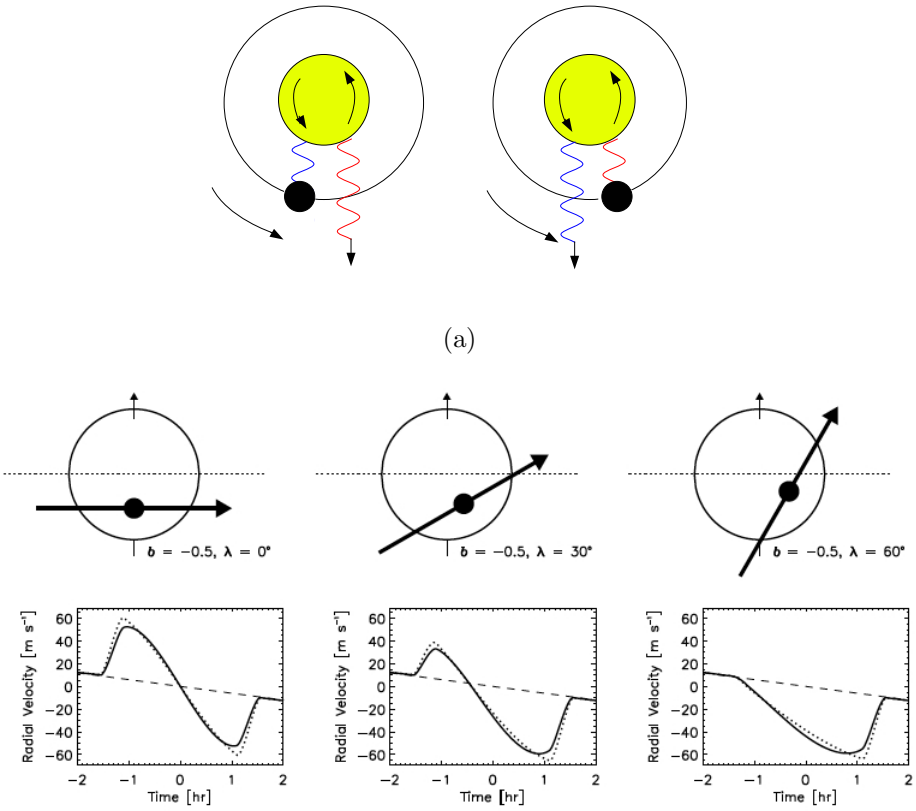

(a)

(b)

Figure 1.5: (a) Illustration of the Rossiter-McLaughlin effect. (b) The Rossiter-McLaughlin effect for three different trajectories of a planet across the disk of a star (representing three values of λ, the angle between the planet's orbital axis and the star's rotation axis), and the corresponding radial velocity waveforms. Part (b) of the Figure is from [91] and reproduced by permission of the AAS.

1.1.4.1 Microlensing

When a massive object is aligned with a background light source (a distant star, galaxy, etc.) from the perspective of the observer, the foreground

massive object acts as a gravitational lens to bend and amplify the light. Generally, the foreground object (lens) is too faint to be observed directly, but the details of the lensing event, which can last from seconds to years, hold information about its mass and geometry. If the lens object is a star, then it is possible to search the lensing light curve for the signature of an orbiting planet superimposed on that of the star. The alignments which lead to these microlensing events are very rare, which is why wide-field surveys are necessary.

The microlensing method is most sensitive to large planet-star separations, but it can detect planets with masses even smaller than that of the Earth. A major disadvantage of this method is that follow-up studies are almost impossible because the lens star is usually too faint.

Two main microlensing surveys - OGLE and MOA (Microlensing Observations in Astrophysics)[1] -, though started for reasons other than exoplanetary research, together have found 15 exoplanets to date.

In addition to populating the parameter space of exoplanets with wide orbits and a large range of masses, this technique has the ability to probe stars that are far beyond the solar neighborhood. Therefore, it can make important contributions toward understanding exoplanet demographics throughout our Galaxy [90].

1.1.4.2 Direct Imaging

Sufficiently bright exoplanets which are far enough from their stars can be directly imaged. Specifically, large planetary companions which emit a lot of infrared radiation are the ideal candidates for this technique. This means that direct imaging is best achieved at infrared wavelengths.

The ages and luminosities of imaged planets together with planet evolution models allow their masses to be estimated. However, the age of the host star, and thus those of the planets (which are approximated as the stellar age), are difficult to determine and suffer from large uncertainties which propagate to the planetary mass values.

HR 8799b, c and d, the first directly imaged exoplanets, were discovered

by this method in 2008 [165]. These three companions have semi-major axes larger than that of Uranus, and masses between 5 and 7 M_{Jup}. A fourth planet of comparable mass but orbiting closer to the star than the other three was detected in this system two years later [166]. As mentioned above, the uncertainty in the masses of these planets stems from the uncertainty on the age of the system, on which are based the models describing how the planet cools after it forms. For HR 8799, the estimate of the age of the star also varies significantly depending on the method used, introducing additional uncertainty.

Over a dozen planetary candidates have so far been imaged in systems other than HR 8799, but the large uncertainties on their parameters mean that at least some of them are probably brown dwarfs[3].

One important advantage of directly imaged exoplanets is that they can also be directly observed spectroscopically. Since 2008, spectroscopic observations of two of the planets in the HR 8799 system have been obtained [30, 123]. As more advanced instruments are developed, imaging and spectroscopy of exoplanets with smaller masses will become possible, progressing towards the first direct image of an Earth-like exoplanet.

1.1.4.3 Astrometry

If the effect is sufficiently pronounced, the wobble induced in the motion of a star by an orbiting companion can in principle also be detected by directly measuring the change in position of the star over time. This technique requires telescopes with very high spatial resolution of a fraction of a milliarcsecond or better. With current technology, this is nearly impossible to achieve from the ground, and can also be very difficult to attain using space-based instruments.

This method is most sensitive to the presence of massive planets orbiting far from their stars, and is therefore complementary to the RV and transit

[3]Brown dwarfs are sub-stellar objects with masses too low to sustain hydrogen fusion but high enough to burn deuterium. Though it is not yet completely clear where the mass limit between planets and brown dwarfs is, an object with a mass greater than 13 M_{Jup} is conventionally considered a brown dwarf.

methods which preferentially find close-orbiting planets. The technique also works best for systems with low-inclination orbital planes.

Though no exoplanet discoveries obtained with astrometric observations have yet been confirmed, the orbital inclination and thus the mass of a previously known planet around the red dwarf GJ 876 have been determined using astrometry acquired with the Hubble Space Telescope [22].

The European Space Agency Gaia mission [152], due to be launched in 2013, is designed to acquire astrometric measurements of over a billion stars with unprecedented precision. These will be used to measure stellar parallaxes, characterize stellar populations, and determine the orbital inclinations and masses of hundreds of previously known (via the RV method) or unknown exoplanets [43, 145].

1.2 Properties of Known Exoplanets

To put exoplanet properties in proper perspective, the statistics of exoplanet detection must first be addressed. One difficulty associated with the task of evaluating these statistics is the presence of selection effects; i.e., certain planets are too small, or are in orbits too large, to be detected with current instruments. Nevertheless, if the selection effects are relatively well understood, it is possible to correct for them and use current numbers of detections to obtain the average number of planets around stars, broken down into types of stars and even types of planets. This is sometimes expressed as the "planet occurrence rate": the percentage of stars which harbour one or more planets. After correction of the detection biases, statistics from the HARPS radial velocity survey indicate this number is 45 $\pm$ 7.8 % for planets with orbital periods less than 50 days, and as high as 75 % for planets with periods less than 10 years [169], based on the sample of stars they surveyed (quiescent, mostly single stars). The HIRES survey yields a bias corrected value of 24 $\pm$ 5 % for planets with periods shorter than 50 days [120] (based on a stellar sample similar to that of HARPS), while the estimate based on results from the Kepler survey (accounting for the transit probability) is 20% [17] (based on the sample of stars in the Kepler field).

Figure 1.6 shows planet occurrence within 0.25 AU of planet host stars, as a function of orbital period and planetary radius, based on Kepler detections. Finally, microlensing surveys indicate the planet occurrence rate per star, for semi-major axes between 0.5 and 10 AU and planet masses greater than 5 $M_{\oplus}$, is 160 $\pm$ 90% (essentially suggesting more than one planet per star) [44], though it is difficult to ignore the large uncertainties. Though estimates from the various surveys have not yet reached complete agreement, it appears that planets around other stars are anything but rare.

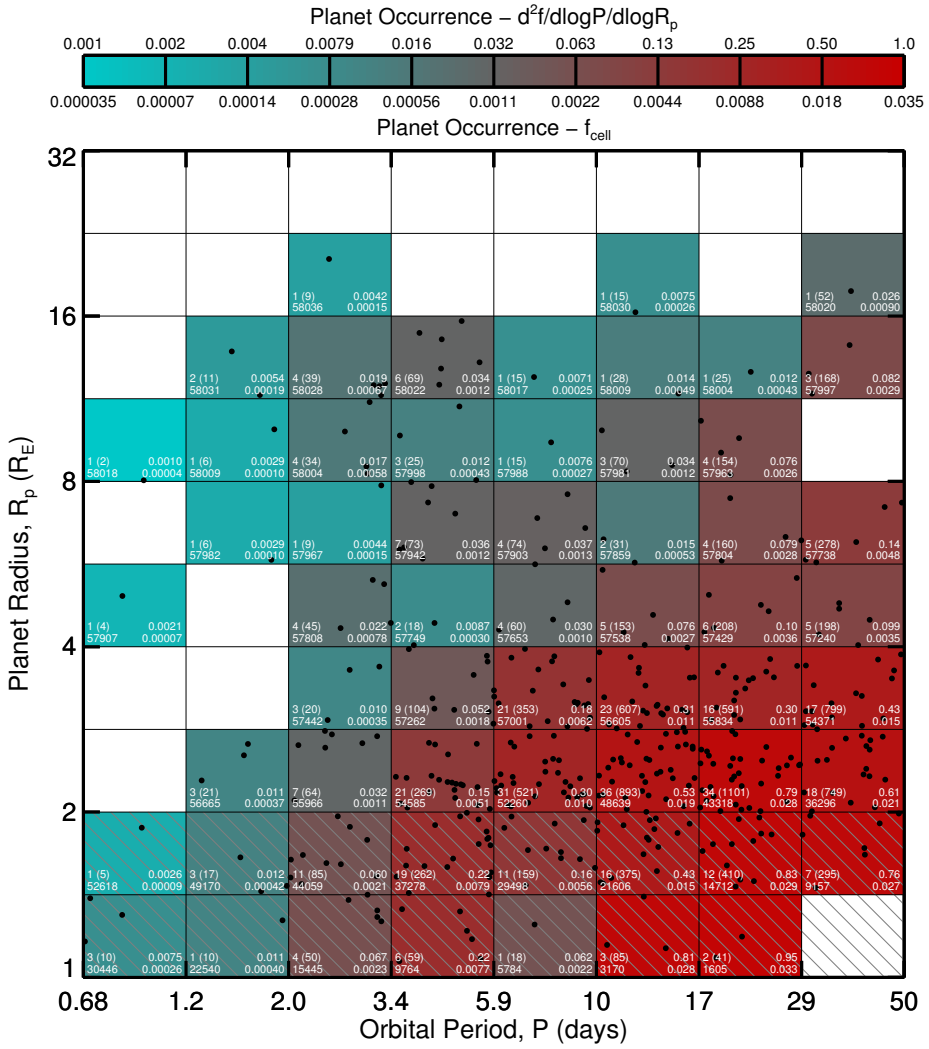
Planet Occurrence – d²f/dlogP/dlogR_p
0.001 0.002 0.004 0.0079 0.016 0.032 0.063 0.13 0.25 0.50 1.0
0.000035 0.00007 0.00014 0.00028 0.00056 0.0011 0.0022 0.0044 0.0088 0.018 0.035
Planet Occurrence – f_cell
Planet Radius, R_p (R_E)
32
16
8
4
2
1
0.68 1.2 2.0 3.4 5.9 10 17 29 50
Orbital Period, P (days)

Figure 1.6: Planet occurrence as a function of orbital period and planetary radius, on logarithmic scales. The black dots correspond to planets detected by the Kepler mission. The color scale represents planet occurrence, as demonstrated at the top, corrected for the *a priori* geometric transit probability. The hatched cells indicate measurement incompleteness for those areas of period-radius parameter space. The white text refers to occurrence statistics: *upper left:* number of planets detected with signal-to-noise ratio (SNR) > 10, with this number corrected for non-transiting geometries in parentheses; *lower left:* the number of stars observed by Kepler around which a planet with the period and radius of the cell could be detected with SNR >10, if it was present; *upper right:* planet occurrence per logarithmic area unit; *lower right:* planet occurrence corrected for non-transiting geometries and survey incompleteness. Figure is from [119] and reproduced by permission of the AAS.

Over the nearly 17 years since the discovery of the first exoplanet around a main sequence star, a few trends relating star and planet properties have been recognised. Planet occurrence and mass seem to increase with stellar mass. There are fewer planets around M dwarf stars than around F/G/K type stars, with the highest occurrence rate being around A type stars [124]. In addition, planets orbiting M dwarfs tend to be less massive than those orbiting F/G/K dwarfs [61]. These effects may reflect the formation of smaller and less massive protoplanetary disks around lower-mass stars. There is also a well-characterised correlation between stellar metallicity and planet occurrence, which is likely related to the quantities of materials required for planet building present in the protoplanetary disk [81, 124, 162]. A related trend is the correlation between stellar metallicity and planet mass, which implies that the likelihood of a giant planet orbiting a F/G/K type star increases with the stellar metallicity [81, 209].

Of particular interest when considering occurrence rates is the frequency of exoplanets within the "habitable zones" of their host stars. The habitable zone is defined as the range of distances from the star where liquid water can exist on the surface of a planet. It is mainly determined by the luminosity of the parent star, but planetary greenhouse gas effects must also be taken into

account, as well as the possibility of tidal coupling [15, 108]. Planets in the habitable zone are considered the most promising for sustaining extraterrestrial life. About 25 exoplanets are so far known to reside in the habitable zone, four of which are super-Earths. Of these four, only one (Kepler-22b) transits so it is the only such planet (outside the Solar System) whose size and density are known (see Section 1.2.3).

1.2.1 Dynamical Properties

Most of the first exoplanets discovered were found to have very short orbits, many with orbital periods of about 3 days. This population of planets

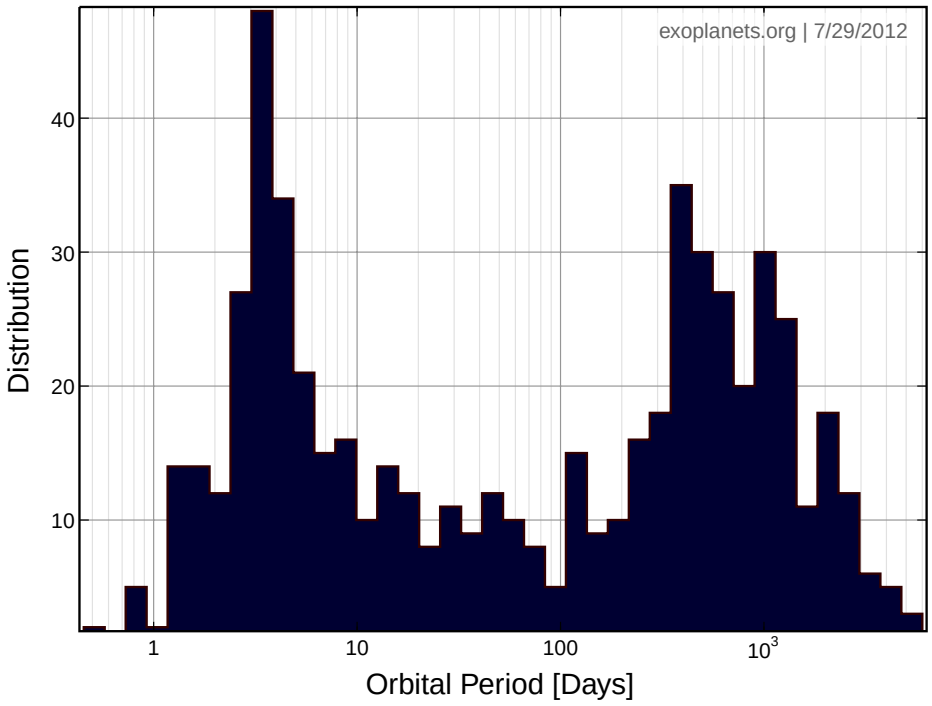

Figure 1.7: Distribution of orbital periods for known exoplanets. The data was obtained from the Exoplanet Orbit Database [268] and the figure was produced interactively using the Exoplanet Data Explorer at exoplanets.org.

was both unexpected and contradictory to formation and evolution models

based on the Solar System. The fact that these were among the first to be detected is due to observational bias, because RV and transit surveys are most sensitive to such short period exoplanets. Even so, about 40% of known exoplanets have a semi-major axis smaller than 0.1 AU (Astronomical Units). It is clear that these planets are too hot to be suitable for life as we know it, but how did they form in or migrate to their current close-in orbits? The most commonly accepted theories are described in Section 1.2.1.1. Figure 1.7 shows the number of known exoplanets as a function of orbital period. The large peak at a period of about 3 days is clearly seen.

Most of these short-period exoplanets have circular orbits. This is likely due to the process of tidal circularization. Gravitational interactions be-

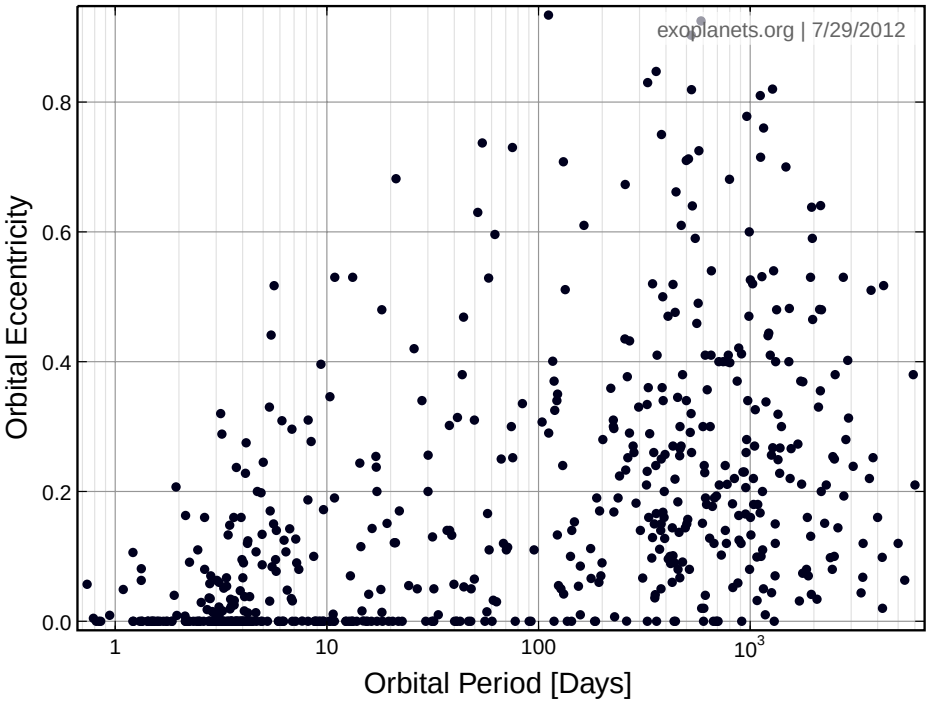

Figure 1.8: Distribution of orbital eccentricities as a function of orbital period for known exoplanets. The data was obtained from the Exoplanet Orbit Database [268] and the figure was produced interactively using the Exoplanet Data Explorer at exoplanets.org.

tween the star and the planet will lead to tidal energy dissipation from within the planet which will slowly act to circularize its orbit. The process can take between a million and a billion years, depending on the initial orbital eccentricity, period and mass of the planet, as well as the mass of the star [102, 234], and has the additional effect of synchronizing the rotation and orbital revolution of the planet such that it always shows the same side to the star. Therefore, the planet is expected to become tidally locked.

While most exoplanets with orbital periods shorter than 20 days have circular orbits, many of those with longer periods tend to have eccentric orbits. This is demonstrated in Figure 1.8, where the dearth of short-period ($\lessapprox$ 3 days) exoplanets in eccentric orbits is noticeable. This discovery also came as a surprise, since it once again differed significantly from the case of the Solar System. Approximately 55% of exoplanets with a period longer than 10 days have an orbital eccentricity greater than 0.2. The vast majority of these have been detected only via the RV method, since their long periods significantly reduce their transit probability. Though this result is not the consequence of an observational bias, it has been recently shown that the RV signal of a planet in an eccentric orbit can sometimes be difficult to distinguish from that of two planets orbiting in 2:1 resonance[4] [4]. In such cases, direct imaging, astrometric or a very large number of RV measurements are needed to distinguish between the two scenarios. This means that at least some of the exoplanets currently thought to be in eccentric orbits may actually be two resonant planets in circular orbits.

During the last three years, several studies of the Rossiter-McLaughlin (RM) effect in exoplanetary systems have been published. These studies can probe system parameters which would be difficult or impossible to determine otherwise, and which are particularly important as they can provide additional information about the formation and dynamical history of these exoplanets. Analyses of the RM effect in over 20 exoplanetary systems found that at least half of those are misaligned, with an angle between the orbital and stellar spin axes statistically significantly larger than 0°,

[4]When the orbital period of a planet is equal to twice the period of another planet in the same system, the two planets are said to be in a 2:1 mean motion resonance.

and that a substantial fraction of these planets are on retrograde orbits [31, 175, 177, 217, 236, 261]. These exotic systems add one more puzzle to solve towards a better understanding of exoplanets.

Studies of multiple exoplanet systems have also revealed new types of dynamical interactions between the planets. Results from the Kepler telescope have uncovered many multiple systems where the motion of the planets is governed by non-Keplerian dynamics [77]. These effects can range from slight deflections due to one planet passing another to ejections of one or more planets from a system.

Another noteworthy Kepler result is the first detection of a circumbinary exoplanet [71]. Kepler-16b orbits a binary star system with a period of 229 days. Its mass is close to that of Saturn, but its radius is smaller, indicating a composition of about half gas and half rock. Because of its relatively long period and orbital parameters which vary over time due to the more complex three-body gravitational interactions, the planet will no longer transit one of the binary stars as early as 2014, and the other in 2018, until around 2042. So far two more circumbinary exoplanets have been discovered, Kepler-34b and Kepler-35b [260].

1.2.1.1 Migration and Exchange of Angular Momentum

Close-in giant exoplanets (a.k.a. hot Jupiters) are unlikely to have formed *in situ* because there would not have been sufficient protoplanetary disk material that close to the star to create them. An alternative explanation is that the planets formed farther out and subsequently migrated toward the stars. Below I describe the two main proposed types of migration mechanisms.

Type I migration consists of gravitational interactions between a newly formed planet and the disk in which it is embedded, causing the planet to migrate via exchange of angular momentum [259]. The orbiting planet gives rise to a non-axisymmetric gravitational potential which varies in time, and drives spiral density waves in the disk gas. These density waves create additional perturbations from which torques acting on the planet originate. The outer disk exerts a negative torque on the planet and leads to inward

migration. The inner disk exerts a positive torque and imposes outward migration. A slight imbalance between the two torques will cause the planet to migrate in one of the two directions. Simulations of the planet and disk's evolution show that the torque from the outer disk generally dominates, leading to inward migration [259].

A massive planet can perturb the disk strongly enough to open a gap. The planet is then maintained in the middle of the gap as follows: if it approaches the inner edge of the gap, the distance between the planet and the inner disk decreases, resulting in an increase of the torque felt from the inner disk, which pushes the planet back toward the centre of the gap; the opposite effect occurs when the planet approaches the outer edge of the gap. Thus the planet (and its gap) is forced to evolve with the disk. The disk extending to a few AU from the star evolves inward [151]. If the planet forms within this portion of the disk, it therefore migrates inward as well. This is called Type II migration and is typically slower than Type I migration [259].

Planets can also exchange angular momentum with planetesimals through close encounters or collisions. However, this mechanism is thought to have a relatively minor contribution to the migration of most observed close-in exoplanets.

1.2.1.2 Planet-Planet Interactions

As already mentioned, the gravitational interactions between exoplanets in multiple systems can lead to very interesting dynamics. Planet-planet scattering can lead to high orbital eccentricities, and in fact represents a viable mechanism for explaining the current distribution of exoplanet eccentricities [52]. The presence of a distant massive planetary or stellar companion in an inclined orbit can also maintain an inner planet in an eccentric orbit.

The latter process, called the Kozai effect, is of particular interest as it provides a way to form the apparently common misaligned systems unveiled by studies of the RM effect. Indeed, since the mechanisms of Type I and Type II migration described in Section 1.2.1.1 are expected to produce

aligned systems, they cannot be used to explain these recent results.

The Kozai effect provides an alternative model. It involves an exchange between the eccentricity and inclination of the orbit of a planet, induced by the influence of an outer companion. If the inner orbit is initially circular but highly inclined, in time it will evolve to high eccentricity and lower inclination, to eventually return to its original state. These oscillations continue in the form of periodic cycles. If the inner planet passes sufficiently close to the parent star at pericenter (the closest point of approach in an eccentric orbit), then tidal dissipation occurs. Over time, this process will circularise its orbit, but the Kozai history of the planet means that at least some misalignment will remain between the planetary orbital axis and the stellar rotation axis [76].

1.2.2 Physical Properties

So far I have discussed the "hot" aspect of the hot Jupiters mentioned in Section 1.1.2, though it is important to emphasize that only a minority of close-in exoplanets are gas giants. With the advent of the first detected transiting hot Jupiters, it became possible to obtain their radius, mass and thus density. It was found that the density of about half of hot Jupiters was significantly lower than that of giant planets in the Solar System and than theoretically predicted [34]. Figure 1.9 shows the masses and radii of known transiting exoplanets. It can be seen that the radii of gas giants ($M_p > 100 M_\oplus$) are often larger than expected even for a pure hydrogen planet.

The first solutions proposed for this anomalous radius problem include the injection of a large amount of incoming stellar radiation deep enough into the atmosphere of the planet to keep it "inflated" by inhibiting its interior cooling and thus its contraction [101], and tidal dissipation, which has been shown to function even when the orbital eccentricity is very small [25]. More recent mechanisms include enhanced atmospheric opacities [33], semi-convection [47], ohmic dissipation [18] and the mechanical greenhouse model [270]. While most of these have been shown to not be sufficiently efficient to

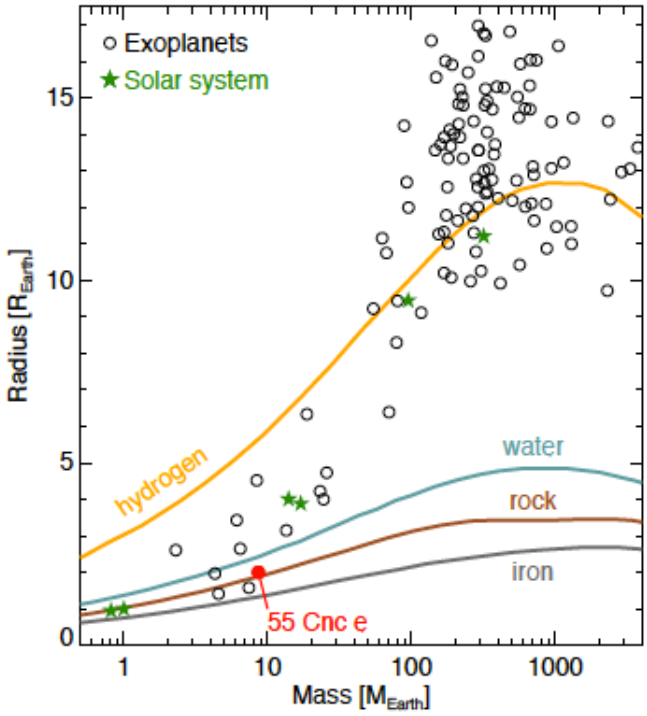

Figure 1.9: The masses and radii of known transiting exoplanets. From top to bottom, the solid lines correspond to densities indicating hydrogen, water, rock (silicate) and iron composition models. From left to right, the green star symbols represent Venus, Earth, Uranus, Neptune, Saturn and Jupiter.

produce hot Jupiters on their own, the latter two theories are more promising. Ohmic dissipation involves heat generated by the dissipation of currents induced by surface winds, which keeps the planet inflated. The mechanical greenhouse model suggests that the outer layers of a hot Jupiter are turbulent due to the stellar irradiation, and this turbulence then transfers the heat toward the interior of the planet. Nevertheless, all these models require more detailed and precise observations of the planetary systems concerned in order to be more thoroughly verified.

Not all hot Jupiters have radii larger than predicted by theory. Some

match theoretical predictions, while some actually have smaller radii. Smaller radii can be relatively easily explained by the existence of a dense core [85].

Further, results from the Kepler mission have shown that the majority of exoplanets with short periods are in fact smaller than Jupiter, with radii closer to that of Neptune (3.9 R_{Earth}) or smaller [28]. This is not too unexpected since ground-based RV and transit surveys are more sensitive to massive and large exoplanets, respectively. The trend seems to persist even without restrictions on the orbital period. Current Kepler statistics indicate that exoplanet candidates with radii $> 6R_{\oplus}$, 4 - 6 $R_{\oplus}$, 2 - 4 $R_{\oplus}$ and 0 - 2 $R_{\oplus}$, make up 3%, 6%, 45% and 46% of the total number of candidates, respectively [17].

As RV surveys reach higher precision and are able to detect companions with smaller minimum masses, it becomes possible to begin determining the mass distribution of exoplanets as well. The HIRES and HARPS surveys find that the majority of RV-detected exoplanets have minimum masses below 30 $M_{\oplus}$, with the peak of the distribution being in the super-Earth/mini-Neptune regime (2-10 $M_{\oplus}$) [119, 169]. These results are difficult to compare with the Kepler sample because they measure different exoplanet properties, but they are in agreement for a physically credible density function.

1.2.2.1 Atmospheres

The measurement of an exoplanet's secondary eclipse, when it is completely blocked by the host star, at infrared wavelengths provides a means of determining its effective temperature. Such observations, taken at different wavelengths, give a low spectral resolution emission spectrum of the planet. This technique was used to discover the existence of an inversion layer[5] in the atmospheres of several hot Jupiters [53, 139, 141, 159, 178]. At optical wavelengths, a similar measurement leads to the detection of or upper limit on an exoplanet's albedo. Until now, most optical observations of hot

[5] An inversion layer is a layer of air where the regular decreasing change in temperature with increasing altitude is reversed. One consequence of such a thermal inversion is that water bands in the near- and mid-infrared are flipped from absorption into emission. So far, it is from the detection of these emission bands that inversion has been inferred in exoplanet atmospheres [33].

Jupiters during secondary eclipse suggest very low albedos [138, 198, 221] as predicted by theoretical models of hot Jupiter atmospheres [164, 213, 226], which suggest that the likely large amounts of sodium and potassium would increase the atmospheric opacity. However, at least one (Kepler-7b) appears to be more reflective than expected with an albedo of 0.32 [68]. This high albedo is likely due to Rayleigh scattering (due to a possible depletion of sodium and potassium) and/or the presence of clouds in the atmosphere of Kepler-7b.

Observing the transit of an exoplanet at several wavelengths allows its transmission spectrum to be characterised. This has been accomplished for over a dozen giant exoplanets and has uncovered the presence of atoms and molecules such as sodium [51, 191, 265], potassium [54, 218], methane [230], water [21, 233], carbon monoxide [220] and carbon dioxide [229]. In addition, hydrogen, carbon and oxygen have been detected in the escaping atmosphere of HD 209458b [248], as well as silicon [153, 210]. Though these elements and molecules are expected in hot exoplanet atmospheres, their actual detection represents a significant technological and scientific achievement which paves the way towards detecting less abundant, and perhaps less predictable, atomic and molecular species.

Additional information about an exoplanet's atmosphere can be obtained by monitoring the system for at least half an orbital period. The phase curve of an exoplanet can reveal details about its atmospheric circulation. If both day and night sides of the planet have the same temperature, then no phase variations can be seen at IR wavelengths. However, this is probably not the case since close-in planets are expected to be tidally locked, and the day side is likely significantly hotter than the night side. But is there any heat re-distribution at all? And if so, then to what extent and by what mechanism? Infrared observations of HD 189733 from transit to secondary eclipse indicate that the stellar radiation absorbed by the planet is efficiently re-distributed, and the day side of the planet is only about 250 K warmer than the night side (973 K) [140]. In this case, strong winds have shifted the hot spot eastward of the sub-stellar point. These same winds are probably also responsible for the heat re-distribution. However, other planets, such

as Ups And b [103] and WASP-12b [55], show temperature differences of $\sim$ 1400 K and $\sim$ 2000 K respectively, between the two sides. This suggests low efficiency heat re-distribution for these planets. If the phase curves of exoplanets can also be measured at different wavelengths (optical and/or UV), they can help constrain phenomena such as polarisation and scattering, and can be combined with IR measurements to provide a more complete picture of these exoplanetary atmospheres. But care must be taken when analysing and drawing conclusions from data exhibiting phase curves, as stellar variability or other transiting planets in the system may cause them to appear different from orbit to orbit, as may star-planet interactions if present, and even significant changes in the "weather" of the planet.

All these types of measurements are facilitated if the host stars of the observed exoplanets are bright, but, as already mentioned, these constitute a small minority of all known transiting systems. Upcoming missions such as the James Webb Space Telescope (JWST, [211]) will enable studies of the atmospheres of exoplanets orbiting fainter stars, and of smaller exoplanets. In the mean time, current resources will continue to focus on bright systems with the goal of improving their characterisation.

1.2.3 Super-Earths

Theoretically, the maximum mass a terrestrial planet can attain lies at roughly 15 $M_\oplus$ [204]. Beyond this critical mass, hydrostatic equilibrium can no longer be maintained in the envelope surrounding the core. The envelope collapses and the gas accretion rate increases, leading to increased energy losses through radiation and consequently a runaway accretion process (which ends when the gas in the protoplanetary disk has dispersed or when the planet has cleared a ring of empty space around its orbit within the disk) [189]. This process can also occur at core masses lower than the critical mass.

A super-Earth is loosely defined as an exoplanet with a mass of 1-10 $M_\oplus$ [242]. Super-Earths are an interesting category of planets because no such exoplanets exist in the Solar System, and thus it is not yet well known what

they are like as an ensemble, nor how diverse.

Until now, about 60 exoplanets with minimum masses in the super-Earth regime have been discovered using the RV method, of which one is known to transit (55 Cnc e, [262]). A few notable examples in this category are GJ 581 d, which orbits within the habitable zone of its star [168, 266], and GJ 581 e, a planet in the same system which holds the current record for the second lowest minimum mass (1.9 $M_{\oplus}$, [168]). The exoplanet 55 Cnc e has the shortest orbital period of all known confirmed exoplanets around main sequence stars, at only 0.74 days [63]. Its radius and mass are 2.0 $R_{\oplus}$ and 8.6 $M_{\oplus}$, respectively [262]. In addition, 55 Cnc e orbits a very bright star (V = 5.95).

Approximately 20 confirmed transiting super-Earths and Earth-size planets have been discovered with transit surveys, mainly Kepler. Several of these represent important milestones in the field. CoRoT-7b is the first transiting super-Earth detected, and has a radius of 1.6 $R_{\oplus}$ [149], a mass of ~ 7 $M_{\oplus}$ [106], and an orbital period of 1.6 days. GJ 1214b is a super-Earth that orbits a M dwarf star only one fifth the size of the Sun, leading to a deep transit accessible to detailed atmospheric studies [49]. Kepler-10b is the first rocky planet discovered [16]. Kepler-22b is the first transiting super-Earth found in the habitable zone [29]. A multiple system composed of two Earth-size planets (0.9 and 1.0 $R_{\oplus}$) and three super-Earths orbits Kepler-20 [88]. The distribution of known super-Earth masses and radii can be seen in the lower left corner of Figure 1.9. Despite low-number statistics, the densities of these intriguing exoplanets span nearly the entire range of possible compositions predicted by theoretical models (see Section 1.2.3.1).

The atmospheres of two hot super-Earths have also been probed. The transmission spectrum of GJ 1214b has caused some controversy, with one study resulting in a flat spectrum and indicating either the absence of a primarily hydrogen-composed atmosphere or clouds or hazes obscuring any hydrogen features [20], and another suggesting a hydrogen-dominated atmosphere [56]. More precise Hubble Space Telescope observations indicate that GJ 1214b's atmosphere is likely hydrogen-poor and possibly water-rich [23]. Very recently, the secondary eclipse of 55 Cnc e was detected, leading

to the first measurement of thermal emission from a super-Earth [67]. The secondary eclipse depth translates to a temperature of approximately 2400 K, consistent with the very close proximity of this planet to its host star.

1.2.3.1 Interior Models

Perhaps among the most intriguing properties of super-Earths is their interior structure, and the proportion of high mean molecular weight materials (such as rock but also water) to the hydrogen/helium atmospheric component.

The main interior composition materials currently used in models [195, 244] can be arranged in three groups: the core (predominantly formed of iron), the mantle (consisting of silicates) and water. Detailed models indicate that there exists a maximum terrestrial (i.e. less than 10% water content) radius for a given planetary mass. Further, planets with small mantles and large core and water contents are unlikely to form [244].

Degeneracies do exist in these models, as some combinations of mass and radius may correspond to several possible distributions of matter in the planet's interior. A more conservative framework for determining exoplanet interior compositions, which takes into account these degeneracies as well as observational and model uncertainties, is presented in [195, 212]. It is found that the level to which a super-Earth's interior composition can be constrained depends on its density and that small planets with extreme densities allow the tightest constraints, assuming comparable uncertainties on the mass and radius. Furthermore, simulations of cored and coreless terrestrial planets indicate that their radii are similar to within a few percent or less [75]. These results indicate that constraints on the interiors of such planets should, at least for the time being, be placed on a case-by-case basis for each discovered super-Earth.

Some theoretical studies on the subject of plate tectonics in super-Earths have also been undertaken. One group found that plate tectonics are inevitable in super-Earths because as the planet's mass increases, convective stresses also increase while the plate thickness would decrease [243]. An-

other group determined that the higher gravity and thus interior pressure of super-Earths would lock the faults and prevent deformation [180]. More recent studies suggest that the ratio of driving to resistive forces is only somewhat dependent on the size of a terrestrial super-Earth [143, 222], but the subject is still under debate.

1.3 Outstanding Questions

Many of the discoveries in the exoplanet field have raised yet more questions than they have answered. One of the very first puzzles, the mechanism by which hot Jupiters have larger radii than predicted, remains unsolved. None of the proposed models can account for the entire population of inflated hot Jupiters, though it is also possible that more than one mechanism is at work, perhaps even within the same planet.

More observations are also needed to verify currently tentative correlations, such as the relations between stellar mass and planet mass and occurrence.

Though current surveys have discovered many multiple planet systems, suggesting they are common, no analog of our Solar System has yet been found. We do not yet know whether its organization (terrestrial planets orbiting between 0.3 and 1.5 AU, and gas giants orbiting further out, all the way to 30 AU from the Sun) is unusual, and to what extent. This question is difficult to answer partly because of detectability issues: the radial velocity signatures of the Solar System terrestrial planets as exoplanets would have amplitudes smaller than 1 m/s, just barely at the limit of current technology. Further, their orbits lead to a very small transit probability (0.8% for Mercury).

The large number of super-Earth ($1 < R_p < 3R_\oplus$) transiting candidates found by Kepler suggests that these are the most frequent types of planets, even more so than small gas giants of sizes similar to that of Neptune. However, their interior and atmospheric properties are still unclear. Are they mostly rocky or mini gas giants? It is also not known how they form: have they formed in the outer regions of their protoplanetary disk and sub-

sequently migrated closer in? In the case of the hot ones, can some of them, perhaps the less massive ones, have formed *in situ*? Is it possible that at least some hot super-Earths are gas giants whose atmospheres evaporated due to their prolonged proximity to the host star?

One important goal is to determine how common or rare are Earth-like planets. Understanding the frequency of Earth-size planets in the habitable zones of solar-type stars will constitute a major step towards assessing the possibility, and perhaps the probability of life arising elsewhere than on our planet.

Another consideration is the frequency of exomoons. No exomoons have yet been detected, though they are strongly suspected to exist [42]. The most promising techniques for detecting such objects consist of searching for them around known transiting exoplanets, by monitoring any transit timing or transit duration variations, but also asymmetries in the shape of the transit light curve [135, 238]. The Kepler mission has the capability of finding signals associated with large moons [137], so if they exist their existence should be announced in the near future [136].

Terrestrial exoplanets and exomoons are thought to be the most likely sites to support life outside the Solar System. The first test of this hypothesis is to probe these objects' atmospheres in search for indications of biomarkers[6] in their spectra. No terrestrial exoplanet spectrum has been measured for the time being, let alone in sufficient detail to search for biomarkers. However, with the launch of JWST and of some possible mission like EChO (Exoplanet Characterisation Observatory) [232] and FINESSE (Fast Infrared Exoplanet Spectroscopy Survey Explorer) [228], this feat will enter the realm of the possible.

Many of the remaining major questions and the more detailed ones that stem from them will be answered with either the acquisition of more data, improved instrumentation, or both. As Kepler continues to collect photometry of hundreds of thousands of stars, the statistics of exoplanet occurrence will become more clear. Radial velocity techniques are becoming increas-

[6] Biomarkers comprise any gas or surface features that is produced by the accumulation of life. Water, ozone and methane are considered likely biomarkers [126].

ingly sensitive to smaller signals, promising accurate mass determinations for terrestrial exoplanets. Upcoming space telescopes represent the best chance at improved characterization of exoplanet atmospheres. The next several years of research in the field will undoubtedly solve at least some of the current puzzles while also generating new and likely unexpected ones.

Chapter 2

Motivations of this Thesis Research

As described in Chapter 1, if an exoplanet can be characterised using both the radial velocity and the transit methods, its density can be measured and its interior structure constrained. In addition, if the host star is bright, studies of the system using additional techniques (spectroscopy, polarimetry, interferometry, etc.) are possible.

The core of this thesis is a systematic search for transits of planets discovered through RV surveys, in particular planets in the super-Earth category. Transit detections mean radius measurements, which mean estimates of the average densities of these planets. These data place strong constraints on the possible internal structures of these planets, testing models of planet formation and evolution. The determined transit parameters will also be useful for planning and calibrating future observations of these systems. Null detections place upper limits on the size of a potentially transiting planet, or altogether exclude a transit for a planet of any physical radius[7].

The transit search was conducted with the MOST (Microvariability and Oscillations of STars) space telescope [167, 257]. MOST photometry is sufficiently precise to distinguish between the transit of a super-Earth with radius corresponding to a rocky planet, an ocean planet or a mini gas giant. Most of the exoplanets selected for the search have been originally detected by the HARPS survey, and the remaining ones by the HIRES survey. They have minimum masses in the super-Earth regime and generally orbit bright

[7] Given a minimum mass for the planet from radial velocity measurements, it is possible to determine the smallest physically plausible radius for that planet. This is generally taken to be the radius of the planet in the case of a 100% iron composition.

stars with magnitudes $6 < V < 10$ for which MOST can produce very precise photometry. The selected super-Earth candidates also have periods shorter than 10 days, which ensures a transit probability of 5% or greater. The majority of the HARPS and HIRES super-Earth candidates are in multi-planet systems. Thus, if one such planet is found to transit, there is an increased chance that another planet in the same system transits as well, under the assumption that their orbits are co-planar or nearly so.

One part of the thesis (Chapter 6) pertains to research I have performed as a Graduate Visiting Fellow at Caltech, as part of the TERMS project. TERMS (Transit Ephemeris Refinement and Monitoring Survey) [131] is a program which aims to detect transits of known radial velocity (RV) exoplanets with intermediate-long periods orbiting bright stars. Currently there are only two exoplanets (both initially detected via the radial velocity method) [13, 89] with periods longer than 20 days which transit stars with V < 10, so any transit discovered by TERMS holds great potential for improving our understanding of the physical properties of longer-period exoplanets.

TERMS has many elements in common with the MOST transit search, but they are also complementary. Both projects aim to explore sparsely populated areas of exoplanet parameter space.

The format of the thesis consists of introductory chapters followed by four chapters corresponding to papers which are in preparation, in review or published. Below I outline the following chapters of this thesis.

In Chapter 3, I describe the observational and analysis techniques employed throughout the thesis. The observational techniques include space- and ground-based photometry as well as spectroscopy. I give a brief overview of both frequentist and Bayesian analysis methods in the context of the transit search, detection and characterisation, and of selected techniques used to search for other types of periodic signals.

I present the MOST super-Earth transit search in Chapter 4. I provide a description of the target selection and the resulting sample followed by a summary of the observing strategy. I then give an overview of the results, including a brief mention of those which are the focus of Chapters 6 to 9.

Chapter 5 establishes the connection between the subjects of Chapters

6 to 9 within the thesis theme.

The results of my research with the TERMS project are presented in Chapter 6. It consists of a transit search of HD 192263b, a Jupiter-mass exoplanet with an orbital period of 24 days and a moderately controversial history. I exclude a transit for most geometric configurations and characterise the stellar activity corresponding to the rotation of the host star.

The GJ 581 multiple-planet system is the subject of Chapter 7. The RV monitoring of this system, believed to host at least one planet in the habitable zone, has been ongoing for several years. I use MOST photometry of GJ 581 to search for transits of the innermost planet, GJ 581e, which has one of the lowest minimum masses of all known exoplanets. I find no transits for a planet less dense than a water planet. I also carry out an analysis of the stellar variability.

In Chapter 8 I present the photometric follow-up of HD 97658b, a RV-detected super-Earth candidate for which transit-like signals had previously been detected. No transits are observed in the MOST photometry, indicating that the previous detection was erroneous. This work made a well timed impact in the field, since several proposals for follow-up studies with large facilities were already under review at the time the null result was announced.

Chapter 9 portrays the analysis and results of follow-up MOST photometry of the 55 Cancri system. These data have led to improved transit parameters, including a more precisely determined planetary radius and orbital inclination for 55 Cnc e, the first super-Earth known to transit a bright star. I have also carried out a search for and have placed limits on the depth of the secondary eclipse of this planet. Finally, my work has more precisely constrained the planet's ephemeris and has led to the exclusion of transits of the other known planets in the system.

I conclude and discuss future prospects in Chapter 10. I provide a brief summary of the thesis and describe the significance of the results. Future research includes the ongoing super-Earth transit search with MOST and the development of improved observing strategies. The 55 Cnc system and new transiting super-Earths will continue to be photometrically monitored.

I will also analyse spectropolarimetric data of 55 Cnc to search for evidence of magnetic star-planet interactions between the transiting super-Earth and the host star.

Chapter 3

Observational and Analytical Techniques

Photometric and spectroscopic measurements are at the core of most exoplanet observations, and the analytical techniques used to extract science from these data have been developed and improved specifically for use in exoplanet research over nearly two decades.

In this Chapter I give an overview of the types of data I have used in this thesis, as well as the techniques I have employed to analyse these data. Some version of the methods I will describe have already been used on similar data in this field to produce results that are widely accepted in the astronomical community.

3.1 Photometry

3.1.1 MOST Space-Based Photometry

The MOST satellite [167, 257] carries a 15-cm telescope which acquires light through a broadband filter spanning the visible wavelengths from 350 to 750 nm. The Science CCD (Charged Coupled Device) camera measures 1024 x 1024 pixels. The satellite is in a Sun-synchronous polar orbit around the Earth with a period of 101.4 minutes. It can monitor stars almost continuously for up to 8 weeks in a Continuous Viewing Zone (CVZ) which covers a declination range of $+36^\circ \geq \delta \geq$ -18 $^\circ$. The satellite can also point to targets outside the CVZ, as long as they are within its Sun Sensor Zone (SSZ). The SSZ corresponds to the part of the sky which MOST can observe without pointing too far away from the Sun-Earth line and risk endangering

its battery lifetime. However, targets that are in the SSZ but not in the CVZ are only observed for part of each MOST orbit, while the remainder is spent observing a star within the CVZ, thus allowing the satellite to point its solar panels back towards the Sun and re-charge its batteries. MOST can achieve a sensitivity to stellar light variations in frequency space of better than a part per million for very bright stars, and a few parts per million for stars as faint as V $\sim$ 6 [12][8].

Most of the targets observed for this thesis consist of stars hosting exoplanets for which the predicted transit time has large uncertainties (Section 4.3.2). As a consequence, the stars must often be observed continuously (or nearly so) for 15-20 hours or even longer in some cases. This is very difficult to accomplish from the ground from a single observatory because night at most latitudes at most times of the year does not last that long. The Sun rises and stops the observations. This limitation does not apply to space-based instruments in the appropriate orbits, so MOST is ideally suited for these observations. Another very important advantage of space-based telescopes for precise photometry is the absence of the Earth's atmosphere between the instrument and the objects to be observed, avoiding the "extinction" (absorption and scattering) and "scintillation" (twinkling) that are major sources of noise and systematic error in ground-based photometry. This characteristic adds to MOST's exquisite photometric precision, required to detect the shallow transits of super-Earth exoplanets.

MOST can collect photometry in three different modes: Fabry Imaging, Direct Imaging and Guide Star photometry (where the data are largely processed on board the satellite). MOST science targets are observed in one of the first two modes, depending on their apparent brightness. The most suitable targets for Direct Imaging observations have an apparent visual magnitude in the range of 6$\geq$V$\geq$12. In Direct Imaging mode, a defocused image of the star is projected directly onto the CCD. For stars brighter than V$\approx$6, the telescope's Fabry imaging mode is used to attain the required photometric stability. The Fabry mode employs an array of 6 x 6

[8]Equivalently, these are the limits for a signal that can be detected above the level of the noise floor in the Fourier spectrum.

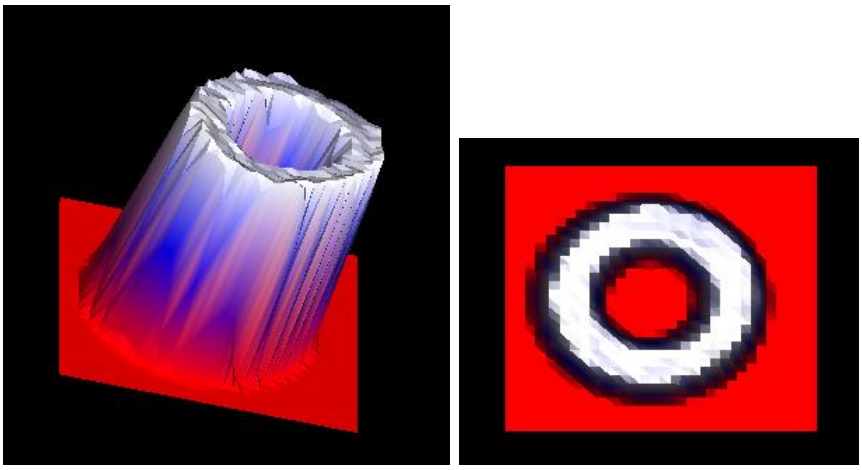

Figure 3.1: Fabry image of Betelgeuse (acquired in 2008), shown from different perspectives.

Fabry microlenses, each of which focuses an image of the telescope pupil on the CCD. A Fabry image of Betelgeuse is shown in Figure 3.1. The light from the star is thus spread over about 1400 pixels, so very bright targets can be observed without saturating the detector. In addition, this technique minimises the impact of sub-pixel and pixel-to-pixel variations. Higher precision can thus be achieved in Fabry mode for bright stars. For fainter targets, the readout noise from such a large number of pixels would become more significant relative to the number of photons received from the star, counteracting the advantages gained by observing in Fabry mode. Therefore, the Direct Imaging mode is used. Nevertheless, targets observed in Direct Imaging mode also result in impressive photometry thanks to the instrument's excellent pointing stability. Multiple targets can be monitored simultaneously in both imaging modes since each uses a different area of the CCD (the Fabry mode uses an exclusive $\sim$ 700 x 700 pixel portion of the CCD). Figure 3.2 shows the target map for the Betelgeuse observations and the location of the array of Fabry microlenses, superimposed on a representation of the CCD. The cross-hairs indicate the microlens under which Betelgeuse was positioned. The "L-shaped" area along the left and top

sides of the CCD is used for Direct Imaging. The squares within this area correspond to subrasters containing Direct Imaging targets and guide stars.

All but one of the stars monitored by MOST for this thesis have V magnitudes $\gtrsim 6$ and thus have been observed in Direct Imaging mode.

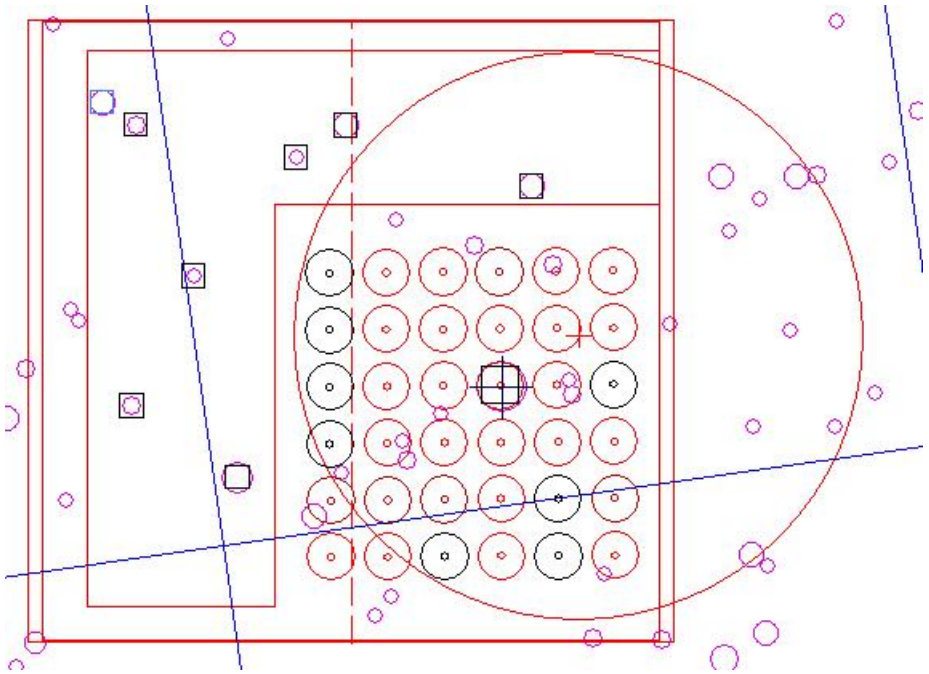

Figure 3.2: Target map and Fabry microlens array superimposed on a representation of the MOST CCD.

3.1.1.1 Data Reduction

Exposure times for individual frames in Direct Imaging mode generally range from a fraction of a second for bright targets to a few seconds for fainter stars. These frames are stacked on board the satellite to produce integrations of the order of about a minute. Further, because of the limited data transfer from the CCD electronics to the on-board computer and limited downlink to Earth, only small image sections containing each of the observed targets are stored. These so-called subrasters usually measure 20 x 20 pixels for Direct

Imaging targets. It is these stacked subraster images that are ultimately downloaded from the telescope.

A package developed by Jason F. Rowe (described in detail in [197, 198]) is used to extract and reduce the photometry. First, bias subtraction (to correct for the base noise level of the CCD) and dark subtraction (to correct for the accumulation of charge introduced by heat in the CCD) are performed. Measurements for these corrections are obtained from areas of the CCD which are kept dark by a chromium mask above the focal plane, and averaged on board the satellite. These averages are downloaded and used for the bias and dark correction.

MOST is affected by two major noise and/or drift sources. One is the flux of cosmic rays (energetic charged protons) reaching the detector and introducing spikes into the subraster. The cosmic ray flux peaks when MOST's orbit carries it through the South Atlantic Anomaly (SAA) - a weakened region of the Earth's magnetosphere. The other is scattered light from the illuminated portion of the Earth ("Earthshine") which is modulated with the orbital period of the MOST satellite. A two-dimensional second order polynomial is fit as a function of the x- and y-pixel positions outside a radius of 8 pixels from the center of the star (to minimise contamination from the star) and subtracted to correct for background gradients associated with stray light. Next, pixels with charge levels greater than 2.5 standard deviations from the median of the background pixels (which have been affected by cosmic ray hits), are rejected. The median is used since it is less sensitive to deviant values. The mean of the remaining pixels is then taken as the sky background level for the star in that particular subraster.

Within a subraster, the star is detected in two steps. First, the user identifies the star by eye via a graphical interface, and this input serves as a first guess for the centroiding algorithm. Next, centroids are calculated from the intensity-weighted averages in x and y position, on a 5 x 5 pixel grid centered on the initial guess. The process is iterated until centroid convergence is achieved.

The total flux of a star in a given image is determined by calculating the total number of counts within a given aperture radius (usually between

3 and 6 pixels[9]) from the center of the stellar source. The flux is then converted to magnitude.

At this point, the stellar magnitudes must be corrected for stray light effects and cosmic ray hits. Magnitudes that are more than three standard deviations from the median are rejected as outliers caused by cosmic rays. For the stray light correction, the sky background described above is used. The two-dimensional fits do not optimally scale the background level, possibly because many of the stray light photons arrive at a grazing angle to the CCD and the projected area and thickness of the detector responds differently to these photons. There are also correlations between the observed magnitudes and the x and y pixel positions of the center of the star in the subraster, because there is always some amount of pointing jitter. These are due to pixel-to-pixel as well as intrapixel sensitivity variations. All of these effects can be corrected as follows. The stellar magnitudes are modeled with polynomial functions of the sky background, and x and y positions. In most cases, a fourth-order polynomial for the sky background and third order polynomials for the x and y positions are sufficient. However, the results of the de-correlation are always inspected to ensure the data was not overfitted.

After this de-correlation process, the light curve often still contains some stray light variations at the orbital period of the satellite, though with significantly smaller amplitudes relative to the raw photometry. Even so, for high-precision photometry, specifically searching for and modeling shallow transits, these variations should be minimized further. This is accomplished in the following way. The light curve is separated into sections spanning several cycles of the MOST orbit. Each section is then folded with the satellite's orbital period, and the boxcar average within a local phase window (usually with a width 0.01 of the MOST orbital phase cycle) is computed for the entire folded section. These running averages represent the stray light waveform during the time interval containing that section of the light curve.

[9]Ideally, the aperture radius should be small so as to minimise the amount of sky background included. However, if the pointing of the telescope is less good than usual, then a larger aperture is chosen to ensure that sufficient light from the star is included even if the target is not always in the centre of the aperture.

Finally, this waveform is subtracted from the data [199].

A final step, often used when the light curve exhibits long term variations, consists of examining any other stars in the direct imaging field of the target (after their photometry has been extracted and reduced in the same way as that of the target). This comparison helps determine whether the variations are systematic (in which case the light curves of the other stars would exhibit similar variations) or astrophysical.

3.1.2 Ground-Based Photometry

Ground-based astronomical facilities are much more numerous than space-based instruments, which are more expensive to build and whose launches are very costly. Ground-based telescopes allow excellent science to be accomplished for a fraction of the cost of space instruments, but they do have important limitations. Some of these can be overcome with careful data reduction and analysis, and some cannot.

As mentioned in the previous section, one such disadvantage is the presence of the day-night cycle which limits continuous observations to the duration of the night at the telescope site. One solution is to build telescopes near the poles where it is possible to have longer nights during winter; a few such endeavours have recently been undertaken [60, 147], but the harsh Arctic and Antarctic conditions make progress slow and maintenance difficult. Another possibility is the development of networks of telescopes longitudinally distributed around the Earth [32]. However, care must be taken to standardise and homogenise observations of the same target acquired with telescopes located at different sites and thus operating under different conditions.

Even during the night, clouds and other atmospheric conditions can render a night's observations unusable. This is the reason why many ground-based telescopes are located in dry and high places. The altitude minimises the amount of atmosphere through which light from astronomical sources must travel, and reduces the water vapour content of the air. This reduces seeing, which consists of atmospheric fluctuations that affect starlight and

induce blurring or twinkling in astronomical images. Speckle and lucky imaging (consisting of taking very short exposures in order to minimise the blurring due to changes in the Earth's atmosphere over time, of which the sharpest images are selected for analysis) and adaptive optics are techniques currently used to further eliminate seeing, but they each have limitations. The imaging methods require bright targets, while adaptive optics systems are expensive and very elaborate. For photometric observations, seeing ultimately adds noise to the data because the images of stellar point sources are blurrier and experience changes in apparent brightness due to the twinkling.

Another major consideration is airmass. As a star travels across the sky during the night, it will be observed at different zenith angles, so through an increasing or decreasing amount of atmosphere. The most common way to account for this and other systematic and instrumental effects is to perform differential photometry. The light curve of the target star is calibrated by subtracting from its magnitude values the magnitudes of references stars in the same field of view. It is important that the reference stars are bright, have a low level of variability and have color similar to that of the target. The brightness reduces noise while similar colors ensure that the stars are affected by airmass in the same way. Indeed, the brightnesses of nearby stars of different spectral types (hence colors) are affected by airmass quite differently, and can thus lead to inaccurate calibrations.

The ground-based HD 192263 photometry presented in this thesis (Chapter 6) was acquired with the Automated Photoelectric Telescopes (APTs) located at Fairborn Observatory in Arizona [109], where they have been established in 1996. Instead of a CCD, the APTs use photomultiplier tubes as detectors. The telescope sizes range from 0.4 to 0.8m, and the one used for the HD 192263 measurements has an aperture of 0.8 m. This telescope has two channels for simultaneous observations in two bandpasses, and therefore two photomultiplier tubes. The target and comparison stars must thus be observed in sequence. The HD 192263 data were acquired, extracted and reduced (using differential photometry) by Gregory Henry, who is a member of the Tennessee State University Automated Astronomy Group which operates and maintains the APTs.

3.2 Spectroscopy

Stellar radial velocities are obtained from spectroscopic measurements. Though a low or medium-resolution spectrograph is often sufficient for studying the motion of fast-moving objects such as binary stars, determining galaxy redshifts or simply examining the elements present in stellar or galactic spectra, a high-resolution instrument is required for measuring the minute shifts in stellar spectral lines induced by a low-mass orbiting object such as a planet. To achieve a radial velocity precision of a few m/s, a spectral resolution (R) greater than 60000 is generally necessary, where R is defined as

$$R = \frac{\lambda}{\Delta\lambda}, \tag{3.1}$$

and $\Delta\lambda$ is the smallest difference in wavelength that can be distinguished at a wavelength λ. High-precision spectrographs such as HIRES and HARPS are Echelle spectrographs which cover the entire visible range. An echelle spectrograph generally uses an echelle grating and a prism placed orthogonally to each other. The result is that the spectrum of the incoming light is separated into successive components (orders) which are then spread in consecutive stripes from the top to the bottom of the CCD, making use of both the X and Y directions. The wavelength calibration is achieved using either the iodine cell or the simultaneous thorium-argon techniques, as described in Section 1.1.2.

Several limitations to high-precision radial velocity measurements exist. There are instrumental challenges ranging from thermal and mechanical instability to pixel sensitivity variations. Telluric spectral lines (i.e., spectral lines resulting from emission, absorption and scattering in the Earth's atmosphere) can contaminate the stellar spectrum, as can light from background objects located close to the target in the field of view. Often the affected spectral regions must be rejected from the data. Finally, the radial velocity precision achievable is often limited by the presence of stellar activity or "jitter". In cases where stellar pulsations or spots induced by magnetic activity

may be present, extra care must be taken to verify whether a radial velocity signal is caused by these occurrences or an orbiting exoplanet. Even relatively low-amplitude phenomena like granulation, which occur in the outer layers of most stars, can be problematic as they may add noise at the level of a few m/s for a G-type star [73]. This is the main challenge for attaining sub-meter per second precision. Currently, this effect can only be mitigated by observing quieter stars and collecting a large number of measurements to beat down the noise due to stellar jitter.

The HD 192263 (Chapter 6) and HD 97658 (Chapter 8) spectroscopic measurements were obtained with the HIRES spectrograph. The data was reduced, calibrated and converted to radial velocities by Andrew Howard (University of California, Berkeley). The ephemerides for the exoplanets presented in Chapters 4 and 7 were provided by Michaël Gillon (Institut d'Astrophysique et de Géophysique, Université de Liège) and are based on measurements acquired with the HARPS instrument.

3.3 Transit Detection

In this section I give an overview of transit geometry and parameters, followed by a description of the main statistical methods commonly used for transit detection and characterisation.

3.3.1 Transit Geometry

For a circular orbit, the basic properties of a transit are shown schematically in Figure 3.3. Points 1, 2, 3 and 4 correspond to the first, second, third and fourth contact, respectively. The sections of the transit between 1 and 2, and between 3 and 4, are referred to as ingress and egress, respectively. During ingress and egress, only part of the planet's disk occults the star. Relative to the out-of-transit flux (before 1 and after 4) normalized to 1, the depth of the transit ΔF is roughly the ratio of the area of the planet's disk area to the area of the star's disk (see Section 1.1.3).

The impact parameter b is a dimensionless quantity which measures how

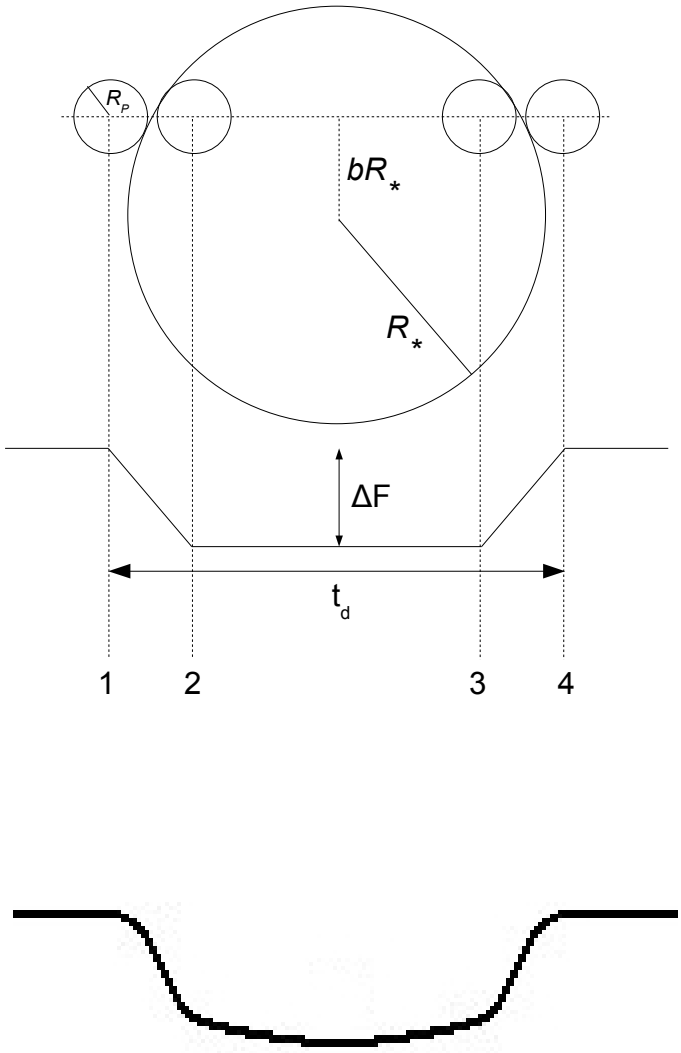

Figure 3.3: *Top:* Schematic representation of transit progression and parameters without limb darkening. *Bottom:* Representation of a limb-darkened transit.

close to the centre of the star's disk the transit path takes the planet. If the planet crosses through the centre of the star, then $b = 0$. In Figure 3.3, $b > 0$. The impact parameter, the orbital inclination and the ratio $a/R_\star$ (also called the scaled semi-major axis) are related as follows:

$$b = \frac{a}{R_\star} \cos i. \tag{3.2}$$

As the transit duration t_d depends on the orbital inclination and scaled semi-major axis, but also on the planet's velocity during transit (obtained from the semi-major axis and the orbital period), the equation for t_d in the case of a circular orbit is

$$t_d = \frac{R_\star P}{\pi a} \sqrt{1 - (\frac{a}{R_\star} \cos i)^2}, \tag{3.3}$$

where P is the orbital period.

I have not considered the effects of limb darkening for this basic overview of transit geometry. Limb darkening affects the shape of a transit and also increases the transit depth slightly, producing a more curved transit such as that shown at the bottom of Figure 3.3. As a consequence, it can also render less clear the boundaries between ingress/egress and the section of the transit during which the planet is completely superimposed on the star. For most of the work in this thesis, I have used the models of Mandel & Agol [160] which are based on the geometry presented above but also incorporate limb darkening.

3.3.2 Frequentist Analysis

Frequentist statistical methods are based on the concept that a given data set comprises samples drawn from a particular underlying population, and that this sampling distribution (the data set) is thus a model of the population. The more measurements are added to the sampling distribution, the closer it approximates the underlying population. Conclusions are drawn under

these assumptions by quantifying how likely it is that the data arise from various parameter values. The parameter values that fit the data best make up the model that is most likely to describe the data. This likelihood is commonly evaluated using the χ^2 goodness-of-fit statistic

$$\chi^2 = \sum_{i=1}^{N} \left(\frac{v_i - f_i}{\sigma_i} \right)^2, \tag{3.4}$$

where v_i is the value of data point i, σ_i is the measurement uncertainty associated with data point i, f_i is the value of data point i predicted by the model and N is the number of data points. The best-fitting model is considered to be the one for which χ^2 is minimised (least-squares analysis). Thus frequentist methods generally result in single-value estimates for model parameters.

It is not straightforward to determine uncertainties on these point estimates of the model parameters, so often Monte Carlo methods such as bootstrapping are used. These involve the generation of a large number of equal size data sets obtained by randomly sampling from the original data. Thus, these data sets are replicates of, though not identical to the original data set. Each of these replicate data sets undergoes the same least-squares analysis to obtain a distribution of values for each parameter, and the parameter uncertainties are based on these distributions. An important advantage of bootstrapping is that there is no assumption about the shape of the parameter distributions, and this technique can therefore show if non-Gaussianic statistics are present in the data. One disadvantage, as described in the first paragraph of this section, is that it relies on the data being a faithful representation of the underlying population. This is not necessarily true, especially when the sample size is small. Bootstrapping can also be computationally intensive since a larger number of generated data sets must be produced and analysed in order to reduce any random sampling errors that might originate from the procedure itself.

In transit detection, frequentist analysis consists of fitting a transit model

to a light curve by varying the transit parameters and computing χ^2. The combination of best-fitting transit parameter values is that which minimises χ^2.

3.3.2.1 Transit Insertion and Recovery

I will now give a general description of the Monte Carlo tests used to analyse the GJ 581 photometry (see Chapter 7 for specific details).

To test the ability to detect transits in a given light curve, I apply a transit insertion and recovery procedure. The first step consists of injecting simulated realistic transits in the light curve. The simulated transits are generated using the analytic approximation for small planets ($R_P/R_\star \leq 0.1$, valid for all the super-Earth candidates analysed throughout this thesis) derived by Mandel & Agol (equation 8 in [160]).

To recover the inserted transits, I fit a box-shaped transit model to the light curve. (While the box-shaped approximation is not accurate enough to properly characterise a transit, it is amply sufficient for the detection of a transit signal and its simplicity significantly reduces computing time.) The model parameters which are allowed to vary are the box-shaped transit depth, duration and phase (constrained to within the predicted transit window), while the orbital period is kept fixed at the value obtained from the RV ephemeris. The combination of parameter values for which χ^2 is minimised represents the best-fit model for the recovered transit. By comparing these best-fit models to the parameters of the inserted transits, I can determine the level of confidence with which transits of various depths and durations are detectable in the data.

I finally apply the transit search code to the original light curve (without any inserted transits) and use the results of the insertion and recovery test to determine the significance of the best (in the χ^2 sense) transit candidate found by the code.

3.3.3 Bayesian Inference

Unlike frequentist inference which treats parameters as unknown but fixed, Bayesian inference generates a probability distribution for each parameter based on the data set and prior knowledge [97, 219]. The use of priors constitutes a critical difference between the two approaches. Priors quantify the level of uncertainty regarding a particular set of parameters *before* data has been observed. When they are combined with a new data set, the state of knowledge about these parameters is updated. Assumptions about the repeatability of the data are not necessary as they are in frequentist statistics.

Another advantage of Bayesian inference is that posterior distributions provide a natural way to estimate uncertainties on the parameters.

Given a set of data D and model parameters θ, Bayes' theorem takes the following form:

$$P(\theta|D) = \frac{P(\theta)P(D|\theta)}{P(D)} \tag{3.5}$$

where $P(\theta)$ is the prior distribution, $P(D|\theta)$ is the probability of obtaining the data given the model parameters (also known as the likelihood) and $P(D)$ is a normalization factor which ensures that the integral of the posterior distribution (the sum of all posterior probabilities) is equal to one. The posterior distribution $P(\theta|D)$ is essentially the probability of a set of model parameters given the data.

An important caveat of the Bayesian method is the dependence of the posterior distributions on the choice of priors. As such, priors must be chosen carefully to ensure they reflect the state of knowledge as accurately as possible. If there is doubt, more conservative priors should be selected.

To test models against each other or against the null hypothesis, Bayesian inference uses a powerful tool called the odds ratio, defined as

$$OR_{1,2} = \frac{P(\theta_1)}{P(\theta_2)} \times \frac{P(D|\theta_1)}{P(D|\theta_2)}. \tag{3.6}$$

$P(\theta_1)$ and $P(\theta_2)$ are the prior distributions for models 1 and 2, and their ratio is the prior odds. If we do not favor one model over the other *a priori*, the prior odds is 1. $P(D|\theta_1)$ and $P(D|\theta_2)$ are the *marginal* likelihoods for models 1 and 2, and their ratio is the Bayes factor, which can also be expressed as

$$\frac{P(D|\theta_1)}{P(D|\theta_2)} = \frac{\int P(\omega_1|\theta_1)P(D|\omega_1,\theta_1)d\omega_1}{\int P(\omega_2|\theta_2)P(D|\omega_2,\theta_2)d\omega_2} \tag{3.7}$$

where ω_1 and ω_2 correspond to the set of parameters for models 1 and 2, respectively. Through its definition, the Bayes factor incorporates Occam's Razor, which penalises over-complex models. Essentially, a model with a larger number of parameters must fit the data not only marginally, but significantly better than a model with fewer parameters in order to be favored.

Finally, in order to obtain the posterior probability distribution for a single parameter, it is necessary to marginalise (integrate) $P(\theta|D)$ over the other parameters. This process can be very computationally intensive, especially for a large number of parameters. A common method used to accomplish this more efficiently is Markov Chain Monte Carlo (MCMC), which I describe below.

3.3.3.1 Markov Chain Monte Carlo

The MCMC program is based on the Metropolis-Hastings (M-H) algorithm [104, 174]. Suppose we have a model with only one parameter θ. We start with an initial guess for this parameter. The M-H algorithm draws a new sample from a proposal distribution (generally Gaussian). The likelihood

$$P(D|\theta) \propto e^{-\frac{1}{2}\sum_{i=1}^{N}\left(\frac{D_i-\theta_i}{\sigma}\right)^2} \tag{3.8}$$

(where N is the number of data points and σ is the measurement uncertainty) is calculated for both the old ($P(D|\theta_{old})$) and new ($P(D|\theta_{new})$) parameter values. The acceptance ratio

$$a = \frac{P(D|\theta_{new})}{P(D|\theta_{old})} \tag{3.9}$$

is computed. If $a \geq 1$, the new parameter value θ_{new} is accepted and replaces θ_{old}. Otherwise, θ_{new} is accepted with probability a. (This is done by generating a uniformly distributed random number r between 0 and 1, accepting θ_{new} if $r \leq a$, or rejecting it and repeating the θ_{old} step otherwise.) The process is repeated until sufficient convergence is achieved, at which point the resulting chain of model parameter values is a representation of the posterior probability distribution.

To check whether convergence has been reached, multiple chains with different initial parameter values must be run. Convergence is commonly quantified using the Gelman-Rubin [92] statistic which verifies if all chains have settled to the same posterior distribution [84]. Even so, chains should also be inspected visually to ensure that convergence as well as full exploration of the relevant parameter space have occurred.

A chain takes some time to reach stationarity and begin to approximate the posterior distribution. This period is called burn-in and the corresponding samples are removed from the chain before inference since they tend to be unrepresentative of the equilibrium posterior distribution. The number of samples to be excised can be determined by visually inspecting the chain's progress, but usually ranges from 1000 to 10000, depending on the length of the chain and the accuracy of the initial guesses.

To fit transit signals, I use not one but several model parameters. Those are the (predicted) time of mid-transit ($T0$), the orbital period (P), the ratio of the planetary and stellar areas ($(R_P/R_\star)^2$), the scaled semi-major axis ($a/R_\star$), the orbital inclination (i) and quadratic limb-darkening coefficients (u_1 and u_2). When a transit is detected, the light curve is folded with the period of the planet, and P is fixed, allowing a transit signal with a higher

signal-to-noise to be fitted, leading to more accurate and precise parameter estimates. Further, if the quality of the data is not sufficient to constrain limb darkening, u_1 and u_2 are fixed to theoretical values based on the host star's properties.

In the search for and characterisation of transits of known RV exoplanets that I conduct, P and $T0$ are estimated from the RV measurements so I use Gaussian priors for these parameters. For each parameter, the mean and standard deviation are equal to the RV-derived value and uncertainty, respectively. For $(R_P/R_\star)^2$, I use a uniform prior ranging from 0 to a value corresponding to the transit of a Jupiter-size planet. This is a more than sufficiently wide range, since the exoplanets for which I have developed the code are super-Earths or super-Earth candidates. Since a is a function of P and $M_\star$ through Kepler's third law, Gaussian priors based on the values and uncertainties of those two parameters and of $R_\star$ are combined to give a Gaussian prior on $a/R_\star$. The prior for i is uniform[10], ranging between the minimum i value that would give rise to a transit based on $R_\star$ and a, and 90°. Finally, when fitting for limb darkening, the associated priors are Gaussian and based on the theoretical u_1 and u_2 values and their uncertainties.

The details of the application of this code to the 55 Cnc photometry are found in Chapter 9.

3.4 Searching for other Periodicities

A photometric data set can also be subjected to a search for periodicities other than transit signals. In the case of MOST space-based photometry, one reason for this is to assess the properties of familiar systematic artifacts such as straylight variations modulated by the satellite's orbit (and the harmonics of these effects). If the artifacts interfere significantly with the analysis of the data, they are removed from the data set using a process called pre-whitening (see Section 3.4.1 for details). For ground-based photometry, artifacts could be caused by the discrete time sampling of observations such

[10]Technically, this prior is actually uniform in $\cos i$. However, for the small range of inclinations that give rise to a transit, a uniform prior is an acceptable approximation.

as those acquired at the same time every night, or on the same day every month, or during the same part of every year. MOST is also affected by aliases, but less so than ground-based measurements thanks to its generally contiguous or near-contiguous data sets.

Periodic signals may also arise from stellar variability such as changes in brightness due to star spots, flares, pulsations or granulation. Although I usually choose to filter these from the light curve before a transit search or the modelling of a transit signal is carried out, these stellar signals are informative both in the context of the star's attributes and that of possible star-planet interactions. The stellar variability of HD 192263 and GJ 581 is addressed in Sections 6.5 and 7.6, respectively.

3.4.1 Fourier Analysis

The algorithm I adopt to Fourier analyse the photometry presented in this thesis, *Period04* [150], was written by Patrick Lenz for the statistical analysis of photometric data sets containing gaps. It is capable of handling discrete Fourier transformations, but also includes tools for least-squares fitting and calculation of parameter uncertainties.

For a typical Fourier analysis, I proceed as follows. I generate a Fourier spectrum, which contains any real (astrophysical or instrumental artifact) frequencies present in the data, the harmonics[11] of those frequencies arising from nonsinusoidal signals, as well as sampling aliases of those frequencies and their own harmonics.

Aliases arise from the discrete sampling of a continuous signal. A Fourier spectrum of such a discretely sampled signal is in reality the Fourier spectrum of the convolution between the continuous signal and the sampling function. The Fourier transform of the sampling function is called the spectral window function. Thus, if there are gaps in the data that occur with a certain frequency, the window function will contain a peak at that fre-

[11] Non-sinusoidal signals are represented in Fourier space by a series of frequencies, the Fourier peaks for which occur at integer multiples of the lowest frequency corresponding to the signal, called the fundamental frequency. These are called harmonics of the fundamental frequency.

quency. Most of the time though, the (not always even) sampling of the data will cause more than one such peak in the window function. *Period04* also generates the window function of a data set.

The Fourier spectrum thus serves to provide a first look at the signals and aliases present in the data set. To determine and characterise the non-alias frequencies in a Fourier spectrum, I use the least squares fitting and bootstrapping capabilities of *Period04* as follows: a) in the Fourier spectrum, identify the largest physical (non-alias) peak; b) perform a least-squares fit using the properties of this frequency obtained from the Fourier transform as a first guess; c) subtract the best-fit solution from the data.

This process is repeated (with step b) consisting of a simultaneous fit of the current and previously identified frequencies) until there is no improvement in the χ^2 value of the residuals. The peaks identified until this point are considered to be the significant frequencies in the data set. The least-squares fit provides values for the frequency, amplitude and phase of those peaks. This procedure is commonly known as pre-whitening.

To obtain uncertainties on these three parameters, I use *Period04*'s bootstrapping tool. A description of bootstrapping in given in Section 3.3.2.

In particular, I have applied the process described above to find and model the frequencies present in the HD 192263 data (see Chapter 6). I have also used this process to filter out frequencies associated with familiar systematic effects from MOST photometry such as the GJ 581 light curves. The main two such effects are the modulation of the stray light with the period of the MOST satellite (101.4 minutes) and the variations due to the fact that the MOST orbit brings it to nearly the same point above the Earth after 1 day, sometimes introducing a signal due to the variations of the Earth's albedo across the planet's surface. Pre-whitening is used to filter out these frequencies and their harmonics to reduce the noise present in the light curve and facilitate the ensuing transit search and/or characterisation.

3.4.2 Other Approaches

In this section, I enumerate and describe other common approaches that can be used for periodicity searches as well as their advantages and disadvantages.

Phase Dispersion Minimisation (PDM) [224] searches for periodic

signals by folding the data at many periods and comparing the scatter of the folded time series to its spread, for each period. Specifically, the folded data is divided into bins and the variance of the data in each bin (intra-bin variance) is calculated. The intra-bin variances are then compared to the overall variance of the folded data. The intra-bin variance should be small compared to the overall variance at periods where a signal exists, and close to unity otherwise.

PDM has no preference for a particular signal shape and is thus well suited for situations where the shape of the signal of interest is unknown. Further, it works well for data sets with gaps. However, one difficulty is deciding how fine a grid to use for the period search. For this reason, and because the already mentioned non-transit periodicities dealt with in this thesis are sufficiently close to sinusoidal, I did not consider this technique preferable to the Fourier analysis procedure described in the previous section, which covers a wide range of frequencies and also naturally supplies the spectral window function.

When the frequency at which a signal is expected is known, a technique called the ***Rayleigh power test*** [148] can be used. A random walk is carried out in two dimensions, each step consisting of a unit vector. The length of the resultant net vector is determined using the following statistic

$$S = \left(\sum_{i=1}^{N} \sin \phi_i \right)^2 + \left(\sum_{i=1}^{N} \cos \phi_i \right)^2 . \tag{3.10}$$

Here ϕ can be the phase parameter of the frequency being explored, and hence ϕ_i designates its value at step (unit vector) i. If the net displacement is statistically insignificant, then all phases are equally likely, suggesting there is no signal at that frequency. Otherwise, it indicates that a signal is present at the frequency of interest. To quantify the level of statistical significance for the Rayleigh power test, the value of the S statistic is compared to a table of critical values to determine the probability that the value would be drawn randomly from the underlying population. If this probability is low,

then the statistical significance of the S value is high, and vice versa.

The Rayleigh test is designed for Poisson-distributed data, and for a large number of samples it becomes analogous to a Fourier analysis. Though relatively easy to implement, the Rayleigh test is not well suited for data containing gaps since it lacks a means to discriminate between a real signal and an alias.

Another technique developed for searches of periodic signals of unknown shape is the Bayesian ***Gregory-Loredo (GL) algorithm*** [100]. The data is folded at different periods. At each period, the folded light curve is divided into n equal-size bins. Using a model with the phase and values of each bin as the free parameters, the best-fitting values are found. The likelihoods corresponding to the best-fit models for various numbers of bins (various models that may describe a potential signal) are each compared to the likelihood obtained by using a single bin (the constant model) via the odds ratio.

Though this is a powerful method to search for periodicities when the shape is unknown and allows models to be penalised for unnecessary complexity, it requires the additional use of a weighting factor applied to each bin when the data contains gaps and/or is unevenly sampled. Further, Fourier analysis is more sensitive to signals whose shape is smooth and close to sinusoidal than stepwise function-based methods such as the GL algorithm, which are more appropriate for phenomena such as pulsar signals (which take the shape of periodically occurring spikes in the signal intensity). To become more analogous to Fourier-based methods, the GL algorithm would have to utilise a very large number of bins, which would adversely affect its efficiency (mainly by decreasing its speed).

Chapter 4

The Transit Search

4.1 Overview of the HARPS survey

The goal of the HARPS survey is to search, using the radial velocity technique, for exoplanets around F, G and K-type stars (though a few M-type stars are also included in the sample). Since 2003, about half the time allocated for the survey has been dedicated to finding very-low-mass planets. The stars selected for monitoring have low chromospheric activity and have low rotation rates. These characteristics are important for minimising confusion between exoplanet signatures and stellar activity or rotation. A final sample of 376 stars are observed as part of the low-mass survey.

To date, the members of the HARPS survey have announced the discovery of over 20 exoplanets with minimum masses $\leq 10M_{\oplus}$ (super-Earth candidates), 16 of which have been published in September, 2011 in Mayor et al. (2011) [169]. Of note among these are two super-Earth candidates in the habitable zone of their stars: GJ 581d orbiting a M dwarf and HD 85512b orbiting a K dwarf.

4.2 Overview of TERMS Project and Results

The TERMS project aims to detect transits of known RV exoplanets with intermediate-long periods. Since RV surveys are mostly sensitive to planets around bright stars, any transit discovered by TERMS would constitute an important addition to the relatively small collection of known transiting exoplanets with longer periods around bright stars. Further, such an exoplanet would be amenable to a variety of follow-up studies, including measurements of the RM effect.

TERMS has two major components: ephemeris refinement and photometric monitoring. The first is especially important for the detection of these transits. A few strategically acquired RV measurements can significantly reduce the uncertainties on the orbital parameters and improve the ephemeris. As the transit windows of these candidates become smaller, the efficiency with which they can be monitored for transits will increase. If the transit window is dominated by the predicted transit duration rather than the uncertainty on the transit mid-point (see Section 4.3.2), it is possible to complete the transit search for that particular planet within a single observing night.

With transit probabilities of most TERMS targets ranging between 1 and 3%, and an efficient observing strategy, there is a strong probability that the first TERMS transit will be discovered within the next 2 years.

HD 192263 is a system on which I carried out a transit search in the context of TERMS. I have also performed an analysis of the host star variability, one aim of which was to explore the possibility of star-planet interactions. The analysis of the HD 192263 system constitutes the subject of Chapter 6.

4.3 Overview of the MOST Target Sample and Observing Approach

4.3.1 Target Sample

As I explained in chapters 1 and 2, exoplanets transiting bright stars can bring in a wealth of information in the form of more numerous photons. Further, both MOST and the RV surveys from which we obtain suitable candidates for the transit search generate more precise measurements for bright targets. RV surveys also tend to avoid early-type (O, B and A) stars because their spectral lines are sparse and often broadened due to rapid rotation, two factors which make it difficult to obtain precise Doppler shifts. For these reasons, the stars in the transit search sample are of F, G or K spectral type, with the exception of GJ 581 which is an M-type dwarf star.

The RV detected exoplanets I selected for the search are those with or-

bital periods shorter than 10 days that, for F, G and K stars which tend to have radii similar to that of the Sun, led to geometric transit probabilities larger than $\sim 5\%$ (see Section 1.1.3). These planets should also have minimum masses in the super-Earth regime, and up to approximately that of Neptune ($M_p = 17.1 M_\oplus$). In essence, at least part of the range of possible radii for these super-Earth and Neptune candidates lies below the size of a planet whose transit could be detected using easily accessible (1 - 2 m) ground-based telescopes. This characteristic then justifies the need for a space-based instrument, which is why MOST is used for this transit search.

When this project began in 2008, the HARPS planet hunting team had informed us they had potentially ∼40 exoplanet candidates with the characteristics described above, many of them unpublished at the time. Some of those turned out to be false positives, while several others did not lie within MOST's CVZ or SSZ. Of those that remained, many had transit windows (the time span during which a transit is predicted, if the planet's orbital planet is favorably aligned) in excess of 30 hours, thus making a $\lessapprox 10\%$ transit search difficult to justify. I have also acquired a few ephemerides from the Keck-HIRES survey, for a final number of 12 targets observed as part of this project.

4.3.2 Observing Approach

The size of the transit window is derived from the uncertainties on the orbital period and the predicted time of transit, and so it depends on the signal-to-noise ratio of the RV measurements. A less massive planet will induce a lower-amplitude RV signal than a more massive planet orbiting the same star with the same orbital period. If additional companions are present in the system, individual RV signals may be difficult to disentangle. Generally, these issues can be resolved as the number of measurements increases, but that can mean that it will take longer for a planet's transit window to be sufficiently narrow for a transit search to be carried out. Some of the super-Earth candidates, even if they were discovered more than two years ago, have not been adequate for the transit search so far and have had to be

postponed until their ephemerides become more refined.

The predicted mid-transit time is determined as follows:

$$T0 = T_p + \frac{PM}{2\pi} + nP \tag{4.1}$$

where T_p is the time of periastron (point of closest approach to the star) passage, M is the mean anomaly[12] and n is the number of complete orbits elapsed since T_p. For a circular orbit, $M = \pi/2$ and equation 4.1 reduces to

$$T0 = T_p + \frac{P}{4} + nP, \tag{4.2}$$

in which case T_p is defined as the time when the planet is a quarter of a period before $T0$.

The values of T_p and M are determined from fitting a model derived from Newton's and Kepler's laws of (planetary) motion to the radial velocities. I obtained the best-fitting orbital parameters for each super-Earth/Neptune candidate that was observable by MOST from the HARPS and HIRES teams. To find a new mid-transit time ($T0_{new}$) from the one they provide ($T0$), I simply used

$$T0_{new} = T0 + nP. \tag{4.3}$$

I used the uncertainties on P and $T0$ to compute the beginning and end of the transit window after n orbits have passed as follows:

$$T_{beg} = (T0 - \delta_{-}T0) + n(P - \delta_{-}P) \tag{4.4}$$

[12]The mean anomaly of the planet is the angle between periastron and the position of the planet at a specific time in its orbit if the orbit, with the same period and semi-major axis, were circular.

$$T_{end} = (T0 + \delta_{+}T0) + n(P + \delta_{+}P) \tag{4.5}$$

The uncertainties on parameters $T0$ and P are represented by $\delta T0$ and δP, respectively. For each parameter, δ_{-} designates the lower uncertainty and δ_{+} the upper uncertainty. These are not always equal, because the posterior distributions which result from the MCMC RV fitting algorithms are not always symmetric. The size of the transit window is obtained by subtracting equation 4.4 from equation 4.5. The transit window derived using the 1σ uncertainties on $T0$ and P will henceforth be called the "1σ transit window". Similarly, for all candidates I have also computed the 2σ windows.

If a host star was observable by MOST and the planet's transit window was not too long, the star was scheduled for observations. We aimed for monitoring each system during three or four transit windows in order to verify whether a potential transit signal repeats. For each star, the duration of observations tends to be short relative to the majority of MOST observing programs, which tend to be contiguous and last from a few days to a few weeks. Most often, one such long-duration program would be interrupted a few times for 10-30 hours at a time, during which a transit search target would be observed. This setup generally worked well, and for the majority of targets we were able to acquire at least 3 transit windows' worth of photometry. However, there were a few targets for which only one window was observed, either because the main observing program would have been severely affected by more interruptions or because the star was too close to the edge of the SSZ and so safely observable for only a few days.

Upon acquisition, I reduced the photometry as described in Section 3.1.1.1 and folded it at the period of the exoplanet. If a possible signal was immediately obvious, an attempt could be made to re-observe the star before it left the CVZ or the SSZ.

For the majority of the systems for which we have acquired MOST photometry as part of this transit search, the duration and spacing of the data

sets are limited to partial or full coverage of transit windows of a known super-Earth candidate. These light curves are thus not adequate for searching for transits of possible additional planets that may not have been detected from the RV measurements.

In the following sections, I provide an overview of the confirmed detections and null results which have resulted from this search. Three of the systems presented (GJ 581, HD 97658 and 55 Cnc) are explored in greater detail in chapters 7, 8 and 9.

4.4 MOST Null Results

I have not detected transits for ten of the super-Earths and Neptune-mass candidates whose host stars have been monitored with MOST. The stellar and planetary parameters of these systems as well as those of HD 97658 are found in Tables 4.1, 4.2 and 4.3. The transit probabilities for these add up to 71%. This means a transit could be statistically expected but is not guaranteed. However, there are two caveats to consider before drawing conclusions from this value. First, for some of these candidates only part of the transit window was covered by the available photometry, so there is still a chance one or more of them transit but with a mid-transit time outside the coverage of the observations. Second, in some cases our photometric precision is not sufficient to exclude transits for the smallest physically plausible planetary radii.

For each candidate, the individual light curves for each transit window as well as the folded and binned photometry with transit models overplotted are shown in figures 4.1 to 4.9. The horizontal axes are in units of orbital phase based on the orbital period of each candidate, while the vertical axes are in units of relative flux, normalised to 1. In each plot, boundaries corresponding to the 1σ and 2σ transit windows are represented by the dotted and dashed vertical bars, respectively. The cadence of the observations (outside of the interruptions clearly visible in many of the light curves) was two data points per minute, unless otherwise noted. The folded light curves are

binned in 8-minute bins such that the number of bins within a hypothetical transit decreases with the predicted transit duration. This facilitates the relative comparison between each candidate's predicted transit duration despite the candidate-specific units of the horizontal axes. In all cases, orbital phase 0.0 corresponds to the predicted mid-transit time.

The first two candidates to appear in both Tables and Figures are GJ 581 and BD-082823, respectively, while the remaining candidates appear in order of increasing HD number. The chronological order in which these candidates were observed is as follows: GJ 581, HD 96700, HD 115617, HD 125595, HD 160691, HD 69830, BD-082823, HD 125612, HD 1461, HD 156668 and HD 97658.

As already mentioned in Section 1.2.3, little is known about the detailed nature of super-Earth exoplanets. Though to date several have been found to transit, allowing their densities to be measured, their composition remains mostly unknown. In addition, super-Earths with similar masses have been found to have very different radii and thus densities, contributing further questions regarding differences in their formation, host star properties, and other factors which may have led to such discrepancies. To provide an approximate notion of the type of planet a super-Earth with a given density could be, theoretical models are used. These are divided in three classes: pure gaseous planets composed entirely of hydrogen or a hydrogen/helium mixture, water ice planets with silicate and/or iron fractions ranging from 0 to 75%, and silicate planets with 0 to 70% iron mass fraction [212].

In this section, I select a composition model for each class and use the corresponding planetary radius given the mass of the planet (assuming $M_p \approx M_p \sin i$ for a transiting planet), together with the orbital properties of each candidate, to determine three resulting transit models for every candidate. These composition models, plotted on the phase-folded and binned light curve of each transit search candidate, are: H/He mixture with 25% He by mass (black solid line), pure water ice (blue solid line) and pure silicate ($MgSiO_3$ perovskite; red solid line). As a reference, in the Solar System Jupiter and Saturn have densities similar to that associated with the first model, Neptune and Uranus have densities between those of the first and

second model, while Mars, Venus and Earth have densities close to that corresponding to the third model.

All exclusions and density limits are based on edge-on orbital inclinations (impact parameter of 0) unless otherwise noted. As an aid for extrapolating the exclusions to larger impact parameter values, it should be mentioned that $b = 0.87$ corresponds to a transit duration of half that of an edge-on transit.

- **GJ 581**

  This is a multiple system with all of its four known planets having minimum masses near that of Neptune or smaller. At the time the MOST photometry of GJ 581 was acquired (May 8-20, 2009), the innermost known planet in the system, GJ 581e, had just been announced. A transit of this planet, which is one of the lowest minimum-mass exoplanets detected with the RV method to date, would be invaluable for detailed studies of its own properties but also potentially those of the other super-Earths in the system. Its "target of opportunity" nature motivated the 11.5 days of contiguous observations of the GJ 581 system. These observations and their analysis are the object of Chapter 7.

- **BD-082823**

  In a two-planet system, BD 082823b orbits the host star closer than its companion. The system was monitored during 4 windows of BD 082823b (top of Figure 4.1), from 24 February to 11 April 2011. This target is within the CVZ and it was possible to observe it without interruptions. The gaps in the third and fourth window light curves arise from the removal of photometry affected by high levels of stray light during the reduction. The phase coverage extends past the limits of the 1σ window but does not encompass the entire 2σ window.

  I rule out transits corresponding to a planet with radius larger than 2.13 $R_\oplus$ within the 1σ transit window (bottom of Figure 4.1). This

translates to a density lower than 7.31 g cm^{-3}, equivalent to a silicate planet.

- **HD 1461**

  HD 1461 is a system of two, possibly up to four known planets. The innermost of those, HD 1461b, was formally monitored during one transit window on 2-3 November 2011 (bottom panel of Figure 4.2). However, it also served as an alternating target for a primary target which was located outside the CVZ, from 7 October to 1 November 2010, and again from 8 October to 1 November 2011 (top of Figure 4.2). The cadence during the window was a point every 61 s, and 2 points per minute otherwise. When combining all the available photometry, the phase coverage spans a range of orbital phase sufficient to ensure a transit would not be missed.

  Unfortunately, in this case the scatter of the light curves is too large to allow a transit detection or any useful limits to be placed on the size of the planet if it transits (bottom of Figure 4.2).

- **HD 69830**

  HD 69830 hosts three known planets. Of those, HD 69830b has the shortest orbital period. It was observed with MOST during three of its transit windows from 11 February to 2 March 2011. However, during the first transit window the star was positioned on the edge of the subraster so the light curve for these observations could not be correctly extracted and thus was not used for the analysis. The remaining two light curves are shown at the top of Figure 4.3. The observations for this star were more difficult to schedule than usual, with the second window interrupting one long-duration program target, while the third window interrupted another. This resulted in the irregular interruptions seen in the second light curve, and the third window not overlapping with the 2σ transit window. The cadence was one data

point every 42 s.

Given the precision of the available photometry and for the available window coverage I can rule out transits for planetary radii larger than 5.4 $R_{\oplus}$ (bottom of Figure 4.3), or a density lower than 0.35 g cm^{-3} corresponding to a H/He composition.

- **HD 96700**

  Three transit windows of HD 96700b, the innermost of two planets in the system, were monitored during 5-30 March 2010. This star is within the SSZ but outside the CVZ, hence it was observed alternately with another target, causing the interruptions seen in the top part of Figure 4.4. Since these data were obtained, new RV measurements have shifted the predicted mid-transit time. Though the photometry covers a portion of the transit window, the most current estimate of the mid-transit time falls outside the MOST observations.

  For the available window coverage, I can only exclude transits for a gaseous planet with radius greater than 5 $R_{\oplus}$ (bottom of Figure 4.4. This corresponds to a density of 0.40 g cm^{-3}, or a composition dominated by hydrogen (H) and helium (He).

- **HD 97658**

  The recent history of the known planet orbiting in the HD 97658 system showcases the importance of follow-up confirmation observations for low SNR discoveries. A transit detection for HD 97658b was announced based on ground-based photometry which showed a partial transit-like feature [111]. To confirm and improve the transit parameters of this super-Earth candidate, we scheduled MOST observations during February-March 2012. In addition, the prospect of MOST photometry of this transit, which could help to better constrain the mid-transit time, lent support to a proposal to obtain Hubble Space Telescope observations of the transit at different wavelengths.

Unfortunately, the MOST data showed no hint of a transit with the parameters published by [111]. It was crucial to announce this null result to the community, since the transiting nature of HD 97658b and the associated discovery paper had both been accepted, and several proposals for follow-up studies using large or space-based telescopes were already underway.

The exclusion of the transit found by [111] make up the object of Chapter 8.

- **HD 115617**

  HD 115617b has the shortest orbital period of the three known planets in its system. It was observed during 4 transit windows from 2 to14 April 2010. It is the only transit search star sufficiently bright to be monitored in Fabry mode. Consequently, the data was reduced by Thomas Kallinger who used a version of the reduction pipeline developed by Reegen (2007) [192] optimised for Fabry photometry. The interruptions (top of Figure 4.5) are due to the fact that this target is just outside the CVZ and thus MOST alternated between it and the primary target at the time. The ephemeris for this planet has also shifted since the observations were acquired, but less drastically than for HD 96700b. The data includes the predicted mid-transit time and covers most of the 2σ transit window.

  For HD 115617b, I can exclude transits of a planet with radius as small as 1.74 $R_{\oplus}$, or density lower than 6.10 g cm^{-3} (bottom of Figure 4.5). This limit is equivalent to a planet with silicate composition.

- **HD 125595**

  HD 125595b is the only known planet orbiting its host star. It was monitored during four transit windows approximately centered on the predicted mid-transit time. The observations (top of Figure 4.6) were acquired between 21 April and 20 May 2010, with interruptions due

to the target's location outside the CVZ. The data covers most of the 1σ transit window.

Within the available orbital phase coverage, I rule out transits for planetary radii greater than 2.75 $R_\oplus$ (bottom of Figure 4.6) corresponding to densities lower than 3.47 g cm^{-3}. This limit represent a planet composed of water ice. Transits of a silicate planet are at the detection limit for this light curve.

- **HD 125612**

  Of the three planets in its system, HD 125612c has the shortest period. MOST observed this target during four of the planet's transit windows (top of Figure 4.7), between 30 April and 30 May 2011, with one integration every 63 s. Though the star is in the CVZ, it was observed alternately with the primary target to minimise the duration of the interruptions for the latter. The large mass and short period of HD 125612c gave rise to a larger SNR of the RV measurements, which in turn led to a narrower transit window that for the previous planets. The photometry extends beyond the 2σ window, albeit with the already mentioned interruptions.

  Given this sampling, I can exclude transits with duration longer than that of an edge-on transit if the planet has a radius greater than 3.02 $R_\oplus$ (bottom of Figure 4.7). The lower limit on the density is thus 3.78 g cm^{-3}, equivalent to a water ice composition.

- **HD 156668**

  HD 156668b is the sole planet orbiting its host star. Two orbital solutions were provided by Andrew Howard of the Keck-HIRES planet search team: one with the eccentricity fixed to 0 (circular orbit) and one with the eccentricity allowed to float. The mid-transit time and its uncertainties as well as those associated with the orbital period differed significantly in each case. Even though the transit window for

the second solution was less well constrained (it was nearly three times longer than in the circular orbit case), given the significant non-zero eccentricity ($e = 0.28^{+0.12}_{-0.11}$) and the absence of other known planets that could introduce a bias in its value, I chose to monitor the star during the eccentric-orbit window.

HD 156668b was monitored during seven transit windows from 8 June to 16 July 2011, with a cadence of one data point every 62 s. Since this system is outside both the CVZ and the SSZ, normally this target would not have been observable. However, from May to July the Sun is below the satellite's horizon for a few minutes during every MOST orbit. During these times, the telescope can be pointed in any direction since the temperature gradient within the satellite does not vary as dramatically with the orientation of the satellite, and thermal constraints are no longer a concern. Thus an unusual observing strategy was employed, where MOST observed the target for 10-15 minutes each satellite orbit during a given transit window. I found that repeating this for seven windows provides adequate phase coverage equivalent to one 1σ window (top and middle sections of Figure 4.8). In reality, the coverage extends past those boundaries, though it does not cover the full 2σ window.

The approach was successful, and I am able to easily rule out transits for a planet with radius larger than 2.05 $R_\oplus$ within the 1σ transit window (bottom of Figure 4.2). This value corresponds to a density of 2.75 g cm^{-3}, or a planet composed of water ice. A transit of a silicate planet ($R_p = 1.59R_\oplus$ and density of 5.90 g cm^{-3}) would be near the detection limit for this light curve.

- **HD 160691**

  MOST acquired photometry during three transit windows of HD 160691c, the innermost of four known planets in the system. The observations (top of Figure 4.9) ranged from June 21 to July 20 2010, and had a cadence of one integration per 16 s. This target, located near the

limit of the SSZ. The predicted mid-transit time has shifted since the observations were obtained, so they just miss it. The phase coverage encompasses a third of the 2σ window.

Within the transit window portion covered by the photometry, I exclude transits of a planet with radius greater than 5.5 $R_\oplus$ (bottom of Figure 4.9). Thus, the transit of a planet less dense than 0.35 g cm^{-3} (corresponding to a H/He composition) would have been detected.

With updated ephemerides in hand, it will be necessary to re-observe those super-Earth candidate systems for which there is insufficient transit window coverage. Foremost among these targets are HD 69830, HD 96700, HD 125595 and HD 160691, for which only partial coverage of the 1σ transit window is available. This will significantly decrease the probability that a transit is missed for these candidates.

Table 4.1: Stellar and RV-derived planetary parameters for GJ 581, BD-082823, HD 1461 and HD 69830

Parameter	**GJ 581e**	**BD-082823b**	**HD 1461b**	**HD 69830b**
Stellar				
Spectral type	M2.5V	K3V	G0V	K0V
V mag	10.5	9.86	6.64	5.95
$[Fe/H]$	-0.14	-0.07	0.18	-0.06
T_{eff} (K)	3498 ± 56	4746 ± 63	5765 ± 18	5360 ± 44
log g[a]	4.96 ± 0.08	4.1 ± 0.3	4.37 ± 0.03	4.46 ± 0.06
$M_\star$ ($M_\odot$)	0.31 ± 0.02	0.74 ± 0.07	1.03 ± 0.04	0.86 ± 0.03
$R_\star$ ($R_\odot$)	0.299 ± 0.010	1.279 ± 0.066	1.11 ± 0.04	0.922 ± 0.033
Age (Gyr)	8^{+3}_{-1}	4.5 ± 4	6.3	7 ± 3
Planetary				
P (days)	3.14945 ± 0.00017	5.59486 ± 0.00090	5.77316 ± 0.00093	8.66644 ± 0.00065
$T0$ (BJD – 2450000)	4749.026 ± 0.056	$5718.49^{+0.27}_{-0.28}$	$5043.02^{+0.24}_{0.25}$	4989.97 ± 0.12
e	0.32 ± 0.09	$0.07^{+0.08}_{-0.05}$	0.13 ± 0.07	0.06 ± 0.03
ω (deg)	236 ± 17	51^{+106}_{-143}	142^{+112}_{-90}	24^{+33}_{-36}
$M_p \sin i$ ($M_\oplus$)	1.95	12.8	7.5	9.9
a (AU)	0.028	0.05557 ± 0.00076	0.06426 ± 0.00061	$0.07671^{+0.00094}_{-0.00098}$
Transit probability (%)	5.0	6.7	8.0	5.2
References	[86, 168, 215, 254]	[107, 235], PCH[b]	[193], PCH[b]	[158, 235], PCH[b]

[a] log g is the logarithm of the surface gravity of the star.

[b] PCH refers to private communication with members of the HARPS team.

Table 4.2: Stellar and RV-derived planetary parameters for HD 96700, HD 97658, HD 115617 and HD 125595

Parameter	**HD 96700b**	**HD 97658b**	**HD 115617b**	**HD 125595b**
Stellar				
Spectral type	G0V	K1V	G5V	K4V
V mag	6.5	7.78	4.74	9.03
$[Fe/H]$	0.00	-0.23	0.02	0.02
T_{eff} (K)	5625 ± 120	5170 ± 44	5577 ± 33	4908 ± 87
log g	4.3 ± 0.2	4.63 ± 0.06	4.45 ± 0.04	4.3 ± 0.2
$M_\star$ ($M_\odot$)	-	0.85 ± 0.02	$0.95^{+0.04}_{-0.03}$	0.756 ± 0.017
$R_\star$ ($R_\odot$)	1.08	0.73 ± 0.02	0.94± 0.03	1.033 ± 0.058
Age (Gyr)	12	-	$9.0^{+2.8}_{-3.0}$	$3.5^{+3.6}_{-3.5}$
Planetary				
P (days)	8.1256 ± 0.0013	9.4930 ± 0.0021	4.21429 ± 0.00045	9.6737 ± 0.0039
$T0$ (BJD – 2450000)	$5716.93^{+0.35}_{-0.40}$	5650.31 ± 0.3	$5718.90^{+0.15}_{-0.14}$	4437.65 ± 0.15
e	0.10 ± 0.05	$0.13^{+0.09}_{-0.06}$	0.11 ± 0.07	0.0 (fixed)
ω (deg)	313 ± 67	120^{+95}_{-67}	86^{+35}_{-55}	-
$M_p \sin i$ ($M_\oplus$)	9.0	7.7	5.8	13
a (AU)	0.0774 ± 0.0012	0.0797 ± 0.0007	0.04970 ± 0.00054	0.0809 ± 0.0014
Transit probability (%)	6.6	4.0	9.8	4.5
References	[169], PCH[a]	[118], PCK[b]	[252], PCH[a]	[214], PCH[a]

[a]PCH refers to private communication with members of the HARPS team.

[b]PCK refers to private communication with members of the Keck-HIRES team.

Table 4.3: Stellar and RV-derived planetary parameters for HD 125612, HD 156668 and HD 160691

Parameter	**HD 125612c**	**HD 156668b**	**HD 160691c**
Stellar			
Spectral type	G3V	K3V	G3IV
V mag	8.31	8.42	5.15
$[Fe/H]$	0.24	0.05	0.29
T_{eff} (K)	5900 ± 40	4850 ± 88	5784 ± 44
log g	4.45 ± 0.05	4.6 ± 0.1	4.30 ± 0.06
$M_\star$ ($M_\odot$)	1.1 ± 0.07	0.77 ± 0.02	1.08 ± 0.05
$R_\star$ ($R_\odot$)	1.043 ± 0.037	0.730 ± 0.043	1.25 ± 0.04
Age (Gyr)	2.1	8.6 ± 4.8	6.4
Planetary			
P (days)	4.15506 ± 0.00033	4.6432 ± 0.0011	9.6389 ± 0.0022
$T0$ (BJD – 2450000)	$5716.508^{+0.034}_{-0.052}$	5104.07 ± 0.24	$5706.30^{+0.43}_{-0.46}$
e	$0.09^{+0.08}_{-0.06}$	0.28 ± 0.12	0.12 ± 0.07
ω (deg)	150^{+66}_{-65}	231^{+27}_{-36}	148^{+60}_{-44}
$M_p \sin i$ ($M_\oplus$)	18.9	4.3	10.6
a (AU)	0.05145 ± 0.00049	0.0500 ± 0.0007	$0.08812^{+0.00089}_{-0.00091}$
Transit probability (%)	13.0	7.0	5.6
References	[82, 155, 235], PCH[a]	[117], PCK[b]	[38, 46, 202, 235], PCH[a]

[a]PCH refers to private communication with members of the HARPS team.

[b]PCK refers to private communication with members of the Keck-HIRES team.

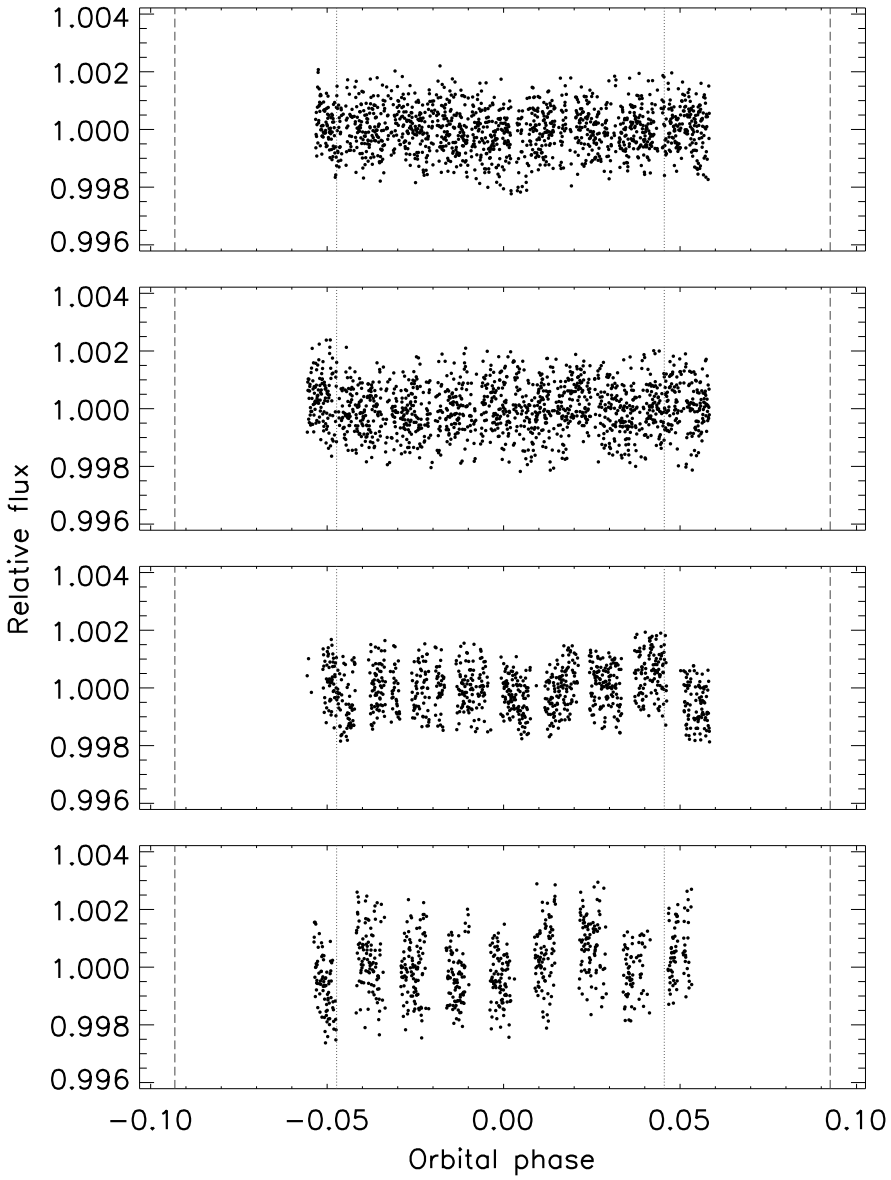
1.004
1.002
1.000
0.998
0.996
Relative flux
−0.10
−0.05
0.00
0.05
0.10
Orbital phase

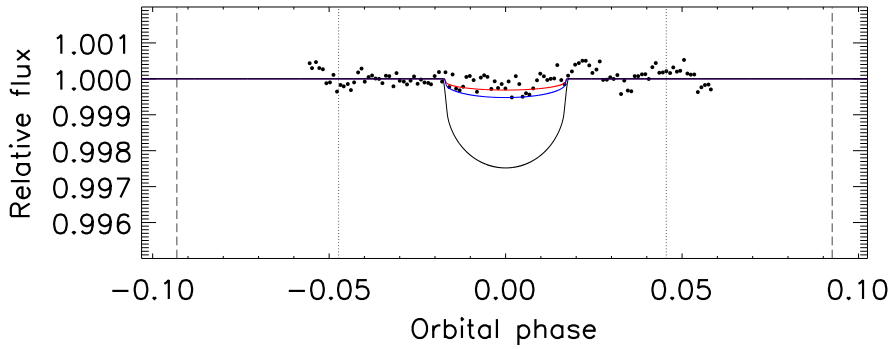

Figure 4.1: *Top:* Light curves for four transit windows of BD 082823b. *Bottom:* All BD 082823b light curves folded to the period of planet b ($P = 5.59486 \pm 0.00090$ days) and binned in 8-min. bins. The horizontal axes for all plots are in units of the orbital phase for this planet. Orbital phase 0.0 corresponds to the predicted mid-transit time. The vertical dotted and dashed vertical lines enclose the 1σ and 2σ transit windows, respectively. Transit models are shown as the red, blue and black solid lines for transits of a planet composed of silicate, water ice, or H/He, respectively.

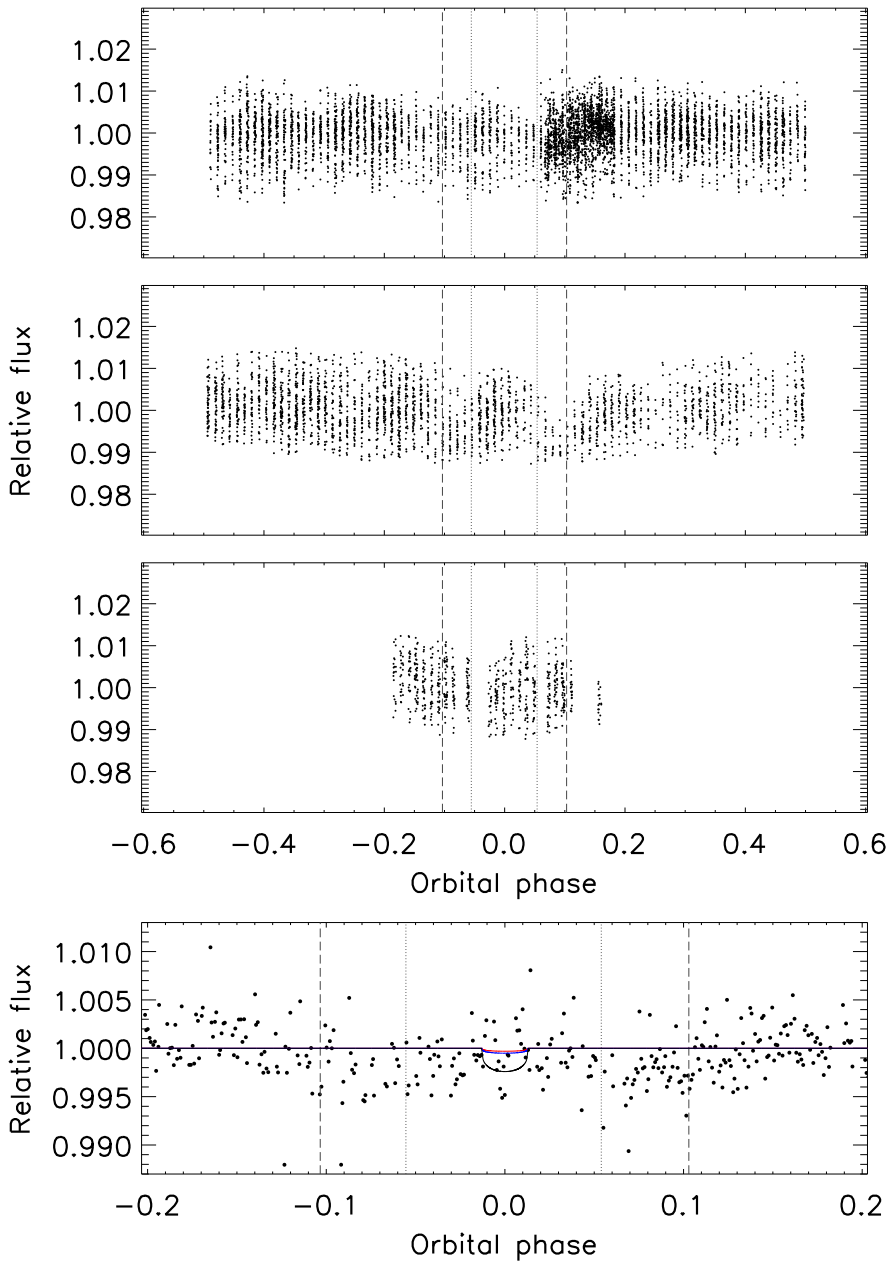

Figure 4.2: *Top:* Two long-term light curves folded with the period of HD 1461b (upper and middle panels) and one light curve covering one transit window of HD 1461b (lower panel). *Bottom:* All HD 1461 light curves folded to the period of planet b ($P = 5.77316 \pm 0.00093$ days) and binned in 8-min. bins. Horizontal axes units and other denotations are as in Figure 4.1.

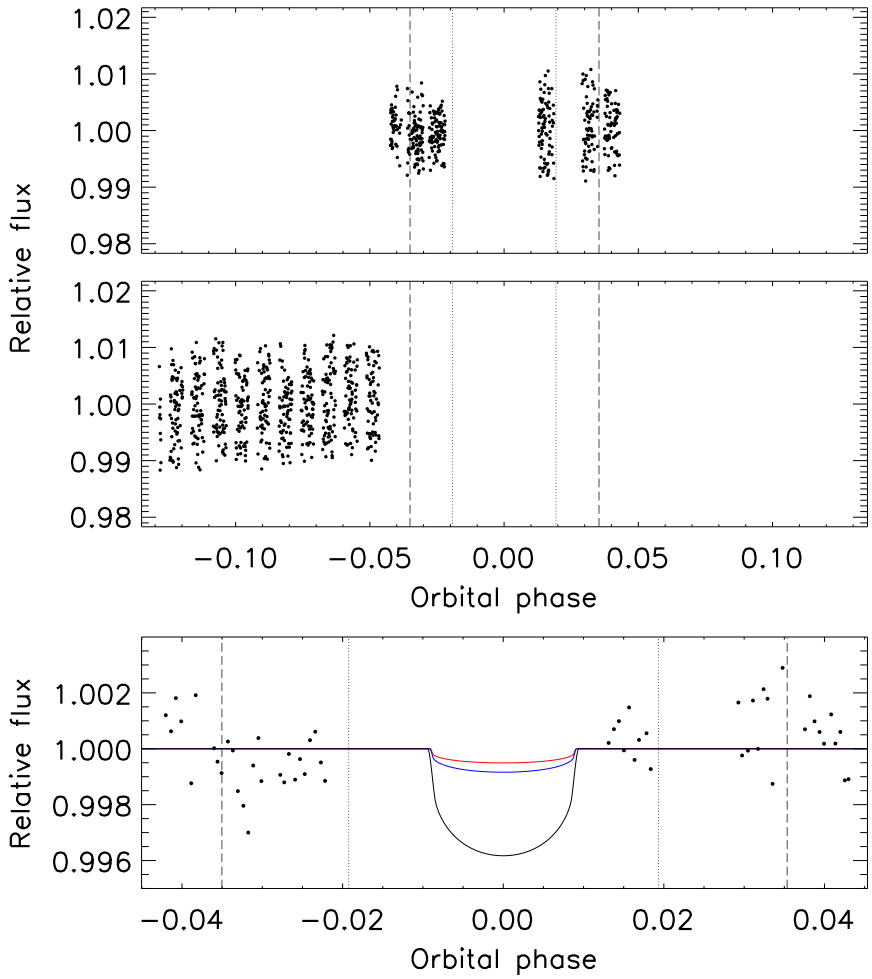

Figure 4.3: *Top:* Light curves for two transit windows of HD 69830b. *Bottom:* All HD 69830b light curves folded to the period of planet b ($P = 8.66644 \pm 0.00066$ days) and binned in 8-min. bins. Horizontal axes units and other denotations are as in Figure 4.1.

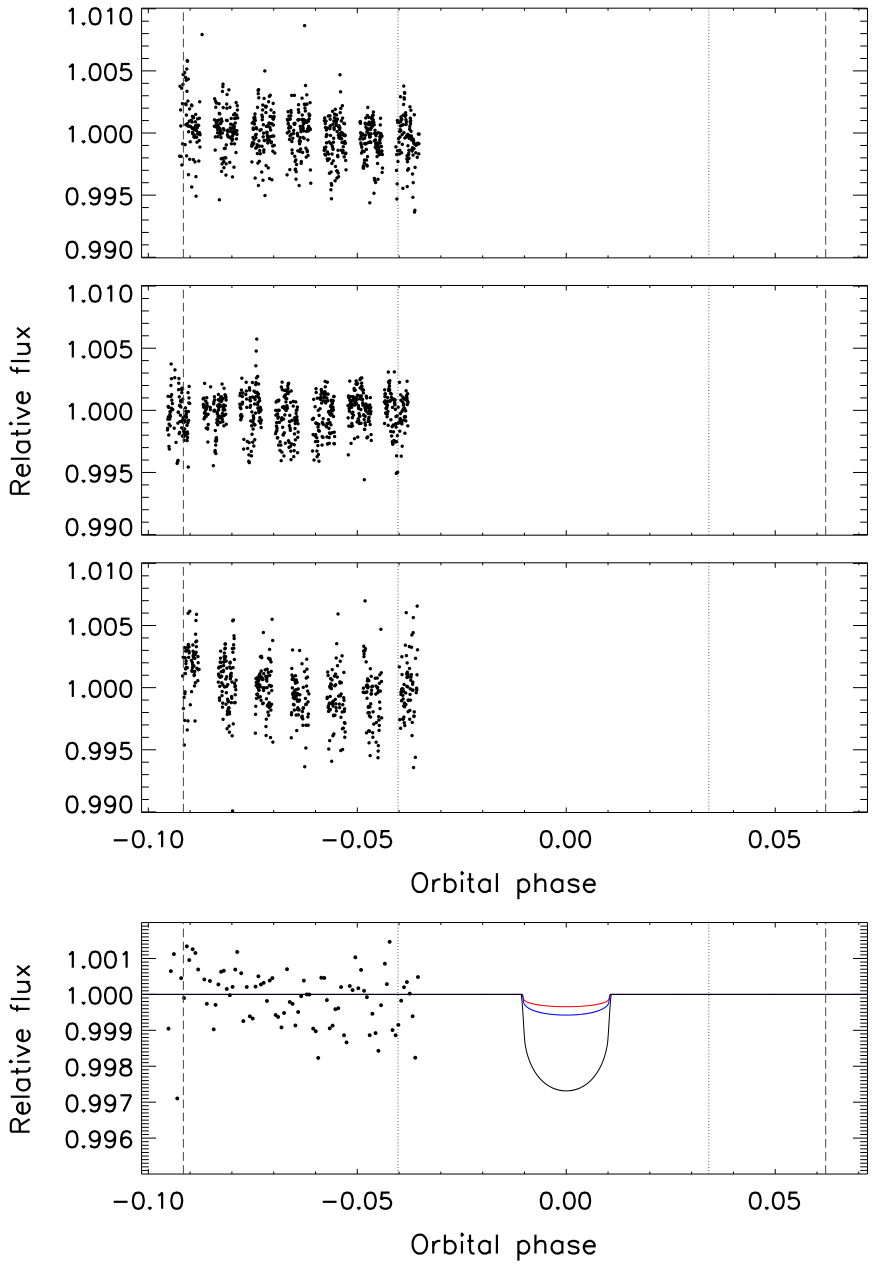

Figure 4.4: *Top panel:* Light curves for three transit windows of HD 96700b. *Bottom panel:* All HD 96700 light curves folded to the period of planet b ($P = 8.1256 \pm 0.0013$ days) and binned in 8-min. bins. Horizontal axes units and other denotations are as in Figure 4.1.

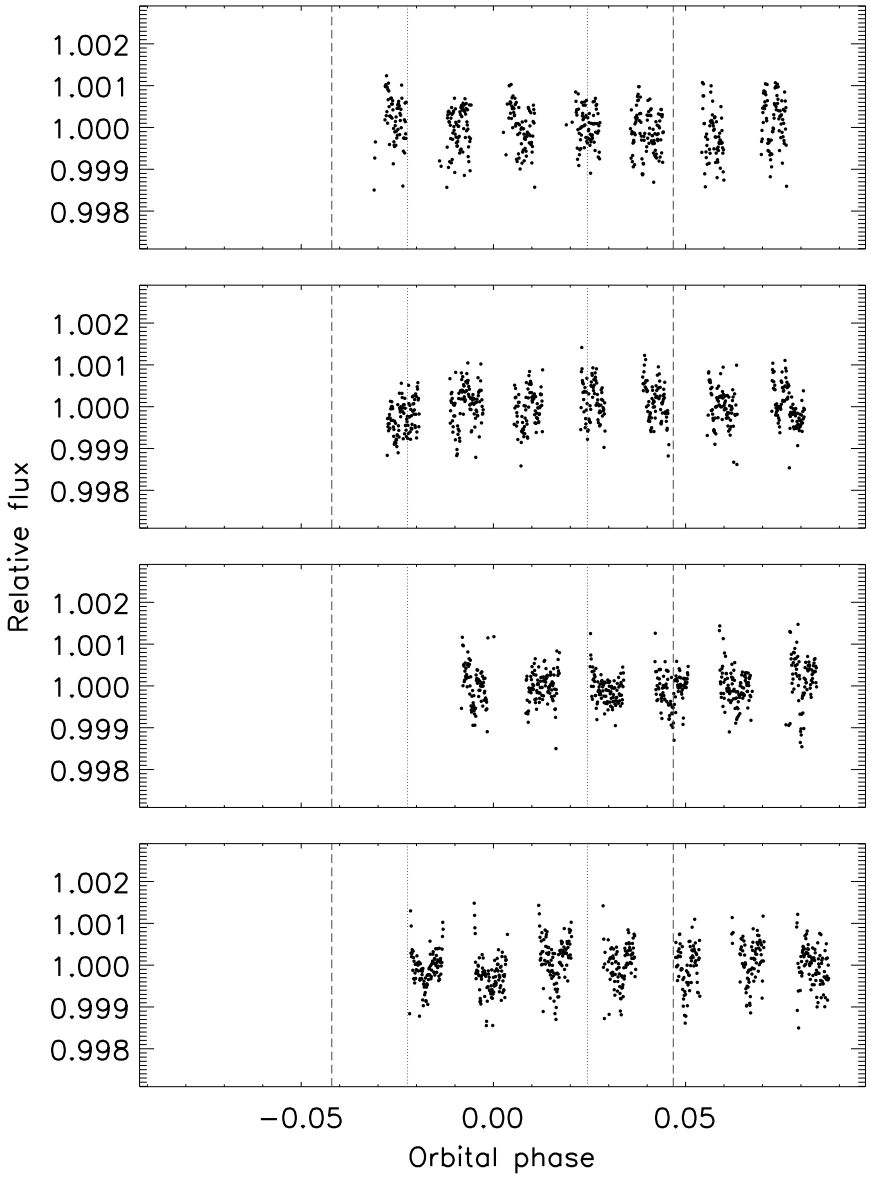
1.002
1.001
1.000
0.999
0.998
Relative flux
−0.05
0.00
0.05
Orbital phase

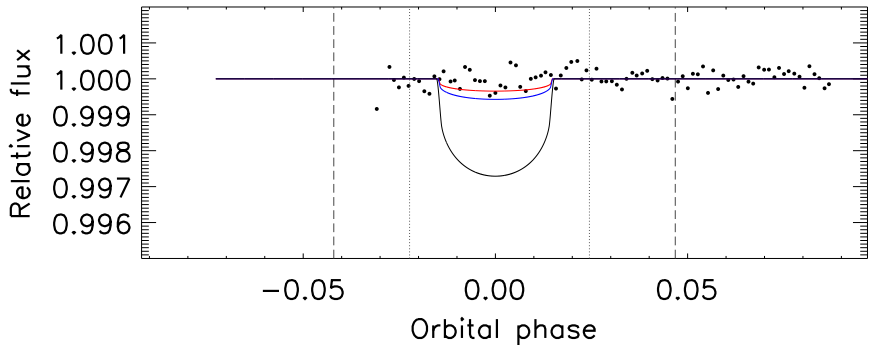

Figure 4.5: *Top panel:* Light curves for four transit windows of HD 115617b. *Bottom panel:* All HD 115617 light curves folded to the period of planet b ($P = 4.21429 \pm 0.00046$ days) and binned in 8-min. bins. Horizontal axes units and other denotations are as in Figure 4.1.

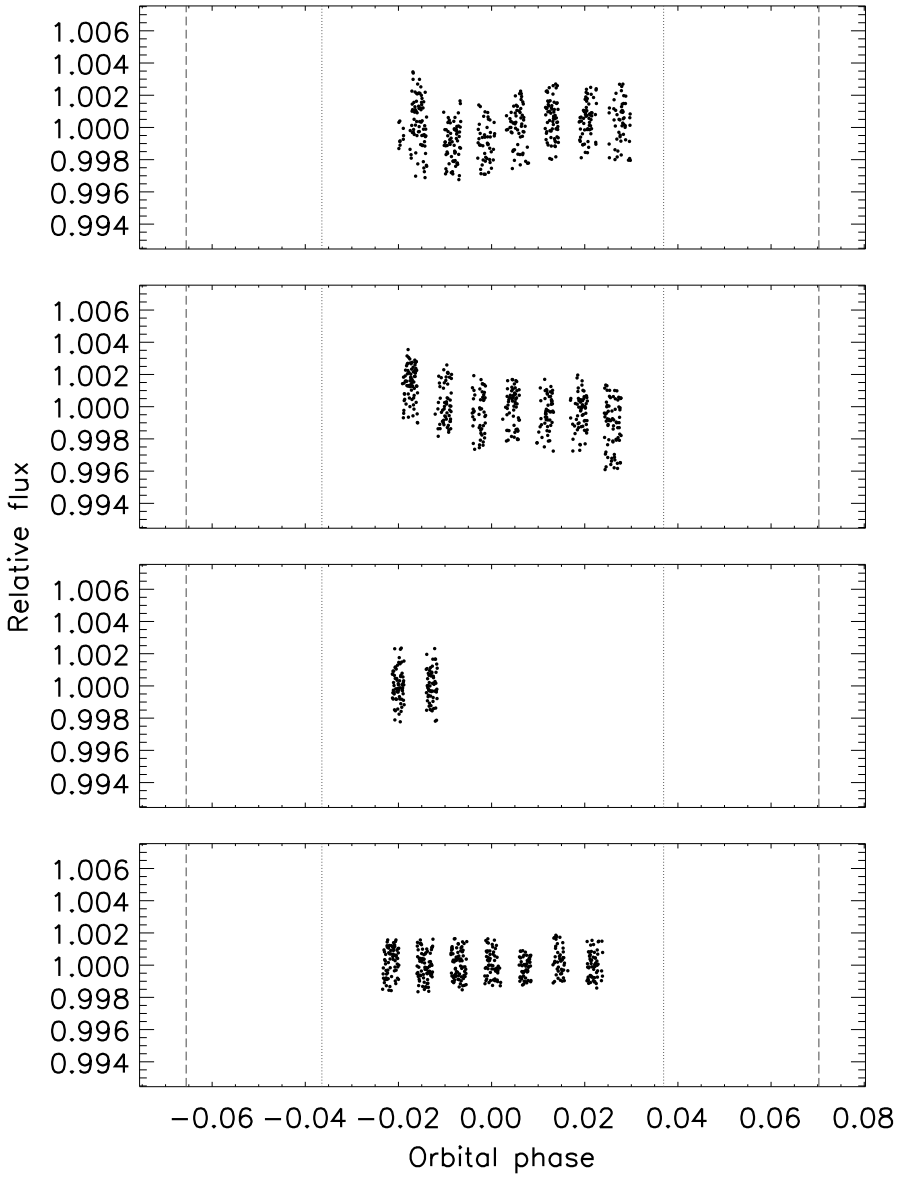
1.006
1.004
1.002
1.000
0.998
0.996
0.994
Relative flux
−0.06 −0.04 −0.02 0.00 0.02 0.04 0.06 0.08
Orbital phase

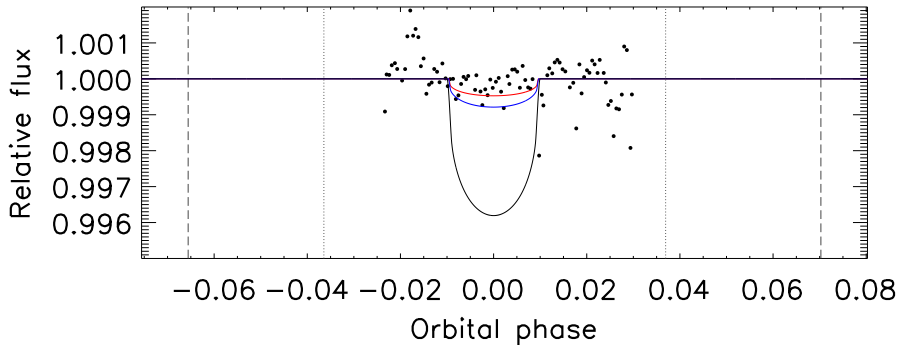

Figure 4.6: *Top panel:* Light curves for four transit windows of HD 125595b. *Bottom panel:* All HD 125595 light curves folded to the period of planet b ($P = 9.6714 \pm 0.0031$ days) and binned in 8-min. bins. Horizontal axes units and other denotations are as in Figure 4.1.

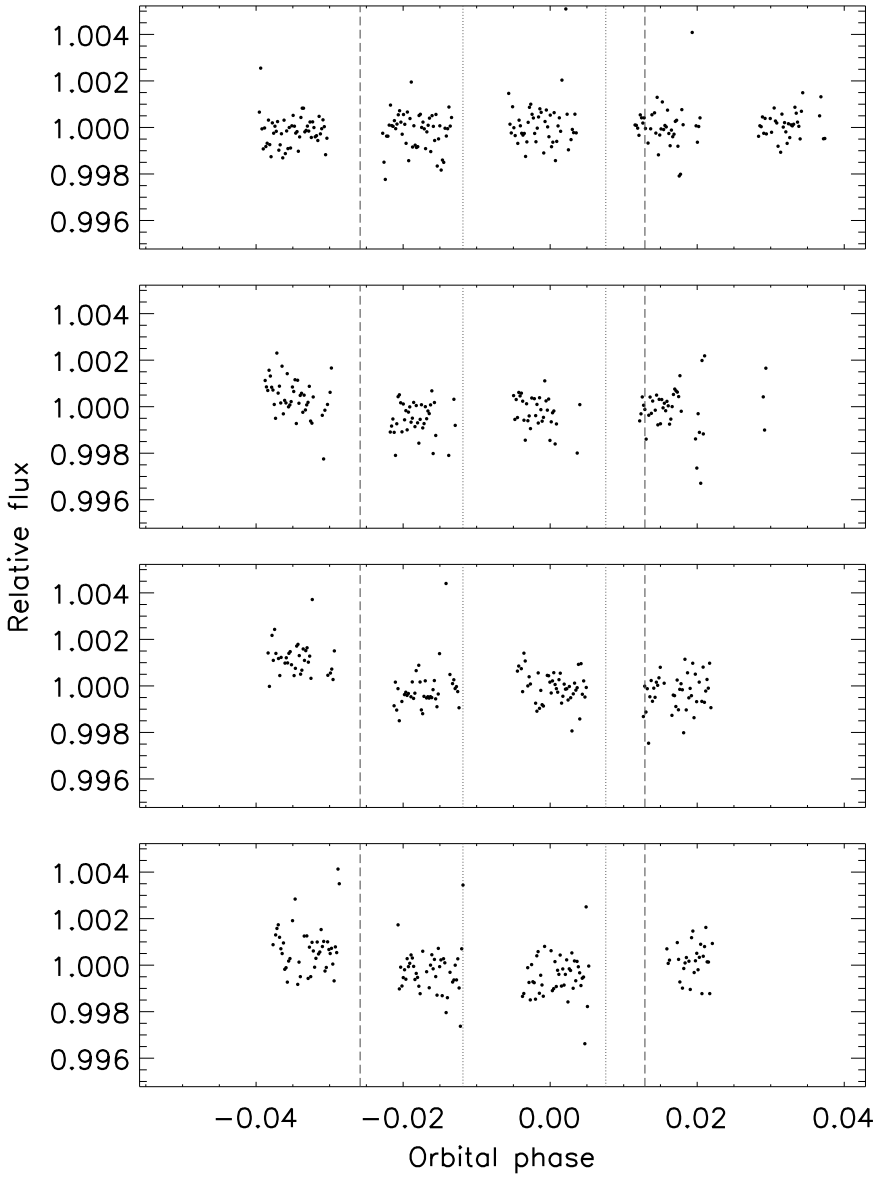
1.004
1.002
1.000
0.998
0.996
Relative flux
−0.04
−0.02
0.00
0.02
0.04
Orbital phase

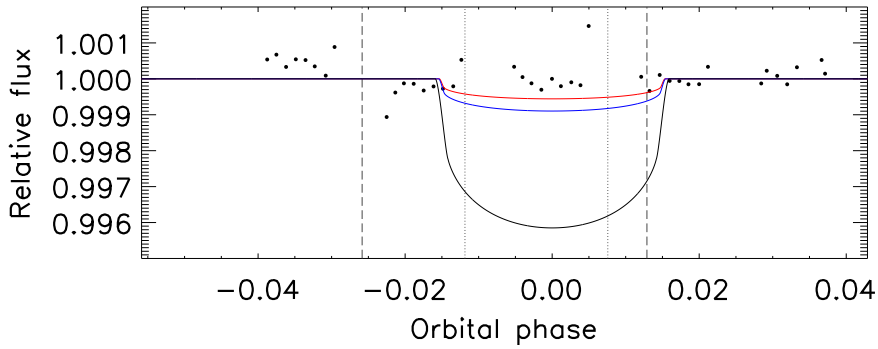

Figure 4.7: *Top panel:* Light curves for four transit windows of HD 125612c. *Bottom panel:* All HD 125612 light curves folded to the period of planet c ($P = 4.15506 \pm 0.00033$ days) and binned in 8-min. bins. Horizontal axes units and other denotations are as in Figure 4.1.

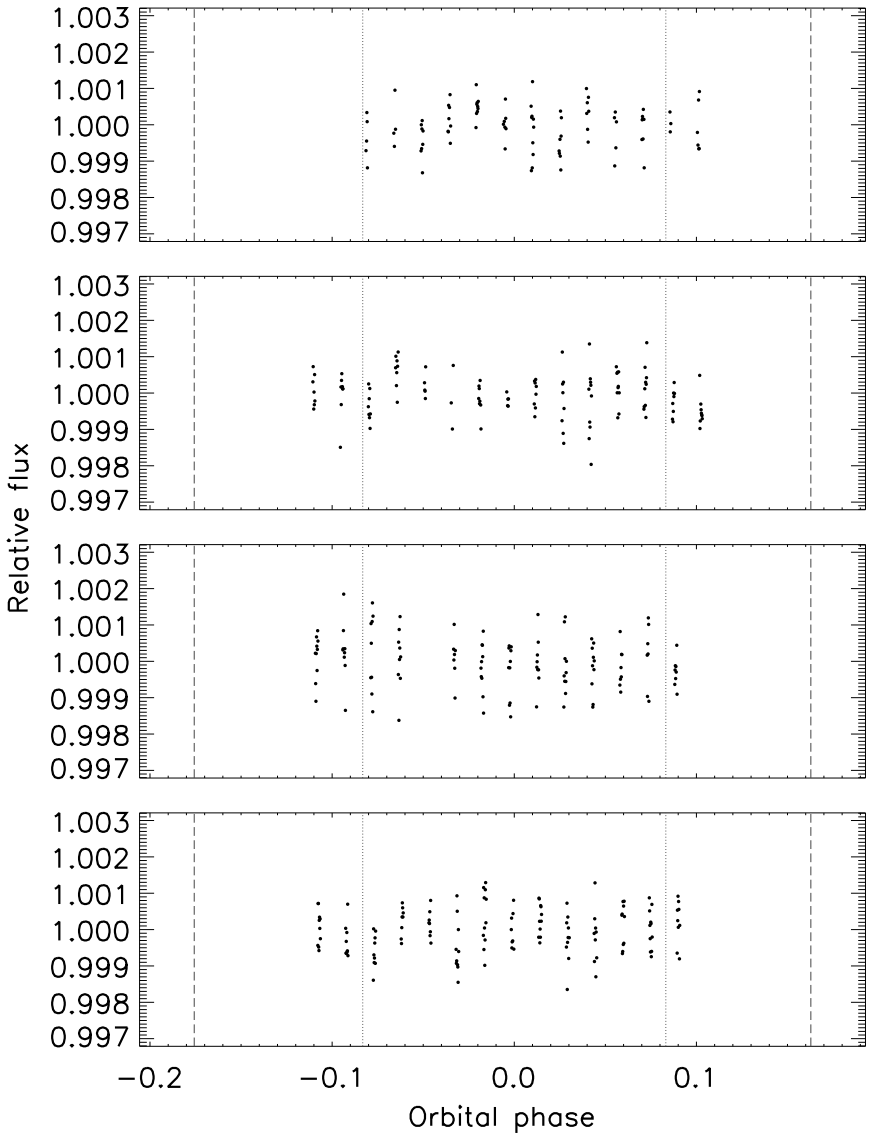
1.003
1.002
1.001
1.000
0.999
0.998
0.997
Relative flux
−0.2
−0.1
0.0
0.1
Orbital phase

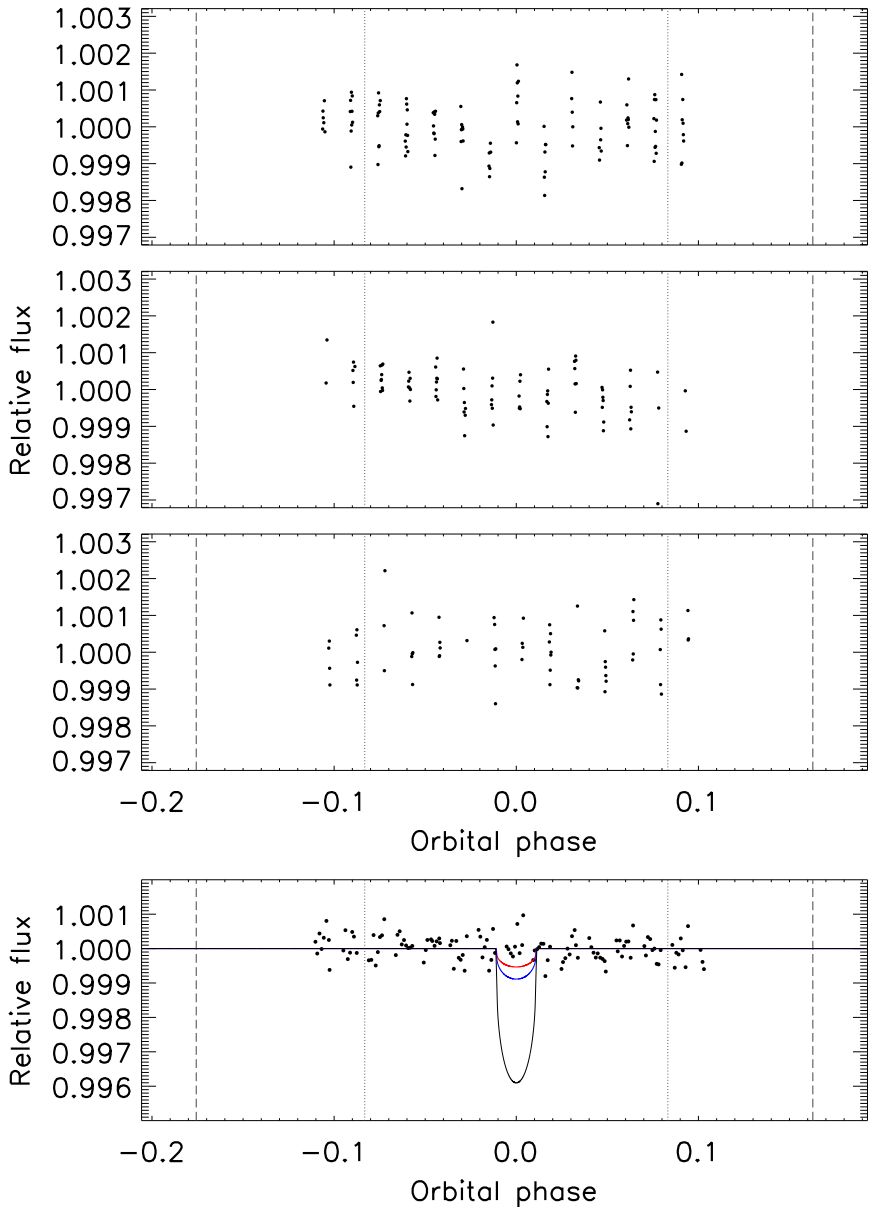

Figure 4.8: *Top panel:* Light curves for four transit windows of HD 156668b. *Middle panel:* Light curves for three (additional) transit windows of HD 156668b.*Bottom panel:* All HD 156668 light curves folded to the period of planet b ($P = 4.6432 \pm 0.0011$ days) and binned in 8-min. bins. Horizontal axes units and other denotations are as in Figure 4.1.

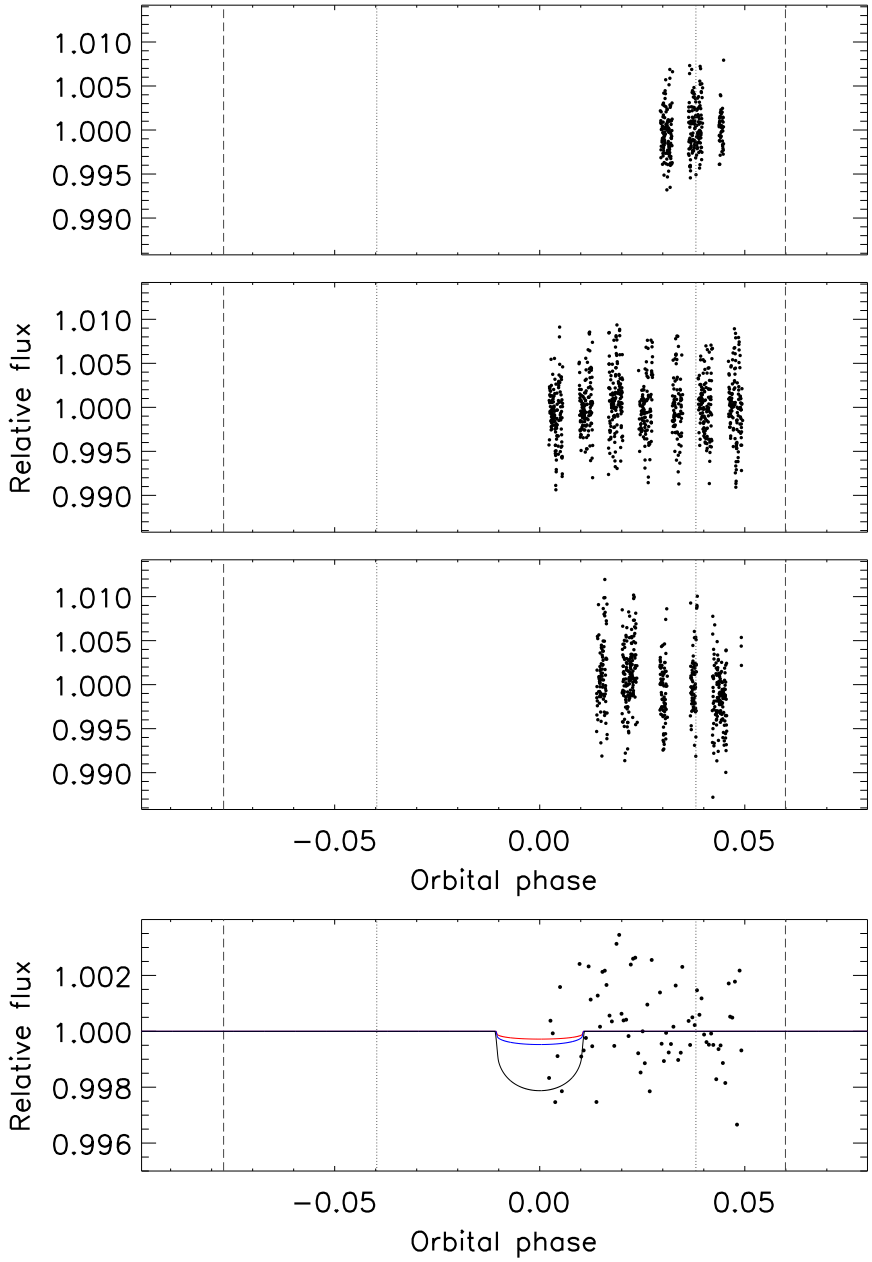

Figure 4.9: *Top panel:* Light curves for three transit windows of HD 160691c. *Bottom panel:* All HD 160691 light curves folded to the period of planet c ($P = 9.6389 \pm 0.0020$ days) and binned in 8-min. bins. Horizontal axes units and other denotations are as in Figure 4.1.

4.5 MOST Confirmed Detection

Of the 12 targets monitored by MOST for this thesis, 55 Cnc e is the only one with a confirmed transit detection. The 55 Cnc system was not originally part of the transit search. Following a re-determination of the orbital period, which increased the transit probability of its innermost planet to over 30%, this system was proposed by Josh Winn as a target for MOST, and the proposal was accepted. As a result of the ensuing 12.5 days of observations acquired in February 2011, the planet 55 Cnc e was found to transit, thus also confirming the new orbital period value (0.74 days). Further, a brightness modulation with the same period (phase variation) was discovered in the photometry. The planet is indeed a super-Earth, with a mass of 8.63 $M_{\oplus}$ and radius of 2.00 $R_{\oplus}$.

The importance of this planet is multi-faceted: 55 Cnc e is one of a handful of known transiting super-Earths, it is the super-Earth with the brightest host star, and its orbit is astoundingly short. The as yet unexplained phase variation adds another layer of interest, and there is the now significant probability that other planets in the system might transit as well.

Thusly motivated, MOST observed the system again in January and February 2012, this time for a duration of 42 days. The aims include refining the planet's physical and orbital properties, verifying whether the phase variation is still present, searching for the secondary eclipse of the planet, searching for transits of other planets, monitoring the stellar variability and looking for any new findings. I carried out the analysis and results of these new data, which are presented in chapter 9.

Chapter 5

A Tale of Four Stars

The following four chapters tackle four different exoplanetary systems in the context of the MOST and TERMS transit searches. The main goals of the TERMS survey are the detection and characterisation of transits of exoplanets discovered through RV surveys like HARPS and HIRES and orbiting bright stars, in particular planets with intermediate and long orbital periods. The goals of the MOST transit search are to detect transits of super-Earth and mini-Neptune candidates which have also been discovered using RV surveys, in order to determine the densities of those planets, and in some instances to better define the orbital and physical properties of previously known transiting planets (e.g. 55 Cnc e). The systems discussed in the next four chapters are examples of target systems that have bright host stars and reasonably high geometric transit probabilities. Of the four, three have host stars brighter than $V = 10$ while the GJ 581 planets orbit a star which is only slightly fainter than the others ($V = 10.6$).

The geometric transit probability depends mainly on the size of the host star and semi-major axis of the planet. However, another factor which can increase the chance of a successful transit detection is the duration of the predicted transit window. Numerous and/or strategically acquired RV measurements help reduce the uncertainties on the orbital parameters, which in turn lead to a narrower transit window and makes a transit detection more likely or an exclusion more certain. Thus, another naturally common aspect of the MOST and TERMS transit searches is the focus on stars whose planets have the most precisely determined orbital parameters.

If photometry spanning at least one orbit of an exoplanet can be obtained, this problem disappears since a transit window of any width can be searched. This was the case for the TERMS target HD 192263b, observed

every one or two nights when visible, for over a decade (see Chapter 6). It was also the case for MOST transit search targets GJ 581e and b (see Chapter 7), and 55 Cnc e and b (though 55 Cnc e was discovered to transit prior to my analysis presented in Chapter 9); each of these systems was observed contiguously for up to several weeks. For all of these it was possible to ensure transits corresponding to most transiting geometries (values of the impact parameter) would not be missed, leaving only the precision of the light curve (and the size of the planet) as the limiting factors of a detection or exclusion.

Another common aspect of these three systems is the possibility of searching for indications of star-planet interactions (SPI). The two main types of SPI believed to occur are tidal and magnetic interactions. These can sometimes be observed in the photometry as brightness variations in phase with the orbit of the planet, as is the case for the τ Bootis system [258]. For the HD 192263 system, improved orbital parameters and new long-term photometry no longer support the previously postulated possibility of SPI. In the GJ 581 system, I find hints of stellar variability near the period of the second innermost planet, GJ 581b. Meanwhile, the brightness variation of the 55 Cnc host star phased with the orbit of its known transiting planet, first apparent in the 2011 MOST photometry, is still present though its amplitude is smaller in the 2012 photometry.

GJ 581, HD 97658 and 55 Cnc are all systems known to host at least one planet whose minimum mass lies in the super-Earth regime. 55 Cnc e is now known to transit and was thus confirmed to be a super-Earth. HD 97658b, a planet with a minimum mass of 7.7 $M_{\oplus}$, was believed to transit but I could not verify the claimed signal with the more sensitive MOST telescope (see Chapter 8). GJ 581e has a minimum mass of just 1.9 $M_{\oplus}$, while dynamical simulations suggest an upper limit of $\sim$ 3.03 $M_{\oplus}$ [168]. A transit of this planet, if present, is expected to be too shallow for the majority of 1-metre-class (i.e. available for full night or longer observing runs) ground-based telescopes to detect. Further, because of its low mass and the presence of other planets in the system, its orbital solution is still not sufficiently well determined to allow full transit window coverage within

a single night. Shortly after its discovery was announced, MOST seized the opportunity to observe the GJ 581 system for over three orbital cycles of GJ 581e in order to search for a transit of this strong super-Earth candidate.

Prior to their respective transit searches, each of these three planets held the possibility of being a super-Earth. A transit detection would confirm this hypothesis for the "lucky" planet. This was indeed the case for 55 Cnc e. Meanwhile, for the other two I was able to place limits on the depth of a transit. Even if they are ultimately found not to transit, they may still be super-Earths for a significant range of orbital inclinations (more likely for GJ 581e than for HD 97658b).

In summary, these four transit searches probe relatively poorly known and sparsely populated areas of exoplanet parameter space: intermediate-period gas giants, and super-Earths. Though between them, these planets orbit stars of three different spectral types (G, K and M), the brightnesses of these host stars are all in the range essential for other detailed follow-up observations (e.g., interferometry, spectropolarimetry, IR spectroscopy, etc.).

Chapter 6

The HD 192263 System: Planetary Orbital Period and Stellar Variability Disentangled

6.1 Introduction

Detecting exoplanets via the radial velocity (RV) method and subsequently monitoring their transit windows is the most fruitful strategy for exoplanets orbiting bright stars, which represent the best candidates for atmospheric and other detailed studies. Ground- and space-based transit surveys have revealed nearly 200 transiting exoplanets (and about 2300 candidates of which a large percentage will almost certainly be confirmed), but most of those orbit faint stars, while the RV technique is best suited for brighter stars. Moreover, searching for transits of known RV planets allows the selective monitoring of intermediate and long-period planets, of which only a few are known to transit so far. The Transit Ephemeris Refinement and Monitoring Survey (TERMS; [131]) aims to improve the orbital parameters of RV exoplanets and monitor them photometrically during their more tightly constrained transit windows.

In [72], we presented new transit observations and improved parameters for several known transiting exoplanets, originally discovered by the SuperWASP survey [188]. We demonstrated that the photometric precision required to detect and characterize transits of giant planets is easily

attainable by modest-sized, ground-based facilities such as the Cerro Tololo Inter-American Observatory (CTIO) 1.0 m telescope. Through TERMS, the ephemerides of HD 156846b, HD 114762b, HD 63454b and HD 168443b have been refined and transit searches conducted in each case (see [130], [129], [127] and [185], respectively).

Exoplanets detections with the RV method can occasionally be controversial, and HD 192263b is one such misfit. It was first announced in 2000 [205] as a planet with a period of 24.13 days and $m \sin i = 0.73$ M_J. These results arose from an analysis of RV measurements obtained using the CORALIE spectrograph. A paper by [251] followed, reporting a similar solution based on their Keck measurements, but noting that the chromospheric activity appeared to vary with a period close to that of the suspected planet. Two years later, [110] attributed the RV signal at least partly to stellar variability, as indicated by their photometric and spectrophotometric data. Indeed, a modulation with a period of $\sim$24 days is clearly visible in the light curves, and the power spectrum of the Ca II H and K spectrophotometric observations exhibits a significant peak at the same period. In the end, unlike other planet-like RV signals that were caused by stellar activity ([190]; [69]), HD 192263b made a convincing comeback in [206]. New CORALIE measurements demonstrated that the RV variation remained coherent in amplitude and phase for over three years, while new photometric observations from La Palma revealed significant changes over time [206].

In this Chapter, I present new Keck RV observations which I use to refine the orbital parameters (Section 6.2) and the transit ephemeris of the "revived" HD 192263b (Section 6.3). I introduce new photometry of the host star obtained between 2002 and 2011 in Section 6.4, and report on the star's variability during this period in Section 6.5. Finally, in Section 6.6 I analyse the photometric measurements acquired during the predicted transit window and exclude transits with the predicted depth of 2.5% with high confidence. I conclude in Section 6.7.

6.2 RV Measurements and Revised Orbital Model

6.2.1 Stellar Properties

A K2 dwarf, HD 192263 is a relatively bright star (V = 7.8) located at a distance of 19.3 parsecs [142]. It is also a BY Dra variable [134], a class of active stars that experience brightness variations due to their spotted surfaces.

We used Spectroscopy Made Easy (SME)[13] on a spectrum of HD 192263 (taken without the iodine cell used for RV measurements), as detailed in [245]. This procedure is based on that described in [246], with an added improvement for self-consistency between values of stellar properties obtained from spectroscopy and those determined from isochrones [245]. The improved method derives a value for the stellar gravity (log g), effective temperature (T_{eff}), iron abundance ($[Fe/H]$) and alpha-element enrichment ($[\alpha/Fe]$) from the spectroscopic analysis. The last three parameters and the luminosity (L) are used to obtain a value for log g from isochrone models (log g_{iso}). The spectroscopic analysis is run again, now with log g fixed at the value of log g_{iso} from the previous iteration. The loop continues until log g and log g_{iso} agree. For HD 192263, the effective temperature resulting from this method is 4996 ± 44 K, and the stellar radius (calculated from L and T_{eff}) is 0.73 ± 0.01 $R_{\odot}$. [231] carried out a Bayesian analysis using the stellar parameters arising directly from the SME procedure (log g_{iso}, T_{eff} and $[Fe/H]$) and a dense grid of theoretical evolutionary tracks, and found a stellar radius of 0.77 ± 0.02 $R_{\odot}$. This value agrees with our SME result within 2σ. Finally, [247] estimated the radius of HD 192263 using spectral energy distribution (SED) fitting and obtained a value of 0.76 ± 0.02 $R_{\odot}$, which agrees with our SME result within 1σ. We adopt the SME stellar radius value for our calculations but compute a predicted transit depth using the largest published value [231] as well, to show that transits can be

[13] SME is a tool for generating synthetic stellar spectra and comparing them with observed stellar spectra.

excluded for both cases.

From the SME analysis we also find values for the effective temperature, surface gravity, iron abundance, projected rotational velocity, and mass of the host star. The observed and derived stellar properties are listed in Table 6.1.

Table 6.1: Stellar properties of HD 192263

Parameter	**Value**	**Reference**
V	7.767	[142]
$B-V$	0.957	[142]
Distance (pc)	19.3	[142]
$T_{\rm eff}$ (K)	4996 ± 44	This work
$\log g$	4.628 ± 0.060	This work
[Fe/H]	0.054 ± 0.030	This work
$v \sin i$ ($\mathrm{km\,s^{-1}}$)	$< 1.0 \pm 0.50$	This work
$logR'_{HK}$	-4.56	[110]
$M_\star$ ($M_\odot$)	0.807 ± 0.015	This work
$R_\star$ ($R_\odot$)	0.73 ± 0.01	This work
age (Gyr)	2.09 ± 2.54	This work

6.2.2 RV Measurements

A total of 181 CORALIE (an echelle spectrograph on the 1.2m Swiss telescope at La Silla, Chile; [240]) RV measurements have been reported in [206], of which those included in [205] are a subset. In addition there are 31 published Keck measurements ([39]; [251]). To these we add five new Keck observations, acquired between 2006 and 2011. All Keck observations were made with the HIRES echelle spectrograph [249] on the 10-m Keck I telescope. The HIRES instrument uses an iodine cell through which the starlight passes before reaching the slit. Minute Doppler shifts in the features of the stellar spectrum are accurately measured against a wavelength reference provided by the dense set of absorption lines in the iodine spec-

trum. The RVs were extracted following the procedure described in [116].

An offset of 10672 m s^{-1} (the median of the CORALIE RVs) was added to each of the CORALIE RVs to place them on the same scale as the Keck RVs. This offset corresponds to the radial velocity of the centre of mass of the HD 192263 system relative to Earth. The complete set of CORALIE (with the offset applied) and Keck RV measurements are shown in Tables A.1 and A.2, respectively. I emphasize that all CORALIE measurements and all Keck measurements except the five I report in this Chapter, have been previously published.

6.2.3 Keplerian Model

I fit the set of 217 available RVs using a single-planet Keplerian model based on the techniques described in [115] and the partially linearized, least-squares fitting method of [269]. Analyzing the data from the two telescopes together rather than separately provides smaller uncertainties on the period and mid-transit time. I allow for an RV offset between the Keck and CORALIE measurements (4.10 ± 1.93 m s^{-1}), because each instrument has its own zero point. I also allow for an offset between Keck measurements taken before and after JD = 2453237, due to a CCD and optics upgrade on that date (1.61 ± 5.84 m s^{-1}). The *rms* of the RV residuals is 13.14 m s^{-1} and the χ^2_{red} is 9.05, likely because HD 192263 is such an active star and its variability is not properly accounted for by the uncertainties on the RV measurements. To correct for this, I added a jitter term (σ_j) in quadrature to the measurement uncertainties (σ_{RV}): $w^2 = \sigma^2_{RV} + \sigma^2_j$, and used w instead of σ_{RV} for the Keplerian fit [267]. I chose $\sigma_j = 10.15$ m s^{-1} to satisfy the condition $\chi^2 = 1$. Furthermore, this value is equivalent to the excess found by [206] in the residuals of their RV measurements, and is within the range of 10 - 30 m s^{-1} predicted by [200][14] from $\log R'_{HK} = -4.56$ [110]. This added measure also reduces the rms to 12.42 m s^{-1}.

[14] Saar et al. (1998) [200] found a correlation between stellar activity (as measured by the R'_{HK} index) and excess dispersion in the radial velocities, based on measurements for a sample of 72 stars. It is their fit to these data that I use here to estimate an expected range of jitter noise.

The parameter uncertainties were determined from the sampling distribution of each parameter through a non-parametric bootstrap analysis [87].

[206] find a long term trend in their CORALIE data, to which they fit a straight line with a slope of 4.8 ± 0.8 m s^{-1} yr^{-1}. They are unable to identify the source of this trend, which could be due to the presence of another companion, or a RV variation caused by stellar activity. I also include a linear velocity trend (dv/dt) in our models. The best-fit value for the offset between the CORALIE and Keck RVs is now 5.14 ± 2.18 m s^{-1}, while the offset between Keck measurements before and after JD = 2453237 becomes -17.67 ± 9.21 m s^{-1}. The best fitted value for the linear velocity trend (when analyzing the Keck and CORALIE data combined) is 0.0070 ± 0.0017 m s^{-1} day^{-1} (or 2.56 ± 0.62 m s^{-1} yr^{-1}). I note that including a trend does not significantly lower the χ^2. When fitting only the CORALIE data I find a linear trend with a slope of 5.21 ± 0.70 m s^{-1} yr^{-1} which agrees with that obtained by [206]. However, fitting only the Keck data (which spans a longer time range encompassing that sampled by the CORALIE measurements) gives a slope of -0.37 ± 0.73 m s^{-1} yr^{-1}, a value consistent with the absence of a trend. Finally, I repeated the analysis for each of the three data sets, this time using the original measurement uncertainties (no jitter term). The results are statistically consistent with those obtained with the jitter term included. I conclude that additional measurements are necessary to firmly determine the source of the linear trend present in the CORALIE data. For the reasons described above, and because the uncertainties on the resulting values for the period and mid-transit time are smaller, I adopt the solution without the trend.

The parameters from my Keplerian fit (both with and without a linear trend as a free parameter) are given in Table 6.2, together with those reported by [39] for comparison. The folded data and adopted model are plotted in Figure 6.1. Figure 6.2 shows a zoomed-in view of the shaded area (top panel) and the residuals to the RVs within this area (bottom panel).

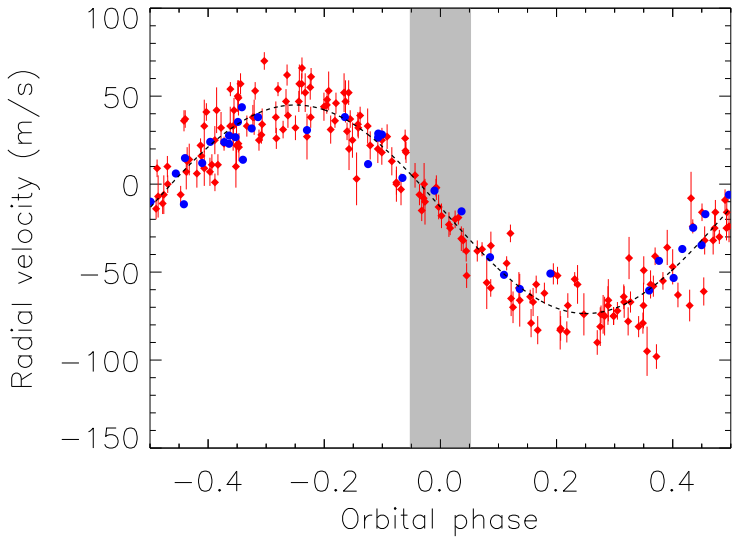

Figure 6.1: CORALIE (red diamonds) and Keck-HIRES (blue dots) radial velocities. The error bars shown are the original measurement uncertainties, with the jitter term (σ_{RV}) not included. For most Keck measurements, the error bars are smaller than the size of the data points. The best-fit orbital solution is overplotted (dashed line). The shaded region corresponds to the 3σ transit window and phase 0.0 is the predicted time of mid-transit.

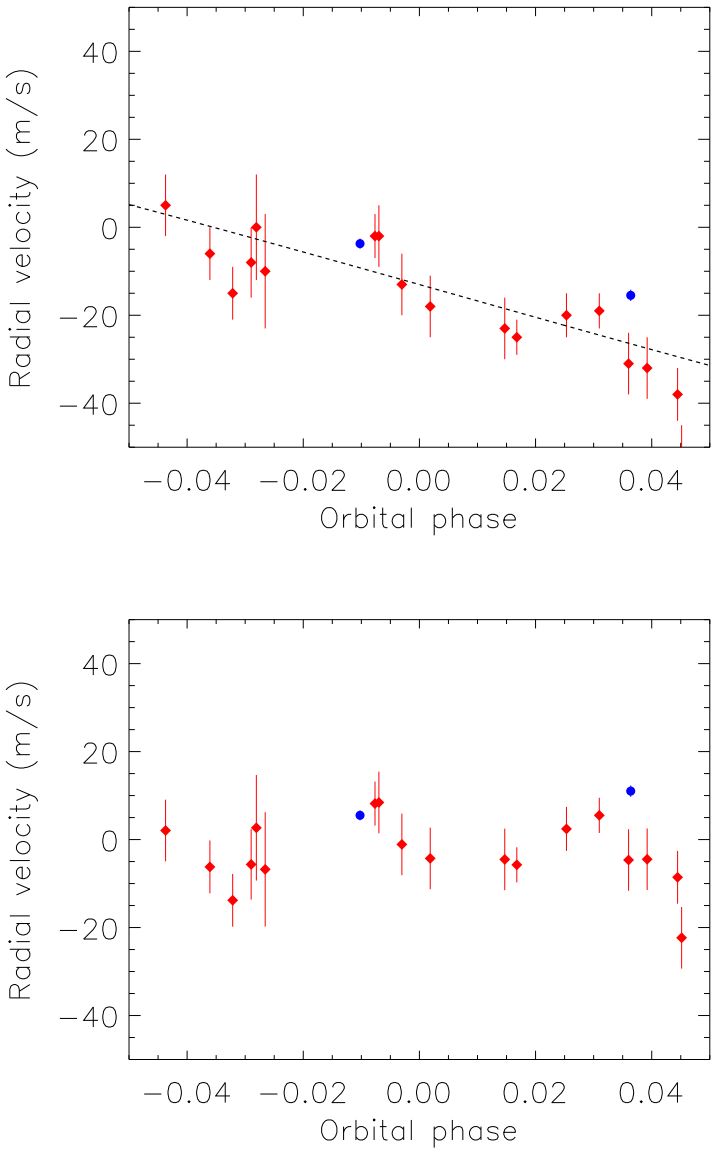

Figure 6.2: Top panel: CORALIE (red diamonds) and Keck-HIRES (blue dots) radial velocities between the edges of the 3σ transit window (shaded region in Figure 6.1), with the best-fit orbital solution overplotted (dashed line). Bottom panel: Residuals to the radial velocities, over the same phase range ($rms = 12.04$ m s^{-1}). The error bars shown are the original measurement uncertainties, with the jitter term (σ_{RV}) not included.

Table 6.2: Keplerian fit parameters for HD 192263b

Parameter	**This work - without trend (adopted)**	**This work - with trend**	**Butler et al. 2006**
P (days)	24.3587 ± 0.0022	24.3581 ± 0.0028	24.3556 ± 0.0046
T_c [a] (BJD – 2440000)	10986.74 ± 0.21	10986.73 ± 0.21	10987.22 ± 0.39
T_p [b] (BJD – 2440000)	11796.9 ± 6.8	11795.0 ± 4.6	11994.3 ± 3.9
e	0.008 ± 0.014	0.008 ± 0.014	0.055 ± 0.039
K ($\mathrm{m\,s^{-1}}$)	59.3 ± 1.2	58.7 ± 1.2	51.9 ± 2.6
ω (deg)	184 ± 90	157 ± 88	200
dv/dt ($\mathrm{m\,s^{-1}\,yr^{-1}}$)	–	2.56 ± 0.62	–
$M_p \sin i$ (M_J)	0.733 ± 0.015	0.726 ± 0.014	0.641
a (AU)	0.15312 ± 0.00095	0.15312 ± 0.00095	0.15
rms ($\mathrm{m\,s^{-1}}$)	12.42	11.87	12.5

[a] Time of transit.
[b] Time of periastron passage.

6.3 Predicted Transit Window and Characteristics

From our newly derived stellar and planetary parameters we can ascertain the properties of the predicted transit. Using the models of [24][15] and our revised measurement of the mass, we estimate a radius for the planet of $R_p = 1.09\ R_J$. It was shown by [132] that the transit probability is a strong function of eccentricity and periastron argument. The eccentricity of this orbit is small enough such that this introduces a minor effect. Based upon our parameters (listed in the first column of Table 6.2), the transit probability is 2.49%, the predicted duration is 0.192 days, and a predicted depth is 2.53%, easily within the range of our photometric precision (rms = 0.0065 within the 3σ transit window; see Section 6.6 for details).

I derived predicted transit times using the non-parametric bootstrap analysis described in Section 6.2.3. The predicted transit mid-point time used to fold the data was 2455882.84 ± 0.37 (JD). Note that the final Keck measurement obtained reduced the uncertainty on the transit mid-point from 0.47 days to 0.37 days, emphasizing the importance of extending the time baseline of the RV measurements when attempting to reduce the total size of the transit window. In this case, the 1σ transit window has a total duration of 0.932 days. Although this is dominated by the transit mid-point uncertainty, it is small enough that I am able to attempt the detection of the transit.

As mentioned in Section 6.2.1, [231] derive a slightly larger stellar radius of $0.77 \pm 0.02\ R_\odot$. Using this radius results in a transit probability of 2.61% and a transit depth of 2.28%. This is still well within our photometric precision such that I am able to make a definitive statement regarding the transit exclusion of this planet.

[15] These are evolutionary models based on the mass of the planet (here taken as the minimum mass determined from RVs) and the amount of energy it receives from the star, used to estimate the planetary radius.

6.4 Photometry

6.4.1 APT Photometry

Gregory Henry acquired 985 photometric observations using the T11 0.8 m automatic photometric telescope (APT), located at Fairborn Observatory in southern Arizona. The data span just over a decade, from April 13, 2001 to November 23, 2011. Measurements were obtained simultaneously in the Strömgren b and y passbands by two EMI 9124QB photomultiplier tubes. The individual b and y differential magnitudes are averaged to obtain the quantity $(b + y)/2$. The observing and data reduction procedures are identical to those described in [109] for the T8 0.8 m APT.

The relative magnitudes $(b + y)/2$ were converted to relative fluxes and normalized to 1 for the plots in Figure 6.3. Two comparison stars were considered for the differential photometry. Comparison star 1 (C1) is HD 193328 (V = 7.48, B-V = 0.12, A2), while comparison star 2 (C2) is HD 193225 (V = 7.35, B-V = 0.29, F0). Typical precision of a single relative flux measurement from T11 is $0.0010 - 0.0020$, depending on the quality of the night and the air mass of the observations. The standard deviation of the (C1/C2) relative fluxes (see Figure 6.3, bottom panel) are slightly larger than this (0.0023). This is probably a combination of the air mass, since HD 192263 lies near the celestial equator, and also suspected low-amplitude variability in C2. For this reason, I analysed the differential photometry of HD 192263 with respect to C1 (see Figure 6.3, top panel).

HD 192263 is observable only during part of the year, which explains the larger gaps in the data between observing seasons. In addition, the star is at opposition around July 24, during the annual Summer Shutdown of the APTs. This gives rise to the shorter (8 - 10 weeks) gaps between the first and second clusters of data points (half seasons), between the third and fourth, etc. As such, the first two sections of the light curve correspond to the first observing season, the third and fourth belong to the second observing season, and so on.

We prepared the data for the transit search by normalizing it such that each half season has the same mean value (see Figure 6.3, middle panel).

This normalization affects the data on a timescale of months, thus preserving the shape and depth of any potential transits which would last less than 8 hours (see Section 6.3).

6.4.2 ASAS Photometry

HD 192263 was also observed as part of the All Sky Automated Survey[16] (ASAS) [187]. A total of 345 data points are available in the ASAS-3 photometric V-band catalogue. These observations were collected between March 27, 2001 and November 10, 2009. The quality and cadence of this data set are lower than for the APT photometry. As a consequence, I use the ASAS observations to test my conclusions regarding the variability of the star, but I do not employ them for the transit search.

6.5 Variability of the Host Star

In this section, I describe an investigation of the stellar variability of HD 192263 based on the 11 seasons of APT photometry described in the previous section. I generate an amplitude spectrum[17] from a discrete Fourier transform of the time series (see top panel of Figure 6.4) and search it for significant peaks. Beyond the frequency range shown in Figure 6.4 (0.00 to 0.07 cycles day^{-1}), only harmonics of the significant frequencies shown in the top plot rise above the noise.

The middle panel and the inset of Figure 6.4 show the spectral window functions for the two significant frequencies[18] shown in the top panel. These indicate the aliases introduced into the amplitude spectrum by the observing cadence, with regular gaps on nightly, biannual and annual timescales.

[16] http://www.astrouw.edu.pl/asas/?page=aasc&catsrc=asas3

[17] An amplitude spectrum shows the amplitude of signals present in the data plotted versus frequency. A power spectrum is obtained by plotting a normalised term proportional to the square of the amplitude versus frequency.

[18] Effectively, these are the Fourier spectra of sinusoids of each of these two frequencies, sampled at the same times as the real time series.

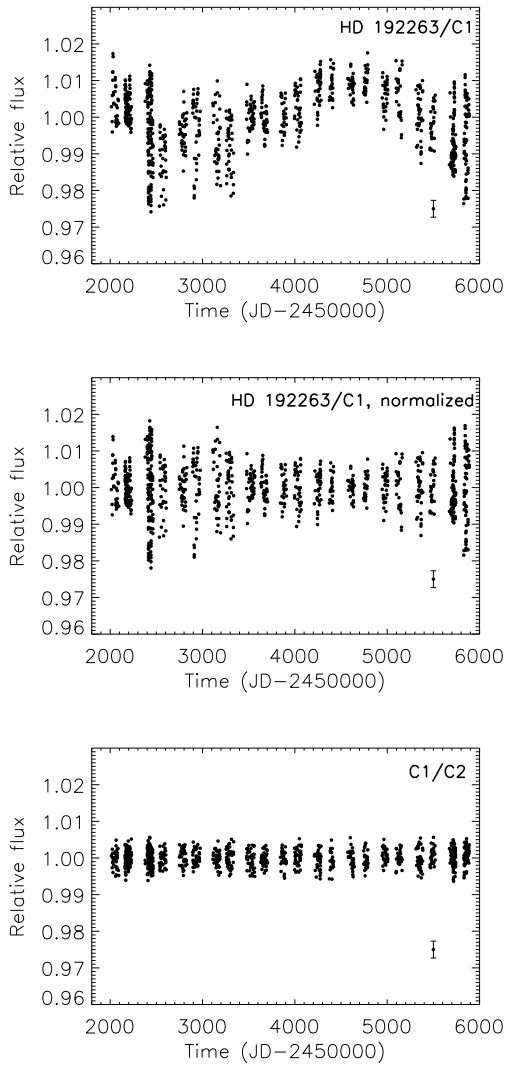

Figure 6.3: T11 APT observations of HD 192263 covering 11 observing seasons from April 2001 to November 2011. The top panel: the photometry for HD 192263, obtained using comparison star C1 ($rms = 0.0085$). Middle panel: same as in the top panel, but with each half observing season normalized to the same mean ($rms = 0.0067$). Bottom panel: photometry of comparison star C1 relative to comparison star C2 ($rms = 0.0023$). It is clear that the large scatter in the HD 192263 observations is mainly due to the target star itself, not to any variability in the comparison stars. The 1σ error bar is shown in each panel.

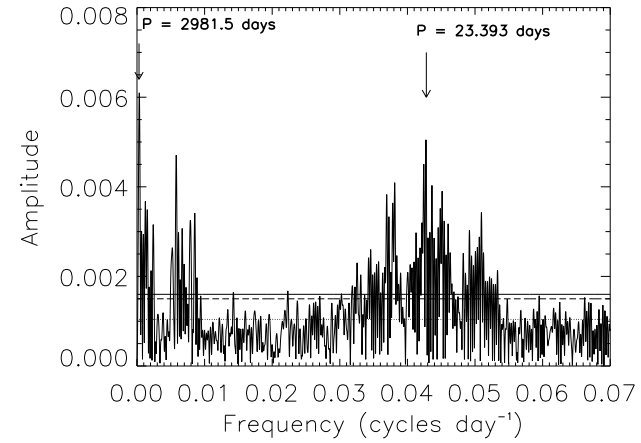
P = 2981.5 days
P = 23.393 days
Amplitude
0.000
0.002
0.004
0.006
0.008
0.00 0.01 0.02 0.03 0.04 0.05 0.06 0.07
Frequency (cycles day^{-1})

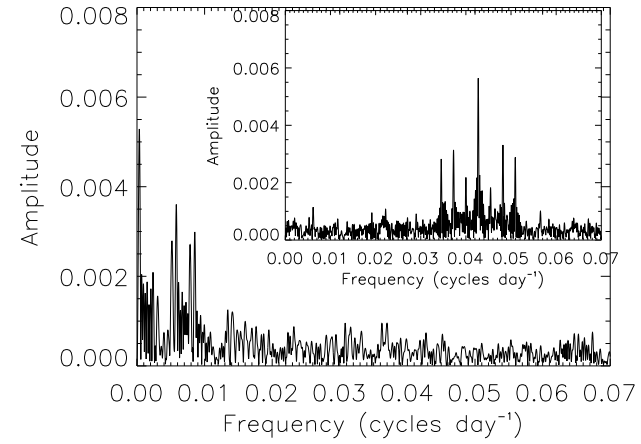
Amplitude
0.000
0.002
0.004
0.006
0.008
0.00 0.01 0.02 0.03 0.04 0.05 0.06 0.07
Frequency (cycles day^{-1})

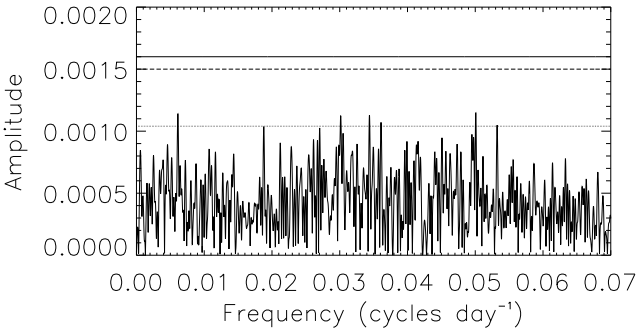
Amplitude
0.0000
0.0005
0.0010
0.0015
0.0020
0.00 0.01 0.02 0.03 0.04 0.05 0.06 0.07
Frequency (cycles day^{-1})

Figure 6.4: Fourier amplitude spectrum (top), window functions for the two significant frequencies described in the text (middle and inset) and Fourier spectrum of the light curve residuals after pre-whitening (bottom) of the APT photometry. The dotted, dashed and solid horizontal lines in the top and bottom panels correspond to false-alarm probabilities of 4.6%, 0.3% and 0.1%, respectively, calculated using the SigSpec routine [192].

The strongest peak in the top panel of Figure 6.4 has a frequency of 0.0003354 ± 0.0000055 cycles day^{-1}, which is equivalent to a period of 8.17 years (or 2982 days $\pm$ 50). This signal is clearly visible in the photometry, as shown in the top panel of Figure 6.3. In light of the already known BY Dra nature of the star, this 8.2-year timescale is consistent with an activity cycle in an early K dwarf like HD 192263, but its cyclical or periodic nature can only be determined with additional observations. The brightness changes are the result of changes in the filling factor of spots or active regions on the stellar photosphere [181]. They may be driven by a stellar dynamo [225], or may arise from random variations in a large number of spots on the surface of an active star without the requirement of a driving mechanism, as shown by the simulations of [74].

The amplitude spectrum further shows a cluster of peaks between 0.03 and 0.06 cycles day^{-1}, of which the largest occurs at 0.0427475 ± 0.0000084 cycles day^{-1} (period = 23.3932 ± 0.0046 days) with an amplitude of 0.005 mag. The window function for a sinusoid of this frequency and amplitude (see inset of Figure 6.4) reveals that not all of these peaks are aliases, but that there are other independent frequencies present in this range. I first "pre-whitened" the light curve by sequentially removing the frequencies of the largest peaks (and their harmonics), until I reached the noise level. Six frequencies in this range were identified; they are listed in Table 6.3, along with the very low frequency discussed above. I then performed simultaneous least-squares fits to the data, where the frequencies, amplitudes and phases of these peaks were allowed to float, with the values obtained from the amplitude spectrum as initial guesses. The Fourier amplitude spectrum of the light curve residuals following the pre-whitening is plotted in the bottom

panel of Figure 6.4. None of the identified frequencies corresponds to the orbital frequency of the exoplanet HD 192263 b. In fact, when I include that frequency and allow the least-squares fit to iterate, the frequency migrates to one of those listed in Table 6.3. Despite the fact that there are at least six frequencies in a narrow range, it is clear that the orbital frequency of the planet is not one of them.

The Fourier peaks tightly clustered around a period of about 23 days are what we would expect for a periodic signal changing in amplitude and possibly slightly in frequency. A Fourier spectrum of a periodic signal which periodically varies in amplitude will have multiplets of peaks associated with the fundamental period, spaced by the amplitude modulation period. If the amplitude variation is not strictly periodic, then the multiplets will not have a simple constant spacing in frequency.

Table 6.3: List of observed frequencies for HD 192263

#	**Frequency (c/d)** σ **frequency**	**Period (days)** σ **period**	**Amplitude (rel. flux)** σ **amplitude**
1	0.0003354	2982	0.00612
	0.0000055	50	0.00059
2	0.037823	26.439	0.00196
	0.000024	0.017	0.00034
3	0.040741	24.5640	0.00273
	0.000017	0.0085	0.00042
4	0.0424	23.5849	0.0024
	0.0015	0.8650	0.0012
5	0.0427475	23.3932	0.00278
	0.0000084	0.0046	0.00012
6	0.043625	22.9226	0.00333
	0.000017	0.0090	0.00040
7	0.04485	22.30	0.00256
	0.00029	0.15	0.00095

The frequency analysis and the behaviour of the light curve are consistent with rotational modulation of the light output of an active K0 dwarf observed for about a decade. If the star is undergoing an activity cycle, then the spottedness will also change on that timescale (varying the amplitude of rotational modulation). In the light curve, shown in the upper two panels of Figure 6.3, one can see the changing width of the envelope of points over the 11-year time span. If the variation at a period around 23.4 days were constant in amplitude, that envelope would maintain the same width (since the photometric scatter of the comparison star remains uniform throughout the data set, as can be seen in the bottom panel of Figure 6.3). All indications are that the amplitude of this signal changes over the span of the ∼8-year variation, and not in a random way.

Although there may also be a Butterfly Effect like the solar sunspot cycle, where the latitudes of starspot groups change and the measured rotation periods will be affected by the star's differential rotation, the changes in amplitude of the rotational signal probably dominate in producing the cluster of peaks near a period of 23.4 days. The equatorial rotation period of the star is likely close to this value, but the amplitude modulation and resultant frequency splitting means its frequency can't be determined to the frequency resolution of the time series.

My findings indicate that the periodic variability reported by Henry et al. (2002) and Santos et al. (2003) persists. To further verify this, I subtracted the 8.17-year signal from the data and phased the residuals at a period of 23.39 days (the largest amplitude signal in this period range), as shown in the top panel of Figure 6.5. A dominant variation, which remains roughly in phase throughout the time span of the photometry, stands out in this phase diagram.

We also see periodicity around 12 days in some of the half-season data sets, and we see the first harmonics of the periods near 23.4 days in the Fourier spectrum. This is in agreement with the period of 12.2 ± 0.1 days obtained by Henry et al. (2002) from their spectrophotometric Ca II H

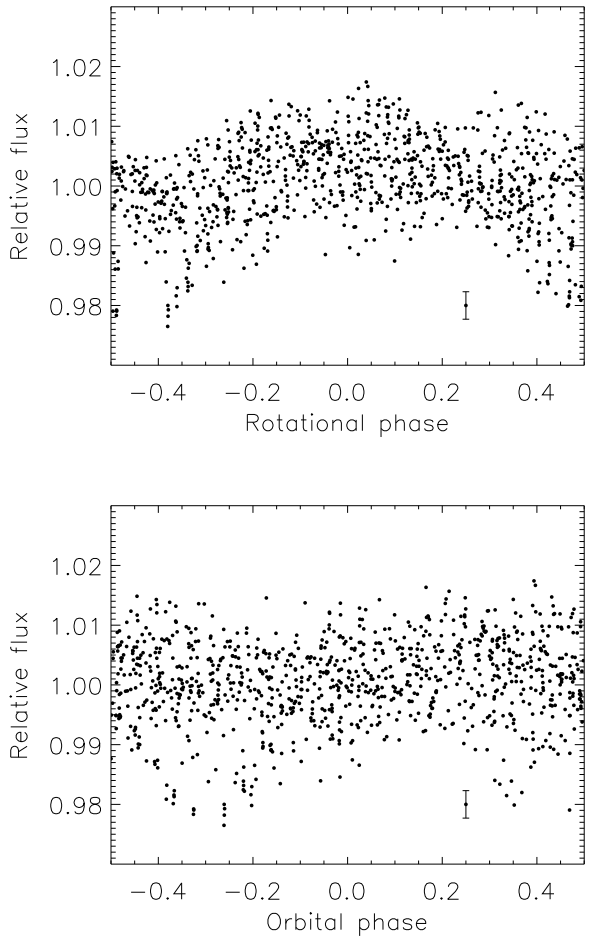

Figure 6.5: APT photometry with 8.17-year trend removed, phased at the strongest period associated with the rotation of the star (23.39 days; top panel) and at the orbital period of the planet (24.36 days; bottom panel). The coherent signal visible in the top panel disappears in the bottom panel, indicating that it is more likely to correspond to the stellar rotation than to star-planet interaction. The 1σ error bar is shown in each panel.

and K observations. They proposed that the 12.2-day period is half the stellar rotation period, arising in the data when active regions are present

on opposite hemispheres of the star.

If I take a value of 23.4 days as the rotation period of the star and our stellar radius of 0.73 $R_{\odot}$, I find a rotational velocity of 1.58 km/s, which is consistent with our measured value of $v \sin i < 1.0 \pm 0.5$ km s^{-1} (i.e. $v_{rot} \geq v \sin i$).

Using photometry spanning just over a year, Henry et al. (2002) found a rotation period of 24.5 ± 0.5 days, which agrees with the period of the planet within the uncertainties. This led Santos et al. (2003) to suggest the possibility of star-exoplanet interactions in the system. However, none of my new, more precise values of the dominant frequencies associated with rotation, based on a much longer data set, match the orbital period of the planet. My least-squares test, trying to force a fit including the orbital period of the planet (24.3587 days), shows that it is not part of a valid solution for the data. As an additional reality check, I phased the photometry at this period and found that the coherent signal visible in the top panel of Figure 6.5 disappears, as can be seen in the bottom panel of the same figure. Based on our data, I conclude that there is no indication of star-planet interactions in the HD 192263 system.

For completeness, I have also examined the ASAS photometry with the goal of verifying the conclusions described above. This time series has a lower cadence, covers a shorter time frame and its rms is three times larger than for the APT data. I find that while the two data sets are consistent with each other, the lower quality of the ASAS photometry prevents it from setting additional constraints on the variability of the star.

6.6 Transit Exclusion and Implications

The long APT photometric dataset for HD 192263 makes possible full coverage of the 3σ transit window. Figure 6.6 shows the photometry phased at the planet's orbital period. Phase 0.0 is the location of the predicted mid-transit time of the planet. The solid line represents the predicted transit signature, based on the analytic models of [160] and using the values for the transit depth and duration calculated in Section 6.3. The short dashed

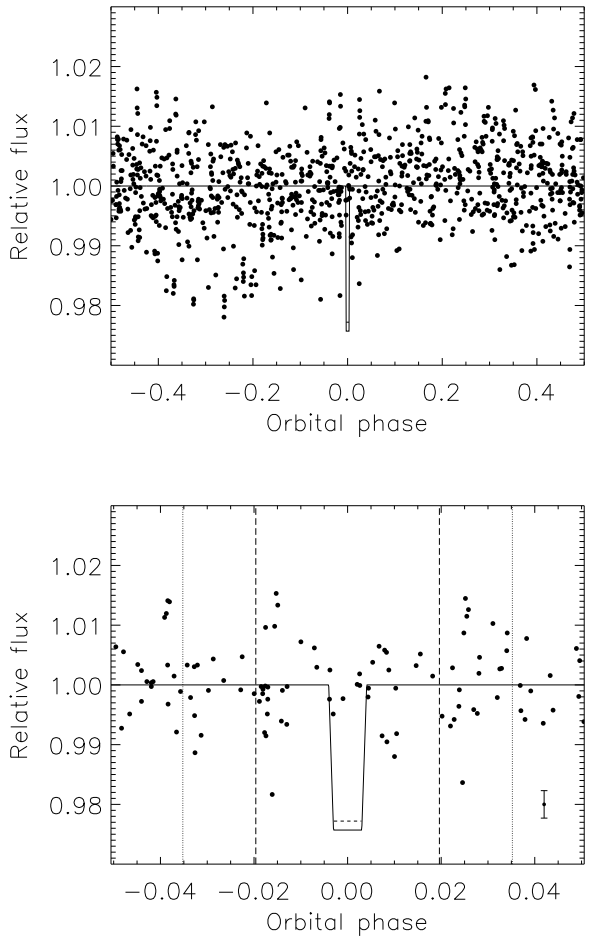

Figure 6.6: APT photometry, with each half-season normalized to the same mean (see text for details) and phased at the orbital period of the planet. The solid line is the predicted transit signature. The overplotted short dashed line is the predicted transit signature if the star has a radius of 0.77 $R_\odot$. Top panel: full orbital phase. Bottom panel: the 3σ transit window (horizontal extent of the plot), with the vertical dashed and dotted lines enclosing the 1σ and 2σ transit windows, respectively. The 1σ error bar is shown in each panel.

line corresponds to the predicted transit depth if the stellar radius is 0.77 $R_\odot$ (see Section 6.3). At the top the entire orbital phase is shown, while the horizontal range of the bottom plot corresponds to the size of the 3σ window. In the bottom panel, the vertical dashed and dotted lines indicate the extent of the 1σ and 2σ transit window, respectively.

The rms of the photometry in Figure 6.6 is 0.0065. I can therefore exclude edge-on ($i = 90°$) transits with the predicted depth of 0.0253 at the 3.9σ level. (If I assume a stellar radius of 0.77 $R_\odot$, then the predicted depth is 0.0228 and I can exclude such transits at the 3.5σ level.) While a grazing transit for this planet requires an orbital inclination of 88.7°, the cadence of the observations only allows us to exclude transits corresponding to i >88.9°. This is equivalent to an impact parameter (b) < 0.86, and a transit duration > 0.01 days = 0.004 orbital phase. The photometric precision is sufficient to rule out transiting planets with radii as small as 0.79 R_J at 2σ confidence. The density of a planet with such a radius would fall outside the range predicted by the models of [24].

The case of HD 192263b shows that deep and more importantly, long transits can be detected or ruled out using existing low-cadence photometry if the dataset covers a sufficiently long time period. An additional benefit of a long time series is the full coverage of the 3σ transit window, providing a higher confidence in the transit exclusion in the case of a non-detection. The utility of the ephemeris refinement component of the TERMS approach is clear: smaller uncertainties on the orbital period and transit time lead to a shorter transit window within which we need to assess whether the phase-folded photometry has adequate cadence and precision.

I perform an additional test to check the presence or absence of a transit by comparing the predicted amplitude of the Rossiter-McLaughlin (RM) effect for this system with our RV measurements. For a system in which the orbital plane of the planet is aligned with the equator of the star, [91] show that the amplitude of the RM effect is given by

$$K_R = v \sin i \frac{\gamma^2}{1 - \gamma^2} \tag{6.1}$$

where $\gamma = R_p/R_\star$. For $\gamma \ll 1$, equation 1 becomes

$$K_R = v \sin i \left(\frac{R_p}{R_\star}\right)^2 \tag{6.2}$$

Using a transit depth $(R_p/R_\star)^2$ of 0.0253 and our upper limit on $v \sin i$, I find $K_R < 25.3$ m s^{-1}. Given the rms of our RV residuals within the 3σ transit window (see Figure 6.2), I can exclude an RM effect with amplitude > 12.0 m s^{-1}. While these limits place a much looser constraint on the existence of a transit than the photometry does, they are consistent with the absence of a transit.

6.7 Conclusions

The planet orbiting HD 192263 is an illustration of the challenges posed by the detection of companions around active stars. In this Chapter, I presented five new RV measurements which I used to refine the orbital parameters of HD 192263b. The new measurements provide continuing support for the existence of the planet, in agreement with the conclusion of [206].

I have also shown new photometry of the system. I perform a Fourier analysis of the photometry and find evidence for variability on a 23 day timescale, which agrees with previous reports of stellar variability. A detailed examination of the Fourier spectrum near this value reveals a multiplet of peaks with periods ranging between 22 and 27 days. The dominant signal in this cluster has a period of 23.3932 ± 0.0046 days. The five surrounding peaks are likely due to the amplitude modulation of this signal over the time span of the observations, with a possible minor contribution from the star's differential rotation. Nevertheless, neither the dominant period nor any of the five other peaks match the orbital period of the planet ($P = 24.3587 \pm 0.0022$ days), so I find no evidence of star-planet interactions.

I also observe a longer-term trend which may be a $\sim$ 8-year magnetic cycle (if the signal remains periodic), or may be due to variations of spots at the surface of the star which would not repeat with a regular cycle. Contin-

uing long-term monitoring of the star should more convincingly discriminate between the two scenarios. It is noteworthy that we do not see a long-term variation in the RV measurements in phase with this long-term photometric trend.

As our photometric dataset spans approximately a decade, we have good coverage of the 3σ transit window when the data is phased to the orbital period of the planet. Thus I am able to thoroughly exclude transits of the predicted depth (2.53%, corresponding to a planet with a radius of 1.09 R_J) for a planet with a mass of 0.733 M_J. The absence of a detectable (> 12.0 m s^{-1}) Rossiter-McLaughlin effect is consistent with this result. I also exclude transit depths as low as 1.3% (corresponding to a planetary radius of 0.79 R_J). In the case of a non-edge-on orbital configuration, the cadence of the data allows us to rule out transits with impact parameter < 0.86.

Chapter 7

A Search for Transits of GJ 581e and Characterisation of the Host Star Variability Using MOST Photometry

7.1 Introduction

Radial velocity (RV) and transit searches are discovering progressively less massive and smaller exoplanets. The HARPS [170], Keck [37] and several other RV surveys have brought forth dozens of planets with minimum masses <10 $M_{\oplus}$, while the *Kepler* mission [27] has so far yielded a wealth of super-Earth candidates with radii <4 $R_{\oplus}$. Furthermore, Kepler has already detected three planetary candidates with radii smaller than that of the Earth in a single system [176].

There are currently a handful of super-Earths for which both the masses and radii have been measured. By determining the density of these planets, of which none exist in the Solar system, it becomes possible to begin constraining their composition and eventually their formation. Thanks to their transiting nature it also becomes possible to perform spectroscopic studies of these planets. Such studies, rendered possible by the large transit depth which is induced by the small size of the host star relative to that of the transiting planet, now exist for the super-Earth GJ 1214b [19, 20, 23, 56].

GJ 581, a small M2.5 dwarf ($R_{\star}$=0.299 $R_{\odot}$; [254]), is known to host up to 6 planets [26, 168, 239, 250]. However, I note that the existence of planets

f and g has been disputed and arguably ruled out by several independent analyses [86, 98, 237]). This system has been observed and studied at length. The published HARPS radial velocity measurements span approximately seven years [86], and the HIRES observations cover more than a decade. The orbital parameters of four planets in the system are well constrained [86]. At least three of those planets (c, d and e) have minimum masses in the super-Earth regime. The habitability of c and d has been assessed by several groups, and while the former orbits too close to the star to sustain liquid water on its surface [215, 253], GJ 581 d was found to reside in the habitable zone of the system [15, 125, 253, 256, 266].

The GJ 581 system was observed by the *MOST* space telescope in order to determine its variability and search for transits of GJ 581e. These observations were acquired as part of a program aiming to search for transits of known RV super-Earth candidates using MOST. The telescope is optimized for bright star ($V < 10$) photometry, a characteristic it shares with radial velocity surveys. Even though GJ 581 is slightly fainter ($V = 10.6$) than the usual MOST targets, the opportunity to obtain continuous coverage of more than one orbital cycle of the planet (thus eliminating the chance that a transit might be missed) motivated the observations.

GJ 581e, the innermost planet in the system, orbits its host star with a period of 3.15 days and has a *a priori* transit probability of 5%. This value corresponds to the geometric probability that the planet crosses the disk of the star and in the case of a circular orbit it is derived from the planet's semi-major axis and the stellar radius. GJ 581e, whose published properties can be found in Table 7.1, is the planet with the smallest radial velocity-derived minimum mass to date. If the planet is found to transit, its size can be determined and spectroscopic studies of its atmosphere become possible.

Table 7.1: Published orbital parameters for GJ 581e from [86]

Parameter	**Circular model**	**Keplerian model**
P (days)	3.14941 ± 0.00022	3.14945 ± 0.00017
T_0[a] (HJD)	2454749.026 ± 0.056	2454750.31 ± 0.13
e	–	0.32 ± 0.09
ω (deg)	–	236 ± 17
K ($\mathrm{m\,s^{-1}}$)	1.754 ± 0.180	1.96 ± 0.20
$M_p \sin i$ ($M_\oplus$)	1.84	1.95
a (AU)	0.028	0.028

Table 7.2: Published orbital parameters for GJ 581b from [86]

Parameter	**Circular model**	**Keplerian model**
P (days)	5.36864 ± 0.00009	5.36865 ± 0.00009
T_0[a] (HJD)	2454751.536 ± 0.012	2454753.95 ± 0.39
e	–	0.031 ± 0.014
ω (deg)	–	251 ± 26
K ($\mathrm{m\,s^{-1}}$)	12.72 ± 0.18	12.65 ± 0.18
$M_p \sin i$ ($M_\oplus$)	15.96	15.86
a (AU)	0.041	0.041

[a]Time of transit.

The duration and nearly continuous nature of the MOST observations presented in this Chapter also invite a search for transits of GJ 581b (P = 5.37 days), regardless of the outcome of my GJ 581e transit search. Indeed, even if GJ 581e does not transit, GJ 581b may still transit if their orbits are not co-planar. [157] have already ruled out transits of GJ 581b, using an orbital solution based on the assumption of circular orbits for all planets in the system. However, if the orbital eccentricities of the planets are allowed to vary during the fitting process, the resulting solution shifts the predicted mid-transit time of GJ 581b outside the observations acquired by [157], as was determined by [86]. The published orbital parameters of GJ 581b are found in Table 7.2.

[86] performed a transit search for GJ 581e using photometry from the 2.5 m Isaac Newton Telescope that was obtained during one transit window between -1 and 2.3 σ from the predicted mid-transit time (a total of 6.5 hours) for a circular orbit. They have found no evidence of a transit. In this Chapter, I present two sets of nearly contiguous MOST space-based photometry of GJ 581, obtained in 2007 and 2009 (Section 7.2). The 2009 data set covers almost four full orbital cycles of GJ 581 e (Section 7.3.1) and thus allows us to perform a more complete transit search using the ephemeris for the circular orbital solution. In addition, I am able to search for transits during the predicted transit window[19] corresponding to the eccentric orbital model. I quantify our sensitivity to shallow transits via Monte Carlo tests (Section 7.3.2). In Sections 7.3.3 and 7.3.4 I place limits on the size and mass of GJ 581e and discuss the implications. I use the MOST photometry (which covers 2 orbital cycles of GJ 581b) to search for transits of this planet within its eccentric orbit-predicted transit window as well, in Section 7.4. In Section 7.5, I briefly address the cases of GJ 581c and GJ 581d. Finally, I combine this data set with a longer light curve obtained in 2007 to carry out a stellar variability analysis for GJ 581 (Section 7.6). I conclude in Section 7.7.

[19]The transit window is the time span during which a transit is predicted to occur, calculated from the uncertainties on the orbital period and those on the predicted mid-transit time.

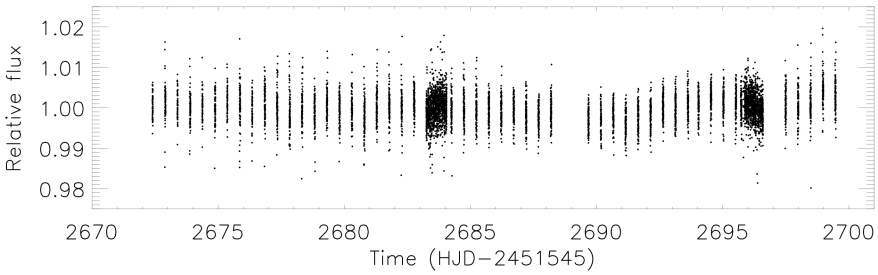

Figure 7.1: Reduced MOST photometry acquired during 2007 April 25 to June 14. The tire-track pattern of the data is due to the fact that MOST alternated between GJ 581 and other stars during these observations.

7.2 Observations and Data Reduction

We obtained photometry of Gliese 581 from the MOST satellite during 2007 April 26 to May 24, and during 2009 May 8-20.

In 2007, MOST observed GJ 581 for 50 days, but alternated between this star and other targets during this period. Because the cadence of the observations is too low, the 2007 photometry (see Figure 7.1) was not used for a transit search, but was combined with the 2009 data for the stellar variability study (see Section 7.6). The exposure time for each individual frame is 3.0 s. In 2009, GJ 581 was observed contiguously during half of every MOST orbit (54 out of every 101.4 minutes), for nearly 12 days. The alternating target, 33 Lib, was monitored during the remainder of each orbit. The GJ 581 photometry was acquired in Direct Imaging mode, with individual exposure times of 3.0 s. For both the 2007 and 2009 observation runs, sets of 8 individual frames were stacked on board the satellite before being downloaded to Earth, leading to a total integration time of 24 s per data point. There is also a modest readout overhead of 3.2 seconds, resulting in a sampling rate of 27.2 s (outside of the interruptions for the alternating target).

The raw data were reduced using aperture photometry. The reduction pipeline (described in detail in [198]) corrects for cosmic ray hits and stray

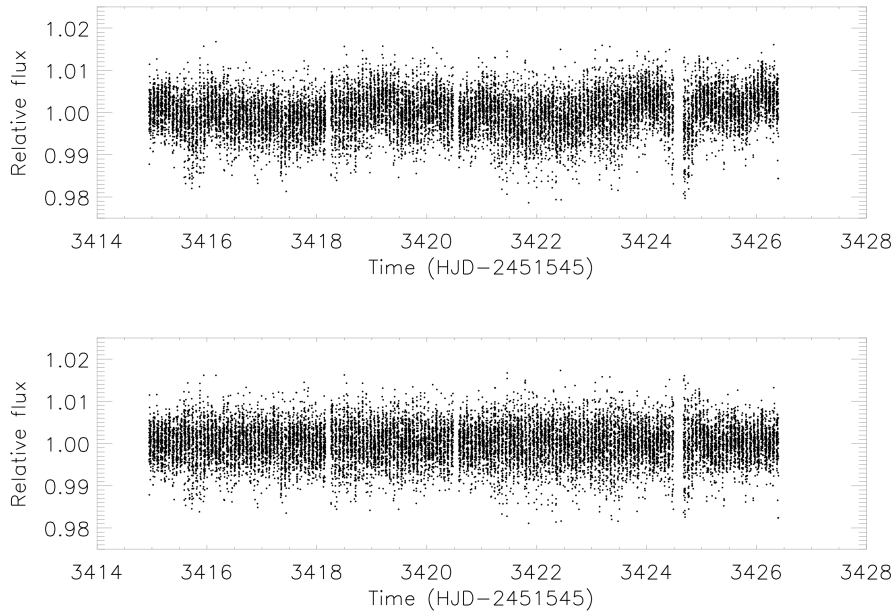

Figure 7.2: *Top:* Reduced MOST photometry acquired during 2009 May 8-20. *Bottom:* Same, but with the modulation visible in the top panel removed (see Section 7.2 for details). The tire-track pattern of the data is due to the fact that MOST alternated between GJ 581 and another star during these observations.

light from scattered Earthshine, which varies with the period of the satellite. The 1-day period variation (due to the Sun-synchronous orbit of MOST) with an amplitude of 1.3 mmag was also filtered from the data.

In addition, for the 2009 data set three short sections of the light curve (at around 3418.2, 3420.5 and 3424.6 days in Figure 7.2) affected by high levels of stray light were conservatively excised. After these steps, a modulation remains in the light curve (Figure 7.2, top panel). A possible origin of this modulation is discussed in Section 7.6. This trend was modelled with a cubic spline interpolated from the data binned every 500 minutes, and removed from the light curve before the transit search and transit-injection tests. The bin size was chosen to be large enough not to interfere with any

transits of GJ 581 e (predicted edge-on transit duration = 1.2 hours) and small enough to remove the slowly varying trend. The final 2007 and 2009 time series contain 7667 and 17312 points, respectively.

7.3 GJ581e

7.3.1 Transit Ephemeris and Predicted Characteristics

I use the ephemerides published in [86] to search for transits of GJ 581e. The authors derived best-fitting orbital models for planets b, c, d and e in two ways: by assuming circular orbits (where the eccentricity is fixed to 0.0 for each planet) and by fitting fully Keplerian orbits (where the eccentricity is allowed to float). While the values of the orbital period for GJ 581e in the two cases are nearly identical, an eccentricity of 0.32 ± 0.09 is found for the Keplerian fit (see Table 7.1 for the [86] orbital parameters of GJ 581e). In addition, $M_P \sin i$ is slightly larger for the Keplerian orbit fit (1.95 $M_\oplus$) than for the circular orbit model (1.84 $M_\oplus$), though no uncertainties are reported for these values. The predicted mid-transit times ($T0$) and associated uncertainties also differ significantly between the two cases, leading to different phase locations and sizes for the transit windows. The coverage of the MOST photometry is adequate for monitoring the transit windows corresponding to both solutions.

For the circular orbit transit search, the photometry was folded on $T0$ =2454969.489. The 1σ uncertainty on this value is 0.071 days, so the size of the 3σ transit window is 11.48 hours (including a predicted transit duration of 1.2 hours). In the Keplerian orbit case, $T0$ =2454970.77 was used to fold the time series. The associated 1σ uncertainty is 0.14 days, leading to a 3σ transit window of 22.03 hours (including a predicted transit duration of 1.6 hours).

I estimate radii for GJ 581e for each of three theoretical compositions: hydrogen, water ice and silicate. I use the models of [212] and the planetary mass obtained by assuming an impact parameter (b) of 0.0 ($i = 90°$). The derived radii are 3.70, 1.68 and 1.25 $R_\oplus$, for a homogeneous hydrogen, water

ice and silicate planet, respectively.

7.3.2 Monte Carlo Simulations

Throughout this section I only use the 2009 data set, because the cadence of the 2007 photometry is too low for a transit search of a super-Earth planet.

My approach is inspired by the methods used in [58], [57] and [9]. However, my analysis differs in that I search for transits of a RV-detected planet with a well-known period rather than additional planets in known transiting systems. Indeed, the orbital period of GJ 581 e is known to within 19 s [86]. As a consequence, for my Monte Carlo simulations and transit search I vary the planetary radius (R_p), orbital inclination (i) and orbital phase at which the transit may occur ($0 < \phi < 1$), but not the orbital period. Carrying out simulations for values of i other than 90° allows us to quantify the effect of the cadence of the MOST observations on our sensitivity to transits of various durations.

To quantify our detection limits for the Gliese 581 photometry, I injected simulated limb-darkened transits (using the models of [160]) in the 2009 light curve and attempted to recover them by fitting a box-shaped transit model and minimizing χ^2. For the simulated transits, I interpolated limb darkening coefficients (c_1 =1.600, c_2 =-1.491, c_3 =1.209, c_4 =-0.398) from tables generated for the MOST bandpass (A. Prsa, private communication) and based on the Kurucz models [45], assuming a stellar effective temperature (T_{eff}) of 3500 K, surface gravity ($\log g$) of 5.0 and metallicity ($[Fe/H]$) of -0.15. The actual values for GJ 581 are $T_{eff} = 3498 \pm 56$ K, $\log g = 4.96 \pm 0.08$ and $[Fe/H] = -0.135$ [254]. I used a grid evenly spaced in R_p and i. The grid consists of 30 R_P values ranging from 1 to 4 $R_\oplus$ and 4 i values ranging from 87.5 to 90° ($0.0 < b < 0.9$). For each combination of radius and inclination, I insert transits at 100 randomly distributed phases spanning the 3σ transit window for the circular ephemeris. Thus I search a total of 12000 light curves.

I sample the χ^2 space at 90 values of the planetary radius (equally spaced from 0.85 to 4.5 $R_\oplus$), 6 values of the orbital inclination (equally spaced from

87.2 to 90°) and between 130 and 2000 values of the orbital phase (equally spaced within the 3σ transit window). For each model, I compute the change in χ^2 relative to the constant flux hypothesis. The model with the largest value of $\Delta\chi^2\% = 100\%(\chi_t^2 - \chi_c^2)/\chi_c^2$ (where χ_t^2 and χ_c^2 correspond to the transit and constant flux model, respectively) becomes the best-fit solution for a particular light curve. I call the values of R_p, i and ϕ associated with the best-fit solution R_{rec}, i_{rec} and ϕ_{rec}, respectively. Since the goal is to identify a statistically significant transit rather than to precisely determine its parameters, I consider a transit as successfully detected if $\Delta\chi^2 > 70$ and the following two conditions are satisfied: $|(R_{rec}/R_{inj})| - 1 < 20\%$ and $|\phi_{rec} - \phi_{inj}| < 0.01$ (corresponding to $\sim$ 45 min). R_{inj} and ϕ_{inj} are the planetary radius and orbital phase of the injected transit signal. The results of my Monte Carlo simulation indicate that I do not always accurately recover the impact parameter of the injected signal. This is not surprising for such shallow and short (1.2 hours for $b = 0$) transits. As a consequence, I do not use an orbital inclination condition as a criterion for detection.

For $b = 0$ ($i = 90°$), I recover the transits corresponding to a planetary radius $\geq$1.42 $R_\oplus$ at least 68% of the time. I recover injected transits for $R_p \geq 1.62R_\oplus$ and for $R_p \geq 1.93R_\oplus$ at least 95% and 99% of the time, respectively. For larger values of b these confidence limits tend to shift to larger radii, though only mildly so for $b \leq 0.6$. This is because the transit duration is shorter and there are less in-transit data points, making the signal more difficult to detect. Further, for larger values of b the planet would cross nearer the limb of the star, thus blocking out less light and leading to a shallower transit than in the case of $b = 0$. In light of these two arguments, I note that while transits with $R_P \leq 4R_\oplus$ and $b = 0.9$ do not meet my detection criteria with sufficient statistical confidence, deeper transits do. Our detection limits as a function of b and R_p are shown in Figure 7.3, in the form of 68%, 95% and 99% confidence contours. A value of $b = 0$ corresponds to an edge-on transit, while $b = 1$ represents a grazing transit.

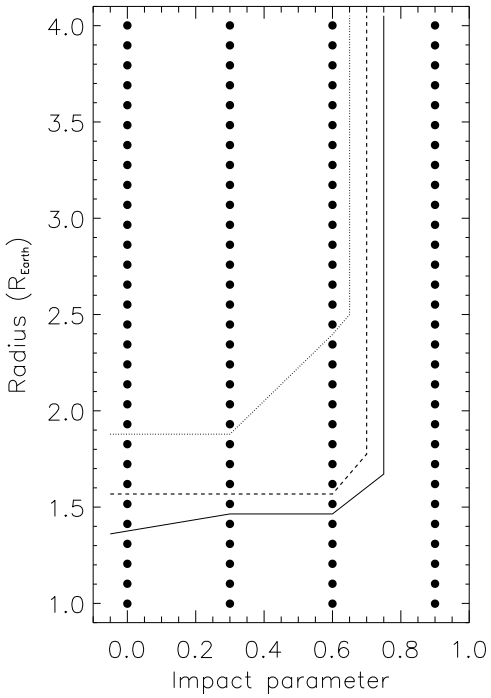

Figure 7.3: Detection limits for injected transits as a function of planetary radius (R_P) and impact parameter (b). The solid points correspond to the values of R_P and b at which I tested our sensitivity. The solid, dashed and dotted lines indicate the 68%, 95% and 99% confidence contours, respectively.

7.3.3 Transit Search

I perform the transit search described above on the 2009 light curve (within the 3σ transit window corresponding to the circular orbit solution). I do not find any transit candidates for a planet with $R_p \geq 1.42\ R_\oplus$, which is my 1σ detection limit (for $b = 0$).

My best transit candidate (for which $\Delta\chi^2 = 15$ was largest) has the following properties: $R_p = 0.912 R_\oplus$, $b = 0.40$ and $\phi = 0.058$, and therefore it occurs near the positive edge of the 3σ window (the predicted mid-transit

time corresponds to $\phi = 0.0$). This signal is significantly below my detection limit and over five times smaller than the rms of the phased data within the 3σ transit window. Such a planet would have a density (ρ) of 13.4 g cm^{-3}, an unrealistic value as it is greater than the maximum iron fraction limit for a rocky planet [161]. For these reasons, I consider this candidate very unlikely to be a transit signal. The phased observations spanning the 3σ transit window and the best-fit model for this candidate are shown in Figure 7.4.

Using the HIRES-based results from [250], [3] find a possible discrepancy between the residuals of a circular orbit solution for the four planets, and the expected Gaussian distributed residuals if the best-fit model was the true model. They suggest this discrepancy may indicate that the planetary orbits are eccentric. Further, when fitting a Keplerian model to the HARPS RV data (see Section 7.3.1), [86] obtain significant values for the eccentricity of planets d and e, and different mid-transit times for all planets than in the circular model case. Motivated by these results, I also carry out a transit search for GJ 581e within the 3σ transit window computed from the orbital parameters associated with the Keplerian model. The rms=0.00425 (in units of relative flux) of the phased photometry within this window is marginally smaller than that of the circular solution transit window (rms=0.00431). Thus our sensitivity to transits should be very similar or marginally better. I find no transit candidate near or above the detection limits reported in Figure 7.3.

The best candidate ($\Delta\chi^2 = 29$) in this case represents a planet with $R_p = 1.19 R_\oplus$, $b = 0.79$ and $\phi = -0.006$, very close to the predicted mid-transit time. With a mass of 1.95 $M_\oplus$ [86], this planet would have ρ =6.41 g cm^{-3} which would make it slightly denser than 55 Cnc e and suggest a silicate composition model [212]. Nevertheless, the statistical significance ($p = 0.26$) of this signal is too low and its best-fitting parameter values are too far below my detection limits to make it a likely candidate. The phased observations showing this candidate can be seen in Figure 7.5.

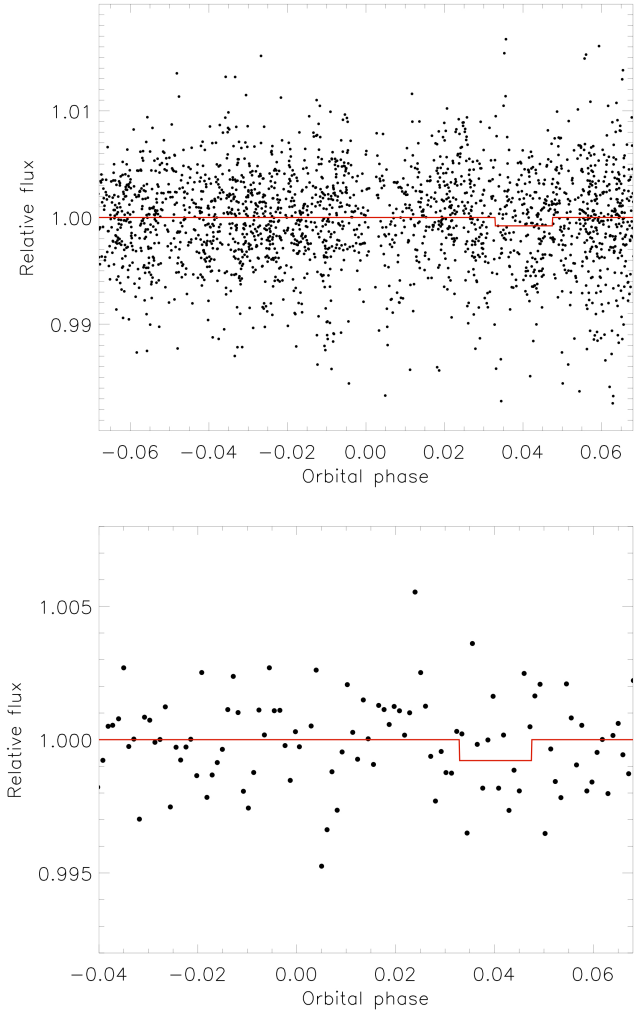

Figure 7.4: The best candidate transit signal for the circular model ephemeris. Phase 0.0 corresponds to the predicted mid-transit time. *Top:* Unbinned photometry folded at the orbital period of 3.15 days. The orbital phase range of the plot is equivalent to the 3σ transit window. *Bottom:* Zoom-in of the folded photometry, binned every 0.001 orbital phase. In both panels, the best-fit box-shaped transit model is shown in red.

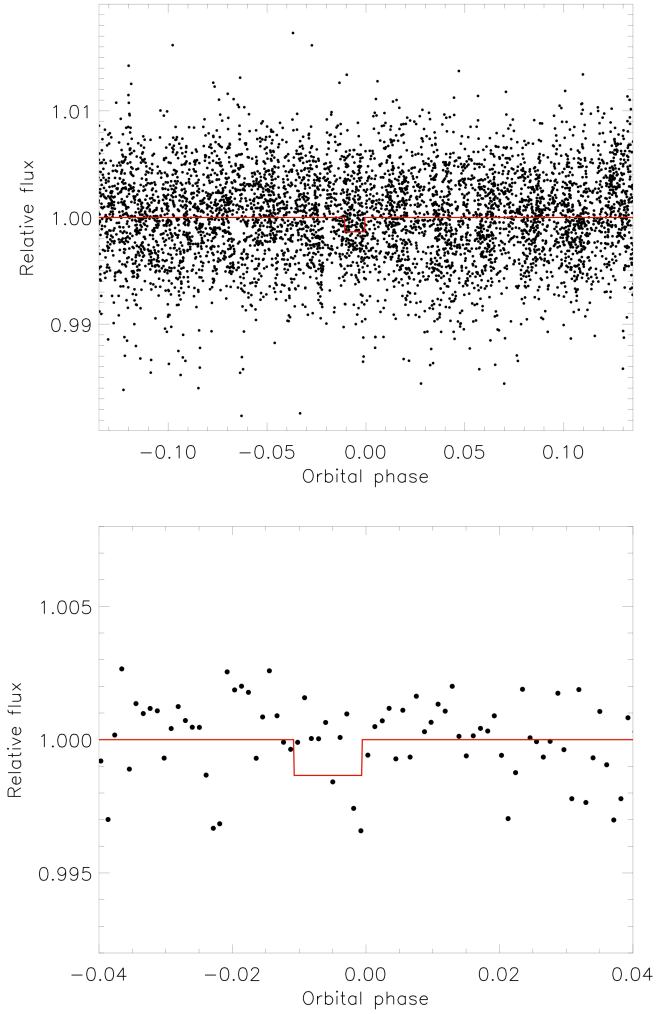

Figure 7.5: The best candidate transit signal for the Keplerian model ephemeris. Phase 0.0 corresponds to the predicted mid-transit time. *Top:* Unbinned photometry folded at the orbital period of 3.15 days. The orbital phase range of the plot is equivalent to the 3σ transit window. *Bottom:* Zoom-in of the folded photometry, binned every 0.001 orbital phase. In both panels, the best-fit box-shaped transit model is shown in red.

7.3.4 Constraints and Implications

Even when a super-Earth transits and its radius can be measured, it is still difficult to gain insight into its detailed composition. Nonetheless, useful

limits can be placed on its interior structure when both its mass and radius are available [195]. Unfortunately, I do not detect a significant transit signal for GJ 581e. If the planet transits, then I can use the limits determined in Section 7.3.2 to constrain its size as follows.

To 1σ confidence, I exclude pure hydrogen, hydrogen/helium, pure water ice and 50% water ice compositions for detectable ($b \leq 0.6$) transiting orbital configurations. To 2σ confidence, I rule out compositions less dense than 75% water for $b \leq 0.6$. I exclude hydrogen and hydrogen/helium compositions with 3σ confidence. Quantitatively, for $M_P = 1.84 M_\oplus$ (based on the circular orbit solution), I rule out densities lower than 3.54 g cm^{-3} , 2.39 g cm^{-3} and 1.41 g cm^{-3} with 1σ, 2σ and 3σ confidence, respectively.

There are so far no transiting planets with a measured mass smaller than 2 $M_\oplus$. Kepler-11f comes close, at 2.3 $M_\oplus$ (determined from dynamical fits of the Kepler-11 system) and a radius of 2.6 $R_\oplus$ [154]. GJ 1214b orbits a star much closer in spectral type (M4.5) to GJ 581, but has a mass of 6.4 $M_\oplus$ and a radius of 2.7 $R_\oplus$ [49]. These two super-Earths are relatively low-density planets, with envelopes of water [23] and/or hydrogen [154]. If GJ 581e transits and has a similar density, then I would have detected the transit in the MOST photometry. However, if a transiting GJ 581e is more similar to the denser 55 Cnc e (ρ =5.9 g cm^{-3}; [262]), Kepler-10b (ρ =8.8 g cm^{-3}; [16]), or Corot-7b (ρ =10.4 g cm^{-3}, assuming a mass of $7.4 M_\oplus$; [106]), then I would not have detected its transit using our data. Nevertheless, 55 Cnc e, Kepler-10b and Corot-7b receive significantly more radiation due to both their proximity to their host stars and the higher temperatures of those stars, compared to Kepler-11f, GJ 1214b and GJ 581e. Therefore, we expect any atmospheres or water envelopes these highly irradiated planets may have acquired to be mostly or entirely evaporated, thus possibly explaining their higher densities.

[168] have performed a stability analysis of the GJ 581 system in order to determine constraints on its orbital inclination. Assuming co-planar orbits and allowing for non-zero eccentricity, they found that GJ 581e was ejected for inclinations less than $i = 40°$. This lower bound leads to a maximum mass for GJ 581e of 2.86 $M_\oplus$ based on the $M_P \sin i$ value from the circular

solution, and 3.03 $M_{\oplus}$, based on the Keplerian solution. A co-planar orbital configuration with $i > 40°$, even if it is not edge-on, should still give rise to observable thermal phase variations of the order of at least 10 ppm in the infrared, dominated by the thermal radiation of planets b and e. A signal of this amplitude is likely within reach of NIRCam on the JWST [211].

7.4 GJ 581b

7.4.1 Transit Ephemeris and Predicted Characteristics

I use the [86] ephemerides for GJ 581b to determine its 3σ transit window for both the circular and Keplerian orbit cases, in the same manner I did for GJ 581e. Although the authors find a nearly circular orbit ($e = 0.031 \pm 0.014$) for GJ 581b itself in the Keplerian orbit case, the planet's predicted mid-transit time is nevertheless affected (and shifted relative to the circular case) due to the overall best-fitting solution which does assign significantly greater than 0 eccentricities to planets e and d. The minimum mass of GJ 581b is not very different in the circular case ($M_P \sin i = 15.96 M_{\oplus}$) compared to the Keplerian case ($M_P \sin i = 15.86 M_{\oplus}$), and is very close to that of Neptune ($M_P = 17.15 M_{\oplus}$).

I find that [157] have conclusively ruled out transits of GJ 581b within its $\sim 2\sigma$ transit window for the circular orbit ephemeris. They exclude planetary radii greater than $1.5 R_{\oplus}$, a value which, given the minimum mass of the planet, would suggest a highly implausible object composed entirely of iron. However, to my knowledge the transit window arising from the Keplerian fit has not yet been searched.

For completeness (the MOST observations allow the search to be carried out beyond the 2σ window), and to confirm the results of [157], I perform this analysis for the circular orbit window as well, using $T0 = 2454966.303$ to fold the photometry. The 1σ uncertainty on this value is 0.016 days. The 3σ transit window (including a predicted edge-on transit duration of 1.4 hours) is thus 3.7 hours long. For the Keplerian orbit window I use $T0 = 2454963.34$ to fold the data, and the associated 1σ uncertainty of 0.39

days leads to a transit window length of 56.2 hours (or 2.34 days).

7.4.2 Transit Search and Constraints

The folded photometry within the 3σ transit window for the circular and Keplerian orbit cases are shown in Figures 7.6 and 7.7, respectively. I considered and overplotted transit models corresponding to three possible planetary radius values. The dashed line represents the minimum radius for a planet of mass equal to the minimum mass of GJ 581b with the maximum iron core mass fraction attainable from collision-induced mantle stripping for a planet ($R_P = 1.9R_\oplus$; [161]). A more realistic transit depth is indicated by the dotted line, which corresponds to a silicate planet ($R_P = 2.3R_\oplus$). Finally, the solid line represents a planet with a density equivalent to that of Neptune ($R_P = 3.8R_\oplus$).

The phase coverage for GJ 581b is incomplete even when ∼2 orbital cycles are phase-folded because of the cadence of the MOST photometry of this system (see Section 7.2). This sets limits on the duration of a transit detectable with the MOST data, depending on where it would occur within the window.

Thus, for both the circular and Keplerian cases, I can rule out transits corresponding to radii associated with any plausible composition for GJ 581b, but only for impact parameter $b \lessapprox 0.4$ (corresponding to a transit duration greater than $\sim 90\%$ of that of an edge-on transit). It is difficult to set more precise (and applicable to the entire transit window) limits on the duration of a detectable transit because the cadence and phase coverage of the phased photometry are uneven throughout the transit window.

For the circular orbit window – based on the results of [157] and my own – I conclude that transits are unlikely to occur. For the Keplerian case, given our observations, transits may still occur for $0.4 \gtrapprox b \leq 1$.

The lower limits on the mass of GJ 581b thus do not change. The dynamical simulations performed by [168] (under the assumption of stable and co-planar orbits for planets a to d) lead to an upper limit of 24.83 $M_\oplus$ for the circular orbit case and 24.67 $M_\oplus$ for the Keplerian orbit case.

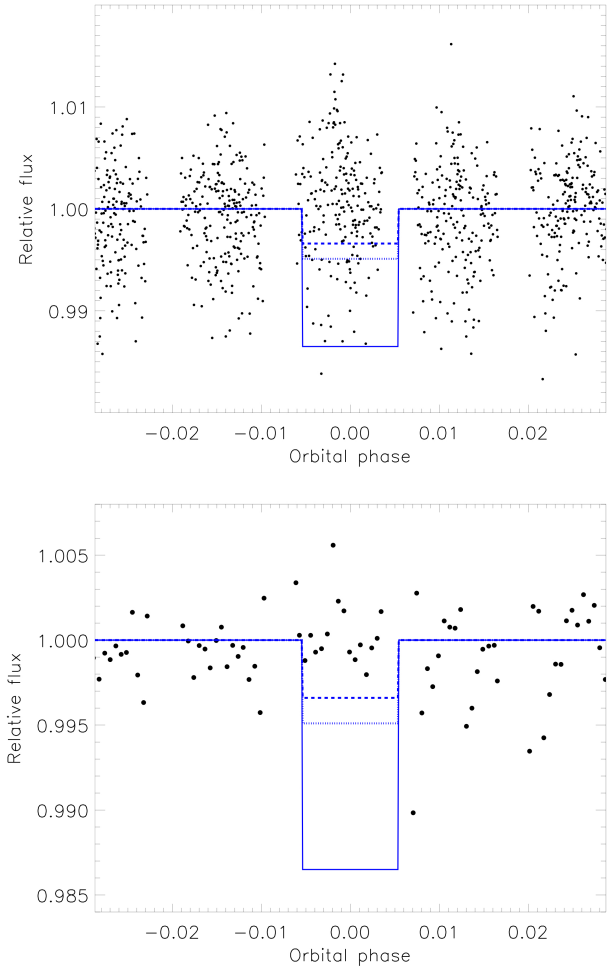

Figure 7.6: The 2009 photometry, folded at the period of GJ 581b (5.37 days). The orbital phase range of both top and bottom plots is equivalent to the 3σ transit window based on the circular orbit ephemeris. Phase 0.0 corresponds to the predicted mid-transit time. Box-shaped predicted transit signatures for three planetary radius values are overplotted in blue. The dashed, dotted and solid lines represent $R_P = 1.9, 2.3$ and $3.8 R_\oplus$, respectively. *Top:* Unbinned photometry. *Bottom:* Vertical zoom-in of the folded photometry, binned every 0.0006 orbital phase.

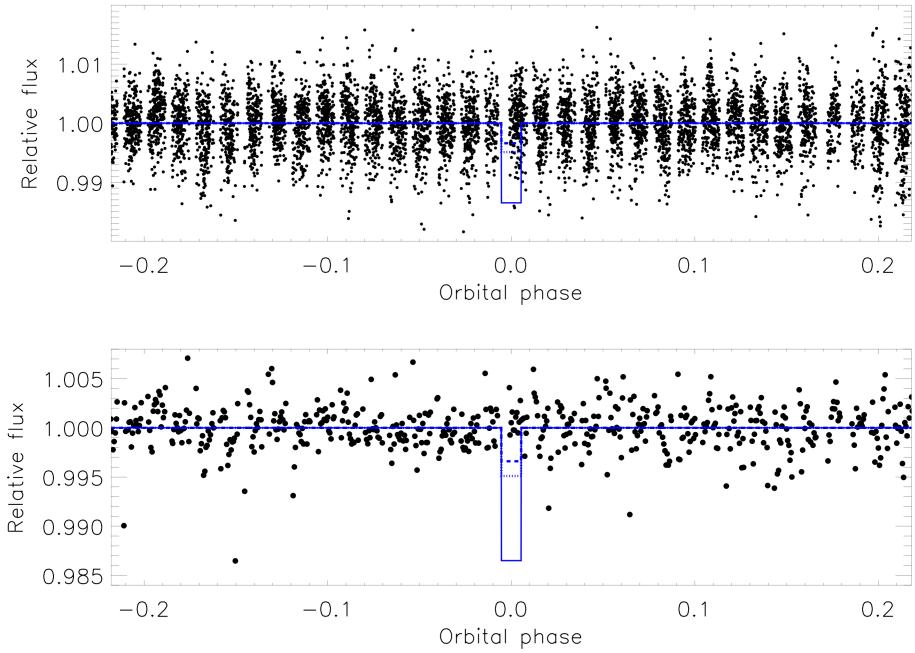

Figure 7.7: The 2009 photometry, folded at the period of GJ 581b (5.37 days). The orbital phase range of both top and bottom plots is equivalent to the 3σ transit window based on the Keplerian orbit ephemeris. Phase 0.0 corresponds to the predicted mid-transit time. Box-shaped predicted transit signatures for three planetary radius values are overplotted in blue. The dashed, dotted and solid lines represent $R_P = 1.9, 2.3$ and $3.8 R_\oplus$, respectively. *Top:* Unbinned photometry. *Bottom:* Vertical zoom-in of the folded photometry, binned every 0.0006 orbital phase.

7.5 GJ 581c and GJ 581d

The third and fourth known planets in the GJ 581 system have orbital periods of 12.92 and 66.6 days, respectively. They are both super-Earth candidates, with a minimum mass of 5.4 $M_\oplus$ for GJ 581c and 5.3 $M_\oplus$ for GJ 581d, in the circular orbit case. Their long orbital periods result in low transit probabilities, but having photometry spanning several days to several weeks motivated us to consider whether the observations may include the

predicted mid-transit times of these two planets.

Unfortunately, no GJ 581 d predicted transit times occur within the 2007 or 2009 data sets, for either the Keplerian or circular orbit ephemerides. No GJ 581c transit times are predicted within the high-cadence sections of the 2007 light curve (visible in Figure 7.1), but the 2009 data set does include one value of $T0$ for each of the two orbital fits. For the circular case, $T0 = 2454970.93$ with a 1σ uncertainty of 0.15 days. For the Keplerian case, $T0 = 2454969.7$ with a 1σ uncertainty of 1.6 days.

The main reason I do not carry out a transit search beyond visual inspection of the light curve is that the MOST photometry only covers one transit window for GJ 581c. Most of the possible radius values for this planet are too small to produce a transit signal that would be believable with a single detection given the precision of our photometry. The relatively long transit windows, especially for the Keplerian orbit case, would further decrease the significance of such a signal. I do note that no transit feature with depth larger than the rms of the light curve (~ 0.005) is visible in the photometry. This limit corresponds to a radius of 2.3 $R_{\oplus}$, which leads to a fairly low density in the realm of water/helium/hydrogen planetary compositions.

7.6 Stellar Variability

The brightness of GJ 581 is stable to less than 1% over the four weeks during which MOST observed the star in 2007. The 11.5-day data set obtained in 2009 supports this conclusion. This level of stability agrees with the finding that the X-ray brightness of GJ 581 lies below ROSAT's detection threshold and supports an advanced age ($\gtrsim 7$ Gyr) for the star, as suggested by [215]. Thus, it constitutes a factor in favour of the potential development of life on any planet residing within the habitable zone of the system, and allows a sufficiently long period of time for its occurrence [207].

I searched the MOST photometry for evidence of variations indicative of the stellar rotation period. [250] report a value of 94.2 days, based on APT photometric observations acquired with the 0.36 m Tennessee State University telescope and spanning 530 nights. They find a semi-amplitude

of 3 mmag (0.0028 in units of flux) for this variation. Though it covers only 31% of the reported stellar rotation period, the MOST 2007 data is contemporaneous with a subset of the 0.36 m photometric observations ranging from 2454217.3 to 2454244.5 (rotational phase 0.84 to 1.13 according to section 4 and Figure 1 of [250]). The MOST 2007 photometry shows a slight long-term curvature, with a minimum at approximately HJD 2454236. This corresponds to phase 1.05 in Figure 1 of [250]. In their figure, the minimum of their folded photometry can also be observed near the same phase. However, our data are insufficient to definitively establish whether they support a rotation period of 94.2 days.

In the 2009 data set I observe a modulation in the light curve with a period of about 5 days and semi-amplitude of $\sim$1.5 mmag (or 0.14% in flux units; see Figure 7.2), which was removed prior to the transit injection tests and transit search as described in Section 7.2. The amplitude spectrum shows a strong peak at a frequency of 0.1790 ± 0.0016 cycles/day (period of 5.586 ± 0.051 days), as can be seen in Figure 7.9. This variation is especially interesting as it has a period comparable to the orbital period of GJ 581b ($P = 5.36865 \pm 0.00009$ days). I generate an amplitude spectrum of the 2007 photometry (see Figure 7.8) to verify whether the same signal is present. A peak of much lower significance is visible at a frequency corresponding to a period of 5.365 ± 0.074 days. In Figure 7.10, I show the 2007 and 2009 photometry phased to the planet's orbital period, separately and together. While the 2007 data is not persuasive, the 2009 photometry shows a coherent signal. This signal persists when the two data sets are combined, and while this is at least in part due to the greater number of observations in the 2009 photometry which dominate the combined data, its persistence is somewhat encouraging.

Regardless of whether this variation persists beyond the duration of our 2009 observations, its period is too short to correspond to the stellar rotation period, as pointed out by [168]. Considering the approximate match between the orbital period of GJ 581b and the period of the variation, I tested the possibility that the variation is due to scattered light from the surface of the planet. Assuming a conservatively large radius of 0.7 R_{Jup} for GJ 581b,

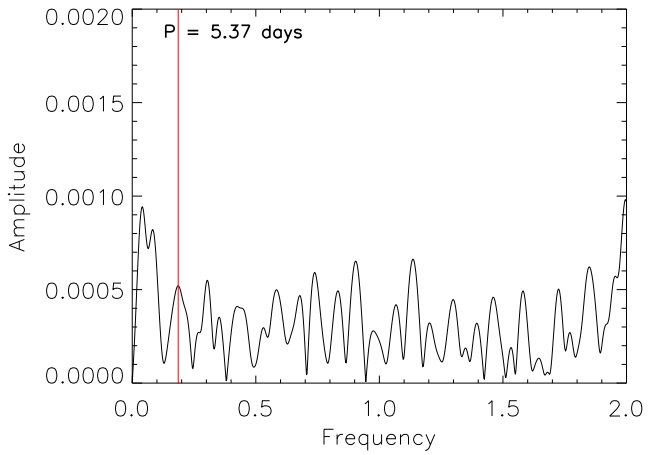

Figure 7.8: Amplitude spectrum (in units of relative flux) for the 2007 MOST photometry. The red line indicates the frequency corresponding to the orbital period of GJ 581b ($P = 5.37$).

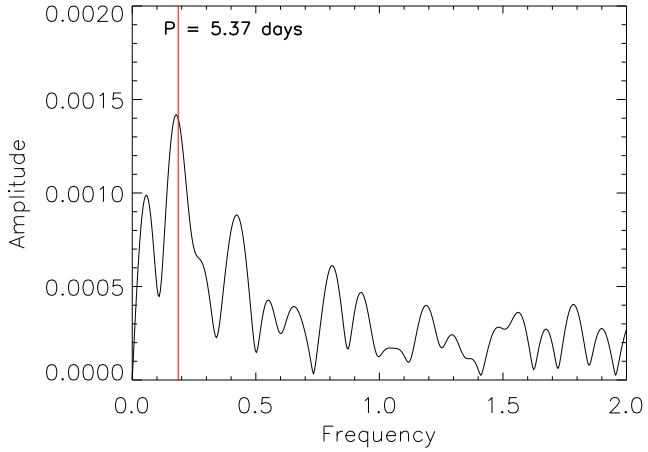

Figure 7.9: Amplitude spectrum (in units of relative flux) for the 2009 MOST photometry. The red line indicates the frequency corresponding to the orbital period of GJ 581b ($P = 5.37$).

$(R_P/a)^2$ gives a signal with a semi-amplitude of approximately 0.006% or 0.07 mmag. This is much smaller than the semi-amplitude of the variation I observe. Thus, the variation is not (solely) due to scattered light. Given the long-term activity trend in the host star (indicating the presence of a magnetic field) observed by [95, 96], another possible explanation is that the planet induces a spot on the stellar surface, which remains synchronized with the planet's orbital motion. The fact that the 2007 photometry does not clearly show a similar strength signal at the same period may be related to the magnetic activity cycle detected by [96].

The most convincing case of magnetic star-planet interactions so far is the Tau Bootis system. A periodicity close to the orbital period of the planetary companion was detected in MOST photometry of the system [258], indicating the possible existence of stellar spots and/or active regions induced by Tau Bootis b. Spectropolarimetric observations suggest the magnetic polarity reversal may be at least partly related to the presence of the planet ([70]; [79]). GJ 581b ($M_P \sin i = 0.05 M_{Jup}$; [86]) is less massive than Tau Bootis b ($M_P \sin i = 3.9 M_{Jup}$; [36]). However, the same can be said for the host stars ($M_\star = 0.3 M_\odot$ and $1.3 M_\odot$ for GJ 581 and Tau Bootis, respectively). Further, the b planet is also the largest in the GJ 581 system. Thus, star-planet interactions are a viable possibility but further monitoring of the GJ 581 system is necessary to better understand the nature of the photometric variability observed in the 2009 MOST photometry.

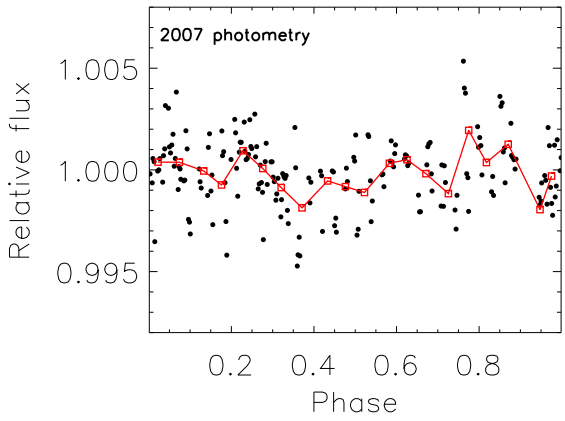
2007 photometry
Relative flux
1.005
1.000
0.995
0.2
0.4
0.6
0.8
Phase

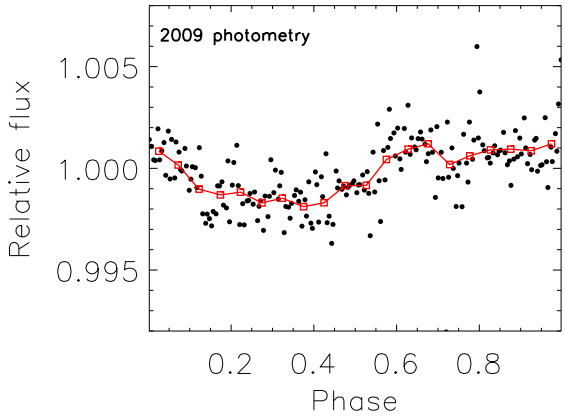
2009 photometry
Relative flux
1.005
1.000
0.995
0.2
0.4
0.6
0.8
Phase

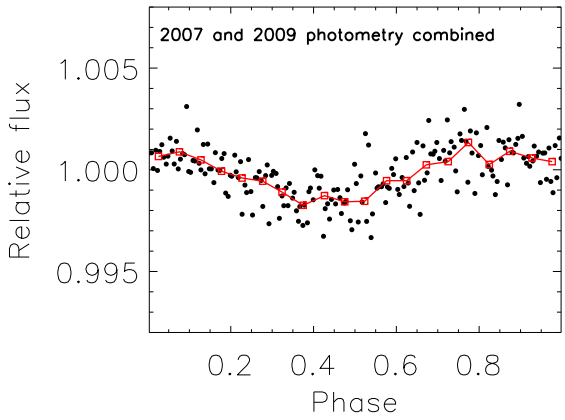
2007 and 2009 photometry combined
Relative flux
1.005
1.000
0.995
0.2
0.4
0.6
0.8
Phase

Figure 7.10: The 2007 and 2009 photometry phased individually (top and middle panels) and combined (bottom panel) at the orbital period of GJ 581b. The black solid points represent the photometry binned every 0.005 orbital phase. The red open squares correspond to the data averaged into 0.05 phase bins.

7.7 Conclusions

We observed GJ 581 with the MOST space telescope for a duration of 28 days in 2007 and 11.5 days in 2009. The 2007 photometry served to determine the level of variability of the host star, while the higher-cadence 2009 photometry was collected with the purpose of searching for transits of GJ 581e. I computed 3σ transit windows using both the Keplerian and circular ephemerides reported in [86]. To quantify the sensitivity of our data to super-Earth transits of various depths, I performed Monte Carlo simulations which involved injecting simulated transits into the light curve and attempting to recover them using a box-shaped model. The simulated transits have planetary radii between 1 and 4 $R_{\oplus}$ and impact parameter values ranging from 0.0 to 0.9.

My transit search returns no significant candidate. This is in agreement with the findings of [86]. However, our data allow a full search of the 3σ circular orbit transit window, and the 3σ Keplerian orbit window as well, ensuring that the potential transit of GJ 581e (if sufficiently deep) was not missed by our observations. I place lower limits on the planetary density of GJ 581e, if it transits. If it does not, then its mass likely lies between 1.84 $M_{\oplus}$ and 3.03 $M_{\oplus}$ (assuming orbital co-planarity and stability over more than a few Myr for planets b, c, d and e) as found by [168], but I cannot constrain its density.

I conclude that if GJ581e has an envelope dominated by water, helium and/or hydrogen (as appears to be the case for GJ 1214b and Kepler-11f), I rule out transits for most geometric configurations ($b \leq 0.6$). I cannot rule out transits for a higher density planet. Given the significance of this plane-

tary system, I recommend that RV measurements continue to be collected in order to constrain the eccentricity of the orbits more precisely. Subsequently, further photometric observations should be undertaken to conclusively determine whether GJ 581e, if it has a density higher than 2.5-3 g cm^{-3}, transits. A positive result would provide much needed insight into the bulk and atmospheric composition of this low-mass super-Earth.

Since the MOST photometry spans two orbital cycles of GJ 581b, I am able to rule out transits for all plausible compositions of this planet, but only for $b \lessapprox 0.4$. This leaves a significant range of unexplored transiting orbital configurations. I recommend the same course of action as for planet e: once the orbital parameters of the system are more tightly constrained, existing GJ 581 photometry combined with a few hours of new strategically acquired photometry should allow a definitive conclusion to be drawn regarding the presence or absence of GJ 581b transits.

Transit searches for GJ 581c and GJ 581d cannot be adequately carried out with the photometry presented in this Chapter, though I am able to place a very loose constraint on the size of GJ 581c in the form of an upper limit of $R_P = 2.3 R_\oplus$.

By combining the 2007 and 2009 photometry, I find that GJ 581 is stable to within 1%, indicating that it is likely a quiet M dwarf and supporting evidence of its advanced age ($\gtrsim 7$ Gyr; [215]). This increases the probability that life may occur and evolve on a planet in the habitable zone of the system. I attempt to verify the stellar rotation period of 94.2 days determined by [250], but our data set does not cover a sufficient portion of a rotation cycle of this length to allow any definite conclusions to be drawn. Finally, in the 2009 data set I detect a signal with a period of 5.586 ± 0.051 days, which is close to the orbital period of GJ 581b. A signal at the same period and of similar strength is not present in the 2007 photometry. I phase the two data sets at the period of the planet, individually and combined, and plot them in Figure 7.10. Though a signal is not apparent in the 2007 light curve, one is clearly visible in the 2009 and the combined light curves. Additional observations are needed to shed more light on the nature of this possible phase variation.

Chapter 8

Non-Detection of Previously Announced Transits of HD 97658b with MOST Photometry

8.1 Introduction

Known transiting super-Earth exoplanets around relatively bright ($V < 10$) stars are still scarce. The first to be announced was 55 Cnc e ([262]; [66]), and more recently transits of HD 97658b were reported by [111].

HD 97658b was discovered through Keck-HIRES radial velocity (RV) measurements [118]. This planet orbits a K1 dwarf ($V \sim 7.8$) with a period of 9.494 ± 0.005 days. Its low discovery mass ($m \sin i = 8.2 \pm 1.2$ $M_\oplus$; [118]) suggests a potential super-Earth.

The system was observed near mid-transit times predicted by the RV ephemeris with two Automated Photometric Telescopes (APTs; by [111]). Four partial transit windows were covered, each two planetary orbital cycles apart (since the orbital period is almost exactly 9.5 days, so if one window occurs at night for a given observing site, the next is during daytime). The individual light curves suggested the presence of transits, and the signal persisted when the photometry was phased with the period predicted from the RV ephemeris. Measurements obtained during nights predicted to be out of transit were consistent with a constant flux model, supporting the apparent transit detection. The feature identified as a transit had a depth

of 1470 ± 260 ppm, corresponding to a 2.93 ± 0.28 $R_\oplus$ planet with an orbital inclination of 90 ± 1°. These values would mean a relatively low density ($1.40^{+0.53}_{-0.36}$ g cm^{-3}) super-Earth.

Given the brightness of its host star, a transiting HD 97658b would be an ideal candidate for follow-up observations aiming to improve the accuracy and precision of the parameters of both the planet and its host star. In addition, these characteristics together with a potentially large atmospheric scale height would make it suitable for detailed atmospheric studies within reach of current space-based and large ground-based facilities, which would contribute to the much needed insight into the physical properties of super-Earth exoplanets.

Motivated by these stakes, we acquired space-based photometry of HD 97658 to better characterize the transit. In this chapter we report and analyze this photometry as well as 21 new Keck RV measurements of the star. Though the RVs continue to confirm the existence of the planet, the results of my photometric analysis show there is no transit with the depth and center times predicted by the [111] observations.

8.2 MOST Photometry

8.2.1 Observations

We used the MOST space telescope to obtain high-precision photometry of HD 97658. The star was observed contiguously in Direct Imaging mode on 2012 February 25 for 11.8 hours and on March 5-6 for 22.8 hours. The exposure time was 1.5 s, but the observations were stacked on board the satellite in groups of 21 for an integration time of 31.7 s per data point. The raw data was reduced using aperture photometry. During the February observations, several sections of the light curve (the gaps in the top panel of Figure 8.1) were removed due to high levels of cosmic ray background caused by the passage of the satellite through the South Atlantic Anomaly (SAA), resulting in a final time series containing 1157 points. The final March data set contains 2638 points. Both light curves are shown at the same scale in

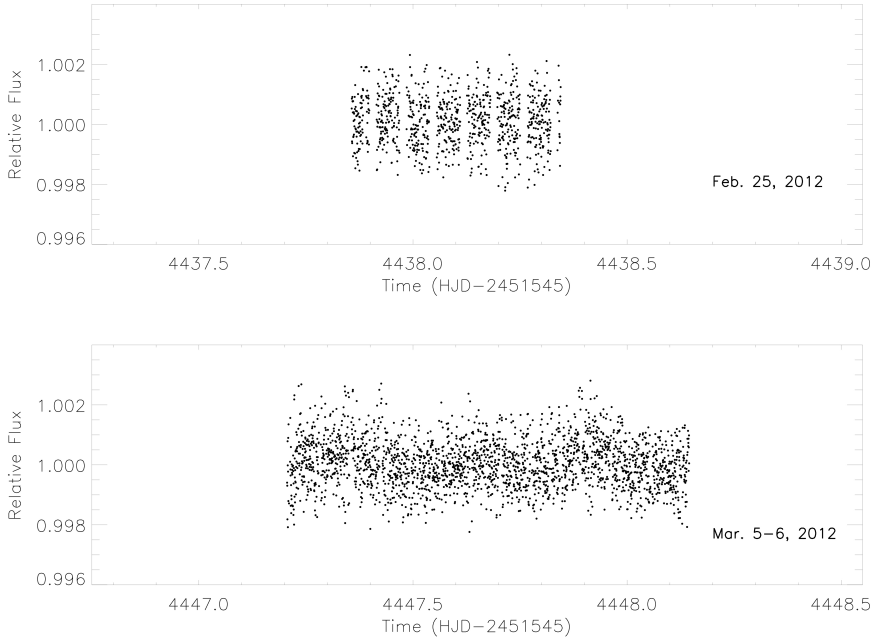

Figure 8.1: Reduced MOST photometry acquired during the predicted transit window of HD 97658b on February 25 (*top*) and March 5-6 (*bottom*). The gaps in the top light curve correspond to the data removed due to increased cosmic ray background (see Section 8.2.1 in the text for details).

Figure 8.1.

The first light curve spans nearly the full 3σ transit window for HD 97658b predicted using the ephemeris from [111] (see the top panel of Figure 8.2). The second light curve covers a significantly longer window as shown in the middle panel of Figure 8.2, virtually eliminating the possibility that the announced transit was missed.

8.2.2 Analysis

8.2.2.1 Henry et al. (2011) Transit Exclusion

From top to bottom, Figure 8.2 shows the binned photometry for the first, second and third data set, and the three time series phased with the orbital

period of HD 97658b and binned in phase are shown in the lowest panel. The bin size was chosen to obtain approximately 20-25 in-transit points. The planetary and stellar radii derived in [111] are 2.93 $R_\oplus$ and $0.70 R_\odot$, respectively. I used these values and non-linear limb darkening coefficients (c_1 =0.685, c_2 =-0.669, c_3 =1.405, c_4 =-0.567; A. Prsa, private communication) generated for the MOST bandpass assuming the stellar properties described in [111] to simulate the predicted transit signature in the MOST light curves. The transit models employed are those from [160]. I find an expected depth of 1920 ppm for a limb-darkened transit in the MOST bandpass.

The precision of the MOST photometry is amply sufficient to verify the existence of a transit with this depth (with $\geq 20\sigma$ significance), but such a transit is clearly absent from the data, as can be seen in Figure 8.2 within the 3σ transit window predicted from the ephemeris of [111]. The solid line corresponds to a planet with the predicted radius (R_P =2.93 $R_\oplus$). I also show predicted transit signatures for planetary radii of 2.43 $R_\oplus$ (water ice planet) and 1.87 $R_\oplus$ (silicate planet), both of which are excluded as well.

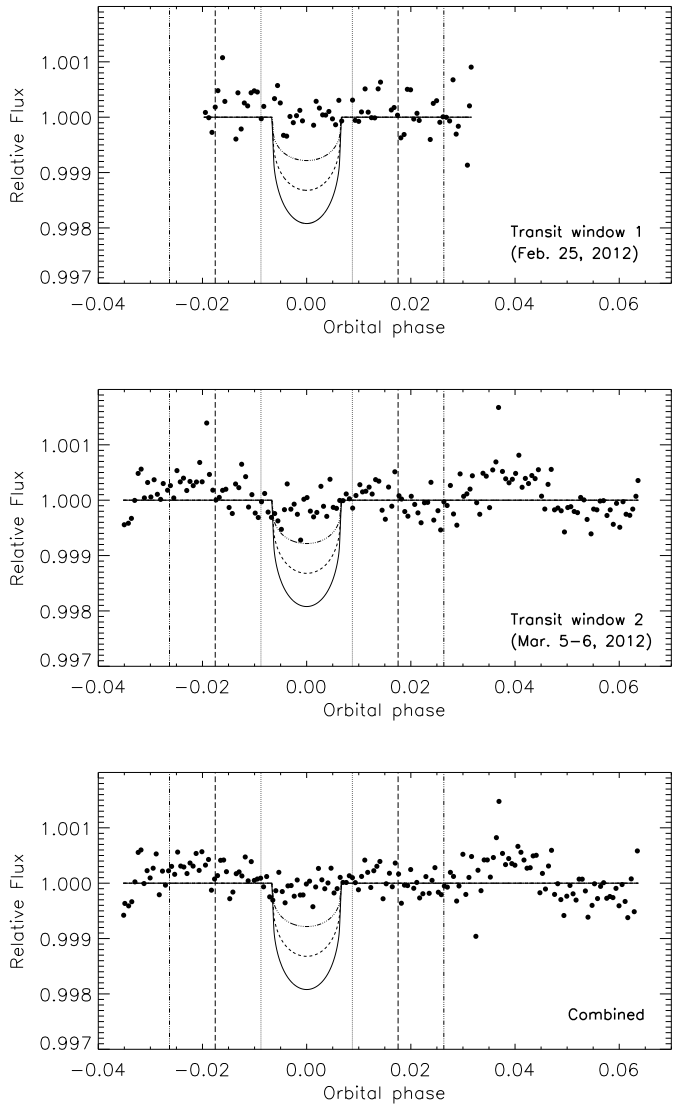

Figure 8.2: HD 97658 MOST photometry acquired on February 25 (*top*) and on March 5-6 (*middle*) and the combined data set (*bottom*) phased to the orbital period of the planet and averaged into 9 min phase bins. Transit models with edge-on configuration for a planet with R_P =2.93 $R_\oplus$ (solid line), 2.43 $R_\oplus$ (dashed line) and 1.87 $R_\oplus$ (dot-dashed line) are shown. The vertical dotted, dashed and dot-dashed lines enclose the 1σ, 2σ and 3σ transit windows (based on the [111] ephemeris), respectively.

8.3 Keck-HIRES Radial Velocity Measurements

Since the publication of [111], we have measured the radial velocity of HD 97658 for nearly one additional observing season (2011–2012) using Keck-HIRES. We used the same observing setup and modeling techniques as in [111]. The full set of 169 RVs and S_{HK} measurements of the $CaIIH\&K$ lines [122] from 2005–2012 are listed in Table A.3. The S_{HK} measurements (indicators of stellar activity) are not correlated with the RVs, consistent with a planetary origin for the RV variation. Twenty one measurements from late 2011 and early 2012 were recorded after the submission of [111]. The 148 RV measurements in common differ slightly here because of modest re-weighting of spectral segments in the Doppler analysis.

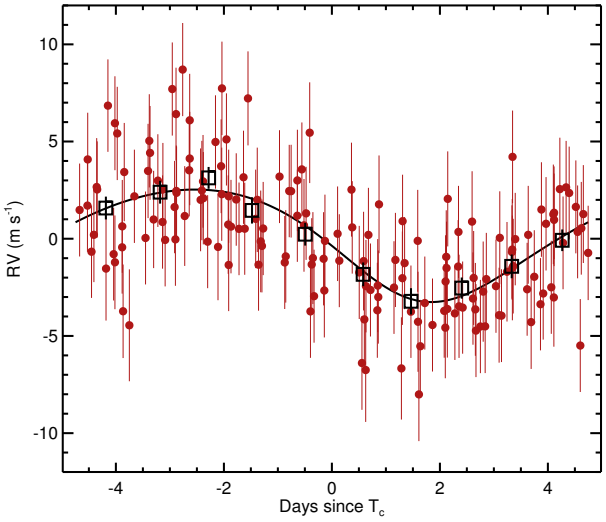

Figure 8.3: RV measurements (red filled circles) phased to the best-fit orbital period and phase of the Keplerian model (see Section 8.3). The best-fit model is overplotted as a black line. RV measurements are binned in 0.1 phase intervals (black open squares) and have an RMS to the model of 0.36 m s^{-1}.

The orbital solution derived from modeling the complete set of RVs in Table A.3 is consistent with the single planet models reported in [118] and

[111]. A Lomb-Scargle periodogram (Figure 8.4, top panel) of the RVs shows a prominent peak at 9.493 days, consistent with those models. We fit the RVs with the partially linearized, least-squares fitting procedure described in [269], giving the best-fit solution shown in Figure 8.3.

To quantify the best-fit orbital solution, we used a Markov Chain Monte Carlo (MCMC) algorithm [83, 84] and report the median, 84.1%, and 15.9% levels of the marginalized posterior distributions. The likelihood was taken to be $e^{-\chi^2/2}$, where χ^2 is the usual sum of the standardized residuals between the observed and calculated RVs. We adopted a Gregory eccentricity prior [99] and non-informative priors on other parameters. As in [111], we excluded three outliers that were $\geq$7 $\mathrm{m\,s^{-1}}$ from the best-fit model that has a residual RMS of 2.44 $\mathrm{m\,s^{-1}}$ with the remaining measurements. The ephemeris based on this analysis (and not including any timing constraints from photometry) is more precise than, but consistent with, the ephemeris reported in [118]. The planetary parameters resulting from this analysis are found in Table 8.1.

Table 8.1: RV-derived planetary properties for HD 97658b

Parameter	**Value**
P (days)	9.4930 ± 0.0021
T_0	JD 2455650.31 ± 0.30
e	$0.13\pm^{+0.089}_{-0.06}$
ω (deg)	120^{+95}_{-67}
K ($\mathrm{m\ s^{-1}}$)	2.86 ± 0.27
$M_p \sin i$ ($M_\oplus$)	7.7 ± 0.7
a (AU)	0.0797 ± 0.0007

The new RVs from 2011–2012 strengthen the evidence for a planet with an orbital period of ≈9.5 days, as shown visually in the bottom panel of Figure 8.4. The plot shows the Lomb-Scargle periodogram power [156, 208]

at the planet's orbital period rising nearly monotonically as additional measurements are added. False periodicities, such as those due to spots, are typically only briefly coherent and may reappear with slightly different periods.

8.4 Discussion

I do not find a transit of the planet HD 97658b with the parameters obtained by [111] in the MOST photometry. Our observations further allow us to rule out transits for planetary radii as small as 1.87 $R_{\oplus}$, corresponding to a density less than 6.92 g cm^{-3}, within the predicted 3σ transit window. Theoretically, it is still possible that the planet transits but is smaller and thus denser than these limits. For example, Kepler-10b [16] and Corot-7b [106, 149] are two known super-Earth exoplanets with densities above 7.0 g cm^{-3}. However, the parameters of such a transit would not match those derived by [111] and thus it could not account for the transit-like feature they observed.

I consider the possibility that the planet could have been previously transiting, but dynamical perturbations have caused its trajectory to drift off the disk of the star. However, this is very unlikely to have occurred after only 29 orbital cycles (since the last transit feature reported based on the APT photometry), especially since there is no sign of an additional companion in the radial velocities.

G. Henry made new APT observations of HD 97658 during the current 2012 observing season in an attempt to obtain improved light curves of the transit. On five separate nights between 18 January and 17 March, he was unable to find transits at the times predicted by [111]. Therefore, he withdrew the paper stating that "Additional observations are required to confirm or exclude transits of HD 97658b". The 2011 APT observations were acquired well past opposition of HD 97658 and so were made at relatively high air mass (up to 2.0) and differential air mass (up to 0.15). Thus, small changes in extinction or small errors in the applied extinction coefficients (as small as 0.01 mag/air mass) could result in systematic errors in the observed

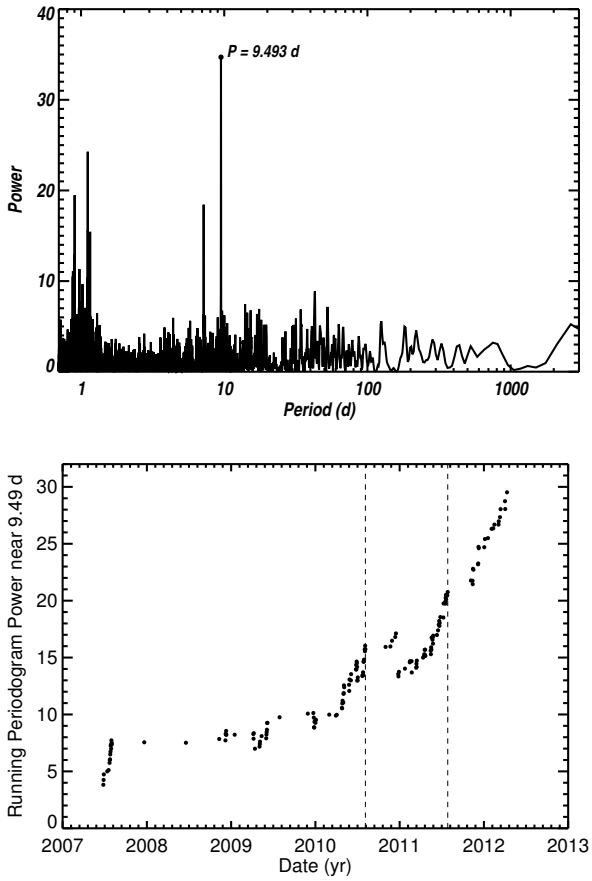

Figure 8.4: *Top*: Lomb-Scargle periodogram of all RV measurements of HD 97658. The tall peak near $P = 9.493$ d suggests a planet with that orbital period. *Bottom*: Running periodogram power near the orbital period of $P \approx 9.493$ days as a function of time. Each dot represents the maximum periodogram power near 9.493 days for the set of RVs up to that point in time. Only periods within 1% of the best-fit orbital period of HD 97658 b were used to compute each maximum periodogram power value. The nearly monotonic rise confirms that the periodic RV signal was present throughout the observations and points to a dynamical origin, supporting the existence of the planet. The dashed lines at 2010.7 and 2011.6 correspond to the cut-off dates for the RVs included in [118] and [111], respectively. The RVs gathered after [111] provide additional support for the planet.

differential magnitudes of 0.001 mag or so, matching the claimed depth of the transits.

I emphasize that the MOST photometry allows us to exclude transits to high confidence given the mid-transit time and uncertainties predicted from the [111] model based on both RV measurements and APT photometry. If I consider the ephemeris derived from the RV measurements alone, I can rule out transits only between 0.55 and 3.6σ of the predicted transit center, for planets with radii larger than 1.87 $R_{\oplus}$.

The results presented in this Chapter highlight the importance of independent follow-up observations, especially for a discovery as notable as that of a transiting super-Earth.

Chapter 9

New MOST Photometry of the 55 Cnc System

9.1 Introduction

The class of "super-Earth" exoplanets was not even being discussed seriously until 2005, because there are no analogues to them in our Solar System. Although planets of several Earth masses orbiting the pulsar PSR B1257+12 were reported in 1992 [264], based on radio pulse timing residuals, the case of planets existing in the wake of a supernova explosion is so different from the case of the Solar System that nobody drew direct comparisons in the literature. In 2005, an exoplanet of minimum mass 7.5 $M_{\oplus}$ was reported around the red dwarf Gliese 876 [194], based on the radial velocity (RV) signature. RV exoplanet surveys have since revealed a few dozen super-Earth candidates, with minimum masses below 10 $M_{\oplus}$ [119, 169]. Two transiting super-Earths were discovered before the *Kepler* telescope [27] was launched and unveiled hundreds of transiting super-Earth candidates.

While Kepler results continue to generate invaluable statistical studies of these exoplanets, very few of the candidates orbit stars sufficiently bright for follow-up. For many Kepler targets, even radial velocity measurements prove difficult. So far, there is one confirmed super-Earth discovered by Kepler (Kepler-21b; [121]) with a host star brighter than $V = 10$. Currently, the most straightforward method for increasing the number of known transiting super-Earths around bright stars is to monitor the host stars of RV-discovered exoplanets with minimum masses in the super-Earth regime. Indeed, RV measurements allow the derivation of the time in an exoplanet's

orbit when it is in inferior conjunction relative to the Earth, during which the system is then observed photometrically to search for a transit.

The planet 55 Cnc e is the first super-Earth whose transiting nature was discovered in this way. The host star of this system is a very bright ($V = 5.95$) G8 dwarf, and 55 Cnc e orbits it in only 0.74 days. The transit detection achieved with the MOST space telescope [262] was based on nearly contiguous photometry acquired over 12.3 days, while the subsequent report of a NASA Spitzer infrared space telescope detection [66] resulted from observations obtained during a 5-hour window which included one of the planet's predicted mid-transit times. This super-Earth's density ($\rho = 5.9^{+1.5}_{-1.1}$ g cm^{-3}; [262]) is lower than it should be in the case of a purely rocky planet [212], indicating that an atmosphere is likely present. However, interior models for such a small, irradiated planet do not support the existence of a substantial H/He envelope so its potential atmosphere is probably dominated by heavier elements.

Beyond the transit detection, both instruments have revealed further properties of this system and its innermost, transiting planet. The MOST light curve hinted at out-of-transit variations in phase with 55 Cnc e's orbit. The modulation, whose amplitude is too large to be due to reflected light from 55 Cnc e, may instead indicate the existence of tidal or magnetic interactions between the planet and its host star.

More recently, Spitzer was employed to observe the four occurrences of the planet's secondary eclipse at a wavelength of 4.5 μm, from which a brightness temperature of 2360 $\pm$ 300 K was determined [67]. If 55 Cnc e has a low albedo, this value lies between the temperature expected if the planet redistributes and reradiates heat uniformly, and the temperature corresponding to reradiation of incoming heat only from the side of the planet facing the star. In this context, the measured brightness temperature may suggest inefficient heat redistribution combined with a low albedo ($\lessapprox 0.5$ within the 1σ uncertainties). However, it is also possible that the 4.5 μm observations probe a deeper layer in the planet's atmosphere, thus potentially indicating the presence of a thermal inversion layer.

[59] obtained NASA InfraRed Telescope Facility (IRTF) spectroscopic

observations of 55 Cnc A and derived an improved flux density for the star, leading to a re-estimate of the Spitzer data-based brightness temperature of 55 Cnc e. The new lower temperature, 1950^{+260}_{-190} K, extends the range of possible albedo values to ~ 0.75, assuming the Spitzer observations probe the planet's upper atmospheric layers.

There are four other known planets in the 55 Cnc system [80]. Given that the innermost one transits the host star, there is a non-negligible probability that one or more of the others may transit as well. Their masses and orbital periods span wide ranges [63], thus forming an extrasolar multiple planet system that is moderately similar to our Solar System. 55 Cnc f holds particular interest because it spends about 74% of its eccentric orbit within the habitable zone of the system [255].

With the aims of searching for the secondary eclipse of 55 Cnc e and for transits of planets b, c, d and f, verifying whether the previously observed phase variations persist, and improving the physical and orbital parameters of this transiting super-Earth, we employed MOST to re-observe 55 Cnc A in 2012. In this Chapter I present, analyse and discuss the new photometry.

I describe the new MOST observations and their reduction in Section 9.2. The data analysis, results and discussion regarding 55 Cnc e are found in Section 9.3. In Sections 9.4, 9.5 and 9.6, I discuss the radius and composition, the phase modulation and the albedo of 55 Cnc e, respectively. In Section 9.7 I perform a search for transits of the other known planets in the system, and I conclude in Section 9.8

9.2 Observations and Data Reduction

55 Cnc was observed nearly continuously using the MOST space telescope for about 42 days from 2012 January 14 to February 25. The observations were acquired in Direct Imaging mode with an exposure time of 0.5 s per individual frame. The images were downloaded from the satellite in stacks of 80 frames, resulting in a total integration time of 40 s per data point. A modest readout overhead gives a cadence of 41.82 s.

A raw light curve was extracted from the images using aperture photom-

etry. Using two iterations, I clipped points that were more than 2σ from the medians of the x- and y-positions, or from the x, y and xy point spread function (PSF) widths. The clipped points correspond to images where either the pointing was sub-optimal or a cosmic ray hit within the subraster biased the centroiding algorithm. The positions and PSF widths of the remaining points are more consistent with each other and thus help minimise the effect of inter- and intra-pixel sensitivity variations on the photometry. This sigma clipping also improved the fit of the polynomials used to model the magnitudes as a function of position (described next), which would otherwise have been biased by the outliers. The following step consisted of fitting the magnitudes with a linear function of a seventh-order sky background polynomial and a first-order x-position polynomial. This choice was based on tests of several combinations of polynomial orders, and provides the best correction. Higher-order polynomials for the sky background were overfitting the data and introducing scatter in the light curve. The y-positions were not visibly correlated with the magnitudes so they were not used in the decorrelation procedure, again to avoid overfitting. The top panel of Figure 9.1 shows the light curve after these corrections have been applied.

The remaining routine correction is the filtering of straylight variations modulated with the satellite's orbit of 101.4 minutes. There are also longer-term variations in the light curve. In order to better normalise the sections corresponding to individual orbital cycles of 55 Cnc e, I divided the light curve into 21 sections approximately 2 days long each. The section duration was chosen to be sufficiently long so as not to affect any phase variations on the timescale of the planet's period. I folded each 2-day section at the satellite's orbital period and computed a running average of this phased data which represents the straylight modulation with MOST's orbital period over that 2-day period. I then removed the resulting waveform from that section of light curve. Once this was accomplished, I normalised each of the 21 sections of the light curve to the same median, and re-connected them. The last step consisted of rejecting as outliers any points that were more than 3σ from the median of the final light curve. The final light curve contains 62 337 points and is shown in the bottom panel of Figure 9.1.

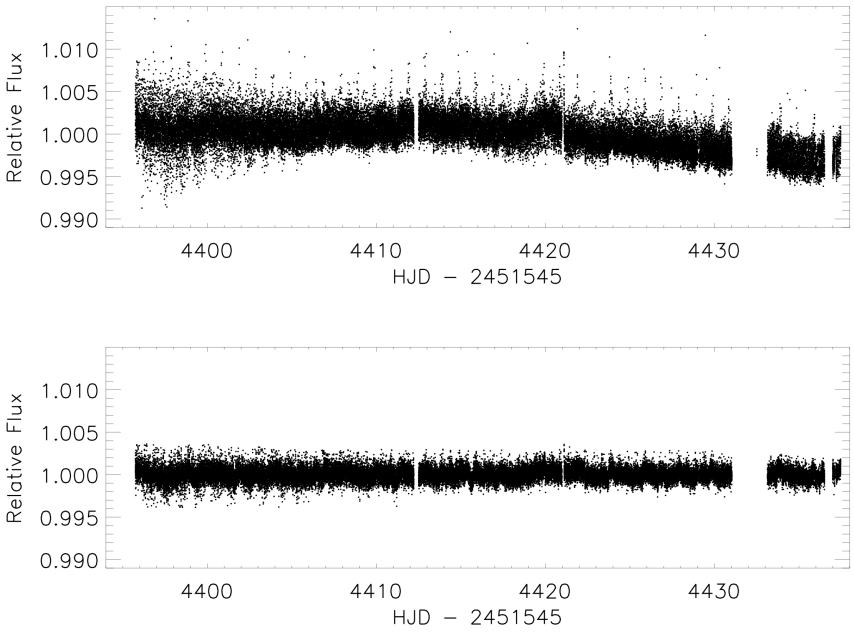

Figure 9.1: MOST 2012 photometry of 55 Cnc. *Top*: light curve after decorrelation of magnitudes from sky background and x and y pixel position. *Bottom*: same as top, but after the additional running average correction for straylight variations at the MOST orbital period.

9.3 Analysis of the Light Curve

I used a Markov Chain Monte Carlo (MCMC) algorithm to analyze the MOST photometry with the goals of improving the values of the transit and orbital parameters of 55 Cnc e and searching for the out-of-transit variation originally observed in 2011 [262] and the secondary eclipse. For model comparison, I use the odds ratio. The Bayesian Information Criterion (BIC) is used as an estimate of the marginal likelihood for each model [133]. The BIC is defined as follows

$$BIC = -2 \ln L + k \ln n, \tag{9.1}$$

where L is the maximum likelihood value, k is the number of free parameters and n is the number of data points. I assume the models have the same prior probability. The odds ratio was always determined relative to a constant flux model with no free parameters.

I fitted the following eight parameters: the orbital period (P), the mid-transit time ($T0$), the ratio of the planet to star radii ($R_P/R_\star$), the scaled semi-major axis ($a/R_\star$), the orbital inclination (i), the depth of the secondary eclipse (δ), the amplitude of the orbital phase modulation assuming a sinusoidal function with its minimum coinciding with the mid-transit time (α) and a normalisation factor corresponding to the flux just outside of transit (F_{norm}). I tried including quadratic limb-darkening coefficients in my fit, but found that this decreased the odds ratio by a factor of 100, suggesting the limb-darkening is not well constrained by our photometry. The best-fitted (median) values of the other parameters did not change significantly with the limb-darkening coefficients held fixed, but the uncertainties were slightly smaller. The limb-darkening coefficients were thus held fixed at $u_1 = 0.648$ and $u_2 = 0.117$, the MOST bandpass values for the grid point of stellar parameters ($T_{eff} = 5200$ K, $\log g = 4.5$, $[Fe/H] = 0.2$; A. Prsa, private communication) nearest to those of 55 Cnc.

Gaussian priors were used for P and $a/R_\star$. The mean and standard deviation values for these priors are the most recent known value and associated uncertainties for a particular parameter, respectively. The period prior, $P = 0.736540 \pm 0.000003$ days, was taken from [63] who derived this value from existing RV measurements of the system. The prior on $a/R_\star$ was obtained from the period prior, and the stellar mass and radius: $M_\star = 0.905 \pm 0.015 M_\odot$ and $R_\star = 0.943 \pm 0.010 R_\odot$ [255]. I used uniform priors for the remaining floating parameters.

The MCMC analysis consists of running 3 chains of 100 000 steps each. Convergence is verified for each fit parameter using the Gelman-Rubin statistic [93]. In each case, the ratio of the intrachain and interchain variances was within 1% of unity. The median of the corresponding posterior distribution is taken as the best-fit value for each parameter, while the uncertainties (1σ) are determined from the 34% confidence interval on either side of the

median.

First, I carried out a MCMC analysis on the new photometry alone (binned in 5-min bins for computational speed) in order to check for consistency with the results from the 2011 MOST data [262]. The results are shown in the first column of Table 9.1. The 2011 and 2012 light curves, phased at the period of 55 Cnc e and averaged in 5-min phase bins, are plotted in the top and middle panel of Figure 9.2, respectively, with the best-fitted model superimposed. Generally, the parameter values agree within the uncertainties, though only marginally for i and $a/R_\star$. In particular, my best-fitted orbital inclination value corresponds to an impact parameter of 0.29 rather than the 0.0 estimate of Winn et al. (2011). This larger value has implications for the transit probabilities of other planets in the system, if their orbits are co-planar with that of 55 Cnc e to within a few degrees. Although a slightly significant (inconsistent with 0.0 within the uncertainties) phase variation is found, it is not nearly as large as that found by Winn et al. (2011) in the 2011 photometry ($\alpha = 84 \pm 35$ ppm).

Next, the MCMC analysis was applied to the combined 2011 and 2012 light curves, binned in 5-min bins. The results of this analysis are listed in column 2 of Table 9.1. I note that I do not detect a significant non-zero secondary eclipse, either in the 2012 data set alone or in the combined data set. However, I am able to use the best-fitted value of δ and its uncertainties to place an upper limit on the depth of the secondary eclipse. The differing values of the amplitude of the orbital phase modulation between the 2011 and 2012 light curves leads to increased uncertainty in the measurement of δ when fitting the combined light curve. To further improve the limit on δ, I remove the respective best-fit phase variation for each of the 2011 and 2012 light curves, and re-run the MCMC algorithm without fitting for α. The ensuing parameter estimates are found in column 1 of Table 9.2. Finally, because fitting for the secondary eclipse does not improve the model likelihood, I ran the MCMC analysis as for column 2 of Table 9.1, but omitting this parameter. As expected, this led to improved uncertainties for the remaining parameters, as can be seen in column 2 of Table 9.2.

The odds ratios for the 8-parameter model used on the 2012 data alone,

the 8-parameter model used on the combined 2011 and 2012 data, and the 7-parameter (no δ) model are 4.9×10^{29}, 3.0×10^{49} and 3.0×10^{51}, respectively. Removing the δ from the free model parameters improves the odds ratio by two orders of magnitude, reinforcing the absence of a secondary eclipse detection.

For all parameters but δ the column of interest is therefore column 2 of Table 9.2 . The combined photometry phased at the best-fitted period of 55 Cnc e is shown in the bottom panel of Figure 9.2, with the best fit model based on the parameters listed in column 2 superimposed. The orbital period I obtain is more precise than any published values for 55 Cnc e, and it is in good agreement with those values, in particular that determined by Dawson & Fabrycky (2010) [63] from RV measurements assuming a circular orbit ($P = 0.736540 \pm 0.000003$ day). My estimates of $T0$, $R_p/R_\star$, $a/R_\star$ and i agree to within 1σ with those of Winn et al. (2011) [262].

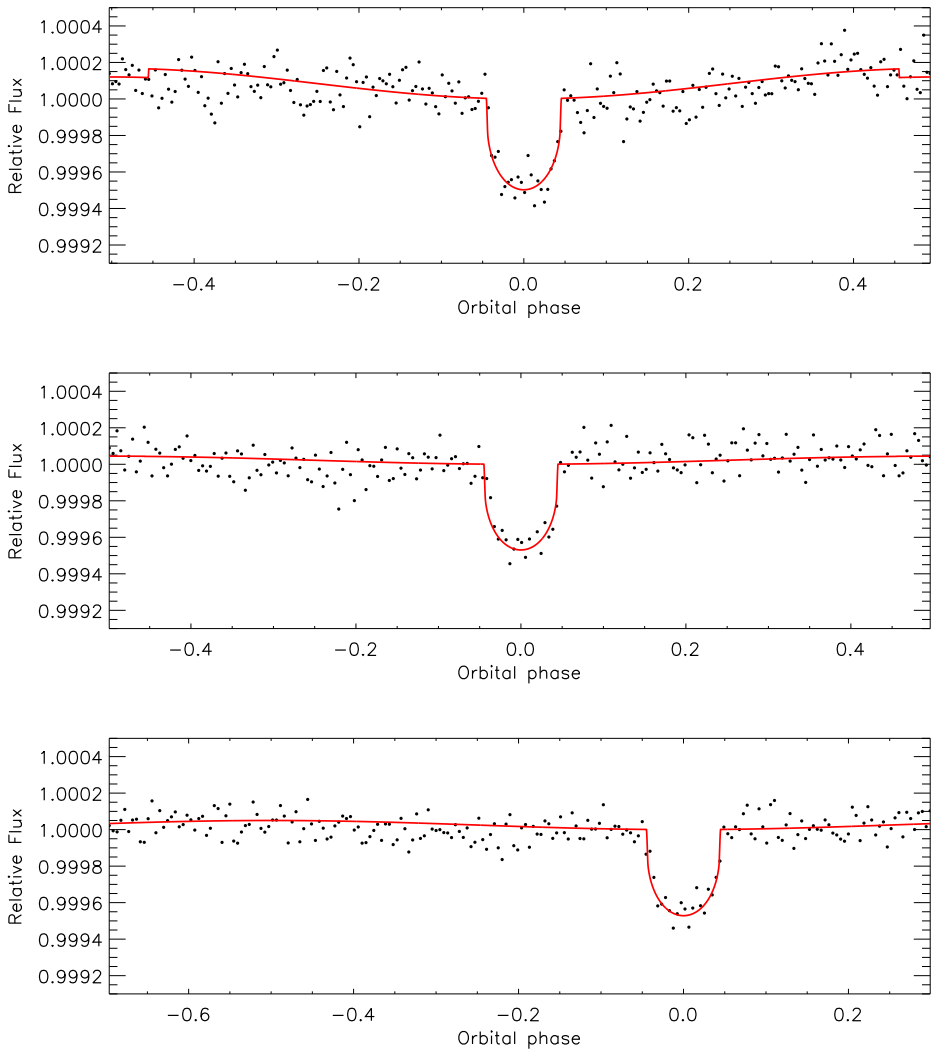

Figure 9.2: *Top:* 2011 photometry phased at the orbital period of 55 Cnc e and averaged in 5-min phase bins. The red line is the best-fitting transit model based on the value of Winn et al. (2011). *Middle:* 2012 photometry phased at the orbital period of 55 Cnc e and averaged in 5-min phase bins. The red line is the best-fitting transit model based on the values in column 1 of Table 9.1. *Bottom:* 2011 and 2012 photometry phased at the orbital period of 55 Cnc e and averaged in 5-min phase bins. The red line is the best-fitting transit model without a secondary eclipse parameter, based on the values in column 2 of Table 9.2. See Section 9.3 for details.

Table 9.1: Orbital and transit parameters for 55 Cnc e (1)

Parameter	**2012 photometry**	**2011+2012 photometry**
Measured parameters		
Period - P (days)	0.7365410 ± 0.0000030	$0.7365417^{+0.0000026}_{-0.0000027}$
Mid-transit time - T_0 [a] (BJD)	2455962.0697 ± 0.0015	$2455962.0692^{+0.0017}_{-0.0018}$
Planet-to-star radii ratio - $R_p/R_\star$	$0.01925^{+0.00092}_{-0.00093}$	$0.01931^{+0.00092}_{-0.00081}$
Transit depth - $(R_p/R_\star)^2$ (ppm)	371^{+35}_{-36}	373^{+36}_{-31}
Scaled semi-major axis - $a/R_\star$	$3.523^{+0.042}_{-0.041}$	3.524 ± 0.042
Orbital inclination - i (deg)	$85.4^{+2.8}_{-2.3}$	$85.5^{+2.6}_{-2.1}$
Amplitude of phase variation - α (ppm)	20^{+14}_{-15}	32^{+12}_{-13}
Eclipse depth - δ (ppm)	-1^{+27}_{-24}	1^{+20}_{-24}
Derived parameters		
Semi-major axis - a (AU)	$0.01545^{+0.00025}_{-0.00024}$	0.01545 ± 0.00025
Planetary radius - R_p ($R_\oplus$)	$1.979^{+0.097}_{-0.098}$	$1.984^{+0.097}_{-0.086}$

Table 9.2: Orbital and transit parameters for 55 Cnc e (2)

Parameter	**2011+2012 photometry (no phase variation)**	**2011+2012 photometry (no secondary eclipse)**
Measured parameters		
Period - P (days)	$0.7365418^{+0.0000027}_{-0.0000026}$	$\mathbf{0.7365417^{+0.0000025}_{-0.0000028}}$
Mid-transit time - T_0 [a] (BJD)	$2455962.0693^{+0.0017}_{-0.0018}$	$\mathbf{2455962.0697^{+0.0017}_{-0.0018}}$
Planet-to-star radii ratio - $R_p/R_\star$	$0.01929^{+0.00074}_{-0.00077}$	$\mathbf{0.01936^{+0.00079}_{-0.00075}}$
Transit depth - $(R_p/R_\star)^2$ (ppm)	372^{+29}_{-30}	$\mathbf{374^{+31}_{-29}}$
Scaled semi-major axis - $a/R_\star$	$3.524^{+0.041}_{-0.042}$	$\mathbf{3.523^{+0.042}_{-0.040}}$
Orbital inclination - i (deg)	$85.5^{+2.8}_{-2.0}$	$\mathbf{85.4^{+2.8}_{-2.1}}$
Amplitude of phase variation - α (ppm)	–	$\mathbf{34^{+12}_{-11}}$
Eclipse depth - δ (ppm)	-1^{+18}_{-22}	–
Derived parameters		
Semi-major axis - a (AU)	$0.01545^{+0.00024}_{-0.00025}$	$0.01545^{+0.00025}_{-0.00024}$
Planetary radius - R_p ($R_\oplus$)	$1.983^{+0.079}_{-0.082}$	$1.990^{+0.084}_{-0.080}$

9.4 The Radius and Composition of 55 Cnc e

Based on two 55 Cnc e transits observed with the Spitzer telescope, Gillon et al. (2012) find a radius for the planet of $2.20 \pm 0.12 R_{\oplus}$. Winn et al. (2011) [262] find $R_p = 2.00 \pm 0.14 R_{\oplus}$. My analysis of all the available MOST photometry of the system results in $R_p = 1.990^{+0.084}_{-0.080} R_{\oplus}$. My new estimate, and the MOST and Spitzer 2011 values agree with each other within their uncertainties. I have determined the radius of 55 Cnc e (as measured in a broad optical passband) with a precision of 4%. To calculate the mean density, I used the planetary mass derived by [66] ($M_p = 7.81 \pm 0.56 M_{\oplus}$), as I believe it results from a more robust fit which involves a joint MCMC analysis of RV and photometric measurements. The planetary mass value and in particular the associated uncertainties used in [262] were obtained using a least-squares and bootstrap approach. The resulting value of the mean density of $5.489^{+0.77}_{-0.80}$ g cm^{-3} is one of the best constrained for a super-Earth. The 1σ upper limit on its density just reaches a composition in the coreless silicate regime [75], but the span of the uncertainty lies mainly within the volatile envelope planets area of theoretical mass-radius models. In this context, a coreless silicate planet is one made entirely of silicate with no iron core and a "volatile" planet is a one with a rocky nucleus surrounded by an atmosphere of vaporised substances.

Gillon et al. (2012)[94] examined two plausible compositions which match their mass and radius measurements for 55 Cnc e: an envelope consisting of 0.1% H/He by mass and one consisting of 20% H_2O by mass. They argue, based on the calculations of Valencia et al. (2010) [241], that the former would evaporate within a few million years. A water vapour envelope would also be depleted over time, but only very slowly; the process is expected to take several billion years. Given the estimated age of the star (10.2 ± 2.5 Gyr [255]), a water vapour atmosphere is by far the more likely scenario. My value for the radius of 55 Cnc e is consistent with this model.

The precision with which I have measured the radius of 55 Cnc e is good enough that it may help constrain atmospheric properties by comparing my radius estimate made in visible light with those made in the infrared

or at other wavelengths. For example, if the planet has an atmosphere composed of 100% water vapor, then its radius at wavelengths near 2 μm should be about 5-6% larger than that measured in the MOST bandpass. This difference is very close to the uncertainties obtained in this analysis. It is worth noting that the planet's radius at infrared wavelengths (4.5 μm) obtained from the Spitzer transits is 2.20 ± 0.12, about 10% larger than the optical one at the 1-2σ level. [94] New observations of 55 Cnc by MOST (20 days scheduled in early 2013; see Chapter 10) are expected to reduce the uncertainty on the optically-determined radius sufficiently to test the 100% water envelope and perhaps other compositions more robustly.

9.5 Brightness Modulation at the Planetary Orbital Period

Winn et al. (2011) [262] suggested the phase modulation, too large to be explained by scattered light from the planet, could be attributed to star-exoplanet magnetic interaction. The orbital motion of the planet and the stellar rotation are unlikely to be synchronised because the stellar rotation period is estimated to be about 43 days [80], not surprising for an old G-type star, while the orbital period of 55 Cnc e is less than a day. Therefore, we do not expect interaction manifesting itself as a region of starspots and chromospheric activity fixed in the co-rotating frame of the star at the sub-planetary point, but rather a travelling wave moving through the photosphere and chromosphere of the star, but remaining close to the sub-planetary point. Such an effect can naturally be expected to have a changing amplitude, and in fact that is what Gillon et al. (2012) [94] found in their re-analysis of the MOST 2011 photometry. The amplitude of the brightness variation at the period of 55 Cnc e changed on a timescale of a couple of days.

When folding the entire 2012 MOST light curve, I do not find a phase variation at the period of 55 Cnc e as strong as that present in the 2011 light curve. This motivated us to inspect the 2012 data set more closely and, while always smaller than in the 2011 data, the amplitude of the phase variation

does appear to change over the course of the observations. Interestingly, if I fold in phase the photometry only between HJD 2455945 (near the end of the portion of the light curve more affected by stray light modulation; see the early part of the curve in Figure 9.1) and HJD 2455969, I find the amplitude of the phase variation (42 ± 16 ppm) is about twice what I find by folding the entire data set. This suggests that the amplitude of the variation varies on a timescale of weeks and perhaps even days, which is consistent with the finding of [94]. This section of the light curve (phased and binned as before) is shown in Figure 9.3, with the best-fitting model superimposed.

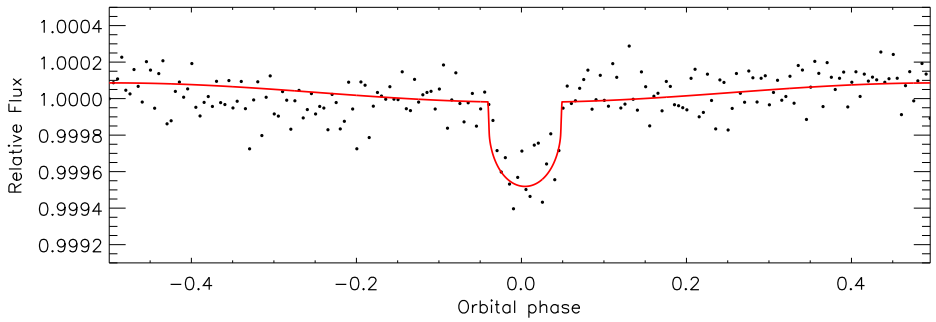

Figure 9.3: Approximately 2/3 of 2012 light curve phased at the orbital period of 55 Cnc e and averaged in 5-min phase bins. The red line is the best-fit transit model without a secondary eclipse parameter, and shows a more pronounced phase variation than when the complete 2012 light curve is used (see Section 9.5 for details).

9.6 Eclipse and Albedo Limits

I have not detected a secondary eclipse for 55 Cnc e. My best estimate for the depth of the eclipse is $\delta = -1^{+18}_{-22}$ ppm, and I can use this result to set an upper limit of $\delta \leq 17$ ppm.

I can express the ratio of the planet-to-star fluxes ($F_p/F_\star$) as a function of the geometric albedo A_g (the fraction of light reflected or scattered by the planet at optical wavelenghts), planetary radius and semi-major axis:

$$\frac{F_p}{F_\star} = A_g(\frac{R_p}{a})^2 \tag{9.2}$$

A geometric albedo of 1 (100% reflective) means the eclipse could be no deeper than 30 ppm. My upper limit on δ leads to an upper limit (1σ) of 0.57 on the geometric albedo.

To be able to use my measurement of the geometric albedo to constrain the planet's surface or atmospheric temperature and reflectivity, we should first convert it to a Bond albedo. The geometric albedo is defined as the brightness of a planet observed at opposition relative to that of a Lambertian disk surface with the same radius (a Lambertian surface is fully reflecting and diffusively scattering). The Bond albedo is the fraction of incident light scattered back into space in all directions and at all wavelengths. I can approximate the albedo of 55 Cnc e in the MOST bandpass as the albedo at all wavelengths at which the planet scatters light, since the intense heat the planet experiences likely means that thermal re-radiation dominates over scattered light at wavelengths redward of the MOST bandpass. However, without information on the planet's brightness variation throughout its orbit, it is difficult to determine the phase function. In the case of the MOST observations of 55 Cnc e, it would be difficult to disentangle such an effect from the larger variation phased with the planet's orbit observed in the photometry.

In Section 9.1, I mentioned that infrared measurements lead to an infrared brightness temperature for the planet of 1950^{+260}_{-190} K [59]. This value and its 1σ error bars include Bond albedo values between 0 and approximately 0.75 [59, 67]. For a Lambert sphere, the Bond albedo is $A_B = 1.5 * A_g$. This relation leads to an estimate of 0.85 for the 1σ upper limit on the Bond albedo of 55 Cnc e[20]. How does this limit compare with what we might expect for this planet? The presence of silicate clouds originating from the

[20]It should be noted that for larger particles ($\geq 1\mu$m), the Bond albedo can even be smaller than the geometric albedo, as the atmosphere of the planet becomes more back-scattering rather than isotropically scattering.

evaporating surface of the planet [227] has been hypothesised in cases of extreme temperatures ($\geq$ 1500 K) such as that measured (and expected) for 55 Cnc e. Such clouds would be highly reflective, with predicted Bond albedos of $\sim$0.55. With the planned MOST observations of 2013, we will enter the territory of signals corresponding to such high albedo values. A more precise measurement of the brightness temperature will also help further constrain the albedo and the overall atmospheric properties of this planet.

If the surface of 55 Cnc e is molten and assuming the absence of an atmosphere (still possible if the planet is coreless and made of pure rock) or the presence of a transmissive atmosphere, the planet's geometric albedo is predicted to be 0.6 [128]. With my measurement of the geometric albedo, I can exclude this model with 1σ confidence.

9.7 Search for Transits of Other Planets in the System

The 42 days covered by the 2012 MOST photometry opens up the possibility to detect transits of planets b, c, d and f in the 55 Cnc system. For this purpose, I obtained updated ephemerides for these planets (B.-O. Demory, private communication). Planet b would undergo a grazing transit with impact parameter of 1 if its orbital inclination i is 87.8 deg. Though more difficult to estimate because they are dominated by uncertain orbital eccentricities, the values of i necessary for $b = 1$ grazing transits for planets c, d and f are much closer to 90 deg. My value of $i = 85.4^{+2.8}_{-2.1}$ deg. for 55 Cnc e suggests that at least those three farthest planets are unlikely to transit if their orbital planes are perfectly aligned with that of 55 Cnc e. However, within our Solar System as well as outside it [78, 203], a planetary system is considered co-planar (thus suggesting the planets have formed within a flat protoplanetary disk and remain in their original orbits) if the orbits are within a few degrees of each other. In addition, it is also possible that one or more of the other four known 55 Cnc planets, in particular 55 Cnc f (which has an eccentric orbit) have orbits significantly inclined relative to that of

the innermost planet.

9.7.1 55 Cnc b

55 Cnc b has the second shortest orbital period ($P = 14.65176 \pm 0.00018$ days) of the known planets in the system, and the highest transit probability (next to 55 Cnc e). The MOST light curve covers three transit windows for this planet. I folded the photometry with the period of 55 Cnc b on $T0 = 2455964.494 \pm 0.045$ (HJD). For an edge-on transit, the predicted transit duration is 4.7 hours. The relevant section of the phased light curve is shown in Figure 9.4, both unbinned (top panel) and binned in 0.0005 phase bins (bottom panel). The dotted, dashed and solid vertical lines

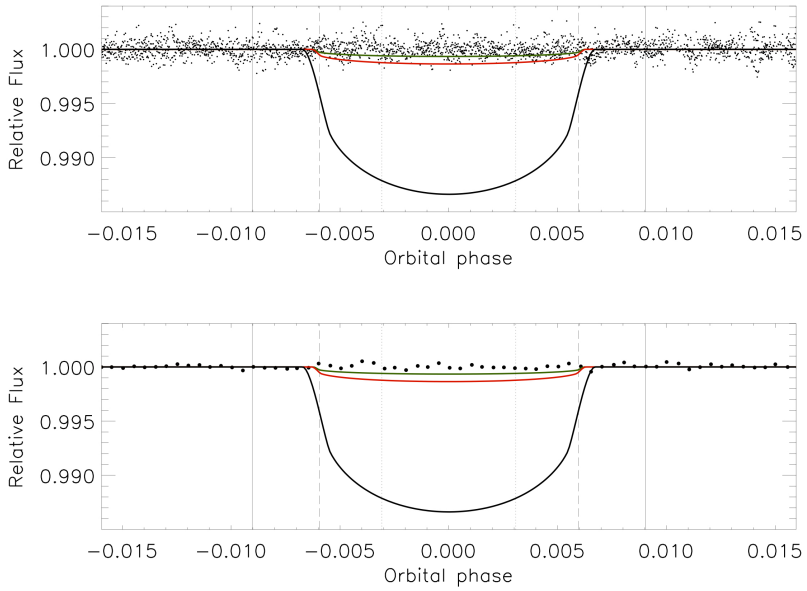

Figure 9.4: 2012 photometry phased at the orbital period of 55 Cnc b unbinned (top panel) and averaged in 10-min phase bins (bottom panel). The solid, dashed and dotted vertical bars enclose the 1, 2 and 3σ transit windows, respectively. The green, red and black lines correspond to a radius of 2.3, 3.3 and 10.4 $R_{\oplus}$, respectively. No transit is detected. See Section 9.7.1 for details.

are the 1, 2 and 3σ boundaries of the predicted transit window. Transit models representing different planetary radii are also shown. The green, red and black lines correspond to planets with radii of 0.21, 0.30 and 0.95 R_J, respectively. Given the minimum mass of 55 Cnc b ($M_P \sin i = 0.826 M_J$; [63]) the two shallowest transit models are associated with a pure iron planet and a silicate planet, respectively, which would make such a massive planet unrealistically dense. Indeed, planetary formation models [182, 189] and current exoplanet observations suggest 55 Cnc b is much more likely to be a gas giant. If 55 Cnc b has a composition similar to Jupiter, it would have a radius of 0.95 R_J (corresponding to the transit model shown as a black solid line in Figure 9.4) or even larger if the planet is inflated [24, 146].

Given the time sampling of the photometry, I can exclude transits of planet b even for a silicate composition for impact parameters up to 0.8. For realistic gas-giant-like compositions, I can even rule out grazing transits, as long as the impact parameter is smaller than 1.02, corresponding to about a third of the area of the planet's disk overlapping with the disk of the star.

9.7.2 55 Cnc c

The orbital period of 55 Cnc c ($P = 44.366 \pm 0.012$ days) is such that there is a high chance that our 42-day-long light curve includes one of its predicted transit windows. A predicted mid-transit time does fall within the MOST observations, though due to the interruptions described in Section 9.2 we do not have full phase coverage of the 3σ window. The MOST photometry spanning slightly more than this 3σ window is shown in Figure 9.5, with orbital phase 0.0 located at $T0 = 2455979.34 \pm 1.1$ (HJD). The unbinned light curve can be seen in the top panel, while the bottom panel shows the photometry binned in 0.0002 phase bins. The vertical bars enclose the transit window limits described in the previous paragraph. The green, red and black transit model lines correspond to planets with radii of 0.18, 0.28 and 0.76 R_J, respectively. The minimum mass of 55 Cnc c ($M_P \sin i = 0.171 M_J$; [63]) also probably places it in the gas giant regime, such that, if it transits, it is unlikely to result in transit depths as shallow as those indicated by the

green (pure iron composition) or red (pure silicate composition) model lines. The deepest transit model shown (black line) corresponds to a composition similar to that of Jupiter, which is expected based on formation models and observations of giant exoplanets with mass close to the minimum mass of 55 Cnc c.

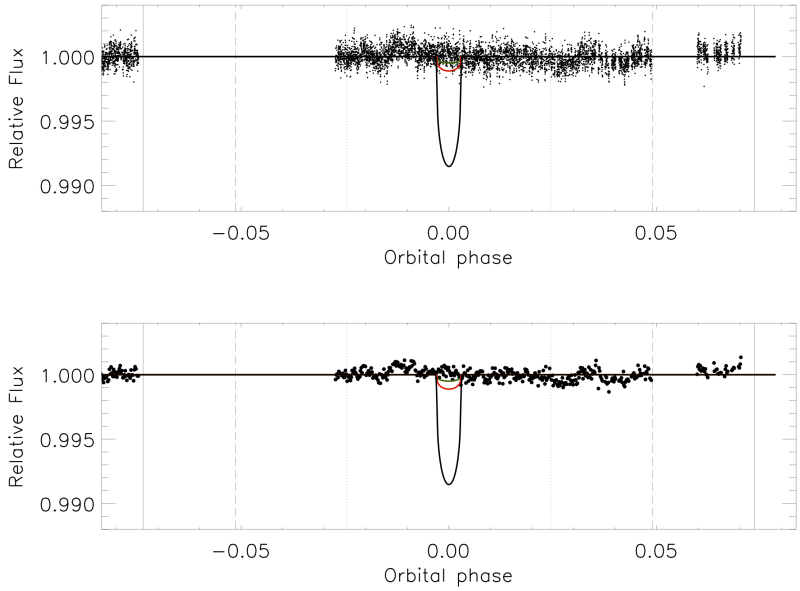

Figure 9.5: 2012 photometry phased at the orbital period of 55 Cnc c unbinned (top panel) and averaged in 13-min phase bins (bottom panel). The solid, dashed and dotted vertical bars enclose the 1, 2 and 3σ transit windows, respectively. The green, red and black lines correspond to a radius of 2.0, 3.0 and 8.3 $R_{\oplus}$, respectively. No transit is detected within the portions of the transit window covered by the MOST observations. See Section 9.7.1 for details).

I can rule out transits of a realistic planet only if they occur in the phase ranges $-1.1 - 2\sigma$, and $2.4 - 2.9\sigma$ relative to the predicted mid-transit time. Under these conditions, the time sampling is sufficient to exclude realistic transits with impact parameter up to about 1.0. Additional photometry to fully sample the transit window will be needed to complete the transit

search for 55 Cnc c.

9.7.3 55 Cnc d and f

55 Cnc d is in a much larger orbit, taking 5205 ± 69 days to complete a full revolution around the host star. It is also the most massive of the known planets in the system ($M_P \sin i = 3.83 M_J$; [63]). The large uncertainties on its orbital parameters lead to a very wide transit window. The predicted mid-transit time nearest to the MOST observations is $T0 = 2456473 \pm 75$ (HJD). Not only does it not occur within the timespan of the MOST photometry, but its uncertainty alone is longer than the duration of the 2012 observations.

55 Cnc f has an orbital period of 260.82 ± 0.72 days and the largest orbital eccentricity ($e = 0.25 \pm 0.06$) of the five known planets. It spends about 74% of its orbit within the habitable zone of the star [255]. Though its minimum mass of 0.150 M_J [63] suggests it is likely a gas giant, the possibility that it could host a rocky moon cannot be excluded. This makes the planet an attractive candidate for follow-up studies, the feasibility of which would increase significantly if it was found to transit. Unfortunately, the MOST photometry does not include a transit window of 55 Cnc f. The nearest mid-transit time is $T0 = 2455759 \pm 14$ (HJD), about one month after the end of the observing run.

9.8 Summary

We have acquired 42 days of new MOST photometry of 55 Cnc. After a careful reduction, I have used these data for several different types of studies. The new photometry has allowed the radius of 55 Cnc e ($R_p = 1.990 R_\oplus$) to be determined to within 4%. My result agrees with the hypothesis of Gillon et al. (2012) that the planet likely has an envelope of high mean molecular weight volatiles such as water vapour and/or silicate clouds. I find that the phase variation observed in the 2011 MOST photometry persists but with an amplitude at most half of that measured in the discovery photometry. The

data also allows us to place a limit on the depth of the secondary eclipse, and thus on the geometric albedo of 55 Cnc e of 0.57. This leads to an upper limit of 0.85 on the Bond albedo of the planet. With this value, I can exclude a highly reflective molten surface with 1σ confidence. MOST photometry to be acquired in winter 2013 will be bring this value into the realm of reflective silicate clouds, allowing to place more constraining limits on the existence of such clouds in the atmosphere of 55 Cnc e.

The long timespan of the 2012 photometry has allowed us to carry out a search for transits of planets b and c. I am able to exclude a transit for 55 Cnc b for all transiting configurations except a barely grazing transit ($b < 1.02$). The photometry does provide full coverage of the wide 3σ predicted transit window for 55 Cnc c, but within the portions during which we have acquired observations I do not detect transits for realistic planetary compositions for $b < 1.0$. Finally, the photometry does not cover predicted transit windows for planets d and f.

Chapter 10

Conclusions and Future Work

10.1 Summary of Findings

In this thesis, I have carried out a search for transits of known exoplanets, in particular super-Earths, orbiting bright stars.

Chapters 4, 7, 8 and 9 present results from the super-Earth transit search and characterisation (where three systems merit their own chapters), and Chapter 6 presents the analysis of a system hosting a massive exoplanet whose orbital period is of intermediate duration.

In those cases for which the MOST photometry provides significant coverage of the predicted transit windows but no detection was made (**BD 082823b, HD 115617b, HD 125595b, HD 125612c** and **HD 156668b**), I have placed upper limits on the radii of these super-Earth candidates; i.e., the largest size allowed by the data if the planet were indeed transiting its host star. For the first three, I can exclude transits for planets with silicate composition or less dense.

My analysis of the **HD 192263** radial velocities and ground-based photometry spanning over a decade has excluded a transit of the only known planet in the system for most transiting orbital configurations ($b < 0.86$). In addition, I have characterised the host star's variability with sufficient precision to show that there is no evidence of the previously suggested star-planet interactions in the system. Finally, the long-term photometry indicates the presence of a possible ∼8-year stellar activity cycle.

Using MOST photometry of the oft-studied **GJ 581** system, I have been

able to rule out transits for the innermost planet (GJ 581e) if it is less dense than a water-ice planet. The observations also hint at stellar variability with a period close to that of the next known planet in the system, GJ 581b. The precise GJ 581 MOST photometry shows that the host star is stable to within less than 1% on the few-week timescales covered by the data.

Carried out in an attempt to confirm the claimed transiting nature and refine the ephemeris of **HD 97658b**, my analysis of MOST photometry of this system revealed instead no transit signature with the parameters determined by [111]. I was further able to rule out transits corresponding to planets with radii as small as 1.87 $R_{\oplus}$ within the transit window predicted by [111].

Using a new data set containing 42 days of MOST photometric observations of the **55 Cnc** system, I have reduced the uncertainty on the radius of 55 Cnc e to ± 4%. I found that the phase variation observed in the 2011 photometry is suppressed but remains detectable. The limit I place on the depth of a secondary eclipse yields an upper limit of 0.57 on the geometric albedo, and thus an upper limit of 0.85 on the Bond albedo of the planet (under the assumption that the surface of 55 Cnc e has the same properties as that of a Lambert sphere, which is both reasonable and conservative under the circumstances, considering that we have no other information about the planet's scattering properties). Finally, I have performed a search for transits of other planets in the system, and excluded all but a barely grazing transit for 55 Cnc b. Similar limits were found for a transit of 55 Cnc c as well, though more observations will be necessary to fully cover the 3σ transit window.

10.2 Significance of the Results

A transiting exoplanet opens the door to a variety of studies of its own physical and atmospheric properties as well as the properties of its host star. However, the brightness of the star also plays an important role: the brighter the star, the more detailed the follow-up observations. While the

Kepler photometric space mission is sensitive to transits of small planets, the host stars are generally too faint for detailed spectroscopic and other follow-up observations requiring a high signal-to-noise ratio. Ground-based photometric transit searches monitor more stars sufficiently bright for follow-up studies, but are limited in finding shallow transits (as those of small planets around Sun-like stars are bound to be) by atmospheric scintillation noise. They also tend not to discover transiting exoplanets in intermediate or long orbits because of limited time sampling and low transit probabilities. So far, the longest orbital period known for such a planet is about 11 days.

Although exoplanets with intermediate and long orbital periods have low *a priori* transit probabilities, carrying out photometric monitoring of known RV planets still has better chances of finding transits of planets in this second category than a blind survey would. This is the goal of the TERMS project. For small close-in planets the transit probability tends to be larger, but their likely shallow transits means that they very rarely show up in ground-based survey data. Therefore, a systematic transit search of known RV-detected super-Earth candidates is arguably the best method to find them, though it is worth noting that the RV confirmation of such low-mass planets can be lengthy as it requires a large number of measurements. The MOST photometric space mission is sensitive to such shallow transits and can obtain continuous coverage over relatively long time windows, allowing for the large uncertainties in the orbital ephemeris that are generally associated with these low-mass planets. Successful detections will bring in a wealth of valuable information about the nature of planets in these two as yet sparsely populated areas of parameter space.

The most frequent outcome of such searches will be null results, either in the form of transit exclusions or upper limits on the size of a planet if it transits. It is crucial to report and publish null results (transit exclusions) for planets in both these categories, because the necessary measurements and results are often challenging to obtain. For longer-period planets, the predicted transit window occurs once every few weeks, months or even years. For planets of small radius, it is necessary to use space-based telescopes to achieve the necessary sensitivity, but observing time on those satellites is

more precious than on many ground-based facilities. In both cases, numerous RV measurements are needed to reduce the size of the transit window to a manageable size of less than ∼30 hours. Therefore, even if no transit is detected, it is important to report the null result to the community in order to avoid unnecessarily redundant observations, and to possibly plan alternate detection strategies.

The exclusion of a transit of **HD 192263b** for most possible transiting configurations is important on its own for the reasons described above. However, in that analysis I have also shown how this can sometimes be accomplished with existing low-cadence, long-term data, especially when the transit signature is expected to be large relative to the scatter of the data, and that dedicated monitoring of the transit window is therefore not always necessary. Yet perhaps the most interesting conclusion of this project is that the similar values of the stellar rotation period and planetary orbital period are in fact distinct, and that this newly found lack of evidence for the existence of star-planet interactions in the system suggests the similarity between those two values may simply be coincidental [206]. Finally, the evidence I find for a possible ∼8-year activity cycle will motivate continuing monitoring of this star over the next decade in order to verify this hypothesis.

The transit window coverage and limits I have set on the presence of transits of several super-Earth candidates in Chapter 4 are important when deciding which of these should be re-observed, or how much of their transit windows remains to be covered for a more complete exclusion (or a possible detection). This is even more crucial as only space-based instruments and large ground-based telescopes can be used to this end, and observing time on both kinds of facilities is difficult to obtain and must be carefully justified. In particular, I am a Co-Investigator on a recently submitted Spitzer telescope proposal, one aim of which is to continue the transit search for newly announced super-Earth candidates as well as one of the targets in my thesis survey (HD 96700) for which the available MOST photometry are not sufficient for a thorough transit search due to incomplete phase coverage of the transit window.

This super-Earth transit search as a whole also provides an extremely useful assessment of how sensitive MOST is to shallow transits, in particular to those of planets orbiting fainter stars. My analysis of the **GJ 581** photometry, complete with a transit injection and recovery test, has led to valuable limits on the photometric precision of stars fainter than $V \approx 10$. More and more surveys and transit searches of RV-detected exoplanets target M dwarfs like GJ 581 because the transit of a super-Earth around such a star will be deeper thanks to these stars' smaller radii ($R_\star \approx 0.1$–$0.6\ R_\odot$). GJ 581 is a "poster child" of these systems, as it is known to host three planets with minimum masses in the super-Earth regime, at least one of which is believed to reside in the system's habitable zone. My work on this system has contributed to placing limits on transits of planet e (one of the super-Earths) and excluding transits for most transiting configurations of planet b. While both results are in agreement with previous work [86, 157], their results are based on partial coverage of the planets' transit windows. The contiguous MOST observations spanning at least two orbits of these planets allow me to extend these conclusions to their full respective transit windows. The sensitivity limits I have determined for the GJ 581 photometry are also useful when estimating the expected outcome of future super-Earth transit searches with MOST, if the host star is close to the faint end of the brightness range for which MOST was designed. Lastly, if the tentative detection of stellar variability with a period similar to that of GJ581b is confirmed, the result would be a valuable contribution to the study of star-planet interactions.

One of the main goals of the **HD 97658b** MOST observations was to confirm the marginal transit detection which was based on the ground-based discovery data. If confirmed, the results based on the MOST data would then be used to better determine the size of this apparent super-Earth, and update the mid-transit time and associated uncertainties. The latter aspect was particularly important in the short-term, since it would have lent support to a then recently submitted Hubble Space Telescope proposal to observe this system, by promising to provide an uncertainty of at most 10 minutes on the mid-transit time which would have facilitated the scheduling

of the observations. It became clear that the discovery result was believed by many in the community even before confirmation with a more sensitive telescope could take place, and that at least a few other groups had also submitted follow-up studies observing proposals for space and large ground-based observatories. Unfortunately, the MOST photometry failed to confirm the transit after monitoring two of its predicted transit windows. I and collaborators wrote a paper announcing this null result, and made it available on the arxiv at the same time as I submitted it to a refereed journal, within less than two months of acquiring the data. This finding and its swift release to the exoplanet community have prevented several proposals from being unnecessarily evaluated and the proposed superfluous observations from taking up valuable telescope time.

The transiting super-Earth **55 Cnc e** is an extremely exciting discovery in many ways, and the potential to answer many of the questions it raises is there, mostly thanks to the brightness of its host star. Perhaps the foremost questions are how long the planet has been in such a close orbit and how it survives there, but also what is this planet like? The results obtained from the analysis of the 2012 MOST photometry of the system has brought us closer to understanding this planet. First, I confirm and measure the $\sim$2 $R_{\oplus}$ radius of the planet with unprecedented precision. This precision is already sufficient, for example, to compare the transit depth with that measured at a IR wavelength with similar precision, and search for the presence of an infrared-absorbing envelope representing 10% or more of the planet's radius. Additional photometry will constrain the planetary radius even further. The continuing presence of a phase variation (though suppressed relative to that observed in the 2011 data) at the period of 55 Cnc e will invite the development of possible models of tidal and/or magnetic star-planet interaction for this pair. Finally, the estimate of the upper limit on the Bond albedo, though not yet more constraining than the Spitzer measurement of the brightness temperature [59, 67] under the assumption of an atmosphere surrounding the planet, should allow us to enter that realm with the acquisition of the next set of MOST observations. Nevertheless, by excluding (to 1σ) the high albedo expected from a molten surface (arguably

the only state the surface could be in at temperatures greater than 1500 K), these results lend additional support to the volatile envelope hypothesis.

Another important way to constrain the atmospheric properties of 55 Cnc e is through photometric observations at multiple wavelengths. For most currently known transiting super-Earths, we will have to wait for the launch of JWST or other dedicated spectroscopic missions such as Finesse or Echo before observing their atmospheres at non-optical wavelengths. Thanks to the brightness of its host star, 55 Cnc e is one for which such observations have already successfully begun using Spitzer [67] and the HST (Ehrenreich et al., in prep). As those results combine with MOST's contribution at optical wavelengths, we should have a more clear picture of the nature of this extremely interesting planet in the very near future.

10.3 Future Research

One of the most common statements in the conclusion of a research report is something to the effect of "more data are needed." In the case of the super-Earth candidate transit search, that is absolutely true. The search will continue.

I plan to select the most promising targets accessible to MOST from a recently released list of RV-detected exoplanets with minimum masses in the super-Earth regime. As in this thesis, those with short orbital periods ($P \leq 10$ days) and the most precisely determined orbital parameters will be favored. I will also propose to the MOST Science Team to re-observe those for which I have not been able to obtain sufficient coverage of the transit window, especially if their updated orbital parameters have significantly narrowed the predicted transit window duration.

If the Spitzer proposal mentioned in the Section 10.2 is granted time, I will collaborate with the PI (Michaël Gillon) and other Co-Is to ensure the transit searches carried out with the two instruments are not redundant but rather complementary. For example, very bright stars ($V < 6$) are more difficult to schedule with Spitzer because the required short exposures must be taken in a special mode which necessitates significant human interven-

tion. Such targets have not been included in the proposal, but they are perfect for the MOST Fabry Imaging mode, which in addition leads to significantly better photometric precision relative to observations acquired in Direct Imaging mode.

Since the HD 97658b transits announced by Henry et al. (2011) [111] proved to be spurious, I can now continue the transit search for this planet as for any other super-Earth candidate, with the exception that a fraction of the RV-derived transit window (between 0.55 and 3.6σ) has already been monitored as part of the analysis presented in Chapter 8. In April 2012, a third light curve of the HD 97658 system was acquired with MOST with the purpose of completing the phase coverage of HD 97658b's RV-derived transit window. These observations, shown in Figure 10.1, cover the transit window between approximately -3.7 and 1.5σ. A shallow dip can be seen at HJD of about 2456029.7 or approximately 1.1σ before the predicted mid-transit time. The depth of this possible candidate transit signal is $\sim$0.1%, corresponding to a planetary radius of $\sim$2.5 $R_{\oplus}$. Unfortunately, it has not been possible to obtain sufficient additional MOST photometry of the system before it left the satellite's CVZ in order to verify the repeatability of this possible candidate signal. The star will become observable again in January 2013, at which time we will be able to acquire new observations and confirm or reject a transit as the origin of this signal.

Another possible project is to monitor the HD 192263 system with MOST. The star is well within the CVZ of the telescope, allowing for several weeks of observations. The goal of this endeavor is to better characterise the photometric variations due to spots on the star's surface, and more precisely determine the stellar rotation period. MOST observations may also allow us to search for the previously suggested presence of active regions on opposite hemispheres of the star.

The transiting super-Earth 55 Cnc e has attracted an enormous amount of attention, and there are current efforts aiming at characterising its likely evaporating atmosphere. I intend to remain involved with some of these projects, and also to initiate one or two new ones. One idea is to search for evidence of sodium in the atmosphere of 55 Cnc e by observing it in the

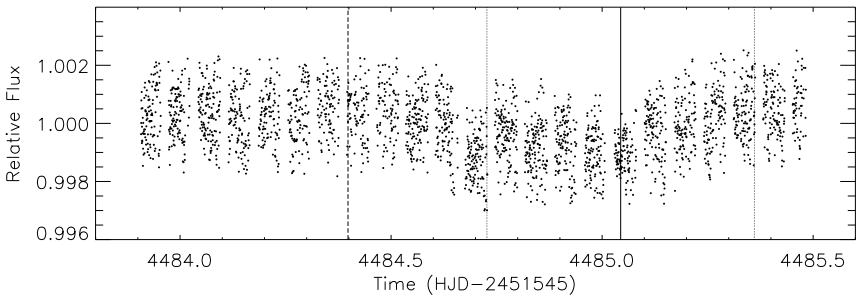

Figure 10.1: HD 97658 MOST photometry acquired on April 11-12. The solid vertical line indicate the predicted mid-transit time (based on the RVs only). The vertical dotted and dashed lines correspond to the 1 and 2σ transit window boundaries respectively. Note that the right-hand side 2σ limit lies outside the timespan of this light curve.

ultraviolet using the Wide Field Camera 3 on the Hubble Space Telescope. But perhaps the most straightforward contribution I can bring is a detection of or an improvement on the limit on the secondary eclipse of 55 Cnc e (and hence on its albedo), which will be possible with the new photometry MOST is scheduled to acquire for this system in winter 2013. An estimate of the albedo would help constrain the composition and structure of the planet's atmosphere. For example, a high albedo would suggest that the atmosphere contains species which scatter light or high clouds, while a low albedo would point to the presence of light-absorbing species such as sodium and potassium.

Finally, the out-of-transit variation with a period matching that of 55 Cnc e observed in the 2011 MOST photometry motivated a Canada-France-Hawaii-Telescope proposal to acquire spectropolarimetric data in order to to measure the magnetic field of the host star and search for evidence between it and the magnetosphere (if any) of its innermost planet.

10.3.1 Spectropolarimetry of 55 Cnc

The CFHT proposal, of which I am the Principal Investigator, was successful. We obtained ten spectropolarimetric observations of the star. Six of the observations sample a full orbital cycle of 55 Cnc e at approximately equal intervals, while the remaining four were acquired in pairs during a transit and a secondary eclipse of the planet, respectively. These data were obtained over the period during which MOST was also observing the system, in order to support the eventual modelling. I will analyse the spectropolarimetry in collaboration with Jaymie Matthews and other experts in this area.

Such measurements have already been performed for giant exoplanets. In the case of tau Bootis, the spectropolarimetric measurements showed that the chromosphere of the star is locked with the orbital period of its hot Jupiter [70]. MOST observations of the system also found a brightness variation at the period of the planet, lending further support to the existence of star-planet interactions in that system [258].

Though the amplitude of the out-of-transit variation observed for 55 Cnc e appears smaller in the 2012 data, it is difficult to speculate on what the spectropolarimetric analysis may reveal. Evidence of star-planet interaction in this system would constitute the first (indirect) detection of a magnetic field in a super-Earth. Whether or not we find such evidence, this study will be the first of its kind for a super-Earth and will set a useful precedent for future applications of spectropolarimetry of exoplanetary systems.

Bibliography

[1] F. Abe, D. P. Bennett, I. A. Bond, S. Eguchi, Y. Furuta, J. B. Hearnshaw, K. Kamiya, P. M. Kilmartin, Y. Kurata, K. Masuda, Y. Matsubara, Y. Muraki, S. Noda, K. Okajima, A. Rakich, N. J. Rattenbury, T. Sako, T. Sekiguchi, D. J. Sullivan, T. Sumi, P. J. Tristram, T. Yanagisawa, P. C. M. Yock, A. Gal-Yam, Y. Lipkin, D. Maoz, E. O. Ofek, A. Udalski, O. Szewczyk, K. Żebruń, I. Soszyński, M. K. Szymański, M. Kubiak, G. Pietrzyński, and L. Wyrzykowski. Search for Low-Mass Exoplanets by Gravitational Microlensing at High Magnification. *Science*, 305:1264–1267, Aug. 2004.

[2] E. Agol, J. Steffen, R. Sari, and W. Clarkson. On detecting terrestrial planets with timing of giant planet transits. *MNRAS*, 359:567–579, May 2005.

[3] R. Andrae, T. Schulze-Hartung, and P. Melchior. Dos and don'ts of reduced chi-squared. *ArXiv e-prints*, Dec. 2010.

[4] G. Anglada-Escudé, M. López-Morales, and J. E. Chambers. How Eccentric Orbital Solutions Can Hide Planetary Systems in 2:1 Resonant Orbits. *ApJ*, 709:168–178, Jan. 2010.

[5] M. Auvergne, P. Bodin, L. Boisnard, J.-T. Buey, S. Chaintreuil, G. Epstein, M. Jouret, T. Lam-Trong, P. Levacher, A. Magnan, R. Perez, P. Plasson, J. Plesseria, G. Peter, M. Steller, D. Tiphène, A. Baglin, P. Agogué, T. Appourchaux, D. Barbet, T. Beaufort, R. Bellenger, R. Berlin, P. Bernardi, D. Blouin, P. Boumier, F. Bonneau, R. Briet, B. Butler, R. Cautain, F. Chiavassa, V. Costes, J. Cuvilho, V. Cunha-Parro, F. de Oliveira Fialho, M. Decaudin, J.-M. Defise, S. Djalal, A. Docclo, R. Drummond, O. Dupuis, G. Exil, C. Fauré, A. Gaboriaud, P. Gamet, P. Gavalda, E. Grolleau, L. Gueguen, V. Guivarc'h, P. Guterman, J. Hasiba, G. Huntzinger, H. Hustaix, C. Imbert, G. Jeanville, B. Johlander, L. Jorda, P. Journoud, F. Karioty, L. Kerjean, L. Lafond, V. Lapeyrere, P. Landiech, T. Larqué, P. Laudet, J. Le Merrer, L. Leporati, B. Leruyet, B. Levieuge, A. Llebaria, L. Martin,

E. Mazy, J.-M. Mesnager, J.-P. Michel, J.-P. Moalic, W. Monjoin, D. Naudet, S. Neukirchner, K. Nguyen-Kim, M. Ollivier, J.-L. Orcesi, H. Ottacher, A. Oulali, J. Parisot, S. Perruchot, A. Piacentino, L. Pinheiro da Silva, J. Platzer, B. Pontet, A. Pradines, C. Quentin, U. Rohbeck, G. Rolland, F. Rollenhagen, R. Romagnan, N. Russ, R. Samadi, R. Schmidt, N. Schwartz, I. Sebbag, H. Smit, W. Sunter, M. Tello, P. Toulouse, B. Ulmer, O. Vandermarcq, E. Vergnault, R. Wallner, G. Waultier, and P. Zanatta. The CoRoT satellite in flight: description and performance. *A&A*, 506:411–424, Oct. 2009.

[6] D. C. Backer, R. S. Foster, and S. Sallmen. A second companion of the millisecond pulsar 1620 - 26. *Nature*, 365:817–819, Oct. 1993.

[7] M. Bailes, S. D. Bates, V. Bhalerao, N. D. R. Bhat, M. Burgay, S. Burke-Spolaor, N. D'Amico, S. Johnston, M. J. Keith, M. Kramer, S. R. Kulkarni, L. Levin, A. G. Lyne, S. Milia, A. Possenti, L. Spitler, B. Stappers, and W. van Straten. Transformation of a Star into a Planet in a Millisecond Pulsar Binary. *Science*, 333:1717–, Sept. 2011.

[8] G. Bakos, R. W. Noyes, G. Kovács, K. Z. Stanek, D. D. Sasselov, and I. Domsa. Wide-Field Millimagnitude Photometry with the HAT: A Tool for Extrasolar Planet Detection. *PASP*, 116:266–277, Mar. 2004.

[9] S. Ballard, J. L. Christiansen, D. Charbonneau, D. Deming, M. J. Holman, D. Fabrycky, M. F. A'Hearn, D. D. Wellnitz, R. K. Barry, M. J. Kuchner, T. A. Livengood, T. Hewagama, J. M. Sunshine, D. L. Hampton, C. M. Lisse, S. Seager, and J. F. Veverka. A Search for Additional Planets in the NASA EPOXI Observations of the Exoplanet System GJ 436. *ApJ*, 716:1047–1059, June 2010.

[10] S. Ballard, D. Fabrycky, F. Fressin, D. Charbonneau, J.-M. Desert, G. Torres, G. Marcy, C. J. Burke, H. Isaacson, C. Henze, J. H. Steffen, D. R. Ciardi, S. B. Howell, W. D. Cochran, M. Endl, S. T. Bryson, J. F. Rowe, M. J. Holman, J. J. Lissauer, J. M. Jenkins, M. Still, E. B. Ford, J. L. Christiansen, C. K. Middour, M. R. Haas, J. Li, J. R. Hall, S. McCauliff, N. M. Batalha, D. G. Koch, and W. J. Borucki. The Kepler-19 System: A Transiting 2.2 $R_\oplus$ Planet and a Second Planet Detected via Transit Timing Variations. *ApJ*, 743:200, Dec. 2011.

[11] A. Baranne, D. Queloz, M. Mayor, G. Adrianzyk, G. Knispel, D. Kohler, D. Lacroix, J.-P. Meunier, G. Rimbaud, and A. Vin.

ELODIE: A spectrograph for accurate radial velocity measurements. *A&AS*, 119:373–390, Oct. 1996.

[12] C. Barban, J. M. Matthews, J. De Ridder, F. Baudin, R. Kuschnig, A. Mazumdar, R. Samadi, D. B. Guenther, A. F. J. Moffat, S. M. Rucinski, D. Sasselov, G. A. H. Walker, and W. W. Weiss. Detection of solar-like oscillations in the red giant star ϵ Ophiuchi by MOST spacebased photometry. *A&A*, 468:1033–1038, June 2007.

[13] M. Barbieri, R. Alonso, G. Laughlin, J. M. Almenara, R. Bissinger, D. Davies, D. Gasparri, E. Guido, C. Lopresti, F. Manzini, and G. Sostero. HD 17156b: a transiting planet with a 21.2-day period and an eccentric orbit. *A&A*, 476:L13–L16, Dec. 2007.

[14] J. W. Barnes. Effects of Orbital Eccentricity on Extrasolar Planet Transit Detectability and Light Curves. *PASP*, 119:986–993, Sept. 2007.

[15] R. Barnes, B. Jackson, R. Greenberg, and S. N. Raymond. Tidal Limits to Planetary Habitability. *ApJl*, 700:L30–L33, July 2009.

[16] N. M. Batalha, W. J. Borucki, S. T. Bryson, L. A. Buchhave, D. A. Caldwell, J. Christensen-Dalsgaard, D. Ciardi, E. W. Dunham, F. Fressin, T. N. Gautier, III, R. L. Gilliland, M. R. Haas, S. B. Howell, J. M. Jenkins, H. Kjeldsen, D. G. Koch, D. W. Latham, J. J. Lissauer, G. W. Marcy, J. F. Rowe, D. D. Sasselov, S. Seager, J. H. Steffen, G. Torres, G. S. Basri, T. M. Brown, D. Charbonneau, J. Christiansen, B. Clarke, W. D. Cochran, A. Dupree, D. C. Fabrycky, D. Fischer, E. B. Ford, J. Fortney, F. R. Girouard, M. J. Holman, J. Johnson, H. Isaacson, T. C. Klaus, P. Machalek, A. V. Moorehead, R. C. Morehead, D. Ragozzine, P. Tenenbaum, J. Twicken, S. Quinn, J. VanCleve, L. M. Walkowicz, W. F. Welsh, E. Devore, and A. Gould. Kepler's First Rocky Planet: Kepler-10b. *ApJ*, 729:27, Mar. 2011.

[17] N. M. Batalha, J. F. Rowe, S. T. Bryson, T. Barclay, C. J. Burke, D. A. Caldwell, J. L. Christiansen, F. Mullally, S. E. Thompson, T. M. Brown, A. K. Dupree, D. C. Fabrycky, E. B. Ford, J. J. Fortney, R. L. Gilliland, H. Isaacson, D. W. Latham, G. W. Marcy, S. Quinn, D. Ragozzine, A. Shporer, W. J. Borucki, D. R. Ciardi, T. N. Gautier, III, M. R. Haas, J. M. Jenkins, D. G. Koch, J. J. Lissauer, W. Rapin, G. S. Basri, A. P. Boss, L. A. Buchhave, D. Charbonneau, J. Christensen-Dalsgaard, B. D. Clarke, W. D. Cochran, B.-O.

Demory, E. Devore, G. A. Esquerdo, M. Everett, F. Fressin, J. C. Geary, F. R. Girouard, A. Gould, J. R. Hall, M. J. Holman, A. W. Howard, S. B. Howell, K. A. Ibrahim, K. Kinemuchi, H. Kjeldsen, T. C. Klaus, J. Li, P. W. Lucas, R. L. Morris, A. Prsa, E. Quintana, D. T. Sanderfer, D. Sasselov, S. E. Seader, J. C. Smith, J. H. Steffen, M. Still, M. C. Stumpe, J. C. Tarter, P. Tenenbaum, G. Torres, J. D. Twicken, K. Uddin, J. Van Cleve, L. Walkowicz, and W. F. Welsh. Planetary Candidates Observed by Kepler, III: Analysis of the First 16 Months of Data. *ArXiv e-prints*, Feb. 2012.

[18] K. Batygin and D. J. Stevenson. Inflating Hot Jupiters with Ohmic Dissipation. *ApJl*, 714:L238–L243, May 2010.

[19] J. L. Bean, J.-M. Désert, P. Kabath, B. Stalder, S. Seager, E. Miller-Ricci Kempton, Z. K. Berta, D. Homeier, S. Walsh, and A. Seifahrt. The Optical and Near-infrared Transmission Spectrum of the Super-Earth GJ 1214b: Further Evidence for a Metal-rich Atmosphere. *ApJ*, 743:92, Dec. 2011.

[20] J. L. Bean, E. Miller-Ricci Kempton, and D. Homeier. A ground-based transmission spectrum of the super-Earth exoplanet GJ 1214b. *Nature*, 468:669–672, Dec. 2010.

[21] J. P. Beaulieu, D. M. Kipping, V. Batista, G. Tinetti, I. Ribas, S. Carey, J. A. Noriega-Crespo, C. A. Griffith, G. Campanella, S. Dong, J. Tennyson, R. J. Barber, P. Deroo, S. J. Fossey, D. Liang, M. R. Swain, Y. Yung, and N. Allard. Water in the atmosphere of HD 209458b from 3.6-8 μm IRAC photometric observations in primary transit. *MNRAS*, 409:963–974, Dec. 2010.

[22] G. F. Benedict, B. E. McArthur, T. Forveille, X. Delfosse, E. Nelan, R. P. Butler, W. Spiesman, G. Marcy, B. Goldman, C. Perrier, W. H. Jefferys, and M. Mayor. A Mass for the Extrasolar Planet Gliese 876b Determined from Hubble Space Telescope Fine Guidance Sensor 3 Astrometry and High-Precision Radial Velocities. *ApJ*, 581:L115–L118, Dec. 2002. arXiv:astro-ph/0212101.

[23] Z. K. Berta, D. Charbonneau, J.-M. Désert, E. Miller-Ricci Kempton, P. R. McCullough, C. J. Burke, J. J. Fortney, J. Irwin, P. Nutzman, and D. Homeier. The Flat Transmission Spectrum of the Super-Earth GJ1214b from Wide Field Camera 3 on the Hubble Space Telescope. *ApJ*, 747:35, Mar. 2012.

[24] P. Bodenheimer, G. Laughlin, and D. N. C. Lin. On the Radii of Extrasolar Giant Planets. *ApJ*, 592:555–563, July 2003.

[25] P. Bodenheimer, D. N. C. Lin, and R. A. Mardling. On the Tidal Inflation of Short-Period Extrasolar Planets. *ApJ*, 548:466–472, Feb. 2001.

[26] X. Bonfils, T. Forveille, X. Delfosse, S. Udry, M. Mayor, C. Perrier, F. Bouchy, F. Pepe, D. Queloz, and J.-L. Bertaux. The HARPS search for southern extra-solar planets. VI. A Neptune-mass planet around the nearby M dwarf Gl 581. *A&A*, 443:L15–L18, Dec. 2005.

[27] W. J. Borucki, D. Koch, G. Basri, N. Batalha, T. Brown, D. Caldwell, J. Caldwell, J. Christensen-Dalsgaard, W. D. Cochran, E. DeVore, E. W. Dunham, A. K. Dupree, T. N. Gautier, J. C. Geary, R. Gilliland, A. Gould, S. B. Howell, J. M. Jenkins, Y. Kondo, D. W. Latham, G. W. Marcy, S. Meibom, H. Kjeldsen, J. J. Lissauer, D. G. Monet, D. Morrison, D. Sasselov, J. Tarter, A. Boss, D. Brownlee, T. Owen, D. Buzasi, D. Charbonneau, L. Doyle, J. Fortney, E. B. Ford, M. J. Holman, S. Seager, J. H. Steffen, W. F. Welsh, J. Rowe, H. Anderson, L. Buchhave, D. Ciardi, L. Walkowicz, W. Sherry, E. Horch, H. Isaacson, M. E. Everett, D. Fischer, G. Torres, J. A. Johnson, M. Endl, P. MacQueen, S. T. Bryson, J. Dotson, M. Haas, J. Kolodziejczak, J. Van Cleve, H. Chandrasekaran, J. D. Twicken, E. V. Quintana, B. D. Clarke, C. Allen, J. Li, H. Wu, P. Tenenbaum, E. Verner, F. Bruhweiler, J. Barnes, and A. Prsa. Kepler Planet-Detection Mission: Introduction and First Results. *Science*, 327:977–, Feb. 2010.

[28] W. J. Borucki, D. G. Koch, G. Basri, N. Batalha, A. Boss, T. M. Brown, D. Caldwell, J. Christensen-Dalsgaard, W. D. Cochran, E. DeVore, E. W. Dunham, A. K. Dupree, T. N. Gautier, III, J. C. Geary, R. Gilliland, A. Gould, S. B. Howell, J. M. Jenkins, H. Kjeldsen, D. W. Latham, J. J. Lissauer, G. W. Marcy, D. G. Monet, D. Sasselov, J. Tarter, D. Charbonneau, L. Doyle, E. B. Ford, J. Fortney, M. J. Holman, S. Seager, J. H. Steffen, W. F. Welsh, C. Allen, S. T. Bryson, L. Buchhave, H. Chandrasekaran, J. L. Christiansen, D. Ciardi, B. D. Clarke, J. L. Dotson, M. Endl, D. Fischer, F. Fressin, M. Haas, E. Horch, A. Howard, H. Isaacson, J. Kolodziejczak, J. Li, P. MacQueen, S. Meibom, A. Prsa, E. V. Quintana, J. Rowe, W. Sherry, P. Tenenbaum, G. Torres, J. D. Twicken, J. Van Cleve, L. Walkowicz,

and H. Wu. Characteristics of Kepler Planetary Candidates Based on the First Data Set. *ApJ*, 728:117, Feb. 2011.

[29] W. J. Borucki, D. G. Koch, N. Batalha, S. T. Bryson, J. Rowe, F. Fressin, G. Torres, D. A. Caldwell, J. Christensen-Dalsgaard, W. D. Cochran, E. DeVore, T. N. Gautier, J. C. Geary, R. Gilliland, A. Gould, S. B. Howell, J. M. Jenkins, D. W. Latham, J. J. Lissauer, G. W. Marcy, D. Sasselov, A. Boss, D. Charbonneau, D. Ciardi, L. Kaltenegger, L. Doyle, A. K. Dupree, E. B. Ford, J. Fortney, M. J. Holman, J. H. Steffen, F. Mullally, M. Still, J. Tarter, S. Ballard, L. A. Buchhave, J. Carter, J. L. Christiansen, B.-O. Demory, J.-M. Désert, C. Dressing, M. Endl, D. Fabrycky, D. Fischer, M. R. Haas, C. Henze, E. Horch, A. W. Howard, H. Isaacson, H. Kjeldsen, J. A. Johnson, T. Klaus, J. Kolodziejczak, T. Barclay, J. Li, S. Meibom, A. Prsa, S. N. Quinn, E. V. Quintana, P. Robertson, W. Sherry, A. Shporer, P. Tenenbaum, S. E. Thompson, J. D. Twicken, J. Van Cleve, W. F. Welsh, S. Basu, W. Chaplin, A. Miglio, S. D. Kawaler, T. Arentoft, D. Stello, T. S. Metcalfe, G. A. Verner, C. Karoff, M. Lundkvist, M. N. Lund, R. Handberg, Y. Elsworth, S. Hekker, D. Huber, T. R. Bedding, and W. Rapin. Kepler-22b: A 2.4 Earth-radius Planet in the Habitable Zone of a Sun-like Star. *ApJ*, 745:120, Feb. 2012.

[30] B. P. Bowler, M. C. Liu, T. J. Dupuy, and M. C. Cushing. Near-infrared Spectroscopy of the Extrasolar Planet HR 8799 b. *ApJ*, 723: 850–868, Nov. 2010.

[31] D. J. A. Brown, A. C. Cameron, D. R. Anderson, B. Enoch, C. Hellier, P. F. L. Maxted, G. R. M. Miller, D. Pollacco, D. Queloz, E. Simpson, B. Smalley, A. H. M. J. Triaud, I. Boisse, F. Bouchy, M. Gillon, and G. Hébrard. Rossiter-McLaughlin effect measurements for WASP-16, WASP-25 and WASP-31. *MNRAS*, page 2920, Apr. 2012.

[32] T. M. Brown, S. F. Taylor, W. Rosing, R. Mann, V. Trimble, and J. A. Farrell. Keeping Astronomy in the Dark Around the Clock: Introducing LCOGT.net. In *American Astronomical Society Meeting Abstracts 208*, volume 38 of *Bulletin of the American Astronomical Society*, page 136, June 2006.

[33] A. Burrows, I. Hubeny, J. Budaj, and W. B. Hubbard. Possible Solutions to the Radius Anomalies of Transiting Giant Planets. *ApJ*, 661: 502–514, May 2007.

[34] A. Burrows, I. Hubeny, W. B. Hubbard, D. Sudarsky, and J. J. Fortney. Theoretical Radii of Transiting Giant Planets: The Case of OGLE-TR-56b. *ApJl*, 610:L53–L56, July 2004.

[35] R. P. Butler, G. W. Marcy, S. S. Vogt, and K. Apps. A Planet with a 3.1 Day Period around a Solar Twin. *PASP*, 110:1389–1393, Dec. 1998.

[36] R. P. Butler, G. W. Marcy, E. Williams, H. Hauser, and P. Shirts. Three New "51 Pegasi–Type" Planets. *ApJL*, 474:L115, Jan. 1997.

[37] R. P. Butler, G. W. Marcy, E. Williams, C. McCarthy, P. Dosanjh, and S. S. Vogt. Attaining Doppler Precision of 3 M s-1. *PASP*, 108: 500–+, June 1996.

[38] R. P. Butler, C. G. Tinney, G. W. Marcy, H. R. A. Jones, A. J. Penny, and K. Apps. Two New Planets from the Anglo-Australian Planet Search. *ApJ*, 555:410–417, July 2001.

[39] R. P. Butler, J. T. Wright, G. W. Marcy, D. A. Fischer, S. S. Vogt, C. G. Tinney, H. R. A. Jones, B. D. Carter, J. A. Johnson, C. McCarthy, and A. J. Penny. Catalog of Nearby Exoplanets. *ApJ*, 646: 505–522, July 2006. arXiv:astro-ph/0607493.

[40] B. Campbell and G. A. H. Walker. Precision radial velocities with an absorption cell. *PASP*, 91:540–545, Aug. 1979.

[41] B. Campbell, G. A. H. Walker, and S. Yang. A search for substellar companions to solar-type stars. *ApJ*, 331:902–921, Aug. 1988.

[42] R. M. Canup and W. R. Ward. A common mass scaling for satellite systems of gaseous planets. *Nature*, 441:834–839, June 2006.

[43] S. Casertano, M. G. Lattanzi, A. Sozzetti, A. Spagna, S. Jancart, R. Morbidelli, R. Pannunzio, D. Pourbaix, and D. Queloz. Double-blind test program for astrometric planet detection with Gaia. *A&A*, 482:699–729, May 2008.

[44] A. Cassan, D. Kubas, J.-P. Beaulieu, M. Dominik, K. Horne, J. Greenhill, J. Wambsganss, J. Menzies, A. Williams, U. G. Jørgensen, A. Udalski, D. P. Bennett, M. D. Albrow, V. Batista, S. Brillant, J. A. R. Caldwell, A. Cole, C. Coutures, K. H. Cook, S. Dieters, D. D. Prester, J. Donatowicz, P. Fouqué, K. Hill, N. Kains, S. Kane,

J.-B. Marquette, R. Martin, K. R. Pollard, K. C. Sahu, C. Vinter, D. Warren, B. Watson, M. Zub, T. Sumi, M. K. Szymański, M. Kubiak, R. Poleski, I. Soszynski, K. Ulaczyk, G. Pietrzyński, and Ł. Wyrzykowski. One or more bound planets per Milky Way star from microlensing observations. *Nature*, 481:167–169, Jan. 2012.

[45] F. Castelli and R. L. Kurucz. New Grids of ATLAS9 Model Atmospheres. *ArXiv Astrophysics e-prints*, May 2004.

[46] G. Cayrel de Strobel, C. Soubiran, and N. Ralite. Catalogue of [Fe/H] determinations for FGK stars: 2001 edition. *A&A*, 373:159–163, July 2001.

[47] G. Chabrier and I. Baraffe. Heat Transport in Giant (Exo)planets: A New Perspective. *ApJl*, 661:L81–L84, May 2007.

[48] D. Charbonneau, L. E. Allen, S. T. Megeath, G. Torres, R. Alonso, T. M. Brown, R. L. Gilliland, D. W. Latham, G. Mandushev, F. T. O'Donovan, and A. Sozzetti. Detection of Thermal Emission from an Extrasolar Planet. *ApJ*, 626:523–529, June 2005. arXiv:astro-ph/0503457.

[49] D. Charbonneau, Z. K. Berta, J. Irwin, C. J. Burke, P. Nutzman, L. A. Buchhave, C. Lovis, X. Bonfils, D. W. Latham, S. Udry, R. A. Murray-Clay, M. J. Holman, E. E. Falco, J. N. Winn, D. Queloz, F. Pepe, M. Mayor, X. Delfosse, and T. Forveille. A super-Earth transiting a nearby low-mass star. *Nature*, 462:891–894, Dec. 2009.

[50] D. Charbonneau, T. M. Brown, D. W. Latham, and M. Mayor. Detection of Planetary Transits Across a Sun-like Star. *ApJ*, 529:L45–L48, Jan. 2000. arXiv:astro-ph/9911436.

[51] D. Charbonneau, T. M. Brown, R. W. Noyes, and R. L. Gilliland. Detection of an Extrasolar Planet Atmosphere. *ApJ*, 568:377–384, Mar. 2002.

[52] S. Chatterjee, E. B. Ford, and F. A. Rasio. Dynamical Outcomes of Planet-Planet Scattering. In *AAS/Division of Dynamical Astronomy Meeting 38*, volume 38 of *AAS/Division of Dynamical Astronomy Meeting*, page 15.01, July 2007.

[53] J. L. Christiansen, S. Ballard, D. Charbonneau, N. Madhusudhan, S. Seager, M. J. Holman, D. D. Wellnitz, D. Deming, M. F. A'Hearn,

and EPOXI Team. Studying the Atmosphere of the Exoplanet HAT-P-7b Via Secondary Eclipse Measurements with EPOXI, Spitzer, and Kepler. *ApJ*, 710:97–104, Feb. 2010.

[54] K. D. Colón, E. B. Ford, S. Redfield, J. J. Fortney, M. Shabram, H. J. Deeg, and S. Mahadevan. Probing potassium in the atmosphere of HD 80606b with tunable filter transit spectrophotometry from the Gran Telescopio Canarias. *MNRAS*, 419:2233–2250, Jan. 2012.

[55] N. B. Cowan, P. Machalek, B. Croll, L. M. Shekhtman, A. Burrows, D. Deming, T. Greene, and J. L. Hora. Thermal Phase Variations of WASP-12b: Defying Predictions. *ApJ*, 747:82, Mar. 2012.

[56] B. Croll, L. Albert, R. Jayawardhana, E. Miller-Ricci Kempton, J. J. Fortney, N. Murray, and H. Neilson. Broadband Transmission Spectroscopy of the Super-Earth GJ 1214b Suggests a Low Mean Molecular Weight Atmosphere. *ApJ*, 736:78, Aug. 2011.

[57] B. Croll, J. M. Matthews, J. F. Rowe, B. Gladman, E. Miller-Ricci, D. Sasselov, G. A. H. Walker, R. Kuschnig, D. N. C. Lin, D. B. Guenther, A. F. J. Moffat, S. M. Rucinski, and W. W. Weiss. Looking for Super-Earths in the HD 189733 System: A Search for Transits in MOST Space-based Photometry. *ApJ*, 671:2129–2138, Dec. 2007.

[58] B. Croll, J. M. Matthews, J. F. Rowe, R. Kuschnig, A. Walker, B. Gladman, D. Sasselov, C. Cameron, G. A. H. Walker, D. N. C. Lin, D. B. Guenther, A. F. J. Moffat, S. M. Rucinski, and W. W. Weiss. Looking for Giant Earths in the HD 209458 System: A Search for Transits in MOST Space-based Photometry. *ApJ*, 658:1328–1339, Apr. 2007.

[59] I. J. M. Crossfield. ACME Stellar Spectra. I. Absolutely Calibrated, Mostly Empirical Flux Densities of 55 Cancri and its Transiting Planet 55 Cancri e. *ArXiv e-prints*, June 2012.

[60] N. Crouzet, T. Guillot, A. Agabi, J.-P. Rivet, E. Bondoux, Z. Challita, Y. Fanteï-Caujolle, F. Fressin, D. Mékarnia, F.-X. Schmider, F. Valbousquet, A. Blazit, S. Bonhomme, L. Abe, J.-B. Daban, C. Gouvret, T. Fruth, H. Rauer, A. Erikson, M. Barbieri, S. Aigrain, and F. Pont. ASTEP South: an Antarctic Search for Transiting ExoPlanets around the celestial south pole. *A&A*, 511:A36, Feb. 2010.

[61] A. Cumming, R. P. Butler, G. W. Marcy, S. S. Vogt, J. T. Wright, and D. A. Fischer. The Keck Planet Search: Detectability and the Minimum Mass and Orbital Period Distribution of Extrasolar Planets. *PASP*, 120:531–554, May 2008.

[62] T. Currie and B. Hansen. The Evolution of Protoplanetary Disks around Millisecond Pulsars: The PSR 1257+12 System. *ApJ*, 666: 1232–1244, Sept. 2007.

[63] R. I. Dawson and D. C. Fabrycky. Radial Velocity Planets De-aliased: A New, Short Period for Super-Earth 55 Cnc e. *ApJ*, 722:937–953, Oct. 2010.

[64] E. J. W. de Mooij and I. A. G. Snellen. Ground-based K-band detection of thermal emission from the exoplanet TrES-3b. *A&A*, 493: L35–L38, Jan. 2009.

[65] D. Deming, J. Harrington, G. Laughlin, S. Seager, S. B. Navarro, W. C. Bowman, and K. Horning. Spitzer Transit and Secondary Eclipse Photometry of GJ 436b. *ApJl*, 667:L199–L202, Oct. 2007.

[66] B.-O. Demory, M. Gillon, D. Deming, D. Valencia, S. Seager, B. Benneke, C. Lovis, P. Cubillos, J. Harrington, K. B. Stevenson, M. Mayor, F. Pepe, D. Queloz, D. Ségransan, and S. Udry. Detection of a transit of the super-Earth 55 Cancri e with warm Spitzer. *A&A*, 533:A114, Sept. 2011.

[67] B.-O. Demory, M. Gillon, S. Seager, B. Benneke, D. Deming, and B. Jackson. Detection of Thermal Emission from a Super-Earth. *ApJl*, 751:L28, June 2012.

[68] B.-O. Demory, S. Seager, N. Madhusudhan, H. Kjeldsen, J. Christensen-Dalsgaard, M. Gillon, J. F. Rowe, W. F. Welsh, E. R. Adams, A. Dupree, D. McCarthy, C. Kulesa, W. J. Borucki, and D. G. Koch. The High Albedo of the Hot Jupiter Kepler-7 b. *ApJL*, 735: L12, July 2011.

[69] S. Desidera, R. G. Gratton, M. Endl, R. U. Claudi, R. Cosentino, M. Barbieri, G. Bonanno, S. Lucatello, A. F. Martinez Fiorenzano, F. Marzari, and S. Scuderi. No planet around HD 219542 B. *A&A*, 420:L27–L30, June 2004.

[70] J.-F. Donati, C. Moutou, R. Farès, D. Bohlender, C. Catala, M. Deleuil, E. Shkolnik, A. Collier Cameron, M. M. Jardine, and G. A. H. Walker. Magnetic cycles of the planet-hosting star τ Bootis. *MNRAS*, 385:1179–1185, Apr. 2008.

[71] L. R. Doyle, J. A. Carter, D. C. Fabrycky, R. W. Slawson, S. B. Howell, J. N. Winn, J. A. Orosz, A. Prsa, W. F. Welsh, S. N. Quinn, D. Latham, G. Torres, L. A. Buchhave, G. W. Marcy, J. J. Fortney, A. Shporer, E. B. Ford, J. J. Lissauer, D. Ragozzine, M. Rucker, N. Batalha, J. M. Jenkins, W. J. Borucki, D. Koch, C. K. Middour, J. R. Hall, S. McCauliff, M. N. Fanelli, E. V. Quintana, M. J. Holman, D. A. Caldwell, M. Still, R. P. Stefanik, W. R. Brown, G. A. Esquerdo, S. Tang, G. Furesz, J. C. Geary, P. Berlind, M. L. Calkins, D. R. Short, J. H. Steffen, D. Sasselov, E. W. Dunham, W. D. Cochran, A. Boss, M. R. Haas, D. Buzasi, and D. Fischer. Kepler-16: A Transiting Circumbinary Planet. *Science*, 333:1602–, Sept. 2011.

[72] D. Dragomir, S. R. Kane, G. Pilyavsky, S. Mahadevan, D. R. Ciardi, J. Z. Gazak, D. M. Gelino, A. Payne, M. Rabus, S. V. Ramirez, K. von Braun, J. T. Wright, and P. Wyatt. TERMS Photometry of Known Transiting Exoplanets. *AJ*, 142:115, Oct. 2011.

[73] D. Dravins. Stellar granulation. In G. Wallerstein, editor, *Cool Stars, Stellar Systems, and the Sun*, volume 9 of *Astronomical Society of the Pacific Conference Series*, pages 27–38, 1990.

[74] J. A. Eaton, G. W. Henry, and F. C. Fekel. Random Spots on Chromospherically Active Stars. *ApJ*, 462:888, May 1996.

[75] L. T. Elkins-Tanton and S. Seager. Coreless Terrestrial Exoplanets. *ApJ*, 688:628–635, Nov. 2008.

[76] D. Fabrycky and S. Tremaine. Shrinking Binary and Planetary Orbits by Kozai Cycles with Tidal Friction. *ApJ*, 669:1298–1315, Nov. 2007.

[77] D. C. Fabrycky. Non-Keplerian Dynamics. *ArXiv e-prints*, June 2010.

[78] J. Fang and J.-L. Margot. Architecture of Planetary Systems Based on Kepler Data: Number of Planets and Coplanarity. *ArXiv e-prints*, July 2012.

[79] R. Fares, J.-F. Donati, C. Moutou, D. Bohlender, C. Catala, M. Deleuil, E. Shkolnik, A. Collier Cameron, M. M. Jardine, and

G. A. H. Walker. Magnetic cycles of the planet-hosting star τ Bootis - II. A second magnetic polarity reversal. *MNRAS*, 398:1383–1391, Sept. 2009.

[80] D. A. Fischer, G. W. Marcy, R. P. Butler, S. S. Vogt, G. Laughlin, G. W. Henry, D. Abouav, K. M. G. Peek, J. T. Wright, J. A. Johnson, C. McCarthy, and H. Isaacson. Five Planets Orbiting 55 Cancri. *ApJ*, 675:790–801, Mar. 2008. arXiv:0712.3917.

[81] D. A. Fischer and J. Valenti. The Planet-Metallicity Correlation. *ApJ*, 622:1102–1117, Apr. 2005.

[82] D. A. Fischer, S. S. Vogt, G. W. Marcy, R. P. Butler, B. Sato, G. W. Henry, S. Robinson, G. Laughlin, S. Ida, E. Toyota, M. Omiya, P. Driscoll, G. Takeda, J. T. Wright, and J. A. Johnson. Five Intermediate-Period Planets from the N2K Sample. *ApJ*, 669:1336–1344, Nov. 2007.

[83] E. B. Ford. Quantifying the Uncertainty in the Orbits of Extrasolar Planets. *AJ*, 129:1706–1717, Mar. 2005. arXiv:astro-ph/0305441.

[84] E. B. Ford. Improving the Efficiency of Markov Chain Monte Carlo for Analyzing the Orbits of Extrasolar Planets. *ApJ*, 642:505–522, May 2006. arXiv:astro-ph/0512634.

[85] J. J. Fortney, D. Saumon, M. S. Marley, K. Lodders, and R. S. Freedman. Atmosphere, Interior, and Evolution of the Metal-rich Transiting Planet HD 149026b. *ApJ*, 642:495–504, May 2006.

[86] T. Forveille, X. Bonfils, X. Delfosse, R. Alonso, S. Udry, F. Bouchy, M. Gillon, C. Lovis, V. Neves, M. Mayor, F. Pepe, D. Queloz, N. C. Santos, D. Segransan, J. M. Almenara, H. Deeg, and M. Rabus. The HARPS search for southern extra-solar planets XXXII. Only 4 planets in the Gl˜581 system. *ArXiv e-prints*, Sept. 2011.

[87] D. A. Freedman. Bootstrapping Regression Models. *Ann. Stat.*, 9: 1218–1228, 1981.

[88] F. Fressin, G. Torres, J. F. Rowe, D. Charbonneau, L. A. Rogers, S. Ballard, N. M. Batalha, W. J. Borucki, S. T. Bryson, L. A. Buchhave, D. R. Ciardi, J.-M. Désert, C. D. Dressing, D. C. Fabrycky, E. B. Ford, T. N. Gautier, III, C. E. Henze, M. J. Holman, A. Howard, S. B. Howell, J. M. Jenkins, D. G. Koch, D. W. Latham, J. J. Lissauer,

G. W. Marcy, S. N. Quinn, D. Ragozzine, D. D. Sasselov, S. Seager, T. Barclay, F. Mullally, S. E. Seader, M. Still, J. D. Twicken, S. E. Thompson, and K. Uddin. Two Earth-sized planets orbiting Kepler-20. *Nature*, 482:195–198, Feb. 2012.

[89] E. Garcia-Melendo and P. R. McCullough. Photometric Detection of a Transit of HD 80606b. *ApJ*, 698:558–561, June 2009.

[90] B. S. Gaudi. Exoplanetary Microlensing. *ArXiv e-prints*, Feb. 2010.

[91] B. S. Gaudi and J. N. Winn. Prospects for the Characterization and Confirmation of Transiting Exoplanets via the Rossiter-McLaughlin Effect. *ApJ*, 655:550–563, Jan. 2007.

[92] A. Gelman, J. B. Carlin, H. S. Stern, and D. B. Rubin. *Bayesian Data Analysis*. CRC Press, 2nd edition, 2003.

[93] A. Gelman and D. Rubin. Inference from iterative simulation using multiple sequences. *Statistical Science*, 7:457–511, 1992.

[94] M. Gillon, B.-O. Demory, B. Benneke, D. Valencia, D. Deming, S. Seager, C. Lovis, M. Mayor, F. Pepe, D. Queloz, D. Ségransan, and S. Udry. Improved precision on the radius of the nearby super-Earth 55 Cnc e. *A&A*, 539:A28, Mar. 2012.

[95] J. Gomes da Silva, N. C. Santos, X. Bonfils, X. Delfosse, T. Forveille, and S. Udry. Long-term magnetic activity of a sample of M-dwarf stars from the HARPS program. I. Comparison of activity indices. *A&A*, 534:A30, Oct. 2011.

[96] J. Gomes da Silva, N. C. Santos, X. Bonfils, X. Delfosse, T. Forveille, S. Udry, X. Dumusque, and C. Lovis. Long-term magnetic activity of a sample of M-dwarf stars from the HARPS program . II. Activity and radial velocity. *A&A*, 541:A9, May 2012.

[97] P. C. Gregory. *Bayesian Logical Data Analysis for the Physical Sciences: A Comparative Approach with 'Mathematica' Support*. Cambridge University Press, 2005.

[98] P. C. Gregory. Bayesian re-analysis of the Gliese 581 exoplanet system. *MNRAS*, 415:2523–2545, Aug. 2011.

[99] P. C. Gregory and D. A. Fischer. A Bayesian periodogram finds evidence for three planets in 47UrsaeMajoris. *MNRAS*, 403:731–747, Apr. 2010.

[100] P. C. Gregory and T. J. Loredo. A new method for the detection of a periodic signal of unknown shape and period. *ApJ*, 398:146–168, Oct. 1992.

[101] T. Guillot and A. P. Showman. Evolution of "51 Pegasus b-like" planets. *A&A*, 385:156–165, Apr. 2002.

[102] J. L. Halbwachs, M. Mayor, and S. Udry. Statistical properties of exoplanets. IV. The period-eccentricity relations of exoplanets and of binary stars. *A&A*, 431:1129–1137, Mar. 2005. arXiv:astro-ph/0410732.

[103] J. Harrington, B. M. Hansen, S. H. Luszcz, S. Seager, D. Deming, K. Menou, J. Y.-K. Cho, and L. J. Richardson. The Phase-Dependent Infrared Brightness of the Extrasolar Planet υ Andromedae b. *Science*, 314:623–626, Oct. 2006.

[104] W. K. Hastings. Monte Carlo sampling methods using Markov chains and their applications. *Biometrika*, 57:97–109, 1970.

[105] A. P. Hatzes, W. D. Cochran, M. Endl, B. McArthur, D. B. Paulson, G. A. H. Walker, B. Campbell, and S. Yang. A Planetary Companion to γ Cephei A. *ApJ*, 599:1383–1394, Dec. 2003.

[106] A. P. Hatzes, M. Fridlund, G. Nachmani, T. Mazeh, D. Valencia, G. Hébrard, L. Carone, M. Pätzold, S. Udry, F. Bouchy, M. Deleuil, C. Moutou, P. Barge, P. Bordé, H. Deeg, B. Tingley, R. Dvorak, D. Gandolfi, S. Ferraz-Mello, G. Wuchterl, E. Guenther, T. Guillot, H. Rauer, A. Erikson, J. Cabrera, S. Csizmadia, A. Léger, H. Lammer, J. Weingrill, D. Queloz, R. Alonso, D. Rouan, and J. Schneider. The Mass of CoRoT-7b. *ApJ*, 743:75, Dec. 2011.

[107] G. Hébrard, S. Udry, G. Lo Curto, N. Robichon, D. Naef, D. Ehrenreich, W. Benz, F. Bouchy, A. Lecavelier Des Etangs, C. Lovis, M. Mayor, C. Moutou, F. Pepe, D. Queloz, N. C. Santos, and D. Ségransan. The HARPS search for southern extra-solar planets. XX. Planets around the active star BD -08deg2823. *A&A*, 512:A46, Mar. 2010.

[108] R. Heller, J. Leconte, and R. Barnes. Tidal obliquity evolution of potentially habitable planets. *A&A*, 528:A27, Apr. 2011.

[109] G. W. Henry. Techniques for Automated High-Precision Photometry of Sun-like Stars. *PASP*, 111:845–860, July 1999.

[110] G. W. Henry, R. A. Donahue, and S. L. Baliunas. A False Planet around HD 192263. *ApJL*, 577:L111–L114, Oct. 2002.

[111] G. W. Henry, A. W. Howard, G. W. Marcy, D. A. Fischer, and J. A. Johnson. Detection of a Transiting Low-Density Super-Earth. *ArXiv e-prints*, Sept. 2011.

[112] G. W. Henry, G. W. Marcy, R. P. Butler, and S. S. Vogt. A Transiting "51 Peg-like" Planet. *ApJL*, 529:L41–L44, Jan. 2000.

[113] M. J. Holman, D. C. Fabrycky, D. Ragozzine, E. B. Ford, J. H. Steffen, W. F. Welsh, J. J. Lissauer, D. W. Latham, G. W. Marcy, L. M. Walkowicz, N. M. Batalha, J. M. Jenkins, J. F. Rowe, W. D. Cochran, F. Fressin, G. Torres, L. A. Buchhave, D. D. Sasselov, W. J. Borucki, D. G. Koch, G. Basri, T. M. Brown, D. A. Caldwell, D. Charbonneau, E. W. Dunham, T. N. Gautier, J. C. Geary, R. L. Gilliland, M. R. Haas, S. B. Howell, D. R. Ciardi, M. Endl, D. Fischer, G. Fürész, J. D. Hartman, H. Isaacson, J. A. Johnson, P. J. MacQueen, A. V. Moorhead, R. C. Morehead, and J. A. Orosz. Kepler-9: A System of Multiple Planets Transiting a Sun-Like Star, Confirmed by Timing Variations. *Science*, 330:51–, Oct. 2010.

[114] M. J. Holman and N. W. Murray. The Use of Transit Timing to Detect Terrestrial-Mass Extrasolar Planets. *Science*, 307:1288–1291, Feb. 2005.

[115] A. W. Howard, J. A. Johnson, G. W. Marcy, D. A. Fischer, J. T. Wright, D. Bernat, G. W. Henry, K. M. G. Peek, H. Isaacson, K. Apps, M. Endl, W. D. Cochran, J. A. Valenti, J. Anderson, and N. E. Piskunov. The California Planet Survey. I. Four New Giant Exoplanets. *ApJ*, 721:1467–1481, Oct. 2010.

[116] A. W. Howard, J. A. Johnson, G. W. Marcy, D. A. Fischer, J. T. Wright, G. W. Henry, M. J. Giguere, H. Isaacson, J. A. Valenti, J. Anderson, and N. E. Piskunov. The NASA-UC Eta-Earth Program. I. A Super-Earth Orbiting HD 7924. *ApJ*, 696:75–83, May 2009.

[117] A. W. Howard, J. A. Johnson, G. W. Marcy, D. A. Fischer, J. T. Wright, G. W. Henry, H. Isaacson, J. A. Valenti, J. Anderson, and N. E. Piskunov. The NASA-UC Eta-Earth Program. II. A Planet Orbiting HD 156668 with a Minimum Mass of Four Earth Masses. *ApJ*, 726:73, Jan. 2011.

[118] A. W. Howard, J. A. Johnson, G. W. Marcy, D. A. Fischer, J. T. Wright, G. W. Henry, H. Isaacson, J. A. Valenti, J. Anderson, and N. E. Piskunov. The NASA-UC Eta-Earth Program. III. A Super-Earth Orbiting HD 97658 and a Neptune-mass Planet Orbiting Gl 785. *ApJ*, 730:10, Mar. 2011.

[119] A. W. Howard, G. W. Marcy, S. T. Bryson, J. M. Jenkins, J. F. Rowe, N. M. Batalha, W. J. Borucki, D. G. Koch, E. W. Dunham, T. N. Gautier, III, J. Van Cleve, W. D. Cochran, D. W. Latham, J. J. Lissauer, G. Torres, T. M. Brown, R. L. Gilliland, L. A. Buchhave, D. A. Caldwell, J. Christensen-Dalsgaard, D. Ciardi, F. Fressin, M. R. Haas, S. B. Howell, H. Kjeldsen, S. Seager, L. Rogers, D. D. Sasselov, J. H. Steffen, G. S. Basri, D. Charbonneau, J. Christiansen, B. Clarke, A. Dupree, D. C. Fabrycky, D. A. Fischer, E. B. Ford, J. J. Fortney, J. Tarter, F. R. Girouard, M. J. Holman, J. A. Johnson, T. C. Klaus, P. Machalek, A. V. Moorhead, R. C. Morehead, D. Ragozzine, P. Tenenbaum, J. D. Twicken, S. N. Quinn, H. Isaacson, A. Shporer, P. W. Lucas, L. M. Walkowicz, W. F. Welsh, A. Boss, E. Devore, A. Gould, J. C. Smith, R. L. Morris, A. Prsa, T. D. Morton, M. Still, S. E. Thompson, F. Mullally, M. Endl, and P. J. MacQueen. Planet Occurrence within 0.25 AU of Solar-type Stars from Kepler. *ApJS*, 201:15, Aug. 2012.

[120] A. W. Howard, G. W. Marcy, J. A. Johnson, D. A. Fischer, J. T. Wright, H. Isaacson, J. A. Valenti, J. Anderson, D. N. C. Lin, and S. Ida. The Occurrence and Mass Distribution of Close-in Super-Earths, Neptunes, and Jupiters. *Science*, 330:653–, Oct. 2010.

[121] S. B. Howell, J. F. Rowe, S. T. Bryson, S. N. Quinn, G. W. Marcy, H. Isaacson, D. R. Ciardi, W. J. Chaplin, T. S. Metcalfe, M. J. P. F. G. Monteiro, T. Appourchaux, S. Basu, O. L. Creevey, R. L. Gilliland, P.-O. Quirion, D. Stello, H. Kjeldsen, J. Christensen-Dalsgaard, Y. Elsworth, R. A. García, G. Houdek, C. Karoff, J. Molenda-Żakowicz, M. J. Thompson, G. A. Verner, G. Torres, F. Fressin, J. R. Crepp, E. Adams, A. Dupree, D. D. Sasselov, C. D. Dressing, W. J. Borucki, D. G. Koch, J. J. Lissauer, D. W. Latham, L. A. Buchhave, T. N. Gautier, III, M. Everett, E. Horch, N. M. Batalha, E. W. Dunham, P. Szkody, D. R. Silva, K. Mighell, J. Holberg, J. Ballot, T. R. Bedding, H. Bruntt, T. L. Campante, R. Handberg, S. Hekker, D. Huber, S. Mathur, B. Mosser, C. Régulo, T. R. White, J. L. Christiansen, C. K. Middour, M. R. Haas, J. R. Hall, J. M. Jenkins, S. McCaulif,

M. N. Fanelli, C. Kulesa, D. McCarthy, and C. E. Henze. Kepler-21b: A 1.6 R $_{Earth}$ Planet Transiting the Bright Oscillating F Subgiant Star HD 179070. *ApJ*, 746:123, Feb. 2012.

[122] H. Isaacson and D. Fischer. Chromospheric Activity and Jitter Measurements for 2630 Stars on the California Planet Search. *ApJ*, 725: 875–885, Dec. 2010.

[123] M. Janson, C. Bergfors, M. Goto, W. Brandner, and D. Lafrenière. Spatially Resolved Spectroscopy of the Exoplanet HR 8799 c. *ApJl*, 710:L35–L38, Feb. 2010.

[124] J. A. Johnson, K. M. Aller, A. W. Howard, and J. R. Crepp. Giant Planet Occurrence in the Stellar Mass-Metallicity Plane. *PASP*, 122: 905–915, Aug. 2010.

[125] L. Kaltenegger, A. Segura, and S. Mohanty. Model Spectra of the First Potentially Habitable Super-Earth Gl581d. *ApJ*, 733:35, May 2011.

[126] L. Kaltenegger and W. A. Traub. Transits of Earth-like Planets. *ApJ*, 698:519–527, June 2009.

[127] S. R. Kane, D. Dragomir, D. R. Ciardi, J.-W. Lee, G. Lo Curto, C. Lovis, D. Naef, S. Mahadevan, G. Pilyavsky, S. Udry, X. Wang, and J. Wright. Stellar Variability of the Exoplanet Hosting Star HD 63454. *ApJ*, 737:58, Aug. 2011.

[128] S. R. Kane, D. M. Gelino, D. R. Ciardi, D. Dragomir, and K. von Braun. Planetary Phase Variations of the 55 Cancri System. *ApJ*, 740:61, Oct. 2011.

[129] S. R. Kane, G. W. Henry, D. Dragomir, D. A. Fischer, A. W. Howard, X. Wang, and J. T. Wright. Revised Orbit and Transit Exclusion for HD 114762b. *ApJL*, 735:L41, July 2011.

[130] S. R. Kane, A. W. Howard, G. Pilyavsky, S. Mahadevan, G. W. Henry, K. von Braun, D. R. Ciardi, D. Dragomir, D. A. Fischer, E. Jensen, G. Laughlin, S. V. Ramirez, and J. T. Wright. Improved Orbital Parameters and Transit Monitoring for HD 156846b. *ApJ*, 733:28, May 2011.

[131] S. R. Kane, S. Mahadevan, K. von Braun, G. Laughlin, and D. R. Ciardi. Refining Exoplanet Ephemerides and Transit Observing Strategies. *PASP*, 121:1386–1394, Dec. 2009.

[132] S. R. Kane and K. von Braun. Constraining Orbital Parameters through Planetary Transit Monitoring. *ApJ*, 689:492–498, Dec. 2008.

[133] D. Kaplan. B. p. carlin & t. a. louis (2008) bayesian methods for data analysis, third edition. *Psychometrika*, 75(2):391–392, 2010. URL `http://EconPapers.repec.org/RePEc:spr:psycho:v:75:y:2010:i:2:p:391-392`.

[134] E. V. Kazarovets, N. N. Samus, O. V. Durlevich, N. N. Kireeva, and E. N. Pastukhova. The 78th Name-List of Variable Stars. *Information Bulletin on Variable Stars*, 5721:1, Aug. 2006.

[135] D. M. Kipping. Transit timing effects due to an exomoon. *MNRAS*, 392:181–189, Jan. 2009.

[136] D. M. Kipping, G. Á. Bakos, L. Buchhave, D. Nesvorný, and A. Schmitt. The Hunt for Exomoons with Kepler (HEK). I. Description of a New Observational project. *ApJ*, 750:115, May 2012.

[137] D. M. Kipping, S. J. Fossey, and G. Campanella. On the detectability of habitable exomoons with Kepler-class photometry. *MNRAS*, 400: 398–405, Nov. 2009.

[138] D. M. Kipping and D. S. Spiegel. Detection of visible light from the darkest world. *MNRAS*, 417:L88–L92, Oct. 2011.

[139] H. A. Knutson, D. Charbonneau, L. E. Allen, A. Burrows, and S. T. Megeath. The 3.6-8.0 μm Broadband Emission Spectrum of HD 209458b: Evidence for an Atmospheric Temperature Inversion. *ApJ*, 673:526–531, Jan. 2008.

[140] H. A. Knutson, D. Charbonneau, L. E. Allen, J. J. Fortney, E. Agol, N. B. Cowan, A. P. Showman, C. S. Cooper, and S. T. Megeath. A map of the day-night contrast of the extrasolar planet HD 189733b. *Nature*, 447:183–186, May 2007.

[141] H. A. Knutson, D. Charbonneau, A. Burrows, F. T. O'Donovan, and G. Mandushev. Detection of A Temperature Inversion in the Broadband Infrared Emission Spectrum of TrES-4. *ApJ*, 691:866–874, Jan. 2009.

[142] C. Koen, D. Kilkenny, F. van Wyk, and F. Marang. UBV(RI)$_C$ JHK observations of Hipparcos-selected nearby stars. *MNRAS*, 403:1949–1968, Apr. 2010.

[143] J. Korenaga. On the Likelihood of Plate Tectonics on Super-Earths: Does Size Matter? *ApJl*, 725:L43–L46, Dec. 2010.

[144] D. W. Latham, R. P. Stefanik, T. Mazeh, M. Mayor, and G. Burki. The unseen companion of HD114762 - A probable brown dwarf. *Nature*, 339:38–40, May 1989.

[145] M. G. Lattanzi, S. Casertano, S. Jancart, R. Morbidelli, D. Pourbaix, R. Pannunzio, A. Sozzetti, and A. Spagna. Detection and Characterization of Extra-Solar Planets with Gaia. In C. Turon, K. S. O'Flaherty, and M. A. C. Perryman, editors, *The Three-Dimensional Universe with Gaia*, volume 576 of *ESA Special Publication*, page 251, Jan. 2005.

[146] G. Laughlin, M. Crismani, and F. C. Adams. On the Anomalous Radii of the Transiting Extrasolar Planets. *ApJL*, 729:L7, Mar. 2011.

[147] N. M. Law, A. L. Kraus, R. Street, B. J. Fulton, L. A. Hillenbrand, A. Shporer, T. Lister, C. Baranec, J. S. Bloom, K. Bui, M. P. Burse, S. B. Cenko, H. K. Das, J. T. C. Davis, R. G. Dekany, A. V. Filippenko, M. M. Kasliwal, S. R. Kulkarni, P. Nugent, E. O. Ofek, D. Poznanski, R. M. Quimby, A. N. Ramaprakash, R. Riddle, J. M. Silverman, S. Sivanandam, and S. Tendulkar. Three New Eclipsing White-dwarf - M-dwarf Binaries Discovered in a Search for Transiting Planets Around M-dwarfs. *ArXiv e-prints*, Dec. 2011.

[148] D. A. Leahy, R. F. Elsner, and M. C. Weisskopf. On searches for periodic pulsed emission - The Rayleigh test compared to epoch folding. *ApJ*, 272:256–258, Sept. 1983.

[149] A. Léger, D. Rouan, J. Schneider, P. Barge, M. Fridlund, B. Samuel, M. Ollivier, E. Guenther, M. Deleuil, H. J. Deeg, M. Auvergne, R. Alonso, S. Aigrain, A. Alapini, J. M. Almenara, A. Baglin, M. Barbieri, H. Bruntt, P. Bordé, F. Bouchy, J. Cabrera, C. Catala, L. Carone, S. Carpano, S. Csizmadia, R. Dvorak, A. Erikson, S. Ferraz-Mello, B. Foing, F. Fressin, D. Gandolfi, M. Gillon, P. Gondoin, O. Grasset, T. Guillot, A. Hatzes, G. Hébrard, L. Jorda, H. Lammer, A. Llebaria, B. Loeillet, M. Mayor, T. Mazeh, C. Moutou, M. Pätzold,

F. Pont, D. Queloz, H. Rauer, S. Renner, R. Samadi, A. Shporer, C. Sotin, B. Tingley, G. Wuchterl, M. Adda, P. Agogu, T. Appourchaux, H. Ballans, P. Baron, T. Beaufort, R. Bellenger, R. Berlin, P. Bernardi, D. Blouin, F. Baudin, P. Bodin, L. Boisnard, L. Boit, F. Bonneau, S. Borzeix, R. Briet, J.-T. Buey, B. Butler, D. Cailleau, R. Cautain, P.-Y. Chabaud, S. Chaintreuil, F. Chiavassa, V. Costes, V. Cuna Parrho, F. de Oliveira Fialho, M. Decaudin, J.-M. Defise, S. Djalal, G. Epstein, G.-E. Exil, C. Fauré, T. Fenouillet, A. Gaboriaud, A. Gallic, P. Gamet, P. Gavalda, E. Grolleau, R. Gruneisen, L. Gueguen, V. Guis, V. Guivarc'h, P. Guterman, D. Hallouard, J. Hasiba, F. Heuripeau, G. Huntzinger, H. Hustaix, C. Imad, C. Imbert, B. Johlander, M. Jouret, P. Journoud, F. Karioty, L. Kerjean, V. Lafaille, L. Lafond, T. Lam-Trong, P. Landiech, V. Lapeyrere, T. Larqué, P. Laudet, N. Lautier, H. Lecann, L. Lefevre, B. Leruyet, P. Levacher, A. Magnan, E. Mazy, F. Mertens, J.-M. Mesnager, J.-C. Meunier, J.-P. Michel, W. Monjoin, D. Naudet, K. Nguyen-Kim, J.-L. Orcesi, H. Ottacher, R. Perez, G. Peter, P. Plasson, J.-Y. Plesseria, B. Pontet, A. Pradines, C. Quentin, J.-L. Reynaud, G. Rolland, F. Rollenhagen, R. Romagnan, N. Russ, R. Schmidt, N. Schwartz, I. Sebbag, G. Sedes, H. Smit, M. B. Steller, W. Sunter, C. Surace, M. Tello, D. Tiphène, P. Toulouse, B. Ulmer, O. Vandermarcq, E. Vergnault, A. Vuillemin, and P. Zanatta. Transiting exoplanets from the CoRoT space mission. VIII. CoRoT-7b: the first super-Earth with measured radius. *A&A*, 506:287–302, Oct. 2009.

[150] P. Lenz and M. Breger. Period04 User Guide. *Communications in Asteroseismology*, 146:53–136, June 2005.

[151] D. N. C. Lin and J. Papaloizou. On the tidal interaction between protoplanets and the protoplanetary disk. III - Orbital migration of protoplanets. *ApJ*, 309:846–857, Oct. 1986.

[152] L. Lindegren, C. Babusiaux, C. Bailer-Jones, U. Bastian, A. G. A. Brown, M. Cropper, E. Høg, C. Jordi, D. Katz, F. van Leeuwen, X. Luri, F. Mignard, J. H. J. de Bruijne, and T. Prusti. The Gaia mission: science, organization and present status. In W. J. Jin, I. Platais, and M. A. C. Perryman, editors, *IAU Symposium*, volume 248 of *IAU Symposium*, pages 217–223, July 2008.

[153] J. L. Linsky, H. Yang, K. France, C. S. Froning, J. C. Green, J. T.

Stocke, and S. N. Osterman. Observations of Mass Loss from the Transiting Exoplanet HD 209458b. *ApJ*, 717:1291–1299, July 2010.

[154] J. J. Lissauer, D. C. Fabrycky, E. B. Ford, W. J. Borucki, F. Fressin, G. W. Marcy, J. A. Orosz, J. F. Rowe, G. Torres, W. F. Welsh, N. M. Batalha, S. T. Bryson, L. A. Buchhave, D. A. Caldwell, J. A. Carter, D. Charbonneau, J. L. Christiansen, W. D. Cochran, J.-M. Desert, E. W. Dunham, M. N. Fanelli, J. J. Fortney, T. N. Gautier, III, J. C. Geary, R. L. Gilliland, M. R. Haas, J. R. Hall, M. J. Holman, D. G. Koch, D. W. Latham, E. Lopez, S. McCauliff, N. Miller, R. C. Morehead, E. V. Quintana, D. Ragozzine, D. Sasselov, D. R. Short, and J. H. Steffen. A closely packed system of low-mass, low-density planets transiting Kepler-11. *Nature*, 470:53–58, Feb. 2011.

[155] G. Lo Curto, M. Mayor, W. Benz, F. Bouchy, C. Lovis, C. Moutou, D. Naef, F. Pepe, D. Queloz, N. C. Santos, D. Segransan, and S. Udry. The HARPS search for southern extra-solar planets . XXII. Multiple planet systems from the HARPS volume limited sample. *A&A*, 512: A48, Mar. 2010.

[156] N. R. Lomb. Least-squares frequency analysis of unequally spaced data. *Ap&SS*, 39:447–462, Feb. 1976.

[157] M. López-Morales, N. I. Morrell, R. P. Butler, and S. Seager. Limits to Transits of the Neptune-Mass Planet Orbiting GJ 581. *PASP*, 118: 1506–1509, Nov. 2006.

[158] C. Lovis, M. Mayor, F. Pepe, Y. Alibert, W. Benz, F. Bouchy, A. C. M. Correia, J. Laskar, C. Mordasini, D. Queloz, N. C. Santos, S. Udry, J.-L. Bertaux, and J.-P. Sivan. An extrasolar planetary system with three Neptune-mass planets. *Nature*, 441:305–309, May 2006.

[159] P. Machalek, P. R. McCullough, A. Burrows, C. J. Burke, J. L. Hora, and C. M. Johns-Krull. Detection of Thermal Emission of XO-2b: Evidence for a Weak Temperature Inversion. *ApJ*, 701:514–520, Aug. 2009.

[160] K. Mandel and E. Agol. Analytic Light Curves for Planetary Transit Searches. *ApJL*, 580:L171–L175, Dec. 2002.

[161] R. A. Marcus, D. Sasselov, L. Hernquist, and S. T. Stewart. Minimum Radii of Super-Earths: Constraints from Giant Impacts. *ApJL*, 712: L73–L76, Mar. 2010.

[162] G. Marcy, R. P. Butler, D. Fischer, S. Vogt, J. T. Wright, C. G. Tinney, and H. R. A. Jones. Observed Properties of Exoplanets: Masses, Orbits, and Metallicities. *Progress of Theoretical Physics Supplement*, 158:24–42, 2005.

[163] G. W. Marcy and R. P. Butler. Precision radial velocities with an iodine absorption cell. *PASP*, 104:270–277, Apr. 1992.

[164] M. S. Marley, C. Gelino, D. Stephens, J. I. Lunine, and R. Freedman. Reflected Spectra and Albedos of Extrasolar Giant Planets. I. Clear and Cloudy Atmospheres. *ApJ*, 513:879–893, Mar. 1999.

[165] C. Marois, B. Macintosh, T. Barman, B. Zuckerman, I. Song, J. Patience, D. Lafrenière, and R. Doyon. Direct Imaging of Multiple Planets Orbiting the Star HR 8799. *Science*, 322:1348–, Nov. 2008.

[166] C. Marois, B. Zuckerman, Q. M. Konopacky, B. Macintosh, and T. Barman. Images of a fourth planet orbiting HR 8799. *Nature*, 468:1080–1083, Dec. 2010.

[167] J. M. Matthews, R. Kuschnig, D. B. Guenther, G. A. H. Walker, A. F. J. Moffat, S. M. Rucinski, D. Sasselov, and W. W. Weiss. No stellar p-mode oscillations in space-based photometry of Procyon. *Nature*, 430:51–53, July 2004.

[168] M. Mayor, X. Bonfils, T. Forveille, X. Delfosse, S. Udry, J.-L. Bertaux, H. Beust, F. Bouchy, C. Lovis, F. Pepe, C. Perrier, D. Queloz, and N. C. Santos. The HARPS search for southern extra-solar planets. XVIII. An Earth-mass planet in the GJ 581 planetary system. *A&A*, 507:487–494, Nov. 2009.

[169] M. Mayor, M. Marmier, C. Lovis, S. Udry, D. Ségransan, F. Pepe, W. Benz, J. . Bertaux, F. Bouchy, X. Dumusque, G. Lo Curto, C. Mordasini, D. Queloz, and N. C. Santos. The HARPS search for southern extra-solar planets XXXIV. Occurrence, mass distribution and orbital properties of super-Earths and Neptune-mass planets. *ArXiv e-prints*, Sept. 2011.

[170] M. Mayor, F. Pepe, D. Queloz, F. Bouchy, G. Rupprecht, G. Lo Curto, G. Avila, W. Benz, J.-L. Bertaux, X. Bonfils, T. Dall, H. Dekker, B. Delabre, W. Eckert, M. Fleury, A. Gilliotte, D. Gojak, J. C. Guzman, D. Kohler, J.-L. Lizon, A. Longinotti, C. Lovis, D. Megevand, L. Pasquini, J. Reyes, J.-P. Sivan, D. Sosnowska, R. Soto, S. Udry,

A. van Kesteren, L. Weber, and U. Weilenmann. Setting New Standards with HARPS. *The Messenger*, 114:20–24, Dec. 2003.

[171] M. Mayor and D. Queloz. A Jupiter-Mass Companion to a Solar-Type Star. *Nature*, 378:355–+, Nov. 1995.

[172] P. R. McCullough, J. E. Stys, J. A. Valenti, S. W. Fleming, K. A. Janes, and J. N. Heasley. The XO Project: Searching for Transiting Extrasolar Planet Candidates. *PASP*, 117:783–795, Aug. 2005.

[173] D. B. McLaughlin. Some results of a spectrographic study of the Algol system. *ApJ*, 60:22–31, July 1924.

[174] N. Metropolis, A. W. Rosenbluth, M. N. Rosenbluth, A. H. Teller, and E. Teller. Equation of State Calculations by Fast Computing Machines. *Journal of Chemical Physics*, 21:1087–1092, June 1953.

[175] C. Moutou, R. F. Díaz, S. Udry, G. Hébrard, F. Bouchy, A. Santerne, D. Ehrenreich, L. Arnold, I. Boisse, X. Bonfils, X. Delfosse, A. Eggenberger, T. Forveille, A.-M. Lagrange, C. Lovis, P. Martinez, F. Pepe, C. Perrier, D. Queloz, N. C. Santos, D. Ségransan, D. Toublanc, J. P. Troncin, M. Vanhuysse, and A. Vidal-Madjar. Spin-orbit inclinations of the exoplanetary systems HAT-P-8b, HAT-P-9b, HAT-P-16b, and HAT-P-23b. *A&A*, 533:A113, Sept. 2011.

[176] P. S. Muirhead, J. A. Johnson, K. Apps, J. A. Carter, T. D. Morton, D. C. Fabrycky, J. S. Pineda, M. Bottom, B. Rojas-Ayala, E. Schlawin, K. Hamren, K. R. Covey, J. R. Crepp, K. G. Stassun, J. Pepper, L. Hebb, E. N. Kirby, A. W. Howard, H. T. Isaacson, G. W. Marcy, D. Levitan, T. Diaz-Santos, L. Armus, and J. P. Lloyd. Characterizing the Cool KOIs. III. KOI 961: A Small Star with Large Proper Motion and Three Small Planets. *ApJ*, 747:144, Mar. 2012.

[177] N. Narita, T. Hirano, R. Sanchis-Ojeda, J. N. Winn, M. J. Holman, B. Sato, W. Aoki, and M. Tamura. The Rossiter-McLaughlin Effect of the Transiting Exoplanet XO-4b. *PASJ*, 62:L61, Dec. 2010.

[178] F. T. O'Donovan, D. Charbonneau, J. Harrington, N. Madhusudhan, S. Seager, D. Deming, and H. A. Knutson. Detection of Planetary Emission from the Exoplanet Tres-2 Using Spitzer/IRAC. *ApJ*, 710: 1551–1556, Feb. 2010.

[179] F. T. O'Donovan, D. Charbonneau, G. Mandushev, E. W. Dunham, D. W. Latham, G. Torres, A. Sozzetti, T. M. Brown, J. T. Trauger, J. A. Belmonte, M. Rabus, J. M. Almenara, R. Alonso, H. J. Deeg, G. A. Esquerdo, E. E. Falco, L. A. Hillenbrand, A. Roussanova, R. P. Stefanik, and J. N. Winn. TrES-2: The First Transiting Planet in the Kepler Field. *ApJl*, 651:L61–L64, Nov. 2006.

[180] C. O'Neill and A. Lenardic. Geological consequences of super-sized Earths. *GeoRL*, 34:19204, Oct. 2007.

[181] O. Özdarcan, S. Evren, K. G. Strassmeier, T. Granzer, and G. W. Henry. Discovery of cyclic spot activity on the G8 giant HD 208472. *Astronomische Nachrichten*, 331:794, Aug. 2010.

[182] J. C. B. Papaloizou and C. Terquem. Critical Protoplanetary Core Masses in Protoplanetary Disks and the Formation of Short-Period Giant Planets. *ApJ*, 521:823–838, Aug. 1999.

[183] F. Pepe, C. Lovis, D. Ségransan, W. Benz, F. Bouchy, X. Dumusque, M. Mayor, D. Queloz, N. C. Santos, and S. Udry. The HARPS search for Earth-like planets in the habitable zone. I. Very low-mass planets around ¡ASTROBJ¿HD 20794¡/ASTROBJ¿, ¡ASTROBJ¿HD 85512¡/ASTROBJ¿, and ¡ASTROBJ¿HD 192310¡/ASTROBJ¿. *A&A*, 534:A58, Oct. 2011.

[184] F. Pepe, M. Mayor, D. Queloz, W. Benz, X. Bonfils, F. Bouchy, G. L. Curto, C. Lovis, D. Mégevand, C. Moutou, D. Naef, G. Rupprecht, N. C. Santos, J.-P. Sivan, D. Sosnowska, and S. Udry. The HARPS search for southern extra-solar planets. I. HD 330075 b: A new "hot Jupiter". *A&A*, 423:385–389, Aug. 2004. arXiv:astro-ph/0405252.

[185] G. Pilyavsky, S. Mahadevan, S. R. Kane, A. W. Howard, D. R. Ciardi, C. de Pree, D. Dragomir, D. Fischer, G. W. Henry, E. L. N. Jensen, G. Laughlin, H. Marlowe, M. Rabus, K. von Braun, J. T. Wright, and X. X. Wang. A Search for the Transit of HD 168443b: Improved Orbital Parameters and Photometry. *ApJ*, 743:162, Dec. 2011.

[186] P. Podsiadlowski. Planet formation scenarios. In J. A. Phillips, S. E. Thorsett, and S. R. Kulkarni, editors, *Planets Around Pulsars*, volume 36 of *Astronomical Society of the Pacific Conference Series*, pages 149–165, Jan. 1993.

[187] G. Pojmanski. The All Sky Automated Survey. *AcA*, 47:467–481, Oct. 1997.

[188] D. L. Pollacco, I. Skillen, A. Collier Cameron, D. J. Christian, C. Hellier, J. Irwin, T. A. Lister, R. A. Street, R. G. West, D. Anderson, W. I. Clarkson, H. Deeg, B. Enoch, A. Evans, A. Fitzsimmons, C. A. Haswell, S. Hodgkin, K. Horne, S. R. Kane, F. P. Keenan, P. F. L. Maxted, A. J. Norton, J. Osborne, N. R. Parley, R. S. I. Ryans, B. Smalley, P. J. Wheatley, and D. M. Wilson. The WASP Project and the SuperWASP Cameras. *PASP*, 118:1407–1418, Oct. 2006.

[189] J. B. Pollack, O. Hubickyj, P. Bodenheimer, J. J. Lissauer, M. Podolak, and Y. Greenzweig. Formation of the Giant Planets by Concurrent Accretion of Solids and Gas. *Icarus*, 124:62–85, Nov. 1996.

[190] D. Queloz, G. W. Henry, J. P. Sivan, S. L. Baliunas, J. L. Beuzit, R. A. Donahue, M. Mayor, D. Naef, C. Perrier, and S. Udry. No planet for HD 166435. *A&A*, 379:279–287, Nov. 2001.

[191] S. Redfield, M. Endl, W. D. Cochran, and L. Koesterke. Sodium Absorption from the Exoplanetary Atmosphere of HD 189733b Detected in the Optical Transmission Spectrum. *ApJl*, 673:L87–L90, Jan. 2008.

[192] P. Reegen. SigSpec. I. Frequency- and phase-resolved significance in Fourier space. *A&A*, 467:1353–1371, June 2007.

[193] E. J. Rivera, R. P. Butler, S. S. Vogt, G. Laughlin, G. W. Henry, and S. Meschiari. A Super-Earth Orbiting the Nearby Sun-like Star HD 1461. *ApJ*, 708:1492–1499, Jan. 2010.

[194] E. J. Rivera, J. J. Lissauer, R. P. Butler, G. W. Marcy, S. S. Vogt, D. A. Fischer, T. M. Brown, G. Laughlin, and G. W. Henry. A $\sim$7.5 $M_\oplus$ Planet Orbiting the Nearby Star, GJ 876. *ApJ*, 634:625–640, Nov. 2005.

[195] L. A. Rogers and S. Seager. A Framework for Quantifying the Degeneracies of Exoplanet Interior Compositions. *ApJ*, 712:974–991, Apr. 2010.

[196] R. A. Rossiter. On the detection of an effect of rotation during eclipse in the velocity of the brigher component of beta Lyrae, and on the constancy of velocity of this system. *ApJ*, 60:15–21, July 1924.

[197] J. F. Rowe. *The Albedo of an Exoplanet Spacebased photometry of the transiting system HD 209458*. PhD thesis, The University of British Columbia, 2008.

[198] J. F. Rowe, J. M. Matthews, S. Seager, E. Miller-Ricci, D. Sasselov, R. Kuschnig, D. B. Guenther, A. F. J. Moffat, S. M. Rucinski, G. A. H. Walker, and W. W. Weiss. The Very Low Albedo of an Extrasolar Planet: MOST Space-based Photometry of HD 209458. *ApJ*, 689: 1345–1353, Dec. 2008.

[199] S. M. Rucinski, G. A. H. Walker, J. M. Matthews, R. Kuschnig, E. Shkolnik, S. Marchenko, D. A. Bohlender, D. B. Guenther, A. F. J. Moffat, D. Sasselov, and W. W. Weiss. Differential Rotation of the Active G5 V Star κ^1 Ceti: Photometry from the MOST Satellite. *PASP*, 116:1093–1104, Dec. 2004.

[200] S. H. Saar, R. P. Butler, and G. W. Marcy. Magnetic Activity-related Radial Velocity Variations in Cool Stars: First Results from the Lick Extrasolar Planet Survey. *ApJL*, 498:L153, May 1998.

[201] P. D. Sackett. Searching for Unseen Planets via Occultation and Microlensing. In J.-M. Mariotti and D. Alloin, editors, *NATO ASIC Proc. 532: Planets Outside the Solar System: Theory and Observations*, page 189, 1999.

[202] C. Saffe, M. Gómez, and C. Chavero. On the ages of exoplanet host stars. *A&A*, 443:609–626, Nov. 2005.

[203] R. Sanchis-Ojeda, D. C. Fabrycky, J. N. Winn, T. Barclay, B. D. Clarke, E. B. Ford, J. J. Fortney, J. C. Geary, M. J. Holman, A. W. Howard, J. M. Jenkins, D. Koch, J. J. Lissauer, G. W. Marcy, F. Mullally, D. Ragozzine, S. E. Seader, M. Still, and S. E. Thompson. Alignment of the stellar spin with the orbits of a three-planet system. *Nature*, 487:449–453, July 2012.

[204] N. C. Santos, W. Benz, and M. Mayor. Extrasolar Planets: Constraints for Planet Formation Models. *Science*, 310:251–255, Oct. 2005.

[205] N. C. Santos, M. Mayor, D. Naef, F. Pepe, D. Queloz, S. Udry, M. Burnet, and Y. Revaz. The CORALIE survey for Southern extra-solar planets. III. A giant planet in orbit around HD 192263. *A&A*, 356: 599–602, Apr. 2000.

[206] N. C. Santos, S. Udry, M. Mayor, D. Naef, F. Pepe, D. Queloz, G. Burki, N. Cramer, and B. Nicolet. The CORALIE survey for southern extra-solar planets. XI. The return of the giant planet orbiting HD 192263. *A&A*, 406:373–381, July 2003.

[207] J. Scalo, L. Kaltenegger, A. G. Segura, M. Fridlund, I. Ribas, Y. N. Kulikov, J. L. Grenfell, H. Rauer, P. Odert, M. Leitzinger, F. Selsis, M. L. Khodachenko, C. Eiroa, J. Kasting, and H. Lammer. M Stars as Targets for Terrestrial Exoplanet Searches And Biosignature Detection. *Astrobiology*, 7:85–166, Feb. 2007.

[208] J. D. Scargle. Studies in astronomical time series analysis. II - Statistical aspects of spectral analysis of unevenly spaced data. *ApJ*, 263: 835–853, Dec. 1982.

[209] K. C. Schlaufman and G. Laughlin. Kepler Exoplanet Candidate Host Stars Are Preferentially Metal Rich. *ApJ*, 738:177, Sept. 2011.

[210] E. Schlawin, E. Agol, L. M. Walkowicz, K. Covey, and J. P. Lloyd. Exoplanetary Transits of Limb-brightened Lines: Tentative Si IV Absorption by HD 209458b. *ApJl*, 722:L75–L79, Oct. 2010.

[211] S. Seager, D. Deming, and J. A. Valenti. *Transiting Exoplanets with JWST*, page 123. 2009.

[212] S. Seager, M. Kuchner, C. A. Hier-Majumder, and B. Militzer. Mass-Radius Relationships for Solid Exoplanets. *ApJ*, 669:1279–1297, Nov. 2007.

[213] S. Seager, B. A. Whitney, and D. D. Sasselov. Photometric Light Curves and Polarization of Close-in Extrasolar Giant Planets. *ApJ*, 540:504–520, Sept. 2000.

[214] D. Ségransan, M. Mayor, S. Udry, C. Lovis, W. Benz, F. Bouchy, G. Lo Curto, C. Mordasini, C. Moutou, D. Naef, F. Pepe, D. Queloz, and N. Santos. The HARPS search for southern extra-solar planets. XXIX. Four new planets in orbit around the moderatly active dwarfs ¡ASTROBJ¿HD 63765¡/ASTROBJ¿, ¡ASTROBJ¿HD 104067¡/ASTROBJ¿, ¡ASTROBJ¿HD 125595¡/ASTROBJ¿, and ¡ASTROBJ¿HIP 70849¡/ASTROBJ¿. *A&A*, 535:A54, Nov. 2011.

[215] F. Selsis, J. F. Kasting, B. Levrard, J. Paillet, I. Ribas, and X. Delfosse. Habitable planets around the star Gliese 581? *A&A*, 476:1373–1387, Dec. 2007.

[216] S. Sigurdsson, H. B. Richer, B. M. Hansen, I. H. Stairs, and S. E. Thorsett. A Young White Dwarf Companion to Pulsar B1620-26: Evidence for Early Planet Formation. *Science*, 301:193–196, July 2003.

[217] E. K. Simpson, D. Pollacco, A. C. Cameron, G. Hébrard, D. R. Anderson, S. C. C. Barros, I. Boisse, F. Bouchy, F. Faedi, M. Gillon, L. Hebb, F. P. Keenan, G. R. M. Miller, C. Moutou, D. Queloz, I. Skillen, P. Sorensen, H. C. Stempels, A. Triaud, C. A. Watson, and P. A. Wilson. The spin-orbit angles of the transiting exoplanets WASP-1b, WASP-24b, WASP-38b and HAT-P-8b from Rossiter-McLaughlin observations. *MNRAS*, 414:3023–3035, July 2011.

[218] D. K. Sing, J.-M. Désert, J. J. Fortney, A. Lecavelier Des Etangs, G. E. Ballester, J. Cepa, D. Ehrenreich, M. López-Morales, F. Pont, M. Shabram, and A. Vidal-Madjar. Gran Telescopio Canarias OSIRIS transiting exoplanet atmospheric survey: detection of potassium in XO-2b from narrowband spectrophotometry. *A&A*, 527:A73, Mar. 2011.

[219] D. S. Sivia. *Data Analysis: a Bayesian tutorial*. 1996. URL `http://epubs.cclrc.ac.uk/work-details?w=7324`.

[220] I. A. G. Snellen, R. J. de Kok, E. J. W. de Mooij, and S. Albrecht. The orbital motion, absolute mass and high-altitude winds of exoplanet HD209458b. *Nature*, 465:1049–1051, June 2010.

[221] I. A. G. Snellen, E. J. W. de Mooij, and S. Albrecht. The changing phases of extrasolar planet CoRoT-1b. *Nature*, 459:543–545, May 2009.

[222] C. Sotin and G. Schubert. Mantle convection and plate tectonics on Earth-like exoplanets. *AGU Fall Meeting Abstracts*, page B2, Dec. 2009.

[223] J. Southworth. Homogeneous studies of transiting extrasolar planets - III. Additional planets and stellar models. *MNRAS*, 408:1689–1713, Nov. 2010.

[224] R. F. Stellingwerf. Period determination using phase dispersion minimization. *ApJ*, 224:953–960, Sept. 1978.

[225] K. G. Strassmeier. Stellar activity cycles: observing the dynamo? *Astronomische Nachrichten*, 326:269–277, Apr. 2005.

[226] D. Sudarsky, A. Burrows, and I. Hubeny. Theoretical Spectra and Atmospheres of Extrasolar Giant Planets. *ApJ*, 588:1121–1148, May 2003.

[227] D. Sudarsky, A. Burrows, and P. Pinto. Albedo and Reflection Spectra of Extrasolar Giant Planets. *ApJ*, 538:885–903, Aug. 2000.

[228] M. R. Swain. Finesse - A New Mission Concept For Exoplanet Spectroscopy. In *AAS/Division for Planetary Sciences Meeting Abstracts 42*, volume 42 of *Bulletin of the American Astronomical Society*, page 1064, Oct. 2010.

[229] M. R. Swain, G. Tinetti, G. Vasisht, P. Deroo, C. Griffith, J. Bouwman, P. Chen, Y. Yung, A. Burrows, L. R. Brown, J. Matthews, J. F. Rowe, R. Kuschnig, and D. Angerhausen. Water, Methane, and Carbon Dioxide Present in the Dayside Spectrum of the Exoplanet HD 209458b. *ApJ*, 704:1616–1621, Oct. 2009.

[230] M. R. Swain, G. Vasisht, and G. Tinetti. The presence of methane in the atmosphere of an extrasolar planet. *Nature*, 452:329–331, Mar. 2008.

[231] G. Takeda, E. B. Ford, A. Sills, F. A. Rasio, D. A. Fischer, and J. A. Valenti. Structure and Evolution of Nearby Stars with Planets. II. Physical Properties of ˜1000 Cool Stars from the SPOCS Catalog. *ApJS*, 168:297–318, Feb. 2007. arXiv:astro-ph/0607235.

[232] G. Tinetti, J. P. Beaulieu, T. Henning, M. Meyer, G. Micela, I. Ribas, D. Stam, M. Swain, O. Krause, M. Ollivier, E. Pace, B. Swinyard, A. Aylward, R. van Boekel, A. Coradini, T. Encrenaz, I. Snellen, M. R. Zapatero-Osorio, J. Bouwman, J. Y-K. Cho, V. Coudé du Foresto, T. Guillot, M. Lopez-Morales, I. Mueller-Wodarg, E. Palle, F. Selsis, A. Sozzetti, P. A. R. Ade, N. Achilleos, A. Adriani, C. B. Agnor, C. Afonso, C. Allende Prieto, G. Bakos, R. J. Barber, M. Barlow, P. Bernath, B. Bezard, P. Bordé, L. R. Brown, A. Cassan, C. Cavarroc, A. Ciaravella, C. O. U. Cockell, A. Coustenis, C. Danielski, L. Decin, R. De Kok, O. Demangeon, P. Deroo, P. Doel, P. Drossart, L. N. Fletcher, M. Focardi, F. Forget, S. Fossey, P. Fouqué, J. Frith, M. Galand, P. Gaulme, J. I. González Hernández, O. Grasset, D. Grassi, J. L. Grenfell, M. J. Griffin, C. A. Griffith, U. Grözinger, M. Guedel, P. Guio, O. Hainaut, R. Hargreaves, P. H. Hauschildt, K. Heng,

D. Heyrovsky, R. Hueso, P. Irwin, L. Kaltenegger, P. Kervella, D. Kipping, T. T. Koskinen, G. Kovács, A. La Barbera, H. Lammer, E. Lellouch, G. Leto, M. Lopez Morales, M. A. Lopez Valverde, M. Lopez-Puertas, C. Lovis, A. Maggio, J. P. Maillard, J. Maldonado Prado, J. B. Marquette, F. J. Martin-Torres, P. Maxted, S. Miller, S. Molinari, D. Montes, A. Moro-Martin, J. I. Moses, O. Mousis, N. Nguyen Tuong, R. Nelson, G. S. Orton, E. Pantin, E. Pascale, S. Pezzuto, D. Pinfield, E. Poretti, R. Prinja, L. Prisinzano, J. M. Rees, A. Reiners, B. Samuel, A. Sanchez-Lavega, J. Sanz Forcada, D. Sasselov, G. Savini, B. Sicardy, A. Smith, L. Stixrude, G. Strazzulla, J. Tennyson, M. Tessenyi, G. Vasisht, S. Vinatier, S. Viti, I. Waldmann, G. J. White, T. Widemann, R. Wordsworth, R. Yelle, Y. Yung, and S. N. Yurchenko. EChO - Exoplanet Characterisation Observatory. *ArXiv e-prints*, Dec. 2011.

[233] G. Tinetti, A. Vidal-Madjar, M.-C. Liang, J.-P. Beaulieu, Y. Yung, S. Carey, R. J. Barber, J. Tennyson, I. Ribas, N. Allard, G. E. Ballester, D. K. Sing, and F. Selsis. Water vapour in the atmosphere of a transiting extrasolar planet. *Nature*, 448:169–171, July 2007.

[234] B. Tingley, M. Endl, J.-C. Gazzano, R. Alonso, T. Mazeh, L. Jorda, S. Aigrain, J.-M. Almenara, M. Auvergne, A. Baglin, P. Barge, A. S. Bonomo, P. Bordé, F. Bouchy, H. Bruntt, J. Cabrera, S. Carpano, L. Carone, W. D. Cochran, S. Csizmadia, M. Deleuil, H. J. Deeg, R. Dvorak, A. Erikson, S. Ferraz-Mello, M. Fridlund, D. Gandolfi, M. Gillon, E. W. Guenther, T. Guillot, A. Hatzes, G. Hébrard, A. Léger, A. Llebaria, H. Lammer, C. Lovis, P. J. MacQueen, C. Moutou, M. Ollivier, A. Ofir, M. Pätzold, F. Pepe, D. Queloz, H. Rauer, D. Rouan, B. Samuel, J. Schneider, A. Shporer, and G. Wuchterl. Transiting exoplanets from the CoRoT space mission. XVI. CoRoT-14b: an unusually dense very hot Jupiter. *A&A*, 528: A97, Apr. 2011.

[235] G. Torres, J. Andersen, and A. Giménez. Accurate masses and radii of normal stars: modern results and applications. *A&ARv*, 18:67–126, Feb. 2010.

[236] A. H. M. J. Triaud, A. Collier Cameron, D. Queloz, D. R. Anderson, M. Gillon, L. Hebb, C. Hellier, B. Loeillet, P. F. L. Maxted, M. Mayor, F. Pepe, D. Pollacco, D. Ségransan, B. Smalley, S. Udry, R. G. West, and P. J. Wheatley. Spin-orbit angle measurements for six south-

ern transiting planets. New insights into the dynamical origins of hot Jupiters. *A&A*, 524:A25, Dec. 2010.

[237] M. Tuomi. Bayesian re-analysis of the radial velocities of Gliese 581. Evidence in favour of only four planetary companions. *A&A*, 528:L5, Apr. 2011.

[238] L. R. M. Tusnski and A. Valio. Transit Model of Planets with Moon and Ring Systems. *ApJ*, 743:97, Dec. 2011.

[239] S. Udry, X. Bonfils, X. Delfosse, T. Forveille, M. Mayor, C. Perrier, F. Bouchy, C. Lovis, F. Pepe, D. Queloz, and J.-L. Bertaux. The HARPS search for southern extra-solar planets. XI. Super-Earths (5 and 8 $M_{\oplus}$) in a 3-planet system. *A&A*, 469:L43–L47, July 2007.

[240] S. Udry, M. Mayor, D. Naef, F. Pepe, D. Queloz, N. C. Santos, M. Burnet, B. Confino, and C. Melo. The CORALIE survey for southern extra-solar planets. II. The short-period planetary companions to ¡ASTROBJ¿HD 75289¡/ASTROBJ¿ and ¡ASTROBJ¿HD 130322¡/ASTROBJ¿. *A&A*, 356:590–598, Apr. 2000.

[241] D. Valencia, M. Ikoma, T. Guillot, and N. Nettelmann. Composition and fate of short-period super-Earths. The case of CoRoT-7b. *A&A*, 516:A20, June 2010.

[242] D. Valencia, R. J. O'Connell, and D. D. Sasselov. Evolution of Super-Earths. *AGU Fall Meeting Abstracts*, page A3, Dec. 2007.

[243] D. Valencia, R. J. O'Connell, and D. D. Sasselov. Inevitability of Plate Tectonics on Super-Earths. *ApJl*, 670:L45–L48, Nov. 2007.

[244] D. Valencia, D. D. Sasselov, and R. J. O'Connell. Detailed Models of Super-Earths: How Well Can We Infer Bulk Properties? *ApJ*, 665: 1413–1420, Aug. 2007.

[245] J. A. Valenti, D. Fischer, G. W. Marcy, J. A. Johnson, G. W. Henry, J. T. Wright, A. W. Howard, M. Giguere, and H. Isaacson. Two Exoplanets Discovered at Keck Observatory. *ApJ*, 702:989–997, Sept. 2009.

[246] J. A. Valenti and D. A. Fischer. Spectroscopic Properties of Cool Stars (SPOCS). I. 1040 F, G, and K Dwarfs from Keck, Lick, and AAT Planet Search Programs. *ApJS*, 159:141–166, July 2005.

[247] G. T. van Belle and K. von Braun. Directly Determined Linear Radii and Effective Temperatures of Exoplanet Host Stars. *ApJ*, 694:1085–1098, Apr. 2009.

[248] A. Vidal-Madjar, J.-M. Désert, A. Lecavelier des Etangs, G. Hébrard, G. E. Ballester, D. Ehrenreich, R. Ferlet, J. C. McConnell, M. Mayor, and C. D. Parkinson. Detection of Oxygen and Carbon in the Hydrodynamically Escaping Atmosphere of the Extrasolar Planet HD 209458b. *ApJl*, 604:L69–L72, Mar. 2004.

[249] S. S. Vogt, S. L. Allen, B. C. Bigelow, L. Bresee, B. Brown, T. Cantrall, A. Conrad, M. Couture, C. Delaney, H. W. Epps, D. Hilyard, D. F. Hilyard, E. Horn, N. Jern, D. Kanto, M. J. Keane, R. I. Kibrick, J. W. Lewis, J. Osborne, G. H. Pardeilhan, T. Pfister, T. Ricketts, L. B. Robinson, R. J. Stover, D. Tucker, J. Ward, and M. Z. Wei. HIRES: the high-resolution echelle spectrometer on the Keck 10-m Telescope. In D. L. Crawford and E. R. Craine, editors, *Society of Photo-Optical Instrumentation Engineers (SPIE) Conference Series*, volume 2198 of *Society of Photo-Optical Instrumentation Engineers (SPIE) Conference Series*, page 362, June 1994.

[250] S. S. Vogt, R. P. Butler, E. J. Rivera, N. Haghighipour, G. W. Henry, and M. H. Williamson. The Lick-Carnegie Exoplanet Survey: A 3.1 $M_\oplus$ Planet in the Habitable Zone of the Nearby M3V Star Gliese 581. *ApJ*, 723:954–965, Nov. 2010.

[251] S. S. Vogt, G. W. Marcy, R. P. Butler, and K. Apps. Six New Planets from the Keck Precision Velocity Survey. *ApJ*, 536:902–914, June 2000. arXiv:astro-ph/9911506.

[252] S. S. Vogt, R. A. Wittenmyer, R. P. Butler, S. O'Toole, G. W. Henry, E. J. Rivera, S. Meschiari, G. Laughlin, C. G. Tinney, H. R. A. Jones, J. Bailey, B. D. Carter, and K. Batygin. A Super-Earth and Two Neptunes Orbiting the Nearby Sun-like Star 61 Virginis. *ApJ*, 708: 1366–1375, Jan. 2010.

[253] W. von Bloh, C. Bounama, M. Cuntz, and S. Franck. The habitability of super-Earths in Gliese 581. *A&A*, 476:1365–1371, Dec. 2007.

[254] K. von Braun, T. S. Boyajian, S. R. Kane, G. T. van Belle, D. R. Ciardi, M. López-Morales, H. A. McAlister, T. J. Henry, W.-C. Jao, A. R. Riedel, J. P. Subasavage, G. Schaefer, T. A. ten Brummelaar,

S. Ridgway, L. Sturmann, J. Sturmann, J. Mazingue, N. H. Turner, C. Farrington, P. J. Goldfinger, and A. F. Boden. Astrophysical Parameters and Habitable Zone of the Exoplanet Hosting Star GJ 581. *ApJL*, 729:L26, Mar. 2011.

[255] K. von Braun, T. S. Boyajian, T. A. ten Brummelaar, S. R. Kane, G. T. van Belle, D. R. Ciardi, S. N. Raymond, M. López-Morales, H. A. McAlister, G. Schaefer, S. T. Ridgway, L. Sturmann, J. Sturmann, R. White, N. H. Turner, C. Farrington, and P. J. Goldfinger. 55 Cancri: Stellar Astrophysical Parameters, a Planet in the Habitable Zone, and Implications for the Radius of a Transiting Super-Earth. *ApJ*, 740:49, Oct. 2011.

[256] P. von Paris, S. Gebauer, M. Godolt, H. Rauer, and B. Stracke. Atmospheric studies of habitability in the Gliese 581 system. *A&A*, 532: A58, Aug. 2011.

[257] G. Walker, J. Matthews, R. Kuschnig, R. Johnson, S. Rucinski, J. Pazder, G. Burley, A. Walker, K. Skaret, R. Zee, S. Grocott, K. Carroll, P. Sinclair, D. Sturgeon, and J. Harron. The MOST Asteroseismology Mission: Ultraprecise Photometry from Space. *PASP*, 115: 1023–1035, Sept. 2003.

[258] G. A. H. Walker, B. Croll, J. M. Matthews, R. Kuschnig, D. Huber, W. W. Weiss, E. Shkolnik, S. M. Rucinski, D. B. Guenther, A. F. J. Moffat, and D. Sasselov. MOST detects variability on τ Bootis A possibly induced by its planetary companion. *A&A*, 482:691–697, May 2008.

[259] W. R. Ward. Protoplanet Migration by Nebula Tides. *Icarus*, 126: 261–281, Apr. 1997.

[260] W. F. Welsh, J. A. Orosz, J. A. Carter, D. C. Fabrycky, E. B. Ford, J. J. Lissauer, A. Prša, S. N. Quinn, D. Ragozzine, D. R. Short, G. Torres, J. N. Winn, L. R. Doyle, T. Barclay, N. Batalha, S. Bloemen, E. Brugamyer, L. A. Buchhave, C. Caldwell, D. A. Caldwell, J. L. Christiansen, D. R. Ciardi, W. D. Cochran, M. Endl, J. J. Fortney, T. N. Gautier, III, R. L. Gilliland, M. R. Haas, J. R. Hall, M. J. Holman, A. W. Howard, S. B. Howell, H. Isaacson, J. M. Jenkins, T. C. Klaus, D. W. Latham, J. Li, G. W. Marcy, T. Mazeh, E. V. Quintana, P. Robertson, A. Shporer, J. H. Steffen, G. Windmiller, D. G. Koch,

and W. J. Borucki. Transiting circumbinary planets Kepler-34 b and Kepler-35 b. *Nature*, 481:475–479, Jan. 2012.

[261] J. N. Winn, J. A. Johnson, A. W. Howard, G. W. Marcy, H. Isaacson, A. Shporer, G. Á. Bakos, J. D. Hartman, and S. Albrecht. The Oblique Orbit of the Super-Neptune HAT-P-11b. *ApJl*, 723:L223–L227, Nov. 2010.

[262] J. N. Winn, J. M. Matthews, R. I. Dawson, D. Fabrycky, M. J. Holman, T. Kallinger, R. Kuschnig, D. Sasselov, D. Dragomir, D. B. Guenther, A. F. J. Moffat, J. F. Rowe, S. Rucinski, and W. W. Weiss. A Super-Earth Transiting a Naked-eye Star. *ApJl*, 737:L18, Aug. 2011.

[263] A. Wolszczan. Confirmation of Earth-Mass Planets Orbiting the Millisecond Pulsar PSR B1257+12. *Science*, 264:538–542, Apr. 1994.

[264] A. Wolszczan and D. A. Frail. A planetary system around the millisecond pulsar PSR1257 + 12. *Nature*, 355:145–147, Jan. 1992.

[265] P. L. Wood, P. F. L. Maxted, B. Smalley, and N. Iro. Transmission spectroscopy of the sodium 'D' doublet in WASP-17b with the VLT. *MNRAS*, 412:2376–2382, Apr. 2011.

[266] R. D. Wordsworth, F. Forget, F. Selsis, E. Millour, B. Charnay, and J.-B. Madeleine. Gliese 581d is the First Discovered Terrestrial-mass Exoplanet in the Habitable Zone. *ApJl*, 733:L48, June 2011.

[267] J. T. Wright. Radial Velocity Jitter in Stars from the California and Carnegie Planet Search at Keck Observatory. *PASP*, 117:657–664, July 2005.

[268] J. T. Wright, O. Fakhouri, G. W. Marcy, E. Han, Y. Feng, J. A. Johnson, A. W. Howard, D. A. Fischer, J. A. Valenti, J. Anderson, and N. Piskunov. The Exoplanet Orbit Database. *PASP*, 123:412–422, Apr. 2011.

[269] J. T. Wright and A. W. Howard. Efficient Fitting of Multiplanet Keplerian Models to Radial Velocity and Astrometry Data. *ApJS*, 182:205–215, May 2009.

[270] A. N. Youdin and J. L. Mitchell. The Mechanical Greenhouse: Burial of Heat by Turbulence in Hot Jupiter Atmospheres. *ApJ*, 721:1113–1126, Oct. 2010.

Appendix A

Radial Velocity Tables

Table A.1: CORALIE radial velocities for HD 192263

Date BJD − 2440000	**Radial velocity ($\mathbf{m\,s^{-1}}$)**	**Uncertainty ($\mathbf{m\,s^{-1}}$)**
11355.814795	-64	4
11367.830021	10	12
11375.760201	-10	13
11381.750648	-69	7
11384.720313	-81	6
11390.738894	16	7
11392.646847	33	6
11394.684897	32	7
11398.728189	13	8
11399.700985	5	7
11400.692008	-13	7
11401.642891	-31	7
11402.709269	-56	15
11403.731085	-65	10
11404.652856	-67	8
11407.652090	-75	11
11408.638923	-78	8
11415.737748	42	13
11416.649804	23	5
11417.616162	28	5
11418.648187	47	7
11423.644434	26	5
11431.702277	-90	7
11433.617802	-79	6
11435.578158	-69	9
11436.563670	-32	8
11437.558242	-14	6
11438.589061	-6	5
11439.578701	9	10
11441.617916	38	7

Continued on next page

Table A.1 – continued from previous page

Date BJD − 2440000	**Radial velocity ($m\,s^{-1}$)**	**Uncertainty ($m\,s^{-1}$)**
11442.601315	26	6
11443.544670	47	6
11444.598305	44	8
11445.500816	47	12
11445.567547	30	5
11446.538281	22	8
11447.637500	0	10
11450.582598	-52	7
11451.593834	-59	5
11454.506436	-83	11
11455.500645	-74	12
11456.510396	-69	11
11456.525164	-66	12
11458.543541	-98	7
11460.566233	-32	8
11464.509627	11	6
11480.545571	-81	11
11481.548543	-67	9
11482.509332	-95	14
11487.540488	7	10
11488.533878	7	8
11489.514319	33	10
11492.528817	52	11
11493.513020	53	11
11494.510104	25	10
11497.516160	0	12
11501.527489	-66	15
11632.900498	10	6
11635.880323	49	10
11635.901609	21	8
11638.892332	55	7
11638.912611	38	6
11640.891269	34	7
11640.907197	32	6
11641.898813	25	7
11645.898571	-38	6
11692.899007	-2	7
11696.871596	-79	8
11699.894033	-74	11
11700.759547	-64	7
11701.883158	-57	8

Continued on next page

Table A.1 – continued from previous page

Date BJD − 2440000	**Radial velocity ($m\,s^{-1}$)**	**Uncertainty ($m\,s^{-1}$)**
11702.811441	-47	10
11749.758293	-67	6
11751.748764	-63	7
11752.831521	-61	8
11753.785607	-25	7
11755.609713	14	9
11756.684211	25	8
11757.644309	50	9
11758.668133	34	9
11759.749373	39	7
11774.674217	-49	8
11777.645005	-25	8
11780.599102	33	15
11782.691547	38	10
11783.601344	38	9
11784.587387	57	11
11786.655597	52	7
11788.657937	1	7
11789.624691	-6	6
11790.548703	-18	7
11791.586226	-38	6
11792.620010	-35	8
11793.549007	-70	9
11794.584698	-83	8
11795.546271	-82	7
11802.608703	-24	9
11830.527909	27	8
11837.567940	-3	9
11838.514912	-8	8
11844.522342	-84	6
11859.538465	52	11
11993.889586	-69	13
11994.885095	-36	10
11995.883729	-8	15
11996.905017	-16	7
11997.891430	-7	12
12000.916073	33	11
12005.898775	20	12
12046.847439	-6	11
12049.896650	22	11
12052.852097	27	13

Continued on next page

Table A.1 – continued from previous page

Date BJD − 2440000	**Radial velocity ($m\,s^{-1}$)**	**Uncertainty ($m\,s^{-1}$)**
12054.932373	3	15
12079.756010	33	10
12086.824065	-57	5
12091.738542	-58	6
12094.745464	-9	6
12105.698104	19	5
12145.668129	6	8
12160.619908	-51	6
12161.634753	-57	11
12162.618834	-74	5
12167.581677	-30	4
12168.591571	-11	6
12169.619022	13	8
12170.656193	11	6
12171.584447	42	7
12172.631916	25	6
12173.642661	31	5
12175.639314	31	8
12177.617597	20	8
12180.599174	-23	7
12183.533005	-59	9
12184.602730	-62	6
12187.505756	-75	5
12187.505756	-75	5
12189.573805	-55	5
12194.539796	22	4
12195.526211	23	4
12224.536314	36	4
12226.501689	18	7
12399.877237	-25	4
12406.892322	-72	5
12434.799636	-16	5
12435.837774	-16	7
12439.802744	57	6
12440.800132	70	5
12441.754566	62	6
12443.805811	46	6
12444.819156	39	5
12448.802684	-20	5
12453.818657	-54	4
12458.771238	-24	4

Continued on next page

Table A.1 – continued from previous page

Date BJD − 2440000	**Radial velocity ($m\,s^{-1}$)**	**Uncertainty ($m\,s^{-1}$)**
12460.661609	9	5
12461.790051	36	6
12461.841025	37	5
12462.728404	41	5
12463.735566	54	4
12464.774891	53	5
12465.732720	54	4
12466.724738	57	6
12466.738245	66	6
12467.779013	45	5
12467.792648	48	5
12487.702588	32	9
12494.668169	27	7
12496.716824	-2	5
12497.657638	-19	4
12498.649699	-37	4
12499.681863	-45	4
12546.575570	-32	7
12548.557269	-28	5
12550.531685	-52	5
12553.532491	-42	12
12554.625416	-41	5
12558.541907	0	5
12560.522063	1	5
12564.554910	61	5
12568.536274	18	6
12590.554966	37	5
12593.554379	-15	6

Table A.2: Keck radial velocities for HD 192263

Date BJD − 2440000	**Radial Velocity m s^{-1})**	**Uncertainty m s^{-1})**
10984.063121	32.75	1.30
11011.914062	-11.45	1.28
11050.879437	26.96	1.38
11069.890238	-32.85	1.16
11312.086411	-56.44	1.23
11313.112603	-49.31	1.30
11342.057784	16.00	1.71
11342.983844	27.90	2.17
11367.915954	39.38	1.77
11409.933630	-39.58	1.96
11411.879482	-13.05	1.58
11438.769456	18.80	1.60
11439.828250	28.04	1.72
11440.887793	30.68	1.87
11441.833444	42.11	1.62
11704.020541	-30.66	1.67
11793.833579	-55.58	1.84
12004.133959	34.71	2.13
12008.138984	7.54	1.45
12031.056206	15.41	1.54
12063.060897	-46.80	1.72
12094.907368	-2.04	1.54
12128.910768	30.51	2.13
12391.141713	47.72	1.87
12536.755506	31.62	1.53
12778.109319	10.06	1.36
12833.916425	42.13	1.63
12853.999751	17.87	1.59
13181.024857	-37.53	1.33
13239.861434	-4.41	1.04
13546.990720	-45.96	1.05
13969.022212	**-19.25**	**0.83**
14810.722283	**1.86**	**1.14**
15043.798793	**-5.86**	**1.04**
15412.021408	**37.22**	**0.85**
15782.862190	**33.76**	**0.98**

The values in bold are the five new RV measurements I report in this Chapter.

Table A.3: Radial velocities and S_{HK} values for HD 97658

Date BJD − 2440000	**Radial velocity ($\mathbf{m\,s^{-1}}$)**	**Uncertainty ($\mathbf{m\,s^{-1}}$)**	S_{HK}
13398.04020	7.64	0.65	0.1970
13748.03542	4.88	0.72	0.1900
13806.96146	2.67	0.71	0.1870
14085.15884	-4.74	0.80	0.1785
14246.87816	-2.15	0.73	0.1760
14247.83980	-4.67	0.94	0.1750
14248.94470	-2.76	1.08	0.1690
14249.80244	0.19	1.09	0.1740
14250.83983	1.60	0.98	0.1740
14251.89455	-0.07	0.95	0.1720
14255.87144	-0.86	0.73	0.1735
14277.81740	-0.86	0.99	0.1770
14278.83838	0.21	0.99	0.1750
14279.83000	2.37	1.01	0.1760
14294.76351	-5.33	1.11	0.1690
14300.74175	-0.33	1.02	0.1720
14304.76223	-5.64	1.17	0.1740
14305.75803	-4.99	0.80	0.1740
14306.77175	-4.08	1.02	0.1690
14307.74766	-0.86	0.78	0.1750
14308.75036	2.43	0.75	0.1755
14309.74773	1.42	1.07	0.1760
14310.74343	-0.04	1.03	0.1750
14311.74391	4.39	1.14	0.1760
14312.74242	-2.21	1.03	0.1770
14313.74419	-1.17	1.21	0.1780
14314.75074	-0.18	1.14	0.1740
14455.15432	-5.21	1.11	0.1820
14635.79759	0.71	0.98	0.1750
14780.12544	-3.78	1.12	0.1770
14807.09051	-7.73	1.22	0.1730
14808.15781	-4.54	1.27	0.1710
14809.14349	-1.62	1.16	0.1730
14810.02507	1.49	1.25	0.1730
14811.11469	-2.60	1.31	0.1730
14847.11818	-2.56	1.34	0.1720
14927.89832	-1.20	1.19	0.1700
14928.96319	-9.26	1.13	0.1700
14929.84171	-7.82	1.30	0.1690
14954.97010	0.11	1.10	0.1710

Continued on next page

Table A.3 – continued from previous page

Date BJD − 2440000	**Radial velocity ($\mathrm{m\,s^{-1}}$)**	**Uncertainty ($\mathrm{m\,s^{-1}}$)**	S_{HK}
14955.92354	0.96	0.59	0.1723
14956.90526	1.39	0.59	0.1717
14963.96620	1.93	0.62	0.1687
14983.87422	-1.21	0.65	0.1703
14984.90305	-0.54	0.66	0.1710
14985.84495	-4.02	0.65	0.1710
14986.88981	-3.70	0.65	0.1697
14987.89641	-4.37	0.64	0.1697
14988.84295	-5.79	0.65	0.1703
15041.75244	0.94	1.33	0.1690
15164.11579	0.94	1.25	0.1730
15188.15834	-3.08	0.73	0.1703
15190.13345	-6.56	0.64	0.1703
15191.15996	-4.79	0.69	0.1700
15192.12876	-1.09	0.63	0.1713
15193.11580	1.12	0.66	0.1720
15197.14377	-1.99	0.66	0.1713
15198.06458	-3.50	0.67	0.1720
15199.08947	-3.56	0.65	0.1723
15256.95734	3.02	0.68	0.1800
15285.94174	-2.27	0.71	0.1750
15289.83018	-1.17	0.61	0.1780
15311.78391	-5.57	0.68	0.1730
15312.85871	-3.88	0.57	0.1727
15313.76705	0.42	0.64	0.1723
15314.78098	1.12	0.67	0.1723
15317.96171	0.24	0.65	0.1740
15318.94529	-2.79	0.66	0.1747
15319.90227	-4.81	0.59	0.1763
15320.86046	-4.60	0.58	0.1800
15321.83394	-1.08	0.59	0.1807
15342.87709	-1.85	0.62	0.1757
15343.83030	-1.12	0.64	0.1757
15344.87915	1.23	0.66	0.1750
15350.78148	-4.43	0.58	0.1730
15351.88523	0.64	0.60	0.1740
15372.75567	2.46	0.59	0.1790
15373.78450	-0.55	0.57	0.1787
15374.75746	0.12	0.58	0.1777
15375.77510	-0.48	0.59	0.1767
15376.74459	-2.32	0.57	0.1773

Continued on next page

Table A.3 – continued from previous page

Date BJD − 2440000	**Radial velocity ($m\,s^{-1}$)**	**Uncertainty ($m\,s^{-1}$)**	S_{HK}
15377.74203	-0.71	0.56	0.1773
15378.74358	3.15	0.61	0.1760
15379.79184	1.29	0.63	0.1763
15380.74383	5.79	0.60	0.1753
15400.74199	-0.20	0.67	0.1767
15401.76937	-1.48	1.43	0.1810
15403.73759	-3.72	0.72	0.1757
15404.73679	-4.06	0.65	0.1813
15405.74070	-5.50	0.65	0.1810
15406.73719	-3.14	0.60	0.1817
15407.75814	0.44	0.77	0.1800
15410.73844	5.03	0.65	0.1790
15411.73481	2.10	0.67	0.1780
15412.73197	1.94	1.18	0.1780
15413.73361	1.46	0.72	0.1633
15501.14886	-2.49	0.64	0.1827
15522.13389	1.58	0.64	0.1820
15529.17006	-12.59	1.56	0.1770
15543.14746	1.47	0.65	0.1847
15546.12332	-2.09	0.66	0.1827
15556.13576	12.54	0.71	0.1843
15557.07525	-3.09	0.68	0.1860
15559.12764	-2.47	0.78	-
15585.09918	-3.47	0.65	0.1810
15605.98568	-5.58	0.67	0.1860
15606.98402	-3.02	0.66	0.1863
15607.98123	-1.79	0.75	0.1847
15614.03861	-0.16	0.64	0.1897
15614.87512	0.99	0.81	0.1890
15633.99315	-4.90	0.66	0.1887
15635.05051	-1.75	0.69	0.1883
15635.99669	-1.28	0.63	0.1883
15636.75731	-1.73	0.59	0.1870
15663.88480	-5.35	0.69	0.1870
15667.96860	-0.55	0.61	0.1893
15668.93400	1.39	0.63	0.1893
15670.83890	-3.57	0.61	0.1887
15671.81197	-2.57	0.63	0.1890
15672.79841	-1.01	0.65	0.1887
15673.80273	-0.09	0.61	0.1873
15696.87321	-1.43	0.64	0.1880

Continued on next page

Table A.3 – continued from previous page

Date **BJD − 2440000**	**Radial velocity** **($m\,s^{-1}$)**	**Uncertainty** **($m\,s^{-1}$)**	S_{HK}
15697.79492	-2.39	0.61	0.1877
15698.79967	-3.50	0.59	0.1883
15699.80627	-6.59	0.62	0.1883
15700.82486	-4.69	0.63	0.1887
15703.77767	-1.50	0.61	0.1873
15704.74908	0.57	0.59	0.1900
15705.75018	-2.41	0.59	0.1903
15706.80704	-1.97	0.59	0.1910
15707.79932	-2.19	0.63	0.1920
15723.76737	1.40	0.43	0.1862
15728.75382	-3.26	0.60	0.1860
15731.79487	1.47	0.88	0.1897
15733.75978	1.02	0.59	0.1890
15734.78290	-2.40	0.55	0.1893
15735.78926	-2.06	0.54	0.1893
15738.75421	-4.14	0.58	0.1877
15751.74696	3.97	0.66	0.1967
15752.74130	1.89	0.62	0.1970
15759.74698	-0.52	0.62	0.1887
15760.73902	-0.42	0.63	0.1913
15761.74431	1.30	0.60	0.1900
15762.75287	-0.44	0.69	0.1883
15763.74854	-2.28	0.65	0.1910
15768.73583	0.27	0.62	0.1883
15770.74725	3.35	0.71	0.1810
15871.12714	-4.77	0.71	0.1830
15878.14302	-4.80	0.64	0.1927
15879.09674	-7.46	0.70	0.1923
15880.15181	-9.07	0.68	0.1907
15882.15606	-3.66	0.64	0.1903
15902.04440	0.58	0.64	0.1940
15903.04465	4.36	0.67	0.1933
15904.13372	5.35	0.63	0.1950
15905.06744	4.05	0.57	0.1950
15929.14692	-5.02	0.62	0.1987
15932.04835	-1.02	0.64	0.1957
15945.09826	-0.81	0.77	0.2053
15961.02344	6.64	0.66	0.2050
15967.94465	-0.29	0.68	0.1963
15972.95568	-0.37	0.62	0.2013
15990.90524	6.16	0.73	0.2030

Continued on next page

Table A.3 – continued from previous page

Date BJD − 2440000	**Radial velocity ($\mathbf{m\,s^{-1}}$)**	**Uncertainty ($\mathbf{m\,s^{-1}}$)**	S_{HK}
15991.90284	2.51	0.71	0.2030
15997.00945	-0.71	0.63	0.2000
15999.79702	3.92	0.68	0.2010
16018.90330	6.67	0.68	0.2040
16019.96914	2.13	0.63	0.2047
16027.79949	3.07	0.67	0.2077